MEASUREMENT OF FLOW BOUNDARY CONDITION DATA AND WING PRESSURES IN A WIND TUNNEL TEST OF A 45 DEG SWEPT WING

by

William P. Dwyer

SUBMITTED TO THE DEPARTMENT OF AERONAUTICS AND ASTRONAUTICS IN PARTIAL FULFILLMENT OF THE REQUIREMENTS FOR THE DEGREE OF

MASTER OF SCIENCE

at the

MASSACHUSETTS INSTITUTE OF TECHNOLOGY

February 1990

Signature of Author _____
Department of Aeronautics and Astronautics
January 5, 1990

Certified by _____
Professor Eugene E. Covert
Thesis Supervisor

Accepted by _____
Professor Harold Y. Wachman
Chairman, Department Graduate Committee

MEASUREMENT OF FLOW BOUNDARY CONDITION DATA AND WING PRESSURES IN A WIND TUNNEL TEST OF A 45 DEG SWEPT WING

by

William P. Dwyer

Submitted to the Department of Aeronautics and Astronautics on February 15, 1990 in partial fulfillment of the requirements for the degree of Master of Science.

Abstract

A low speed wind tunnel test has been carried out for one of the McDonnell Aircraft Company Generic Fighter Research Wing Model configurations, having 45 deg leading edge sweep, aspect ratio 3.0, and taper ratio 0.25. Testing was conducted at a Mach number of 0.15 and a Reynolds number based on the mean geometric chord of 2.6 million. The objective was acquisition of static pressure distributions from 368 taps on the wing surface as a database for the wing performance under the given tunnel conditions and for comparison with viscous computational field studies to validate the computational results and to assess wind tunnel wall interference. This comparison requires complete definition of the flow conditions on all of the boundaries of the test section, specifically, the wind tunnel walls and reflecting plane as well as the inlet and exit planes of the test section. The boundary condition measurements included static pressures along the walls and reflecting plane, and flow direction and dynamic pressure distributions across the entrance and exit planes. The range of angle of attack was purposely chosen to represent "large" interference, and to include substantial separation of the flow over the wing. Conical five-hole pressure probes were used to make the entrance and exit plane measurements. A study was conducted prior to the wing test to determine the characteristics of the five-hole probe measurements over a range of incident flow angles from -45 deg to 45 deg.

Thesis Supervisor: Professor Eugene E. Covert
Title: Department Head, Aeronautics and Astronautics

Acknowledgements

This research was carried out as a project of the Center for Aerodynamic Studies. Funding and support for this project were provided by the McDonnell Aircraft Company and the Center for Aerodynamic Studies. Acknowledgement is made to contributions from Jeffrey DiTullio, Michael R. D'Angelo, and Donald E. Robinson. I express sincere thanks to Frank H. Durgin for his helpful suggestions throughout this work, to Professor Judson R. Baron who offered the benefits of his experience while acting as my advisor through the wind tunnel testing period, and Professor Eugene E. Covert who advised me for the second half of the project. I would also like to thank my family for their support and Karen for helping me through it all.

W.P.D.

Table of Contents

List of Tables

List of Figures

Nomenclature

α	wing angle of attack corrected for $\Delta\alpha_i$
α	flow pitch angle refernced to tunnel coordinates
α'	flow pitch angle referenced to probe coordinates
α_o	probe machining error in pitch direction
α_{align}	pitch error in probe alignment with freestream flow
α_{geom}	wing geometric angle of attack
AR	aspect ratio
b	wing span
$B/2$	distance between top of test section and ground board
β	flow yaw angle referenced to tunnel coordinates
β'	flow yaw angle referenced to probe coordinates
β_o	probe machining error in yaw direction
β_{align}	yaw error in probe alignment with freestream flow
c	local section wing chord
C	tunnel cross-sectional area
C_D	drag coefficient
C_{D_f}	skin friction drag coefficient
C_{D_p}	pressure drag coefficient
C_{D_i}	correction to pressure drag
C_L	wing lift coefficient
C_l	section lift coefficient
C_p	pressure coefficient

C_{p_i}	pressure coefficient from scanivalve tap i
$(C_{p_i})_c$	corrected pressure coefficient from tap i
$C_{p_{zero}}$	pressure coefficient from transducer zero reading
C_r	root chord
C_t	tip chord
$\Delta\alpha_i$	correction to α_{geom}
ΔC_p	change in pressure coefficient
δ_{le}	wing leading edge flap deflection angle
δ_{te}	wing trailing edge flap deflection angle
E	ground board extension length
ε	accuracy of pressure coefficients
F	ground board trailing edge flap length
ϕ	probe roll angle
ϕ_{err}	error in roll angle setting
G	distance from tunnel centerline to ground board
H	minor axis of tunnel elliptical system
HL	hinge line of wing flaps
K_α	five-hole probe coefficient for pitch angle
K_β	five-hole probe coefficient for yaw angle
K_q^*	five-hole probe coefficient for dynamic pressure
K_{q^*calib}	K_q^* calculated using measured angles and calibration data
K_{q^*inner}	approximation to K_q^* for $\sqrt{\alpha'^2 + \beta'^2} \leq 12°$
K_{q^*outer}	approximation to K_q^* for $\sqrt{\alpha'^2 + \beta'^2} > 12°$
λ	taper ratio

Λ_{LE}	sweep of wing leading edge
$\Lambda_{1/4}$	sweep of wing quarter-chord
L_E	ground board length
L_o	length of short ground board
M	Mach number
P_1–P_5	pressures from individual holes of five-hole probe
P_s	tunnel static pressure
P_t	tunnel total pressure
ψ	probe yaw angle
q	tunnel compressible dynamic pressure
q_{inc}	tunnel incompressible dynamic pressure
q_{local}	dynamic pressure at probe tip
Re	Reynolds number
Re_p	Reynolds number based on five-hole probe diameter
$Re_{\bar{x}}$	Reynolds number based on mean geometric chord
R_E	distance from wing t.e. to ground board flap hinges
R_o	distance from wing t.e. to end of short ground board
ρ	density of air
S	wing planform area
t/c	ratio of maximum airfoil thickness to chord length
U_x'	x velocity component in probe coordinates
U_y'	y velocity component in probe coordinates
U_z'	z velocity component in probe coordinates
U_x	x velocity component in tunnel coordinates

U_y	y velocity component in tunnel coordinates
U_z	z velocity component in tunnel coordinates
V_{ave}	average velocity across test section
W	major axis of tunnel elliptical section
$\overline{x}$	x/c
$\overline{y}$	y/(b/2)
$\overline{z}$	z/c

Chapter 1

Introduction

Interference effects due to the proximity of wind tunnel walls to a model in the test section have been present in experimental data since the Wright Brothers conducted the first wind tunnel tests in the development of their airplanes. Most wind tunnel tests are run in an effort to measure the aerodynamic characteristics of a model in free air, but the test section walls constrict the flow around the model which would normally be free to expand outward, thus altering the data. Literature began appearing in the 1930's regarding corrections to the acquired data for wind tunnel wall interference and continues to be a matter of great concern. With the increasing sophistication of modern aircraft the influence of Reynolds number effects becomes more important. High Reynolds number requirements have been followed by an increase in the size of the models and hence the amount of wall interference. The standard corrections for wall interference are accurate up to 7.5% geometric blockage (reference [16]) which becomes a limiting factor in the design of a model to be used in a wind tunnel test.

A three-dimensional Navier-Stokes computer code has been developed at the McDonnell Aircraft Company (MCAIR) with hopes that one of the applications may be to calculate the flow about a body within the test section of a wind tunnel. In an effort to validate the use of the code for such an application, a wind tunnel test was conducted at the Wright Brothers Facility (WBF) using the MCAIR Generic Fighter Research Wing model at angles of attack representing as much as 11.4% geometric blockage based on the projected frontal area. The model is a semi-span wing with the leading edge swept back 45°, having 64A005 airfoil sections oriented parallel to the plane of symmetry, with an aspect ratio of 3.0, and a taper ratio of 0.25. The model was instrumented with 370 surface

static pressure taps covering both the upper and lower surfaces of the wing. To determine wall effects on the wing pressures, additional data was obtained for static pressures along the wind tunnel walls and reflecting plane, as well as flow direction and dynamic pressure at the entrance and exit planes of the test section. These measurements made up a complete set of boundary conditions to be used in the computer code to represent the tunnel environment accurately. The code can be used to numerically compute the wing pressures resulting from the given boundary conditions and its accuracy can be determined by comparing the computed and experimentally measured wing pressures. If successful, the computer code could then be run using unconstrained freestream boundary conditions, with the influence of wall interference upon the wing pressures being inferred from the difference between the two computer solutions. In addition to advancing the understanding of wind tunnel wall interference, it is foreseen that use of the code would reduce the amount of wind tunnel testing currently required in aerodynamic design, saving considerable testing time and expense. In addition to the pressure data, flow visualization runs were made during the test in order to identify the different flow regimes present on the wing model, and combined with the pressure measurements, to help better understand the overall performance of the wing model in the wind tunnel.

Acquisition of the flow direction and dynamic pressure at the entrance and exit planes of the test section was accomplished using conical five-hole pressure probes. It was known from previous use of the probes that the calibration coefficients used were linear for pitch and yaw angles of $\pm 10°$. It was desired to calibrate the probes over a wider range of angles to determine the character of the nonlinearity in the calibration coefficients to allow measurements of incident flow angles greater than 10° if necessary. To obtain this data a single five-hole probe was calibrated prior to the wing test for incident pitch and yaw angles of $\pm 45°$.

Chapter 2

Five-Hole Probe Study

2.1 Introduction

Differential pressure probes have been used to measure flow directions for many years. They afford the user an accurate measurement of flow direction with a relatively simple calibration and measurement procedure. Pressures are measured at orifices in a common plane on opposite sides of the probe face. The pressure difference can be related to the flow angle in that plane, by applying a calibration constant or calibration equation. A common probe used to measure flow speed and direction is the five hole probe. Five-hole probes having hemispherical, pyramidal, and conical tips are all common. References [2], [10], [12], and [15] contain discussion of methods to calibrate various types of five-hole probes. Calibration and measurements were documented for a hemispherically tipped probe in reference [12]. The probe was calibrated at 8 different freestream velocities for $|\alpha,\beta| \leq 45°$. The probe was found to have an RMS accuracy of 0.5° in pitch and 1.5° in yaw, and accuracy of ±0.02 psf in dynamic pressure.

The probes used in this study were conically tipped five-hole probes with a 60° cone angle. The probes were calibrated and used at a nominal dynamic pressure of 30 psf (110 mph) which corresponds to a probe Reynolds number of $Re_p=30x10^3$. Reference [8] showed that 60° conical probes were relatively insensitive to variations in the probe Reynolds number between $20x10^3<Re_p<80x10^3$. The probe body had a diameter of 0.38" and the probe side pressure orifices were cut perpendicular to the probe face. Figure B-1 shows a diagram of the five-hole probes.

A general method for their use had been developed previously at the Wright Brothers Facility (WBF) and the factors influencing measurements with the probes was available (see reference [3]). The calibration coefficients used were defined as

$$K_\alpha = \frac{(P_1 - P_3)}{q^*} \tag{2.1}$$

$$K_\beta = \frac{(P_2 - P_4)}{q^*} \tag{2.2}$$

$$K_{q^*} = \frac{q^*}{q} \tag{2.3}$$

$$q^* = P_5 - \frac{P_1 + P_2 + P_3 + P_4}{4.} \tag{2.4}$$

where the probe hole numbers are shown in figure B-1.

2.2 The M.I.T. Wright Brothers Wind Tunnel

The M.I.T. Wright Brothers Facility is a single return, closed circuit facility. The test section is 15' long and has a 7.5' by 10.0' elliptic cross-section (see figure B-2). The wind tunnel is currently capable of producing wind speeds from 0 to 250 ft/s (0 - 170 mph) at atmospheric pressure, and can be pressurized up to 2.0 atmospheres. All of the testing mentioned in this report was performed at atmospheric pressure.

2.3 Calibration Procedure

A single five-hole probe was mounted in the test section for the calibration runs (figure B-3). The tip of the probe was located on the centerline of the tunnel and was directly above the axis of rotation of the force balance turnable on which it was mounted. This positioning kept the probe tip fixed spatially as it was rotated with the turnable. The probe was mounted in a stainless steel tube of 0.38" ID and 0.5" OD, such that the tip of the probe extended 3.5" (9.2 diameters) from the end of the tube and the tube itself extended 15" (40.0 diameters) forward from the vertical 1" standard steel pipe as shown in the diagram. Thus the probe tip was 49.2 diameters in front of the standard steel pipe.

The five-hole probe was calibrated over a range of total included flow angles from

-45° to 45°. The flow angles included pure pitch and yaw angles, as well as combined pitch and yaw measurements. Figure B-4 defines the coordinate axes and angles of rotation used during the calibration. In calibrating, the probe roll angle was initially set to $\phi = 0°$. The turntable was rotated from -45° to 45° in 5° increments with the probe orifice pressures being measured at each setting. Non-dimensional pressure coefficients were computed and the data was stored for later reduction in which the three calibration coefficients were calculated. This procedure was repeated for roll angles from $\phi = 0°$ to 180° in 15° increments. A pure yaw angle corresponded to $\phi = 0°$ and 180° roll settings while the $\phi = 90°$ roll angle corresponded to a pure pitch angle. The intermediate roll angles gave combinations of both pitch and yaw angles.

2.4 Data Acquisition

The data acquisition for all of the wind tunnel testing was controlled using a DEC PDP 11/23 computer. Five channels were used to acquire the test data from the single probe calibration. All of the transducer signals were converted from analog to digital (A-D) by a PDP11 DR11-C data converter before the data was read by the computer. The probe pressures required one channel, while measurement of the the tunnel dynamic pressure, tunnel static pressure, total temperature, and A-D board zero offset used the remaining four channels. The A-D board offset was used to correct all data for a small but constant zero offset voltage of the A-D board in the computer. All measured quantities for the single probe calibration represented averages over 10 seconds of data which were sampled at a rate of 100 per second. It had been determined in previous tests at the WBF, that at a sampling rate of 100 per second, the minimum data time interval which produced repeatable pressure measurements was 2.0 seconds. The 2.0 second time interval was required to account for a low frequency oscillation in the tunnel flow caused by a separated flow region between the fan and the stilling section. The interval was increased to 10

seconds in an attempt to decrease the random error in the measurements by averaging additional data points.

The wind tunnel static pressure (P_s) was measured using an Omega PX-176, 0-50 psi absolute pressure transducer. The pressure was measured by 4 static pressure taps located in a vertical plane at the centerline of the turntable of which the locations are shown in figure B-3. The taps were connected to a large (0.25" ID) tube which acted as a reservoir volume within which the pressures could come to equilibrium to yield an average pressure in the cross-plane of the balance. A lead from this tube was connected to the Omega transducer.

The dynamic pressure (P_t) of the flow was measured using an MKS series 398 Baratron differential pressure transducer. The Baratron measured the difference between the tunnel total pressure (P_t), which was measured just upstream of the test section, and static pressure (P_s) giving the incompressible dynamic pressure of the flow.

$$q_{inc} = P_t - P_s \tag{2.5}$$

The pressure tubes from the five-hole probe were connected into a scanivalve along with leads from the wind tunnel total and static pressure. The pressures were measured using a Druck model PDCR differential pressure transducer which used the tunnel static pressure as a reference. The scanivalves had 48 taps which could be consecutively applied to the differential pressure transducer. Taps 48 and 1 were used for the tunnel static and total pressure respectively, and taps 2 through 7 were connected to holes 1 through 5 of the five-hole probe. The scanivalve was stepped through all of the occupied taps with the Druck measuring the pressure at each tap. In addition to the Druck pressure reading at the tap, the tunnel total pressure, static pressure, total temperature, and A-D board zero offset were measured at each tap.

Before the data was stored the 10 seconds of raw data were averaged and converted to non-dimensional coefficients, and the Reynolds number, Mach number, and compressible dynamic pressure were calculated for the flow.

All scanivalve measuring sequences started at tap 48. Tap 48 input the tunnel static pressure to both sides of the transducer to provide a reading that represented the zero offset of the transducer.

$$C_{P_{zero}} = \frac{P_{48} - P_s}{q_{inc}} \tag{2.6}$$

This pressure coefficient was subtracted from all of the scanivalve measurements that followed.

Tap 1 was applied to the transducer to measure the tunnel total pressure.

$$C_{P_1} = \frac{P_1 - P_s}{q_{inc}} - C_{P_{zero}} \tag{2.7}$$

The pressure taps from the five-hole probe were then read in succession with a pressure coefficient calculated for each tap.

$$C_{P_i} = \frac{P_i - P_s}{q_{inc}} - C_{P_{zero}} \quad (i = 2, 3, \ldots, 7) \tag{2.8}$$

Tap 48 was read again after tap 7 to determine the zero offset of the transducer at the end of a run.

$$C_{P_{48}} = \frac{P_{48} - P_s}{q_{inc}} - C_{P_{zero}} \tag{2.9}$$

This provided a means of correcting for any shift in the transducer zero that occurred during the run.

2.5 Data Reduction

Before any analysis was performed the pressure data from the five-hole probe was corrected for transducer zero shift and small errors in the transducer calibration as discussed below.

The Druck transducer zero was sensitive to temperature variations in the surrounding environment. The zero offset appears to change linearly with temperature over the normal

temperature range encountered in the wind tunnel. The transducer was mounted directly below the floor of the wind tunnel and thus was subject to any temperature change taking place within the tunnel. The temperature in the wind tunnel tends to change continually due to the energy added by the fan driving the flow and also due to the radiant energy of the sun shining on the exterior. The data runs lasted approximately 2 minutes each, and although the temperature change during any given run was small (less than 0.5°C) the transducer would experience a small zero shift and thus required correcting. Assuming that the scanivalve pressure measurements were taken at approximately equal time intervals, and also assuming that the temperature variation was approximately linear during any given run, a linear correction for the zero shift was applied as follows:

$$(C_{p_i})_c'' = C_{p_i} - \frac{i}{7} C_{p_{48}} \quad (i = 1, 2, \ldots, 7) \tag{2.10}$$

Prior to the calibration runs the Druck transducer itself was carefully calibrated so as to convert output voltages accurately for a reading of the corresponding applied pressure difference. As with any calibration there are limits to the accuracy of the procedure. Measuring the dynamic pressure across the transducer gave a means to correct for inaccuracy in the calibration. The pressure coefficient from tap 1 (total pressure) was expected to equal 1.00 ($C_{p_1} = 1.00$). A value which was less than 1.00 would indicate that the gain for all the pressure measurements was too small, or if C_{p_1} was greater than 1.00 then the gain was too large. Because C_{p_1} was never exactly equal to 1.00 the coefficients were all corrected to make $C_{p_1} = 1.00$.

$$(C_{p_i})_c' = \frac{(C_{p_i})_c''}{C_{p_1}} \quad (i = 1, 2, \ldots, 7) \tag{2.11}$$

The correction was generally less than 1% of the uncorrected value.

Finally the dynamic pressure was corrected to allow for compressibility. Although the flow was relatively low speed (110 mph) the small compressibility correction was included. The Mach number of the tunnel flow was computed from isentropic flow relations and the compressible dynamic pressure was calculated.

$$M^2 = 5\left(\frac{P_t}{P_s}\right)^{2/7} - 5. \tag{2.12}$$

$$q = 0.7\, P_s M^2 \tag{2.13}$$

The non-dimensional pressure coefficients were then corrected for compressibility.

$$(C_{p_i})_c = (C_{p_i})_c' \frac{q_{inc}}{q} \quad (i = 1, 2, \ldots, 7) \tag{2.14}$$

An error analysis was performed to determine the accuracy of the calculated pressure coefficients. Using the accuracy of the measuring equipment supplied by the manufacturers, and the test conditions under which the data was acquired, the accuracy of a pressure coefficient calculated from one pressure reading was calculated as $\varepsilon = \pm 0.03$. Because the final coefficients represented an average of 1000 readings it is expected that the error would decrease slightly. A comparison of repeated data from the McAir wing test performed after this probe study showed that the coefficents had a repeatability of ± 0.02.

2.6 Calibration Results

2.6.1 Calculation of Angles and Calibration Coefficients

Figures B-5 - B-7 plot the final pressure coefficients for the individual orifices of the five-hole probe for nominal roll angles of ϕ = 0°, 45°, and 90°. The plots show the symmetry of the probe and the behavior of the holes over the entire range of measurement. For the ϕ = 0° and 90° roll angle configurations it can be seen that the orifices in the wake of the probe tip enter a region of separated flow while at ϕ = 45° no holes were in the wake so no effects of separation are seen.

A coordinate transformation had to be performed in order to convert angles in the tunnel coordinate system to the probe coordinates (refer to figure B-4). The following equations were used to calculate the angles measured in the probe coordinates.

$$U_x' = U_x \cos(\psi) - U_y \sin(\psi) \tag{2.15}$$

$$U_y' = U_x \sin(\psi)\cos(\phi) + U_y \cos(\phi)\cos(\psi) + U_z \sin(\phi) \tag{2.16}$$

$$U_z' = -U_x \sin(\psi)\sin(\phi) - U_y \sin(\phi)\cos(\psi) + U_z \cos(\phi) \tag{2.17}$$

$$\alpha' = \text{atan}\,\frac{U_z'}{U_x'} \tag{2.18}$$

$$\beta' = \text{atan}\,\frac{-U_y'}{U_x'} \tag{2.19}$$

The primes indicate components or angles relative to the probe coordinate system, the unprimed quantities are referenced to the tunnel coordinate system. Initially the transformation was made assuming that the flow incident upon the probe was comprised only of the U_x component in the tunnel coordinate system; i.e. there was no upflow or crossflow ($U_y = U_z = 0$) in the freestream flow. The velocity was normalized so that an incident velocity vector had magnitude of 1, thus $U_x = 1$ was used in the initial transformation. In reality there were components of U_y and U_z due to errors in probe alignment with the freestream flow. Corrections for these flow components were made after determining U_y and U_z. The determination of these flow components follows in section 2.6.2.

After the data was reduced to the final corrected pressure coefficients the calibration coefficients K_q^*, K_α, and K_β were calculated and plotted.

$$K_q^* = C_{p_5} - \frac{C_{p_1} + C_{p_2} + C_{p_3} + C_{p_4}}{4.} \tag{2.20}$$

$$K_\alpha = \frac{C_{p_1} - C_{p_3}}{K_q^*} \tag{2.21}$$

$$K_\beta = \frac{C_{p_2} - C_{p_4}}{K_q^*} \tag{2.22}$$

These equations are identical to equations (2.1) - (2.3) but are expressed in terms of the non-dimensional pressure coefficients. Figure B-8 is a plot of K_α vs α' with β'

nominally zero, and figure B-9 is a plot of K_β vs β' with α' nominally zero. The figures show that the calibration curves are linear for $-10° < \alpha', \beta' < 10°$. Figures B-10 - B-12 are carpet plots of K_α, K_β, and K_{q^*} over the entire range of calibration angles. The character of the nonlinearities encountered at angles greater than 10° are similar to plots from reference [15] where the calibration was carried out using a hemispherical probe over $-25° < \alpha', \beta' < 25°$.

2.6.2 Determination of Calibration Errors

The next step in the data analysis was to calculate the probe machining errors and error in alignment with the flow. The procedure used is similar to that of reference [12]. This analysis was performed using the linear portion of the calibration curves ($-10° < \alpha', \beta' < 10°$).

The probe machining errors are comprised of two different errors: 1) incorrect placement of the orifices on the probe face and 2) holes being drilled non-perpendicular to the probe face. Determination of the errors will be described for the yaw direction, but the same procedure is used to find the errors in pitch as well.

To find the machining error the calibration lines (K_β vs β') from roll angles 180° apart were plotted. The machining error is equal to one-half the difference in values of the β' intercept between the two calibration lines. The machining error in α' was denoted by α_o' while the error in β' was denoted by β_o'. Errors made in aligning the probe with the freestream flow can also be found from plots of the calibration data from roll angles 180° apart. If no alignment error exists then the spread due to machining error should be centered about $\beta' = 0°$. If an alignment error does exist then the machining error will be centered about a non-zero angular value. This value is the flow alignment error. The alignment errors are denoted by α_{align} and β_{align}. Figure B-13 is a diagram showing the machining and alignment errors as found from the calibration plots for the yaw direction.

Because the probe was only rotated in the tunnel x-y plane by the balance turntable, angles outside this plane (pitch alignment angle) could not be deduced by the same method. Instead, the machining error in pitch was calculated as one-half the difference between the two pitch angles indicated by the probe measurement at the $\phi = 0°$ and 180°, $\beta' = 0°$ settings. The alignment error in pitch was taken as the average of the two pitch angles indicated by the probe measurement at the two positions. The probe machining error in yaw was found to be $\beta_o' = 0.3°$ while the alignment error was $\beta_{align} = 0.3°$. The values obtained for the pitch direction were $\alpha_o' = 0.3°$ and $\alpha_{align} = 1.2°$.

It was expected that even if there was an upflow at the probe the plot of K_α vs β' for the $\phi = 0°$ and 180° cases should be a straight line, or at least resemble an even function due to the symmetry of the probe. This was also expected for the K_β vs α' line at $\phi = 90°$ roll. Neither of these expected conditions were found. It was postulated that if the roll angle were in error it would effect the plots by causing the calibration line to have a non-zero slope at $\alpha', \beta' = 0.0$. Figure B-14 plots K_β vs α' for the $\phi = 75°$, 90°, and 105° roll angle settings. The slopes of all three lines were calculated. The difference in slope between the $\phi = 75°$ and 90° roll cases was the same as the difference between the $\phi = 90°$ and 105° roll cases. This verified that the roll angle increment was consistent, but the absolute value of the roll angle setting was in error. The error in roll was deduced by interpolating the roll value corresponding to the K_β vs α' slope equal to zero. This value was found to be $\phi_{err} = 2.8°$. The error in roll was caused by a set screw hole in the probe casing which was out of alignment with the measuring orifices in the tip of the probe.

To complete the corrections to the data, the values of α_{free} and β_{free} were used with

$$\tan(\alpha_{align}) = \frac{U_z}{U_x} \tag{2.23}$$

$$\tan(\beta_{align}) = \frac{U_y}{U_x} \tag{2.24}$$

$$\sqrt{U_x^2 + U_y^2 + U_z^2} = 1 \tag{2.25}$$

to calculate the components of the velocity vector incident upon the probe. Equation (2.25) is used to normalize the velocity vector. Using the new values of U_x, U_y, U_z, and the correction to the roll angle, the calibration angles were recalculated using equations (2.15) - (2.19). After the new angles were calculated the values of α_o' and β_o' were subtracted to account for the probe asymmetry errors yielding the final values for α' and β' vs K_α, K_β, and K_q*.

2.6.3 Least Squares Fit to Calibration Data

For practical application the calibration data is most useful if put into a form yielding the flow angles as a function of K_α and K_β.

$$\alpha' = f(K_\alpha, K_\beta) \tag{2.26}$$
$$\beta' = f(K_\alpha, K_\beta) \tag{2.27}$$

To achieve this the calibration data was fit to polynomials of varying order using the least squares method in a fashion similar to that used in reference [21]. The calibration data used in the least squares fits was limited to include only data for total flow angles less than or equal to 25°. The data was limited to this range because it was known that it would be increasingly difficult to fit the curves for wider ranges of data, and because the curve fits were performed after the MCAIR wing test, where preliminary indications were that the magnitude of the largest flow angle encountered was 25°.

In an attempt to evaluate the order of the polynomial required to accurately fit the data, a set of curves were fit to approximate α' vs K_α and β' vs K_β for the nominal $\phi = 0°$ and 90° roll angle settings. Only odd functions of order 1, 3, and 5 were fit to the data. Figures B-15 - B-17 show the experimental data and the approximating functions. The figures show that the fifth order polynomial best approximated the calibration data. The following equations describe the fifth order curves.

$$\alpha' = -0.29 - 29.42K_\alpha + 8.12K_\alpha^3 - 2.41K_\alpha^5 \tag{2.28}$$

$$\beta' = 0.24 + 29.21K_\beta - 7.26K_\beta^3 + 1.83K_\beta^5 \tag{2.29}$$

This data yielded an RMS error in α' of 0.2° and an RMS error in β' of 0.1°.

Next a fifth order function with full coupling between K_α and K_β was fit to the calibration data over the range $-25° \le \sqrt{\alpha'^2 + \beta'^2} \le 25°$. After discarding terms with small contributions the following 14 term polynomials resulted.

$$\alpha' = -0.38 - 30.10K_\alpha + 10.31K_\alpha^3 - 3.75K_\alpha^5 + 0.33K_\beta + 0.30K_\beta^3 - 0.10K_\beta^5 + 0.20K_\alpha K_\beta - 1.44K_\alpha^2 K_\beta + 5.85K_\alpha K_\beta^2 + 1.03K_\alpha^4 K_\beta - 2.15K_\alpha K_\beta^4 - 3.02K_\alpha^3 K_\beta^2 + 0.27K_\alpha^2 K_\beta^3 \quad (2.30)$$

$$\beta' = 0.25 + 0.14K_\alpha - 0.04K_\alpha^3 - 0.05K_\alpha^5 + 29.75K_\beta - 8.86K_\beta^3 + 2.80K_\beta^5 - 0.52K_\alpha K_\beta - 7.77K_\alpha^2 K_\beta - 0.01K_\alpha K_\beta^2 + 3.02K_\alpha^4 K_\beta + 0.12K_\alpha K_\beta^4 - 0.05K_\alpha^3 K_\beta^2 + 4.03K_\alpha^2 K_\beta^3 \quad (2.31)$$

The curve for α' yields an RMS error of 0.2° and a maximum error of 0.4° when compared with the calibration data. The curve for β' yields an RMS error of 0.1° and a 0.4° maximum when compared with the calibration data.

To complete the analysis of the calibration data a functional form for K_q^* was derived from the calibration data to calculate the dynamic pressure at the probe tip. The coefficient was denoted by $K_{q^*_{calib}}$ and was calculated using the following equations:

$$K_{q^*calib} = K_{q^*inner} = 0.985 \quad for \ \sqrt{\alpha'^2 + \beta'^2} < 12.0° \quad (2.32)$$

$$K_{q^*calib} = K_{q^*outer} = -1.66 - 0.84CA + 1.58CA^2 - 0.09CA^3 - 0.59CA^4 - 0.47CA^5 - 0.67CB + 1.02CB^2 + 0.02CB^3 + 0.88CB^4 - 0.04CB^5 + 0.94CA{\cdot}CB + 0.91CA^2CB + 0.65CA{\cdot}CB^2 + 1.17CA^2CB^2 + 2.09CA^3CB - 0.74CA{\cdot}CB^3 - 1.47CA^4CB + \quad (2.33)$$

$$0.60CA^3CB^2 - 0.71CA^2CB^3 - 1.53CA \cdot CB^4$$

where $CA = \cos(\alpha')$
$CB = \cos(\beta')$

$$for \ \sqrt{\alpha'^2 + \beta'^2} > 12.0°$$

The second equation for $K_{q^*_{calib}}$ was derived by least squares fitting a power series of cosine terms to the calibration data for K_{q^*} corresponding to $12° < \sqrt{\alpha'^2 + \beta'^2} \leq 25°$. It was decided to use an inner and outer form for K_{q^*} after unsuccessfully attempting to fit curves to the entire range of data. Because the curve for K_{q^*} vs α',β' was so level for total flow angles less than 12°, and so highly sloped for total angles greater than 12° (figure B-12), it was unreasonable to assume a single function could fit both regions of the curve, thus the average value of the inner portion was used as the value of $K_{q^*_{inner}}$. This was calculated as $K_{q^*_{inner}} = 0.985$. The outer portion of the data was best fit by the 21 term, fifth order, cosine series (equation (2.33)). The maximum error between $K_{q^*_{inner}}$ and the calibration data was found to be 1.0% of the dynamic pressure (0.30 psf) while the RMS error was 0.4% (0.12 psf) while the maximum difference found for $K_{q^*_{outer}}$ was 1.4% (0.42 psf) with an RMS error of 0.7% (0.21 psf).

To obtain $K_{q^*_{calib}}$ the flow angles must first be calculated using equations (2.30) and (2.31) and then $K_{q^*_{calib}}$ can be obtained from equations (2.32) and (2.33). The local dynamic pressure is then calculated by the following equation.

$$q_{local} = \frac{K_{q^*}}{K_{q^*_{calib}}} \cdot q \tag{2.34}$$

In this equation K_{q^*} is the value of the coefficient calculated from equation (2.20), $K_{q^*_{calib}}$ is the value of K_{q^*} from equations (2.32) and (2.33), and q is the measured freestream dynamic pressure of the flow. This equation can be written in an alternate form to more readily show how the dynamic pressure is calculated.

$$q_{local} = \frac{q^*}{q} \cdot \frac{q_{local}}{q^*_{calib}} \cdot q \tag{2.35}$$

Here q_{local} is the tunnel dynamic pressure that was measured during the calibration runs and which was also equal to the dynamic pressure at the probe. The value of q^* calculated from the experimental data and q^*_{calib} are nearly equal except for any variation in the probe measurements due to Reynolds number effects. Reference [8] showed that the variation of probes measurements was negligible for the conditions at which the probe was be used (Re_p=30.1x10^3), hence the right hand side of equation (2.35) reduces to q_{local}, which is the dynamic pressure at the probe tip.

2.7 Summary of Single Five-Hole Probe Study

A conical five-hole probe was calibrated at a dynamic pressure of 30 psf (110 mph) for pitch and yaw angles between $-45° \le \alpha', \beta' \le 45°$. Three calibration coefficients, K_α, K_β, and K_{q^*} were calculated using equations (2.20) - (2.22). The calibration data was corrected for errors in probe manufacturing and alignment with the freestream flow in the wind tunnel. Two fifth order polynomials were fit to the calibration data for total flow angles $\le 25°$ to give the measured pitch and yaw angles as a function of K_α and K_β. A fifth order cosine series was fit to the K_{q^*} data resulting in a method of calculating the dynamic pressure as a function of K_α, K_β, and K_{q^*} for total flow angles $\le 25°$. The use of these calibration functions resulted in angular measurements with an accuracy of 0.4° in both pitch and yaw, and dynamic pressure measurements accurate to 0.42 psf for $\sqrt{\alpha'^2 + \beta'^2} \le 25°$.

Chapter 3

Experimental Setup and Procedure

3.1 Introduction

A wind tunnel test of a wing with 45° leading edge sweep was conducted at the Wright Brothers Facility (WBF) at the end of May, 1989. The test was part of the Generic Research Wing Wind Tunnel Wall Interference Program which was a joint research venture undertaken by the McDonnell Aircraft Company (MCAIR) and the Center for Aerodynamic Studies (CAS). The objective of the wind tunnel test was to measure the static pressure over the wing surface as well as to measure the flow conditions on all of the boundaries surrounding the test section. The boundary conditions were to be implemented in a three-dimensional Navier-Stokes computer code developed at MCAIR to numerically evaluate the wing pressures in a tunnel situation. Such pressures are to be compared with those experimentally measured as one means of validating the computer code. If successful one could foresee applying the codes to boundary conditions for an unconstrained freestream flow as well as providing corrections for wind tunnel wall interference.

3.2 Wall Static Pressure Taps

Measuring the static pressure at the walls along the length of the test section was included as part of the boundary measurements to be made in the wind tunnel test of the wing. To facilitate the pressure measurements static pressure taps were installed at 6 streamwise locations with 10 taps in a row around the test section at each location. The streamwise stations are shown in figure B-21. The positions of the taps around the test section at each streamwise location are shown in figure B-22. In addition to the new pressure taps, 6 existing pressure taps, 3 along each side of the test section were also used.

The static pressure taps were made from elevator screws with a 1.25" diameter head and 1.38" long shaft. The head of the screws were machined flat and a 0.057" hole was drilled in the middle of each head, extending down through the body of the screw. The hole was enlarged at the back of the screw to 0.072" in diameter so a short length (about 1.0") of stainless steel tubing (0.072" OD, 0.057" ID) could be soldered into the back of the screw. The stainless steel tubing was used as a connection for the plastic pressure tubing used between the tap and the scanivalve assembly which measured the pressure.

After installing the pressure taps the wall pressures were measured at a tunnel dynamic pressure of 30 psf with the test section completely empty. Because the reference static pressure is measured at the walls it was expected that all of the pressure coefficients would be $C_p = 0.00 \pm 0.03$, where $\varepsilon = \pm 0.03$ was a liberal allowance for the error associated with the pressure coefficients as calculated in section 2.5. Wall pressure measurements made with the test section empty indicated that several pressure coefficients differed from zero by more than 0.05. Upon investigation it was found that the pressure taps yielding these readings were either set in the wall with the tap face slightly skewed, or with the tap head not flush with the surface. The faulty taps were reset and the static pressures were again measured with the test section empty. The new pressure readings indicated that the taps had been sufficiently corrected for use in the wind tunnel test.

3.3 Five-Hole Probe Rake Calibration

A rake had been constructed during the month of April to hold 9 five-hole probes for flow measurement across the test section of the wind tunnel. The rake had a main support tube made from a 54" long, 1.5" OD stainless steel tube. The probes were mounted at the end of 0.5" OD stainless steel sleeves which extended 12.5" outward from the main support tube. The sleeves were spaced 6" apart along the length of the rake. The five-hole probes were inserted into the ends of the support sleeves such that the probe tip extended 3.5"

ahead of the probe sleeve, i.e. the probe tips were located 16" (42 probe diameters) upstream of the main support tube. Figure B-24 shows a diagram of the five-hole probe rake. The 5 plastic pressure tubes from each probe were run inside the sleeves into the main support tube, then out both ends of the main tube and through the top of the tunnel. Two 24" extensions of the rake were also fabricated, so that the rake would span the width of the test section. These sections were made for two reasons. The first was to facilitate mounting the rake in the test section with a minimum of hardware that might interfere with the tunnel flow. The second was an attempt to make the rake as 2-dimensional as possible to minimize any effects caused by flow around the main support tube or by flow around the row of probes. The extensions were made similar to the main rake, but due to a limited number of five-hole probes, wooden dowels were employed to simulate conical five-hole probes and were inserted in the sleeves as image probes.

At the time of the rake calibration it was expected that the flow angles to be measured in the MCAIR wing test would not exceed 10° in either pitch or yaw. It was felt that the wing would not have a large effect on the upstream flow and that the large angles induced by the vorticity shed from the wing would be confined to small regions covered by one or two probes. Also it was desired to minimize the time required to calibrate the rake due to scheduling constraints. For these reasons the five-hole probe rake was calibrated for $\pm 10°$ in α,β.

It was conjectured that there would be errors in probe alignment due to inexact machining of the rake. Such errors were measurable corrections to be accounted for in the pitch and yaw angle calculations. The errors were measured by leveling the center probe, (#5), with the rake held horizontally using a sensitive bubble level, and then measuring the relative pitch angle of the remaining 8 probes using an electronic digital inclinometer. Probe #5 was then used as the reference when aligning the rake in pitch during the MCAIR wing test. The errors in yaw were measured using the same procedure but with the rake held vertically.

The five-hole probe rake was set up in the tunnel as shown in figure B-23 for the calibration runs. The probe numbering scheme along the rake is also shown in the figure. The calibration runs were made at a tunnel dynamic pressure of 30 psf. The runs included roll angles ϕ = 0°, 90°, 180°, 270°, and 45°. For each roll angle the turntable was set from -10° to 10° in 5° increments. It was only possible to keep the center probe of the rake spatially fixed in the tunnel as the rake was rotated by the turntable for the ϕ = 90° and 270° roll angle settings, thus the procedure for calculating probe machining and flow alignment errors used in the single five-hole probe study would only be valid on the center probe. The probe used in the single probe study was placed in the center position to provide a direct comparison between the two calibrations and determine what affect, if any, the rake had on the characteristics of the five-hole probes.

3.4 Wing Model in the Tunnel

The description of the wing model setup in the tunnel follows from reference [18].

The wing was a semi-span model with the leading edge swept back 45°. It had an NACA 64A005 symmetric cross-section oriented parallel to the plane of symmetry, taper ratio λ = 0.25, and aspect ratio AR = 3.0. The wing had deflectable leading and trailing edge flaps extending from the root of the wing outboard to the 0.75 semi-span line as shown in figure B-25. The leading edge flap was hinged at the 20% chord line and could be set to 0°, 10°, and 20° deflection. The hinge line for the trailing edge flap was at the 75% chord line and had settings of 0°, 10°, and 30°. The wing was instrumented with 10 chordwise rows of static pressure taps with a spanwise distribution given by

$$\bar{y} = \frac{y}{b/2} = 0.05 + 0.95 \cdot \cos\left(\frac{10-k}{20}\right) \quad (k = 0, 1, \ldots, 9) \tag{3.1}$$

where k is the tap row number as shown in figures B-26 and B-27. Each row had a tap at the leading edge, 24 taps on the wing upper surface, and 12 taps on the lower surface. The tap locations can be found in table A-2.

The wing had a semi-span length $b/2$ = 48" and root chord measuring C_r = 51.2". It was mounted vertically in the wind tunnel test section on top of a turntable which allowed for rotation from α_{geom} = -5° to 35° angle of attack. Since the wing was a semi-span model, a reflecting plane (ground board) was used to provide the symmetric induced affects of the opposing semi-span of the wing. The ground board was 104" wide and was mounted 20.5" below the centerline of the test section. The distance from the top of the test section to the ground board was 65.5". The 48" semi-span of the wing corresponded to 73% of the distance from the ground board to the top of the test section. Figure B-28 is a view looking downstream at the wing and the ground board in the test section.

The ground board was 4" thick, so the leading edge was made as a half-ellipse with 8.5" semi-major axis and 4.0" minor axis. The leading edge of the ellipse was positioned 9" downstream of the entrance to the test section. The ground board extended 179" downstream, which placed the end 8.0" into the diffuser at the end of the test section. Figure B-29 shows a side view of the wing and ground board in the test section. The last 18" of the ground board was made of deflectable flaps designed to adjust the stagnation point on the front of the ground board by deflecting the flaps upward. An investigation into the best flap configuration is described in reference [18]. The investigation showed that the best configration for testing the MCAIR wing was with the ground board flaps undeflected to avoid imposing a positive pressure gradient on the trailing edge of the wing which was found to accompany an upward deflection of the flaps.

The ground board was instrumented with static pressure taps aligned in three streamwise rows (figure B-30). One row was along the tunnel centerline while the other two were offset 20" to either side. The portion of the ground board surrounding the wing was made as a circle to allow it to rotate with the wing. There were 11 static pressure taps located on this portion of the ground board which rotated with the ground board as the wing was set to different angles of attack. The tap locations are listed in table A-3.

3.5 Data Acquisition

The data acquisition was handled in the same manner for the wall static pressure tests, rake calibration runs, and wing test as was used in the single five hole probe study. The DEC PDP 11/23 was used to control all data acquisition. The number of channels of data taken was equal to 4 plus the number of scanivalves used. Four channels were reserved for wind tunnel total pressure, static pressure, total temperature, and the zero offset reading of the A-D board in the computer.

The equipment used to measure all of the needed quantities for the mentioned runs was the same as was used in the single five-hole probe study. The incompressible dynamic pressure of the wind tunnel was measured using a Baratron series 398 differential pressure transducer; the test section static pressure was measured using an Omega model PX-176 0-50 psi absolute pressure transducer; the test pressures were measured using Druck model PDCR differential pressure transducers; and all data was converted from analog to digital by the PDP11 DR11-C data converter before being read by the computer.

3.5.1 Wall Static Pressures

Two scanivalve and pressure transducer assemblies were used in acquiring the pressure data during the wall static pressure tap tests. The scanivalves were mounted on top of the exterior of the test section. The first three rows of wall taps were connected to one transducer while the last three rows were connected to the second. All data was sampled at a rate of 100 per second for 5 seconds. Taps 48 and 1 on the scanivalves were reserved for the tunnel static and total pressure respectively while the next 30 taps were used for the wall pressures.

3.5.2 Five-Hole Probe Rake Calibration

The setup from the wall static pressure tap runs was used for the calibration of the five-hole probe rake, with an extra scanivalve added for the probe rake. Again tap 48 and 1 were reserved for the tunnel static and total pressure on all three scanivalves. Taps 2-46 on the third scanivalve were used for the pressures from the 9 five-hole probes on the rake. Wall static pressures were measured during the calibration to determine whether any changes in the wall pressures were induced by the rake in the tunnel.

3.5.3 MCAIR Wing Test

All of the data acquisition setups for the MCAIR wing test used 12 channels of data. These included the 4 usual quantities mentioned above, plus 8 scanivalve and pressure transducer assemblies. Figures B-31 and B-32 map the different regions of the wing covered by the 8 scanivalves required to measure the wing static pressures. These scanivalves were mounted in a hollow box in the ground board located adjacent to the wing. The two reference static pressure taps nearest the floor were covered for the entire wing test because they were located below the ground board, thus the tunnel static pressure represented the average of the pressures measured by the two remaining taps. All of the data taken in the test was sampled at a rate of 100 per second for 5 seconds.

In order to measure the wall and ground board pressures, four "shared" scanivalves were removed from the wing. Scanivalves #2 and #3 were used to measure the ground board static pressures while scanivalves #4 and #7 were used to measure the wall static pressures. The pressures were also read on the four scanivalves remaining on the wing.

Five-hole probe rake measurements required the removal of another scanivalve from the wing. Scanivalve #5 was used for the rake. The wall and ground board pressures were again measured along with the pressure from the three scanivalves remaining on the wing.

3.6 Wing Test Procedure

The wind tunnel test was run at a nominal dynamic pressure of 30 psf which corresponds to a wind speed of 110 mph, a Reynolds number of 1.0 million/ft, and a nominal Mach number $M = 0.15$. This represents a Reynolds number based on the mean aerodynamic chord of the wing of $Re_{\bar{x}} = 2.6$ million. The test was run with the 45° swept wing in two different configurations. The first configuration was with leading and trailing edge flaps set to zero deflection ($\delta_{le} = \delta_{te} = 0$). This configuration was tested at $\alpha_{geom} = 0°$, 6°, 18°, and 30° angle of attack. The given angles represent 1.2%, 2.4%, 7.2%, and 11.6% geometric blockage of the wind tunnel test section respectively. The second configuration had both the leading and trailing edge flaps deflected $\delta_{le} = \delta_{te} = 10°$. This case was run at $\alpha_{geom} = 6°$ angle of attack. This configuration had approximately 2.4% geometric blockage.

Measurement of the wing pressures, which required all 8 scanivalves, was performed first. The wing pressures were measured at $\alpha_{geom} = 0°$. After the data was acquired, chordwise pressure plots were made to check the data for accuracy. Because the airfoil has a symmetric cross-section the upper and lower surface pressure plots should have been identical at $\alpha_{geom} = 0°$. It was found that slightly different pressures existed on the two surfaces so the zero angle was adjusted and the pressure data was taken again. Upon inspecting the second set of data it was found that the zero angle had been reset satisfactorily, and the wing pressures were measured at $\alpha_{geom} = 0°$, 6°, 18°, and 30°.

After the wing pressure readings were obtained scanivalves #2 and #3 were removed from the wing and connected to the ground board taps and scanivalves #4 and #7 were removed and connected to the wall static pressure taps. The tunnel was run again with the wing at the 4 angles of attack with pressure readings taken on all 8 scanivalves.

When the wall and ground board pressures had been acquired the five-hole probe rake was set up at the test section entrance and scanivalve #5 was removed from the wing to

measure the five-hole probe pressures. The rake was leveled horizontally using the digital inclinometer set on the main rake tube. The pitch angle of the rake was set by leveling probe #5 on the rake and the yaw angle of the rake was set by measuring the distance from the ends of the rake to a pair of holes drilled in the walls at the resolving center of the balance. Ten different rake positions were used to cover the entrance and exit planes of the test section (see figure B-33). The rake measurements were made for the 4 angles of attack with the pressures on all 8 scanivalves measured at each setting. When the rake measurements at the test section entrance had been completed the process was repeated at the test section exit.

The procedure for the wing with deflected flaps was carried out in the reverse order as the case with undeflected flaps. The rake measurements at the exit plane were taken first, followed by the entrance plane measurements, then wall and ground board pressures, and finally the wing static pressures were measured.

Flow visualization runs were made for each of the wing configurations. Flow visualization techniques included both yarn tufts and smoke. The yarn tuft runs were made with the wind velocity set to 110 mph. The smoke runs could not be made at a wind velocity greater than 15 mph, because above this limit the smoke would diffuse too rapidly to be seen flowing over the wing. Still photographs and videotape movies were made of the flow visualization runs. For the runs with undeflected flaps the wing was rotated from $\alpha_{geom} = 0°$ to 30° in 3° increments. For the case with $\delta_{le} = \delta_{te} = 10°$ the flow visualization runs were used to determine the angle of attack at which separation first occurred on the flaps. This was used to determine the angle of attack at which the wing pressures and boundary conditions were measured for that wing configuration.

A complete listing of the run schedule is given in table A-4.

Chapter 4

Experimental Results

4.1 Wall Pressure Tap Tests

After the wall static pressure taps had been seated, measurements were taken with the wind tunnel test section empty. It was expected that all pressure readings would result in non-dimensional coefficients of $C_p = 0.00 \pm 0.03$ (0.03 was the stated accuracy of the pressure coefficients). However, the first set of readings showed several pressure coefficients to be approximately 0.05 in magnitude, which was considered unacceptably large. All of the taps were reflushed and the static pressures were again measured with the tunnel empty. The results of the initial and final pressure readings are shown in figures B-34 - B-39. The tunnel outline corresponds to the C_p = 0.00 locus, and the graduations to the interior and exterior of the tunnel cross-section indicate negative and positive pressure coefficients respectively. Virtually all of the pressure coefficients deviated from zero by less than 0.02 in magnitude. One tap in row 3 was found to have a pressure coefficient C_p = 0.03. This reading was considered to be marginally acceptable. While resetting the new wall static pressure taps it was noticed that the reference static pressure taps were not flush with the wall surface. The reference taps had a thin bronze face plate (approximately 3" in diameter), which sat with the back of the plate flushed to the wall, such that the front of the plate protruded approximately 0.063" from the wall. The taps were reset such that the front edge of the face plate was flush with the wall surface. The taps were tested against the average pressure of 4 of the new wall taps which had been purposely located next to the reference pressure taps for such a procedure. The newly seated reference taps proved to yield incorrect pressure readings. Upon closer investigation it was found that the center of the face plate had a slight concavity. It was inferred that the concavity at the center of the

tap acted to offset the effects of the bump created by the edge of the face plate. The taps were left mounted with the front of the face plate flush with the wall surface, but the concavity was filled with wall patching compound. When tested again, the reference static pressure taps gave correct pressure readings. It was inferred from the experience with the reference taps that even small changes in the wall surface would effect the static pressure reading in the vicinity of the changes in the wall. The walls have small bumps due to light fixtures and window casings as well as local dips and bumps due to imperfections in the plywood panels of which the walls are composed. Any of these anomalies if near a pressure tap could induce local variations in the flow producing non-zero pressure coefficients.

4.2 Five-Hole Probe Rake Calibration

After the data from the five-hole probe rake calibration was reduced, a least squares line was fit to the data for each probe in both the pitch and yaw directions. Figures B-40 and B-41 show the calibration lines of probe #5 which was typical of all the probes on the rake. The slopes of the calibration lines varied only slightly along the length of the rake. Figure B-42 shows the variation of calibration slopes. In general the slopes from the yaw calibration were slightly larger than those in pitch, making the probe readings more sensitive to changes in yaw than in pitch (an average of 1.5% more sensitive, with a 3.0% maximum difference).

The probe used in the single probe study was intentionally used as probe #5 (the middle probe) on the rake, so that comparisons could be made to determine any effects on the probe measuring characteristics caused by the rake mounting. The slopes in the linear calibration range compare favorably between the single probe study and the rake calibration data. The slope in pitch from the rake calibration was 3% less than the slope from the single probe study, and in yaw it was 2% less for the rake than the single probe. One would

expect the slopes from the calibation of a single five-hole probe to be equal in both pitch and yaw due to the symmetry of the probe. It is also reasonable to expect the same from the rake calibration with the probe mounted at the center of the rake for the same reason. This assertion is supported by the data from both the single probe study and the rake calibration, where the slopes in pitch and yaw differed by 0.1% and 0.7% respectively.

It was desired to correct for errors in the calibration due to misalignment with the freestream flow, probe asymmetry, and error in roll angle setting. Throughout the rake calibration procedure the center probe, (#5) was the only probe to remain spatially fixed in the tunnel. The method used to calculate the calibration errors depends on the flow being uniform in direction and magnitude over the probe tip for all of the calibration positions. Probe #5 was the only probe to remained fixed spatially throughout the calibration, so for this reason probe #5 was the only probe for which the error calculations could be performed. The error in alignment with the freestream flow was found to be $\alpha_{align} = -1.5°$ in pitch and $\beta_{align} = 0.7°$ in yaw. The alignment errors are a result of the fact the flow in the test section in not everywhere uniformly downstream. The rake was aligned by referencing the center probe to be perpendicular to gravity (set in pitch using a level), and by referencing the support tube to be perpendicular to the tunnel centerline in yaw. The final alignment errors are a combination of errors in aligning the rake with the centerline, and errors due to the fact that the flow in the tunnel at probe #5 did not coincide exactly with the centerline of the test section. The errors due to probe asymmetry were found to be the same in pitch and yaw directions with $\alpha_o' = \beta_o' = 0.1°$. The error in roll angle setting was found to be $\phi_{err} = 2.8°$. It is noted that the roll angle error was found to be the same in the single five-hole probe study. This was expected because the probe was held within the stainless steel sleeve using the same set screw hole as the single probe study. The location of the set screw hole was found to be the cause of the roll error in the single probe study. It was also expected that the same probe machining errors would be found for the probe in the

rake as were found in the single probe study. The machining errors were equal in pitch and yaw as was found previously, but the magnitude of the errors was found to be smaller with the probe mounted in the rake (0.1° in the rake compared to 0.3° from the single probe study). This was not considered a cause for great concern because the magnitude of the difference is very small and can be due to factors other than the method of calibration. One possible source of the error could be that the rotational axes of the rake and probe #5 did not coincide, causing probe #5 to change its orientation to the freestream flow when rotated, thus causing errors in the calculation of the probe machining error.

Geometric errors were found for the position of the probes along the rake relative to probe #5. The measurements can be found in table A-1. The measured angles were used as corrections to the calculated flow angles.

4.3 Results of the Wing Test

4.3.1 Non-dimensional Coefficients

Carpet plots for the upper surface pressure coefficients are presented in figures B-43 - B-48. Figure B-43 is the zero plane for the pressure coefficients. The view shown is looking upstream at the airfoil with the airflow parallel to the X/C_r axis. Each grid node represents the pressure coefficient at a wing surface tap. The lines forming the mesh were determined by fitting a second order spline to the pressure coefficients. The 10 mesh lines parallel to the X/C_r axis represent the pressure coefficients for each of the 10 pressure tap rows. Each was determined from a spline fit to the 25 pressure coefficients measured along that tap row. The 25 mesh lines extending from the wing root to the wing tip represent the pressure coefficients along the span at the 25 x/c locations. Each was determined from a spline fit to the 10 pressure coefficients measured at a specific x/c tap location. Mesh lines which would not be visisble from the viewing perspective were not plotted.

The distributions for $\alpha_{geom} = 6°$ shows that the flow is attached over all but the outer 5% of the wing semi-span. The pressure coefficients along the leading edge of the wing decrease moving outboard until there is a sudden rise in the pressure at 60% of the semi-span. This rise in pressure was believed to be caused by a 0.009" gap between the outboard leading edge flap and the wing tip section of the model. Outboard of this gap the pressure again decreases as a result of a vortex attached to the leading edge. The vortex detaches from the leading edge at 90% of the semi-span and travels downstream off the airfoil.

At $\alpha_{geom} = 18°$ (figure B-46) the outboard 80% of the semi-span is in stalled flow. The extreme suction peak at the inboard leading edge is due to a leading edge vortex that can be seen to detach at about 15% of the semi-span and travel downstream over the airfoil. The vortex only remains attached to the wing upper surface back to about 30% of the chord. Beyond this the vortex detaches from the wing and travels downstream in the separated wake. For $\alpha_{geom} = 30°$ (figure B-47) the airfoil has completely separated flow over the entire upper surface. The $\alpha_{geom} = 6°$, $\delta_{le} = \delta_{te} = 10°$ case (figure B-48) has a smaller suction peak at the leading edge than the $\alpha_{geom} = 6°$ case with undelfected flaps, but there are also suction peaks at the 20% and 75% chord locations corresponding to the flap hinge lines.

Lift and profile drag coefficients for the airfoil were determined by integrating the pressure coefficients over the upper and lower surfaces using a spline fit to the data in the chordwise direction. Ten lines of integration were used in the calculation, corresponding to the 10 spanwise rows of taps. This procedure also allowed for the calculation of section lift and drag coefficients. Details of the discrete integration can be found in reference [17]. It was shown in the same reference that discrete integration of the pressures is an accurate method for calculating the lift and profile drag of the model.

4.3.2 Wind Tunnel Wall Corrections

The flow over an airfoil in a wind tunnel is affected by the presence of the wind tunnel walls, inducing pressures and forces on the airfoil which must be accounted for. Corrections are made to account for the effects of horizontal bouyancy, solid blockage, wake blockage, and induced upwash. Reference [16] states that the normal corrections may be in error by several percent when the model blockage exceeds 7.5% of the test section. This implies that the corrections as applied to the MCAIR data are within the stated range for all but the α_{geom} = 30° wing setting. The corrections are discussed briefly below. Reference [16] contains a more detailed discussion of the wind tunnel wall corrections.

Horizontal bouyancy is caused by a thickening of the boundary layer in the streamwise direction along the test section, causing a reduced flow area (reference [16]). The reduced area causes the freestream velocity to increase as it travels through the test section. A gradual decrease in static pressure accompanies the increase in velocity creating a negative pressure gradient in the downstream direction which induces a drag on the airfoil. Reference [16] states that the effect is usually small for wings, and figures B-87 - B-98 showing wall pressure distributions at successive stations along the test section for α_{geom} = 0° and 6° show that the pressures at stations 2 (at the leading edge of the wing), and 4 (at the trailing edge) are nearly the same. The average difference in pressure coefficients between the two stations was calculated as $\Delta C_{p_{ave}}$ = 0.0010 for α_{geom}=0° and $\Delta C_{p_{ave}}$ = -0.0057 for α_{geom}=6°. Both of these values are well below the repeatability of the pressure coefficients of 0.02 (see section 2.5), thus the horizontal bouyancy was neglected.

The error due to *solid blockage* is a result of the flow being accelerated around the model due to the constricted flow area. A dynamic pressure measured upstream of the model, is then lower than the dynamic pressure at the model location. At the WBF the total pressure is measured upstream of the model, but the static pressure is measured in the plane of the model as an average of the reference static pressure taps, eliminating the need for a solid blockage correction.

Wake blockage is similar to solid blockage in that it is a correction to the dynamic pressure of the flow over the model. The model leaves a trailing wake with lower velocity flow in it. Given that the flow can be considered incompressible, and that cross-sectional area of the test section is essentially constant, the continuity equation requires

$$(\rho V_{ave} A)_{entrance} = (\rho V_{ave} A)_{exit} \tag{4.1}$$

If the flow within the wake is slower than V_{ave}, then the flow external to the wake must be faster than V_{ave}. This creates a velocity increment at the model in the manner as the solid blockage correction. The need to correct for this effect also is eliminated by measuring the static pressure in the plane of the model.

The alteration to the normal downwash manifests itself as increments to both the angle of attack of the airfoil and the calculated drag coefficient. The so-called *induced upwash* requires the following correction to the angle of attack:

$$\alpha = \alpha_{geom} + \Delta\alpha_i \tag{4.2}$$

$$\Delta\alpha_i = \delta \frac{S}{C} C_L \tag{4.3}$$

where $\delta \approx 0.125$ as in reference [16] for a circular test section, S/C is a ratio of the wing planform to tunnel cross-section areas, and C_L is the wing lift coefficient which is assumed to be correct. Approximating the tunnel cross-section as a semi-circle of radius R = 65.5" (see figure B-49) and given that the wing planform area is S = 1536 sq.in., equation (4.3) becomes

$$\Delta\alpha_i = 1.63\, C_L \quad (degrees) \tag{4.4}$$

The correction for induced drag is a geometric consequence of rotating the lift vector through the induced angle of attack $\Delta\alpha_i$. The contribution to drag is

$$C_{D_i} = C_L \sin(\Delta\alpha_i) \tag{4.5}$$

but for small $\Delta\alpha_i$ equation (4.5) reduces to

$$C_{D_i} = C_L \Delta\alpha_i = 0.0285\, C_L^2 \tag{4.6}$$

Finally from reference [16] the skin friction drag of a model with a fully turbulent boundary layer is

$$C_{D_f} = \frac{0.910}{[\log_{10}(Re)]^{2.58}} \tag{4.7}$$

which yields $C_{D_f} = 0.007$ for $Re_{\bar{x}} = 2.6\text{x}10^6$. The final corrected drag coefficient becomes

$$C_D = C_{D_p} + 0.0285\, C_L^2 + 0.007. \tag{4.8}$$

The corrected values of α, C_L, and C_D can be found in table A-5. Although the corrections were developed for unswept wings, reference [18] shows that the errors are small for the MCAIR wing test configuration. Rough calculations also were made for the same corrections based on reference [20] which is applicable to swept wings. The results supported the claim of [18] that the errors were small.

4.3.3 Comparison to Literature

A plot of C_L vs α is shown in figure B-50 for the data acquired for the MCAIR wing. The Reynolds number based on the mean geometric chord was $Re_{\bar{x}} = 2.6\text{x}10^6$ and the Mach number was M = 0.15. Also presented are the results from the 1987 test of the same wing under the same conditions. The slope of the 1989 lift curve from 0° to 6° was calculated as 0.056/deg while the slope for the 1987 lift curve was 0.059/deg. The 5% difference in slope between the two tests may be attributed to reparations made to the reference static pressure tubing prior to the current wind tunnel test. A small piece of tape had been found to be partially blocking the reservoir tube, thus causing one tap to contribute more to the average pressure than the other. Therefore the same measured dynamic pressures may actually have been different between the two tests. It is felt that the restriction in the tube affected the results of the previous test, and so it is believed that the lift curve slope calculated from the current test more accurately describes the performance of the MCAIR wing in the given configuration. Both of the calculated slopes are greater than the theoretically predicted slope of reference [16] of 0.052/deg and 0.053/deg of reference [5].

Comparisons between the lift and drag data of the MCAIR wing and wings with similar geometric charactistics are made below. The wings were tested at slightly different Reynolds number and Mach number, and also the aspect ratio and taper ratio of the reference wings was usually greater than that of the MCAIR wing. Table A-6 lists the geometric characteristics of the different reference airfoils used for comparison with the MCAIR wing. Figures B-51 and B-52 from reference [5] plot the values of the lift curve slope for wings of taper ratio $\lambda = 0.25$ and 0.50 for wings of different quarter-chord sweep and aspect ratio. The values of the lift curve slopes were calculated using a lifting line coincident with the quarter-chord of the wings. All wings were modelled as flat plates, so the plots do not show any effects of airfoil section thickness. Three general trends indicated by the plots are: 1) the lift curve slope increases with decreasing taper ratio for wings with equal sweep and aspect ratio, 2) the lift curve slope increases with increasing aspect ratio for wings with equal sweep and taper ratio, and 3) the lift curve slope decreases with increasing sweep for angles greater than 10° and wings with equal aspect ratio and taper ratio. It is also noted that although the leading edge of the MCAIR wing was swept back 45°, the quarter-chord line was swept 38.8°.

Figure B-53 compares the MCAIR test data to that from reference [13]. The wing tested in [13] had an NACA 64A010 airfoil section normal to the quarter-chord which was swept back 45°, and it had an aspect ratio AR = 3 and a taper ratio $\lambda = 0.5$. The wind tunnel test was run at a Mach number M = 0.25 and a Reynolds number $Re_{\bar{x}} = 4.0 \times 10^6$. The lift curve slope from [13] is 0.050/deg which is 13% less than the MCAIR wing lift curve slope. Although data between 20° and 30° is lacking for the MCAIR wing, it appears that the data from the two wings may match within this region.

Two wings from reference [7] are plotted with the MCAIR wing data in figure B-54. The wings from [7] both had an aspect ratio AR = 3.10. Wing A had a taper ratio $\lambda = 0.36$ and the quarter-chord line was swept back 50° while wing C had a taper ratio of $\lambda = 0.38$

with the quarter-chord swept back 48.8°. Wing A had an RAE 101 airfoil section with thickness to chord ratio $t/c = 0.075$ and maximum thickness at $x/c = 0.31$. Wing C also had an airfoil section with $t/c = 0.075$, but the maximum thickness was located at $x/c = 0.38$ which is similar to the NACA 64 series airfoil sections with maximum thickness at $x/c = 0.40$. Both wings were tested at a Mach number M = 0.18 and Reynolds number $Re_{\bar{x}} = 1.8 \times 10^6$. The lift curve slope for wing A is 0.056/deg while the slope for wing C is 0.061/deg. The slope from wing A is the same as the slope from the current MCAIR wing test despite the difference in sweep of the quarter-chord lines while the slope of wing C differs by 9% from the current MCAIR data. It is also noted that the value of $C_{L_{max}}$ for the more highly swept wings is greater than that of the MCAIR wing.

Figure B-55 shows the C_L vs α data plotted with data from two wings listed in reference [11]. The Javelin wing had an aspect ratio AR = 2.92, taper ratio $\lambda = 0.17$, and thickness to chord ratio $t/c = 0.10$. The leading edge of the wing was swept back 48°. The Swift wing had a leading edge sweep of 40°, an aspect ratio AR = 3.43, a taper ratio $\lambda = 0.35$, and thickness to chord ratio $t/c = 0.10$. Both wings were tested at 120 ft/s (80 mph) which corresponds to a Reynolds number $Re_{\bar{x}} = 1.2 \times 10^6$ for Javelin and $Re_{\bar{x}} = 0.9 \times 10^6$ for Swift, and Mach number approximately M = 0.10. Both wings had a smaller lift curve slope (0.054/deg for Javelin, 0.052/deg for Swift) than the MCAIR wing and the $C_{L_{max}}$ for both wings was less than the lift coefficient of the MCAIR wing at 18° angle of attack.

Data is presented in reference [9] for 4 wings with symmetric airfoil sections, 10% thickness ratios, and 40° swept quarter-chords. All of the wings had aspect ratio AR = 3.5 and taper ratio $\lambda = 0.4$. Lift curves were presented for Mach numbers 0.5 and greater (figures B-56 - B-59). In order to match the Mach number between the reference data and the MCAIR data, the values of the lift curve slope were calculated for each wing at M = 0.5 and 0.65. The slopes were then linearly extrapolated back to M = 0.15 to match that of the MCAIR test. The slopes were 0.051/deg for the wing with RAE 101 airfoil section,

0.054/deg for the wing withRAE 104 section, 0.054/deg for the wing with HSA I section, and 0.056/deg for the wing with NACA 64A010 airfoil section. These represent differences of 9%, 4%, and 0% respectively, compared with the lift curve slope from the current MCAIR wing test. Data from reference [13] for lift curve slope vs Mach number was plotted to determine the linearity of the data (figure B-60). The data appears linear up to M = 0.6, but data is not available for M = 0.65. If it can be assumed that the data is linear up to M = 0.65 and that the data for the wings in reference [9] behaves in the same manner, then the linear extrapolation is valid. If the M = 0.65 data point was in the nonlinear region of the curve, then the extrapolation would have predicted a slope which was too low. Three of the predicted slopes were less than the MCAIR slope, so a correction for the nonlinearity would most likely bring the majority of the data closer to that of the MCAIR wing.

Figure B-61 is a plot of C_D vs α for the MCAIR wing. The data from the 1989 test and the 1987 test are in close agreement. Figures B-62 and B-63 plot the MCAIR data along with the data from reference [13] and [11] respectively. The wings from both references had lower drag coefficients than the MCAIR wing for angles of attack greater than 6°.

Figure B-64 plots a C_L vs C_D polar for the MCAIR data from 1989 and 1987. Again, the data appears to match identical curves as would be expected. Figures B-65 - B-67, plot the MCAIR data along with data from references [13], [7], and [11] respectively. The data from reference [13] follows that of the MCAIR wing up to a lift coefficient of about C_L = 0.4, at which point the wing from reference [13] has higher lift coefficients for a given drag than the MCAIR wing. The data of wing A from reference [7] matches the MCAIR wing data almost identically throughout the entire range of operation. Wing C of the same reference has significantly greater lift at a given drag for lift coefficients greater than C_L = 0.4. The data from both wings of reference [11] appears to follow closely that of the

MCAIR wing up to $C_{L_{max}}$ of the reference wings. The data from the Swift wing appears to match slightly better which was expected because the Swift wing had a planform similar to the MCAIR wing while the Javelin wing was shaped more like a delta wing.

Section lift coefficients were calculated for the MCAIR wing for all angles of attack. Figure B-68 shows the data from the 1987 MCAIR test and figure B-69 shows the results from the 1989 test. The 1987 data shows the inward progression of the separated flow region on the outboard section of the wing. Figure B-70 plots the normalized spanwise loading coefficient vs location on the semi-span for cases with attached flow over the entire upper surface of the wing model. The data includes the 1989 MCAIR wing results from $\alpha_{geom} = 6°$, the 1987 MCAIR data for $\alpha_{geom} = 2°$ and $\alpha_{geom} = 6°$, and the test results from reference [13]. All of the data appear to match the theoretical curve from reference [5] for $\lambda = 0.5$ somewhat better than the theoretical curve for $\lambda = 0.25$. The wing from reference [13] had a taper ratio $\lambda = 0.5$ while the MCAIR wing had a taper ratio $\lambda = 0.25$. Figure B-71 plots the spanwise loading for the 1989 MCAIR data only, including the 6°, 18°, and 30° angle of attack data. At $\alpha_{geom} = 18°$ the outboard 60% of the semi-span had separated flow while the entire semi-span was separated at $\alpha_{geom} = 30°$.

Figures B-72 - B-78 are sketches of the wing flow patterns drawn from photographs taken of yarn tuft flow visualization runs from $\alpha_{geom} = 6°$ to 24°. The diagrams show stall (steady separation) starting at the leading edge of the wing tip at $\alpha_{geom} = 6°$, moving inboard as the angle of attack was increased. All of the diagrams for $\alpha_{geom} > 6°$ have three distinct flow regions. The inboard portion of the wing had flow in the streamwise direction which ended at a line dividing the streamwise flow from a flow region which fed into a vortex moving back over the wing. Outboard of the vortex is recirculating flow within a region of steady separation. For $\alpha_{geom} \geq 15°$ there is a band of nearly stagnant flow within the separated flow region at the point where the flow turns sharply from spanwise to the upstream direction. The yarn tufts in this region remained quite steady. A similar region is

present in oil flow photographs presented in reference [6]. For angles beyond 24° the entire airfoil had separated flow.

4.3.4 Wall and Ground Board Static Pressures

The ground board pressure coefficient distributions (figures B-79 - B-82) are shown for α_{geom} = 0°, 6°, 18°, and 30°, and also for α_{geom} = 6° with $\delta_{le} = \delta_{te}$ = 10° (figure B-83). The abscissa shows values of the distance from the leading edge of the ground board in inches. Two pressure coefficient values are plotted for several small values of distance from the leading edge. These points correspond to lower and upper surface taps on the ellipse that makes up the leading edge of the ground board. It should also be noted that the taps in the rows directly alongside the wing were mounted in the turntable portion of the ground board which rotated with the wing and the turntable. Also, the row of taps noted as "nearest to door" was located on the wing upper surface side of the test section.

The plot for α_{geom} = 0° shows that in the region adjacent to the wing, the flow was slightly accelerated due to flow around the wing causing the pressure coefficients to be slightly negative. Downstream of the wing, the average of the coefficients appears to be zero with a reasonable experimental scatter in the data. As the wing angle of attack was increased the pressure coefficients decreased on the suction side of the ground board and increased on the pressure side as expected. The wing at α_{geom} = 30° shows the effect of drastic wake blockage. It can be seen that the region of low pressure immediately behind the wing indicates accelerated flow due to wake blockage. Figures B-84 - B-86 plot the difference in ground board pressure coefficients with the α_{geom} = 0° measurements subtracted out to show the changes in the tunnel flow induced by the wing at angle of attack.

Wall pressure coefficients were calculated and plotted in figures B-87 - B-110 around the tunnel outline with the cross-section viewed looking downstream. The positive

direction for pressure coefficients is outward away from the tunnel outline, while negative coefficients are plotted on the scales in toward the center of the tunnel. The negative pressure coefficients near the ground board indicate an accelerated upflow over the front of the ground board. This upflow is inevitable when using a ground board in a wind tunnel test. It is caused by flow blockage under the ground board created by the wing support structure and the structure supporting the ground board itself. The positive pressure coefficients in the plots from $\alpha_{geom} = 0°$ indicate that the flow in the rear of the test section is slightly slower than the flow in the plane of the wing. This could be caused by two factors, the first being the absence of solid blockage which accelerates the flow around the wing, and the second being the divergence of the wind tunnel walls. The walls were built with a slight divergence angle to account for boundary layer growth along the walls in the streamwise direction. The rate of growth of the boundary layer depends upon the flow Reynolds number. It appears that the test was run at a condition such that the divergence angle of the wind tunnel walls over-corrected for the boundary layer growth.

The tunnel static pressure was measured in the plane of the third row of taps. Specifically, the two reference static pressure taps used to measure the average test section pressure were mounted in close proximity to the third wall taps up from the ground board on both sides of the wind tunnel. Thus the average of the two pressure coefficients at these taps should be zero. The average pressure coefficient reading at the two taps over all of the runs was found to be $C_{P_{ave}} = 0.005$, which is acceptably close to zero given the repeatability of the pressure coefficients was 0.02.

Also plotted are the change in wall pressure from $\alpha_{geom} = 0°$ to $\alpha_{geom} = 6°$, 18°, and 30° (figures B-111 - B-128). The data shows that at $\alpha_{geom} = 6°$ which corresponds to 2.4% geometric blockage, a change in pressure coefficient of $|\Delta C_p| = 0.05$ is found in the plane of the model. At $\alpha_{geom} = 18°$, (7.2% geometric blockage), a change of pressure coefficient of $|\Delta C_p| = 0.13$ is found in the plane of the model, while at $\alpha_{geom} = 30°$ (11.6% geometric

blockage) the change is $|\Delta C_p| = 0.25$. It is interesting to note that the largest change in wall pressure took place at $\alpha_{geom} = 30°$ in the fourth row of taps which is at the trailing edge of the wing. The large change in pressure was believed to be caused by both solid blockage from the trailing edge of the wing and wake blockage from the fully separated flow. The wake was believed to have contracted, (decreased in cross-sectional area), as it travelled downstream. The pressure measurements taken at the trailing edge of the wing corresponded to the location where the wake had the greatest cross-sectional area, thus the flow was most accelerated by the wake blockage and the static pressure was the least. The claim that the wake decreased in size as it travelled downstream is supported by all of the wall data from the $\alpha_{geom} = 18°$ and 30° runs. There was a large separated wake region behind the wing in each of these cases, and the wall data shows the pressures increasing, moving from row 4 to row 6. The increase in pressure would be a result of the flow moving slower due to an increase in flow area created by the contracted wake (see equation (4.1)). The overall effects of wake blockage can also be seen in the wall pressure plots for both $\alpha_{geom} = 18°$ and 30°. All changes in the pressure coefficients downstream of the wing are negative, which indicates accelerated flow around the outside of the wake, as caused by the slower moving flow within the wake of the wing.

4.3.5 Five-Hole Probe Rake Measurements

Preliminary indications of the flow angles measured at the exit of the test section indicated flow angles to be much larger than the anticipated $-10° < \alpha,\beta < 10°$ range for which the rake was calibrated. Application of the linear calibration equation would produce significant errors for angles greater than 10° in magnitude due to the nonlinearity of the calibration coefficients K_α, K_β, and K_q*. Given that all of the five hole probes should have similar measuring characteristics, and that the characteristics were described by the calibration equations from the single five-hole probe study, equations (2.30), (2.31), (2.32), and (2.33) from the single probe study were fit to the probes on the rake. The flow angles and dynamic pressure were calculated using

$$\alpha' = \alpha_{14term} \frac{m\alpha_{rake_i}}{m\alpha_{single}} \tag{4.9}$$

$$\beta' = \beta_{14term} \frac{m\beta_{rake_i}}{m\beta_{single}} \tag{4.10}$$

$$q = q_{21term} \frac{K_{q^* rake_i}}{K_{q^* single}} \tag{4.11}$$

where α_{14term}, β_{14term}, and q_{21term} are the results obtained by applying the measured coefficients to equations (2.30), (2.31), (2.32), and (2.33). Also $m\alpha_{rake_i}$ and $m\beta_{rake_i}$ are the slopes of the individual probes from the rake calibration, $m\alpha_{single}$ and $m\beta_{single}$ are the slopes of the linear portion of the single probe calibration, $K_{q^* rake_i}$ are the values of K_q* for the rake probes at $\alpha,\beta = 0°$, and $K_{q^* single}$ is the value of K_q* from the single five-hole probe at $\alpha,\beta = 0°$. Multiplying by the ratio of the slopes in the angular calculations scaled the single probe equations such that the linear portion of the single probe calibration matched the linear portion of the rake calibration. Multiplying by the ratio of the zero angle values of K_q* produces the same effect for the calculation of dynamic pressure. The flow angles were then calculated using the above equations for the rake measurements at the entrance and exit planes of the test section with the wing at $\alpha_{geom} = 0°$, 6°, 18°, and 30° with the leading and trailing edge flaps undeflected, and $\alpha_{geom} = 6°$ with both leading and trailing edge flaps deflected $\delta_{le} = \delta_{te} = 10°$. The maximum flow angle calculated was $\beta' = 25.3°$ at the test section exit for $\alpha_{geom} = 30°$. The single five-hole probe calibration equations were fit for flow angles in the range $-25° < \alpha', \beta' < 25°$, hence the flow angles calculated all fall within the known limits of accuracy.

A study was conducted to determine any effects of the five-hole probe rake on the flow over the wing. The only change to the flow over the wing took place in the wake of the rake. The wake seemed to cause the transition from laminar to turbulent flow to occur sooner on the wing, increasing the suction on the leading edge of the wing. Transition

effects are discussed further in reference [17]. The maximum increase in suction was 10% and it was confined to the forward 30% of the chord (figure B-129). Outside of the wake of the rake the wing pressures were essentially unchanged.

Vector plots showing the measured flow angles are found in figures B-130 - B-137 The tunnel cross-section shown in the plots is viewed looking downstream. The length of a 5° flow angle vector is indicated in the upper right hand corner for the entrance flow plots while the length of a 15° flow angle vector is indicated for the exit flow plots.

Figures B-130 and B-131 show the entrance flow angles for the wing set to α_{geom} = 0°. The ground board induced upflow is present and nearly uniform over the lower half of the test section. The vectors indicated by the probes nearest the wind tunnel walls seem unusually large. Reference [21] discusses the effects of nearby solid surfaces on five-hole probe readings. The reference states that alterations to normal measurements using the probe were found with the probe 3 diameters from the solid surface. The probes in the MCAIR wing test were never closer to the walls than five probe diameters. There was no data presented for distances farther than 3 probe diameters from the solid surface. It was also stated that the only reliable method of correcting for the effects of the solid surface was to calibrate the probes in a similar configuration. This was not performed in the current study and so no correction was made. There is also some question as to whether the large angles near the wall are due to hardware interference or whether they are simply a true indication of the actual flow in those regions.

The entrance flow angles for α_{geom} = 6°, 18°, and 30° indicate the growing presence of a flow across the test section from left to right which was the upwash induced by the wing as it was rotated to larger angles of attack. With the exception of the α_{geom} = 30° case, the upwash angles measured at the test section entrance were of the same order of magnitude as the ground board upflow angle. This made graphical distinction of the induced affects difficult. To graphically show the induced affects the α_{geom} = 0° case was

used as a datum. The datum was subtracted from all of the measurements to yield the flow changes induced by the change in α_{geom}. Figures B-138 - B-143 show the plots of the measured flow angles with the datum subtracted out. It is noted that there is a small induced upwash at the $\alpha_{geom} = 6°$ setting, with the amount of upwash increasing with the angle of attack. It can also be seen from the $\alpha_{geom} = 30°$ case that not only is there an induced upwash present at the test section entrance, but there is also a small component of flow in the spanwise direction. This flow is a result of the blockage created by the wing at the high angle of attack.

The flow angles at the test section exit indicate the amount of circulation present in the wake of the wing. The vector plot of the $\alpha_{geom} = 0°$ case shows that there is no circulation and that the flow is strictly in the streamwise direction behind the wing. The $\alpha_{geom} = 6°$ plot shows the downwash created by the wing. Indications of the wing tip vortex can be seen in the upper portion of the tunnel. The $\alpha_{geom} = 18°$ and 30° cases both show large regions of circulatory flow at the test section exit. As the angle of attack was increased, the center of the circulatory region moved inboard. It is noted that the circulatory region is skewed such that the inboard portion has moved further in the direction of the downwash. This phenomenon is predicted in reference [14]. Wings swept backward generally stall at the tip first, and as the angle of attack is increased the stall moves inboard. The lift coefficient of the wing increases beyond the point where separation first occurs. Therefore, as stall moves inboard and the lift coefficient continues to increase, the loading on the inboard portion of the wing increases; thus the downwash behind the inboard portion of the wing is increased. This increase in downwash results in the skewed circulatory region at the exit of the test section.

Figures B-144 and B-145 show the entrance and exit flow measured for the leading and trailing edge flaps deflected $\delta_{le} = \delta_{te} = 10°$ and the wing at $\alpha_{geom} = 6°$. In comparison to the $\alpha_{geom} = 6°$ case with undeflected flaps it is clear that the circulatory region at the exit

of the test section has grown due to the larger lift generated by the wing with deflected flaps.

Vector plots at the test section exit using the the $\alpha_{geom} = 0°$ case as the datum look similar to the absolute vectors because the flow changes at the test section exit are large in comparison to the flow angles measured at $\alpha_{geom} = 0°$.

Flow direction and dynamic pressure contour plots at the entrance and exit planes have also been made (figures B-146 - B-169). The increment between contour lines is indicated in the upper right hand corner of each plot. The dynamic pressure is plotted as a percentage of the dynamic pressure measured in the plane of the wing model. At $\alpha_{geom} = 0°$ the upflow created by the ground board is seen to be uniform across the test section as indicated by the yaw angle and dynamic pressure contours. The pitch angle contours show the flow to be uniformly distributed about $\alpha = 0°$.

At $\alpha_{geom} = 6°$ the plots at the entrance of the test section indicate that the flow is essentially unchanged in yaw and only slightly affected in pitch angle and dynamic pressure. The only clearly visible change in the upstream conditions is a shift in the ground board upflow toward the suction side of the wing. As the angle of attack is increased to $\alpha_{geom} = 18°$ and $30°$ the upstream affects become more pronounced. The pitch angle plots indicate that a major portion of the entrance has been affected by the upwash induced by the lifting wing. The dynamic pressure contours show a continuing shift in the ground board upflow toward the suction side of the wing. The dynamic pressure contours at $\alpha_{geom} = 30°$ show a general slowing of the flow at the entrance of the test section due to the blockage of the model. In fact the maximum dynamic pressure contour for $\alpha_{geom} = 30°$ is only 98% of the value measured in the plane of the wing compared to a maximum of 108% at $\alpha_{geom} = 18°$.

The contours at the exit of the test section show the same effects as the vector plots of the same flow. The dynamic pressure contours at $\alpha_{geom} = 0°$ show the slight wake due to

the skin friction drag over the wing. It was not expected that the skin friction drag would be detected because the width of the wake due to skin friction was much less than the horizontal probe spacing. An estimate of the width of the wake based on $Re_{\bar{x}} = 2.6x10^6$ and $\bar{x} = 32"$ for a turbulent boundary layer was 0.2" at the at the trailing edge of the midspan of the wing. Given that the five-hole probes were spaced 6" apart on the rake it is unlikely that the probes would coincidently fall within this region. The reason the wake was detected was because the rake was lined up such that one of the probes was directly behind the wing on the centerline of the tunnel. If the probe measuring the skin friction drag had been an inch to either side, it probably would not have given an indication of the skin drag. At $\alpha_{geom} = 6°$ the pitch angle plots show the downwash behind the wing and the dynamic pressure plot locates a region of deficit in the dynamic pressure corresponding to the wing tip vortex. There is a discrepancy in the location of the wing tip vortex indicated by the contour and vector plots. The contour plots indicate that the vortex is located approximately 6" inboard of the location shown by the vector plot. In this instance it is believed that the vector plot more accurately shows the location of the vortex because the lower portion of the wing tip vortex can be seen in the fourth row of vectors at the center of the tunnel. The disparity was caused by the relatively large grid spacing of the rake in the vertical direction compared to the size of the flow structure being measured.

The contours for $\alpha_{geom} = 18°$ and 30° clearly show the circulatory flow at the exit of the test section. The plots also show the skewed circulatory region mentioned in the discussion of the vector plots. At the test section exit it is seen that the dynamic pressure drops to as low as 50% of the value measured in the plane of the wing for $\alpha_{geom} = 18°$, and as low as 35% for the $\alpha_{geom} = 30°$ case. The contour plots at the test section exit show the same flow characteristics as similar contour plots presented in reference [11] for flow behind the Swift wing.

Contour plots using $\alpha_{geom} = 0°$ as the datum are shown in figures B-170 - B-187 help

to illustrate the changes induced by the wing being set to the different angles of attack. The plots are most helpful at the entrance to the test section. The plots from $\alpha_{geom} = 6°$ show that little changes over the test section entrance with the exception of $\alpha = 0.5°$ contours directly in front of the wing. The contours are vertical lines traversing the entire test section showing that the wing induced upwash affects the entire entrance flow. Also present are vertical contours in the dynamic pressure indicating that the entrance flow had shifted over toward the suction side of the wing. The same features at the entrance to the test secton are also present in the plots for $\alpha_{geom} = 18°$ and 30° except that they are more clearly visible. The induced pitch angle (upwash) is as large as $\alpha = 1.5°$ for $\alpha_{geom} = 18°$ and $\alpha = 2.5°$ for $\alpha_{geom} = 30°$. The change in dynamic pressure is clearly evident at $\alpha_{geom} = 18°$. The dynamic pressure of the entrance flow is as much as 4% higher than the reference value on the suction side of the wing and 10% lower than the reference on the pressure side of the wing. At $\alpha_{geom} = 30°$ the overall blockage is apparent in that the dynamic pressure is still shifted toward the suction side of the wing, but the highest value of dynamic pressure was 6% less than the reference value of the dynamic pressure measure in the plane of the wing. The plots at the test section exit are similar to those without $\alpha_{geom} = 0°$ used as the datum because the flow changes at $\alpha_{geom} = 6°$, 18°, and 30° were large compared to the cross flow angles at $\alpha_{geom} = 0°$.

Figures B-188 - B-193 show contour plots of $\alpha_{geom} = 6°$ for leading and trailing edge flaps deflected 10°. The effects seen at the entrance to the test section are similar to the same angle of attack with undeflected flaps but all of the effects are more pronounced due to the larger lift generated by the deflected flaps. The same holds true for the contours at the test section exit. The vortex off the wing tip is larger, and thus more easily visible in the plots. It is interesting to note that the dynamic pressure plots show the wake in two distinct sections. There is one area of lower dynamic pressure directly behind the tip section of the wing which appears to have relatively little downwash, while a region of

reduced dynamic pressure exists approximately 8" toward the pressure side of the tunnel at the inboard portion of the wing.

Chapter 5

Discussion of Results

5.1 Wing Pressure Data

The performance of the MCAIR wing section is best described by comparing the experimental data to published data from tests of similar airfoils. Reference should be made to Table A-6 for a comparison of the geometric characteristics of the different wings.

Comparisons between the MCAIR wing lift curve slope and the slopes of the reference wings with approximately the same quarter-chord sweep angle ($\Lambda_{1/4} = 40°$), show the MCAIR wing to have a higher value of lift curve slope than the wings of references [9], [11], and [13]. The wings of reference [9] were most like the MCAIR wing, but unfortunately there wasn't any data presented for Mach numbers less than $M = 0.5$. The data was linearly extrapolated to the same Mach number as the MCAIR test, however, there is uncertainty regarding the applicablity of such a procedure. It was determined that if the slopes were in error, they were less than the actual slope. If so, then the data would become more like the MCAIR data, but there was insufficient evidence to support the claim that they were actually less than the actual value. The wings of reference [9] all had greater aspect ratios and taper ratios than the MCAIR wing.

In comparing the overall performance characteristics of the airfoils (C_L *vs* C_D), it was found that the data from the two wings (Javelin and Swift) of reference [11] most closely matched that of the MCAIR wing. The Swift wing had a planform similar to that of the MCAIR wing, except for a slight increase in the sweep angle of the trailing edge at 50% of the semi-span. Although the lift curve slopes of the wings from reference [9] were closest to the MCAIR wing, there was not any applicable drag data presented.

Wing A of reference [7] has the same lift curve slope and plots to the same curve on the C_L *vs* C_D polar as the MCAIR wing, despite having its quarter-chord line swept back 50°. Wing C of the same reference also has similar characteristics, but does not fit the MCAIR data as well as wing A. Both wings had aspect ratios and taper ratios that were close to that of the MCAIR wing.

In general, it was noted from figures B-51 and B-52 that the value of the lift curve slope is affected by aspect ratio, taper ratio, and sweep angle of the wing. The MCAIR wing had a smaller taper ratio than the majority of reference wings, which would indicate a greater slope than the reference wings, but it also had a smaller aspect ratio than the reference wings, which indicates a smaller value of the slope. The thickness ratio of all of the reference wings was greater than the MCAIR wing. It is known that a thinner airfoil section will experience leading edge separation sooner than a thick airfoil (reference [14]), but due to the small size of the separated region there is not a substantial decrease in lift. The formation of the leading edge separation bubble is generally accompanied by an increase in drag, thus a plot of C_L *vs* C_D for wings of identical planform but different thickness ratios would show the data from the thinner wing lying below that of the thicker wing section due to the earlier increase in drag caused by the leading edge separation bubble. The preceding discussion explains why the C_L *vs* C_D data from reference [11] matches the MCAIR data even though the lift curve slope is smaller for for the wings of [11]. The wings had t/c = 0.10 while the MCAIR wing had t/c = 0.05, thus the thicker wings delayed the onset of leading edge separation which compensated for the smaller values of lift, making the C_L *vs* C_D curves very similar.

5.2 Flow Visualization Data

Descriptions of the flow over the upper surface of the MCAIR generic fighter research wing are based upon still photographs and videotape movies of the yarn tuft and smoke flow runs. Carpet plots of the upper surface pressure coefficients from the 1987 MCAIR wing test and the current test were also used in making the observations that follow.

A leading edge vortex appears near the wing tip at $\alpha_{geom} = 3°$. Flow separation begins at the wing tip at $\alpha_{geom} = 6°$, and moves inboard as the angle of attack is increased. At $\alpha_{geom} = 6°$ the vortex covers the outboard third of the wing leading edge. Reference [14] refers to a leading edge separation bubble which has constant static pressure in discussing the flow over swept wings. It is believed that this may be the case for wings with smaller leading edge sweep angles, but for the MCAIR wing the flow along the leading edge was a well defined vortex, not just a circulatory flow pattern within a separation bubble. Tests were performed using a smoke wand to investigate this point more thoroughly. It was found that the smoke stream could be positioned such that it was split into two branches; one being entrained into the leading edge vortex, clearly showing the vortex traveling outboard along the leading edge of the semi-span, and the other flowing over the top of the vortex moving downstream in the attached flow over the wing upper surface.

The physical dimensions of the vortex were relatively small, with the width of the vortex in the streamwise direction never exceeding 10 percent of the local section chord. As the angle of attack was increased the point of origin of the vortex moved inboard along the semi-span. By $\alpha_{geom} = 12°$ the beginning of the vortex had moved inboard such that only 10% of the semi-span leading edge was left with uniformly attached flow. This flow condition persisted until approximately $\alpha_{geom} = 21°$ where the beginning of the vortex

moved to the point of intersection of the leading edge of the wing and the reflecting plane. As the vortex moved inboard a region of fully separated flow covered the wing tip and moved inboard as well. The fully separated flow was characterized by spanwise flow outward along the trailing edge, and flow moving upstream along the the leading edge (figures B-75 - B-78). The separation appeared to be quite steady with no apparent time dependent variations. Reference [14] asserts that the attached flow inboard is separated from the stalled flow outboard by a part span vortex sheet which travels downstream over the wing and rolls up in the wake. For angles of attack equal to 9° or greater a substantial portion of the wing upper surface was covered by spanwise flow which was separated from the attached flow at the inboard portion of the semi-span by the part span vortex sheet. As the angle of attack was increased, the part span vortex sheet moved inboard until the entire wing was stalled. This did not follow the prediction of [14] which stated that the part span vortex sheet would only move inboard to a certain point and then separation of the inboard section of the airfoil would take place from the trailing edge.

5.3 Boundary Condition Data

The issue of upflow at the test section entrance was addressed in the 1987 test of the MCAIR wing. It was known apriori that the wing and ground board mounting hardware would add resistance to flow underneath, inducing the upflow at the entrance. It was decided in the test that the positive pressure imposed on the trailing edge of the wing from ground board flaps deflected to counter the upflow, would be more detrimental to the test data than the non-uniform entrance flow. Hence, the test was run acknowledging that there was an upflow, but without means to measure the magnitude of the upflow angles.

The current test produced measurements of the magnitude of the flow angles and local dynamic pressure at the test section entrance. It was found that the upflow angle was greatest near the surface of the ground board and decreased moving upward, with the

dynamic pressure being higher near the ground board and decreasing also with vertical distance (refer to the contour plots of the entrance flow). The measurements were made at stations 6", 18", 30", 42", and 54" above the ground board. The average upflow angle seemed to be independent of the wing angle of attack up through $\alpha_{geom} = 18°$. The measured average upflow angle was 2.4° at 6", 2.2° at 18", 1.5° at 30", 0.4° at 42", and 0.0° at 54" above the ground board. For the $\alpha_{geom} = 30°$ wing setting the measured average remained the same at the station 6" above the ground board, but the average at the 4 stations above this level were all 0.2° to 0.3° larger. This additional upflow was caused by the larger amount of blockage near the ground board than near the top of the tunnel due to the 0.25 taper ratio of the wing.

Implementation of this boundary condition data in the MCAIR computer code will provide a better representation of the tunnel flow than specifying uniform streamwise flow. If the computer code proves to be accurate, a study that may be beneficial to wind tunnel test design would be to calculate a solution for the wing pressures using the measured boundary conditions, and then calculate a solution using uniform entrance flow conditions. The difference between the two sets of computed wing pressures would indicate the severity of the effects of the ground board upflow on the flow over the wing, and provide an indication as to the possible merits of focusing further efforts on reducing the upflow.

The vertical gradient in dynamic pressure at the test section entrance caused by the reflecting plane indicates that when conducting a wind tunnel test with such a configuration, and the dynamic pressure is measured using a pitot-static probe upstream of the model, careful thought should be given to the vertical placement of the probe. If time permits, a survey of dynamic pressure measurements covering the distance between the reflecting plane and the top of the test section should be performed with the model in place prior to the test in order to determine the best location for the measurement. If time does not allow for such a survey, then a vertical position midway between the reflecting plane and the top of the test section should be used for the dynamic pressure measurement.

The dynamic pressure gradient mentioned in the previous section makes analyzing the wall static pressure coefficients difficult at the first 3 wall pressure tap stations. By subtracting the measurements taken at $\alpha_{geom} = 0°$ from the measurements taken at the other angles of attack, the effects due to the dynamic pressure gradient are subtracted out leaving only the effects of the wing at angle of attack. For $\alpha_{geom} = 6°$ the reference static pressure tap on the side of the wing lower surface experienced a 4% increase in pressure, while the tap on the side of the wing upper surface experienced a 4% decrease in pressure. At $\alpha_{geom} = 18°$ the wall pressure changed by 9% at the reference static pressure taps on either side of the tunnel, and at $\alpha_{geom} = 30°$ the static pressure changed by 10% on either side of the tunnel.

The gross effect of model blockage is reflected by the average pressure at the test section entrance. Again, the stated numbers have the $\alpha_{geom} = 0°$ measurements subtracted out. There was not any change in the average pressure for $\alpha_{geom} = 6°$ because the blockage was small (2.4%). For $\alpha_{geom} = 18°$ and 30° the average static pressure at the entrance was greater by 3% and 9% of the dynamic pressure at the model. At these two wing settings the flow was accelerated around the model due to the large amount of test section blockage (7.2% and 11.6%). Because the flow area was larger at the test section entrance, it travelled more slowly such that it satisfied the continuity equation (equation (4.1)). Downstream of the wing the wall pressures indicate the presence of wake blockage for the $\alpha_{geom} = 18°$ and 30° settings. The average static pressure coefficients are negative due to faster moving flow external to the separated wake. There are also indications that the wake contracts as it travels downstream because the average static pressure, although always negative, increases moving from row 4 to row 6.

5.4 Implementation of Boundary Condition Data

In applying the experimentally measured boundary condition data to a computer code the spatial location of the data points must be matched with the nodes or cell centers of a computational grid or lattice. It is expected that the computational boundary conditions will require the definition of the conditions at more points on the boundaries than is provided by the measured data, hence numerical interpolation must be performed. In all cases of interpolation it is felt that a second order spline fit of the type used in reference [17] should be used to obtain intermediate data points for the computational boundary conditions. Although a linear interpolation would be easier to perform, it would create discontinuities in the changes of the conditions across the boundaries which may corrupt the numerical solution. With only slightly more work the second order spline yields smooth changes across the boundaries, and lessens the concern that numerical discontinuities are introduced into the solution by the boundary conditions. Therefore spline fits should be made to the dynamic pressure and flow direction at the entrance and exit planes of the test section in both the horizontal and vertical directions to obtain intermediate data points. Likewise the wall and reflecting plane pressure data should be fit in both the streamwise direction and around the cross section of the tunnel to obtain any intermediate data points.

Chapter 6

Conclusion

A low speed wind tunnel test has been conducted using the 45° leading edge sweep MCAIR Generic Fighter Research Wing Model. The model was a semi-span wing with NACA 64A005 airfoil sections oriented parallel to the plane of symmetry, it had an aspect ratio of 3.0, a taper ratio of 0.25, and it was instrumented with 370 surface static pressure taps covering both the upper and lower surfaces. To determine wall effects on the wing pressures, additional data was obtained for static pressures along the wind tunnel walls and reflecting plane, as well as flow direction and dynamic pressure at the entrance and exit planes of the test section. These measurements made up a complete set of boundary conditions to be used in a three-dimensional Navier-Stokes computer code developed at MCAIR. The boundary conditions are to be used as input to the computer code to represent the tunnel environment accurately. The numerically calculated wing pressures can be compared to the experimentally measured values to determine the accuracy of the computational results.

The measurement of flow direction and dynamic pressure was accomplished using conically tipped, five-hole pressure probes. A study was conducted prior to the MCAIR wing test to determine the measuring characteristics of a single five-hole probe. The probe was calibrated for a range of flow angles of ±45° in both pitch and yaw, and functions were fit to the data using linear regression for angles less than 25°. Use of the functions to calculate the flow angles resulted in an accuracy of 0.4° in both pitch and yaw when compared to the calibration data, and an accuracy of 0.42 psf in the calculation of dynamic pressure. A rake holding 9 five-hole probes was constructed for use in the MCAIR wing test and was calibrated for incident flow angles less than 10°. After the wing test, the rake

calibration was extended to calculate flow angles less 25° by fitting the polynomials from the single probe study to each probe on the rake.

The MCAIR wing was tested at 0°, 6°, 18°, and 30° angle of attack with the leading and trailing edge flaps undeflected. These settings corresponded to 1.2%, 2.4%, 7.2%, and 11.6% geometric blockage based on the projected frontal area. It was also tested at 6° angle of attack with the leading and trailing edge flaps deflected 10° which represented approximately 2.4% blockage. The results of the test indicate the following conclusions:

1. The wing pressure data agrees well with the data from the wind tunnel test of the same wing conducted in 1987. The lift curve slopes differed by 5%, but this was attributed to a restriction in the tubing connecting the reference static pressure taps, which had been removed between the two tests. It is believed that the current results better indicate the performance of the MCAIR wing in the given configuration.

2. The calculated lift and drag coefficients are in general agreement with published data from wind tunnel tests of similar wings. The lift curve slope of the MCAIR wing was 5% to 10% larger than those presented for wings with the same sweep of the quarter-chords. The data most closely matched that of wing A presented in reference [7] which had its quarter-chord swept back 50°. The lift curve slopes were equal and the C_L vs C_D polars matched extremely well.

3. The upflow at the test section entrance induced by the wing and ground board installation was measured and the average values were calculated as 2.4° at 6", 2.2° at 18", 1.5° at 30", 0.4° at 42", and 0.0° at 54" vertically above the reflecting plane. These average angles remained constant for wing angles of attack up to 18° (7.2% blockage), and the angles measured at a vertical distance higher than 6" above the reflecting plane increased by 0.2° to 0.3° for the 30° angle of attack setting (11.6% blockage).

4. The reflecting plane induced a vertical gradient in the dynamic pressure at the entrance to the test section of 16% of the freestream value measured at the wing model for $\alpha_{geom} = 0°$. The dynamic pressure was greater near the reflecting plane and decreased with vertical distance upward. The magnitude of the gradient increased with angle of attack becoming as large as 24% at $\alpha_{geom} = 18°$. Because the dynamic pressure was measured in the plane of the model it was not affected by this upstream gradient, however, if the dynamic pressure is to be measured using a pitot-static probe upstream of the model, care should be taken in positioning the probe so that it provides a reading close to the average dynamic pressure of the entrance flow.

5. Changes in the wall pressures were evident for all of the non-zero angle of attack settings. At 6° angle of attack the changes were confined to regions of the wall in the vicinity of the wing, where pressures changed by as much as 5% of the dynamic pressure from those measured at the 0° angle of attack setting. At the 18° and 30° angle of attack settings the wall pressures are seen to change along the length of the test section with the maximum changes compared to the 0° setting being 13% and 26% respectively, of the dynamic pressure measured at the model.

6. Blockage effects are clearly evident along the entire test section for the 18° and 30° angle of attack settings. The dynamic pressure at the test section entrance was as much as 10% and 18% lower for the 18° and 30° settings respectively, than the entrance dynamic pressure at 0° angle of attack.

References

[1] Abbot, Ira, H., and Von Doenhoff, Albert, E.
Theory of Wing Sections, Including a Summary of Airfoil Data.
Dover Publications, Inc., New York, 1959.

[2] Bryer,D.,W. and Pankhurst, R.,C.
Pressure Probe Methods for Determining Wind Speed and Flow Direction.
Technical Report, National Physical Laboratory, London:HMSO, 1971.

[3] D'Angelo, Michael, R. and Durgin, Frank, H.
The Measurement of Static and Dynamic Flow Angles With and Without an Upstream Wing.
Technical Report WBWT-TR-1243, M.I.T. Wright Brothers Facility, Cambridge, MA, Dec, 1987.

[4] DeYoung, John.
Theoretical Additional Span Loading Characteristics of Wings with Arbitrary Sweep, Aspect Ratio, and Taper Ratio.
Technical Report No. 1491, U.S. National Advisory Committee for Aeronautics, Dec, 1947.

[5] DeYoung, John and Harper, Charles, W.
Theoretical Symmetric Span Loading at Subsonic Speeds for Wings Having Arbitrary Plan Form.
Technical Report NACA Rep. 921, U.S. National Advisory Committee for Aeronautics, 1948.
(Formerly TN's 1476, 1491, and 1772).

[6] Haines, A., B.
Some Notes on the Flow Patterns Observed Over Various Swept-back Wings at Low Mach Numbers (in the R.A.E. 10-ft x 7-ft High Speed Tunnel).
Technical Report R&M No. 3192, Aeronautical Research Council, Great Britain, Sept, 1954.

[7] Haines, A.,B. and Rhodes, C.,W.
Tests in the Royal Aircraft Establishment 10-ft x 7-ft High-Speed Tunnel on 50-deg Swept-back Wings.
Technical Report R&M No. 3043, Aeronautical Research Council, Great Britain, Sept, 1954.

[8] Hodson, H.P and Dominy, R.G.
An Investigation Into the Effects of Reynolds Number and Turbulence upon the Calibration of 5-Hole Cone Probes.
Technical Report, Cambridge University, Whittle Laboratory, Great Britain, 1988.

[9] Holmes, L.N. and Haines, A.B.
High Speed Wind Tunnel Tests on Six Wings of 40-deg Sweepback, with Various Section Shapes.
Technical Report R&M No. 2930, Aeronautical Research Council, Great Britain, Jan, 1952.

[10] Huffman, David, G., Rabe,D.C, and Poti,N.D.
Flow Direction Probes from a Theoretical Point of View.
Journal of Physics E: Sci. Instrum. (Vol 13), 1980.

[11] Kirby, K.,A. and Spence, A.
Low-Speed-Tunnel Model Tests on the Flow Structure Behind a Delta-Wing Aircraft and a 40 deg Swept-Wing Aircraft at High Incidences.
Technical Report R&M No. 3078, Aeronautical Research Council, Great Britain, Apr, 1955.

[12] Kjelgaard, Scott, O.
Theoretical Derivation and Calibration Technique of a Hemispherical-Tipped, Five-Hole Probe.
Technical Report NASA-TM-4047, National Aeronautics and Space Administration, Langley Research Center, Hampton, VA, 1988.

[13] Kolbe, Carl, D. and Boltz, Frederick, W.
The Forces and Pressure Distribution at Subsonic Speeds on a Plane Wing Having 45 deg of Sweepback, an Aspect Ratio of 3, and a Taper Ratio of 0.5.
Technical Report NACA-RM-A51G31, Ames Aeronautical Laboratory, Moffet Field, CA, Oct, 1951.

[14] Kuchemann, D.
Types of Flow on Swept Wings - With Special Reference to Free Boundaries and Vortex Sheets.
Technical Report, Journal of the Royal Aeronautical Society, Vol. 57, Great Britain, Nov, 1953.

[15] Lee, C.S. and Wood, N.J.
Calibration and Data Reduction for a Five-Hole Probe.
Technical Report JIAA-TR-73, Stanford University, June, 1986.

[16] Rae, W.H. and Pope, A.
Low Speed Wind Tunnel Testing.
Wiley and Sons, Inc., New York, NY, 1984.

[17] Robinson, Donald, E.
Surface Pressure Distributions on the 45 Degree Leading Edge Sweep MCAIR Generic Fighter Research Wing.
Technical Report WBWT-TR-1242, M.I.T. Wright Brothers Facility, Cambridge, MA, Nov, 1987.

[18] Robinson, Donald, E.
Implementation of a Separated Flow Panel Method for Wall Effects on Finite Swept Wings.
Master's thesis, Massachusetts Institute of Technology, 1988.

[19] Schlichting, Hermann, and Truckenbrodt, Erich.
Aerodynamics of the Airplane.
McGraw-Hill, New York, 1979.

[20] Sivells, James, C. and Salmi, Rachel, M.
Jet Boundary Corrections for Complete and Semispan Swept Wings in Closed Circular Wind Tunnels.
Technical Report NACA-TN-2454, U.S. National Advisory Committee for Aeronautics, Sept, 1951.

[21] Tamigniaux, T.L.B. and Oates, G.C.
An Experimental Investigation of the Effect of a Nearby Solid Surface on a Five-Hole Pressure Probe.
Technical Report AIAA-85-0334, American Institute of Aeronautics and Astronautics, Jan, 1985.

Appendix A

Tables

	Probe Number								
	1	2	3	4	5	6	7	8	9
α_{align}	0.0	-0.3	0.0	-0.3	0.0	-0.1	-0.1	-0.1	-0.2
β_{align}	-0.2	-0.3	-0.2	-0.2	0.0	-0.1	0.0	-0.1	0.0

Table A-1: Five-hole probe rake machining errors.

upper surface		*lower surface*	
chordwise tap number	x/c	chordwise tap number	x/c
0	0.000	0	0.000
1	0.005		
2	0.015	25	0.015
3	0.025		
4	0.040	26	0.050
5	0.070		
6	0.100	27	0.100
7	0.150		
8	0.200	28	0.200
9	0.250		
10	0.300	29	0.300
11	0.350		
12	0.400	30	0.400
13	0.450		
14	0.500	31	0.500
15	0.550		
16	0.600	32	0.600
17	0.650		
18	0.700	33	0.700
19	0.750		
20	0.800	34	0.800
21	0.850		
22	0.900	35	0.900
23	0.950	36	0.950
24	0.980		

Table A-2: Wing pressure tap locations.

distance from leading edge of ground board (in.)

upper surface side	centerline	lower surface side
3.75	3.75	3.75
2.0	2.0	2.0
0.85	0.85	0.85
0.0	0.0	0.0
0.85	0.85	0.85
2.0	2.0	2.0
3.75	3.75	3.75
11.25	11.25	11.25
	18.0	
23.25		23.25
	27.5	
35.0		35.0
47.0	W	47.0
59.0	I	59.0
71.0	N	71.0
83.0	G	83.0
	91.0	
95.5		95.5
	103.0	
107.5		107.5
120.0	120.0	120.0
138.5	138.5	138.5
156.5	156.5	156.5

* ground board tap locations for the turntable vary with angle of attack

* tap locations presented above are for the wing at 0° angle of attack

* root chord locations: leading edge 31.8", trailing edge 83.0"

Table A-3: Ground board static pressure tap locations

Date	Time	Run no.	Reynolds number (x10E6/ft)	Mach no.	Q (psf)	alfa geom. (deg)	Flap Deflections le (deg)	Flap Deflections te (deg)	Remarks
6/3	15:14	286	0.95	0.14	30.4	0.0	0	0	Wing pressures using initial zero angle
	15:31	287	0.93	0.14	30.3	6.0	0	0	
	16:06	288	0.93	0.15	30.9	18.0	0	0	
	16:24	289	0.92	0.15	30.9	30.0	0	0	
	16:53	290	0.94	0.15	32.1	6.0	0	0	
6/6	8:32	291	1.00	0.14	30.8	0.0	0	0	Wing zero was reset, large transducer drift
	10:37	292	0.98	0.15	30.8	0.0	0	0	Transducer had large drift
	11:10	293	0.97	0.14	30.4	0.0	0	0	Everything is O.K.
	11:26	294	0.95	0.14	30.1	6.0	0	0	
	14:30	295	0.96	0.14	30.5	18.0	0	0	
	14:46	296	0.95	0.14	30.3	30.0	0	0	
6/7	10:30	-	-	-	-	-	0	0	Flow visualization
	16:43	297	0.99	0.14	30.5	0.0	0	0	Ground board and wall pressure runs
	17:05	298	0.98	0.14	30.3	6.0	0	0	
	17:23	299	0.94	0.14	28.7	18.0	0	0	
	17:41	300	0.96	0.14	30.6	30.0	0	0	
6/8	17:59	301	0.99	0.14	30.3	0.0	0	0	Rake position #1 at entrance
	19:24	302	0.98	0.14	30.1	6.0	0	0	
	19:40	303	0.93	0.14	28.4	18.0	0	0	
	19:58	304	0.95	0.14	30.3	30.0	0	0	
6/9	8:00	305	1.00	0.15	31.1	0.0	0	0	Rake position #2 at entrance
	8:17	306	0.97	0.14	30.5	6.0	0	0	
	8:34	307	0.95	0.14	30.1	18.0	0	0	
	8:51	308	0.94	0.14	30.0	30.0	0	0	
	9:40	309	0.96	0.14	30.6	0.0	0	0	Rake position #3 at entrance
	9:56	310	0.95	0.14	30.5	6.0	0	0	
	10:12	311	0.91	0.14	28.9	18.0	0	0	
	10:27	312	0.93	0.14	30.0	30.0	0	0	
	11:09	313	0.94	0.14	30.5	0.0	0	0	Rake position #4 at entrance
	11:26	314	0.94	0.14	30.5	6.0	0	0	
	11:43	315	0.92	0.14	29.7	18.0	0	0	
	12:00	316	0.92	0.14	29.9	30.0	0	0	
	14:55	317	0.98	0.14	30.8	0.0	0	0	Rake position #9 at entrance
	15:10	318	0.96	0.14	30.6	6.0	0	0	
	15:26	319	0.95	0.14	30.5	18.0	0	0	
	15:43	320	0.95	0.14	30.5	30.0	0	0	
	17:19	321	0.97	0.14	30.6	0.0	0	0	Rake position #10 at entrance
	17:34	322	0.97	0.14	30.5	6.0	0	0	
	17:50	323	0.97	0.14	30.8	18.0	0	0	
	18:06	324	0.96	0.14	30.8	30.0	0	0	
6/10	8:59	325	1.01	0.15	30.6	0.0	0	0	Rake position #8 at entrance
	9:16	326	0.98	0.14	30.1	6.0	0	0	
	9:33	327	0.97	0.14	30.3	18.0	0	0	

Table A-4: Run schedule

Date	Time	Run no.	Reynolds number (x10E6/ft)	Mach no.	Q (psf)	alfa geom. (deg)	Flap Deflections le (deg)	Flap Deflections te (deg)	Remarks
6/10	9:49	328	0.95	0.14	30.3	30.0	0	0	
	10:37	329	0.96	0.15	30.6	0.0	0	0	Rake position #7 at entrance
	10:53	330	0.95	0.14	30.5	6.0	0	0	
	11:11	331	0.91	0.14	28.8	18.0	0	0	
	11:28	332	0.93	0.14	30.5	30.0	0	0	
	12:32	333	0.94	0.14	30.2	0.0	0	0	Rake position #6 at entrance
	12:48	334	0.93	0.15	30.7	6.0	0	0	
	13:04	335	0.93	0.14	30.5	18.0	0	0	
	13:19	336	0.91	0.14	30.3	30.0	0	0	
	15:55	337	0.95	0.14	30.3	0.0	0	0	Rake position #5 at entrance
	16:11	338	0.94	0.14	30.4	6.0	0	0	
	16:27	339	0.93	0.14	29.9	18.0	0	0	
	16:42	340	0.93	0.14	30.3	30.0	0	0	
6/12	8:44	341	0.98	0.14	30.2	0.0	0	0	Rake position #5 at exit
	9:01	342	0.96	0.14	30.7	6.0	0	0	
	9:53	343	0.95	0.14	30.0	18.0	0	0	
	10:09	344	0.94	0.14	30.7	30.0	0	0	
	10:51	345	0.94	0.14	30.5	0.0	0	0	Rake position #6 at exit
	11:07	346	0.92	0.14	30.3	6.0	0	0	
	11:22	347	0.90	0.14	28.8	18.0	0	0	
	11:40	348	0.89	0.14	29.1	30.0	0	0	
	12:24	349	0.92	0.14	30.2	0.0	0	0	Rake position #7 at exit
	12:40	350	0.91	0.14	30.0	6.0	0	0	
	12:58	351	0.91	0.14	30.1	18.0	0	0	
	13:13	352	0.90	0.14	30.1	30.0	0	0	
	14:11	353	0.91	0.14	30.1	0.0	0	0	Rake position #8 at exit
	14:27	354	0.91	0.14	30.2	6.0	0	0	
	14:42	355	0.88	0.14	28.8	18.0	0	0	
	14:58	356	0.90	0.14	30.0	30.0	0	0	
	16:13	357	0.94	0.15	31.0	0.0	0	0	Rake position #10 at exit
	16:29	358	0.94	0.15	30.9	6.0	0	0	
	16:45	359	0.91	0.14	29.5	18.0	0	0	
	17:01	360	0.91	0.14	29.7	30.0	0	0	
	18:40	361	0.94	0.14	30.6	0.0	0	0	Rake position #9 at exit
	19:17	362	0.93	0.14	30.3	6.0	0	0	
	19:33	363	0.91	0.14	30.2	18.0	0	0	
	20:02	364	0.90	0.14	30.2	30.0	0	0	
6/13	9:41	365	0.99	0.15	30.7	0.0	0	0	Rake position #4 at exit
	9:56	366	0.96	0.14	30.3	6.0	0	0	
	10:14	367	0.93	0.14	28.8	18.0	0	0	
	10:36	368	0.95	0.15	30.9	30.0	0	0	
	11:36	369	0.96	0.14	30.1	0.0	0	0	Rake position #3 at exit
	11:51	370	0.95	0.14	29.9	6.0	0	0	
	12:08	371	0.92	0.14	28.7	18.0	0	0	
	12:23	372	0.94	0.14	30.4	30.0	0	0	
	13:02	373	0.95	0.14	30.4	0.0	0	0	Rake position #2 at exit
	13:18	374	0.95	0.14	30.2	6.0	0	0	
	13:34	375	0.94	0.14	30.3	18.0	0	0	

Table A-4, continued

Date	Time	Run no.	Reynolds number (x10E6/ft)	Mach no.	Q (psf)	alfa geom. (deg)	Flap Deflections le (deg)	te (deg)	Remarks
6/13	12:49	376	0.94	0.14	30.5	30.0	0	0	
	14:32	377	0.95	0.15	30.7	0.0	0	0	Rake position #2 at exit
	14:47	378	0.95	0.14	30.5	6.0	0	0	
	15:03	379	0.93	0.14	29.9	18.0	0	0	
	15:18	380	0.93	0.14	30.1	30.0	0	0	
6/15	9:28	-	-	-	-	-	10	10	Flow visualization
	13:46	381	0.99	0.14	30.0	6.0	10	10	Rake position #8 at exit
	15:17	382	1.01	0.14	30.6	6.0	10	10	Rake position #7 at exit
	16:03	383	0.99	0.14	30.3	6.0	10	10	Rake position #6 at exit
	16:43	384	0.98	0.14	30.0	6.0	10	10	Rake position #5 at exit
	17:39	385	0.99	0.14	30.2	6.0	10	10	Rake position #10 at exit
	19:14	386	1.00	0.14	30.2	6.0	10	10	Rake position #9 at exit
	21:33	387	0.99	0.14	29.7	6.0	10	10	Rake position #4 at exit
	21:49	388	0.95	0.14	28.7	12.0	10	10	
	22:34	389	0.98	0.14	30.3	6.0	10	10	Rake position #3 at exit
6/16	8:17	390	1.00	0.14	30.5	6.0	10	10	Rake position #2 at exit
	9:01	391	0.99	0.14	30.1	6.0	10	10	Rake position #1 at exit
	9:52	392	0.99	0.14	30.7	6.0	10	10	Wall and ground board pressures
	10:08	393	0.97	0.14	30.4	12.0	10	10	
	12:11	394	0.97	0.14	30.1	6.0	10	10	Rake position #1 at entrance
	13:33	395	0.94	0.14	30.0	6.0	10	10	Rake position #2 at entrance
	14:10	396	0.95	0.14	30.0	6.0	10	10	Rake position #3 at entrance
	14:45	397	0.95	0.14	30.4	6.0	10	10	Rake position #4 at entrance
	15:01	398	0.92	0.14	29.3	12.0	10	10	
	16:26	399	0.95	0.14	30.6	6.0	10	10	Rake position #9 at entrance
6/17	9:20	400	0.98	0.14	30.1	6.0	10	10	Rake position #10 at entrance
	10:36	401	0.96	0.14	30.6	6.0	10	10	Rake position #8 at entrance
	10:55	402	0.93	0.14	30.5	12.0	10	10	
	11:32	403	0.93	0.14	30.6	6.0	10	10	Rake position #7 at entrance
	12:15	404	0.92	0.14	30.2	6.0	10	10	Rake position #6 at entrance
	13:00	405	0.92	0.14	29.9	6.0	10	10	Rake position #5 at entrance
	16:32	406	0.93	0.14	30.4	6.0	10	10	Wing pressures
	16:48	407	0.92	0.14	30.1	12.0	10	10	
	17:05	408	0.90	0.14	29.2	18.0	10	10	
	17:19	409	0.90	0.14	29.0	30.0	10	10	

Table A-4, continued

Run	q (psf)	$Re_{\bar{x}}$ ($x10^6$)	M	α (deg)	δ_{le} (deg)	δ_{te} (deg)	C_L	C_D
293	30.4	2.59	0.14	0.0	0	0	0.000	0.000
294	30.1	2.53	0.14	6.6	0	0	0.370	0.029
295	30.5	2.56	0.14	19.5	0	0	0.929	0.311
296	30.3	2.53	0.14	31.4	0	0	0.870	0.533
406	30.4	2.45	0.14	7.1	10	10	0.668	0.058
407	30.1	2.45	0.14	13.5	10	10	0.939	0.167
408	29.2	2.40	0.14	19.7	10	10	1.068	0.333
409	29.0	2.40	0.14	31.7	10	10	1.012	0.609

Table A-5: Coefficients of lift and drag.

	$\Lambda_{1/4}$	AR	λ	Λ_{LE}	t/c
MCAIR	38.7°	3.0	0.25	45.0°	0.05
Reference 13	45.0°	3.0	0.50	48.5°	0.10
Reference 7 wing A	50.0°	3.10	0.36	-	0.075
Reference 7 wing C	48.8°	3.10	0.38	-	0.075
Reference 11 Javelin	-	2.92	0.17	48.0°	0.10
Reference 11 Swift	-	3.43	0.35	40.0°	0.10
Reference 9 RAE 101	40.0°	3.50	0.40	-	0.10
Reference 9 RAE 104	40.0°	3.50	0.40	-	0.10
Reference 9 HSA I	40.0°	3.50	0.40	-	0.10
Reference 9 64A010	40.0°	3.50	0.40	-	0.10

Table A-6: Geometric characteristics of wings.

Appendix B

Figures

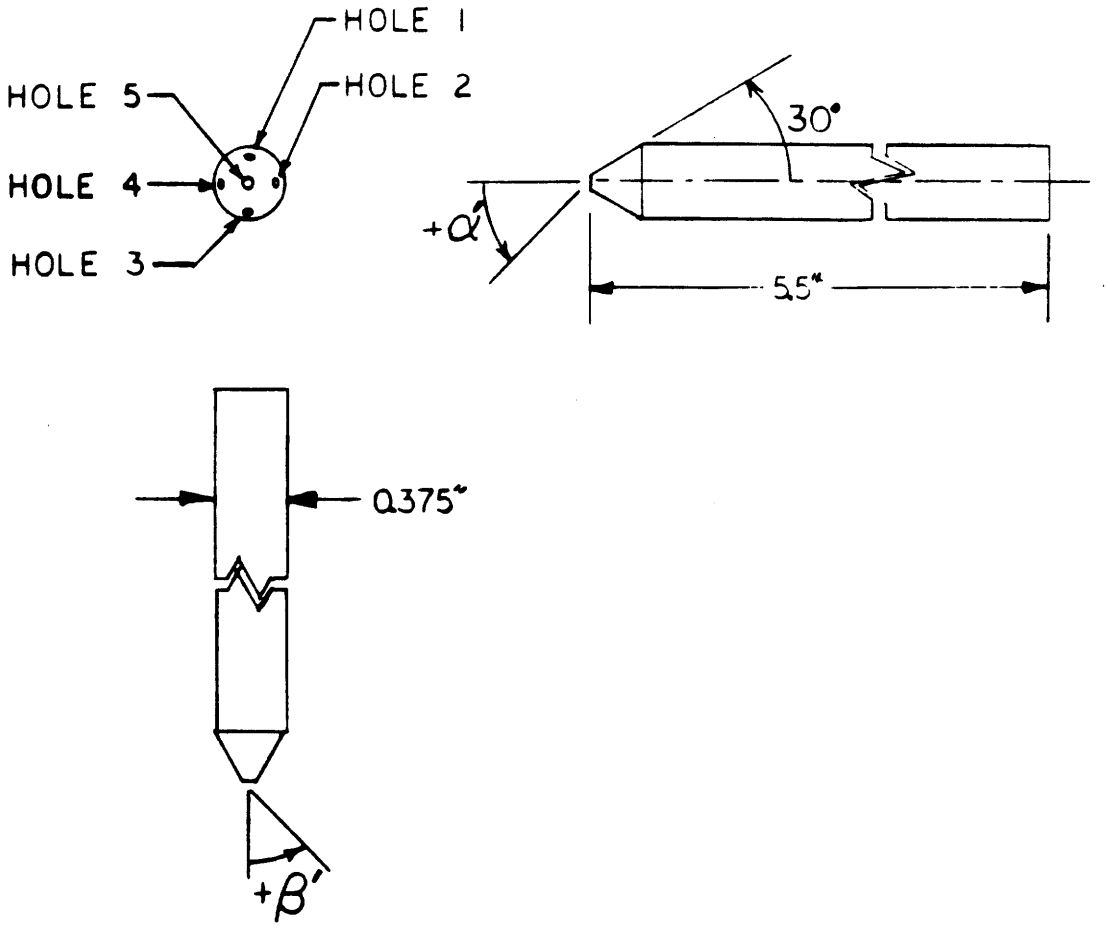

Figure B-1: Diagram of five-hole probes.

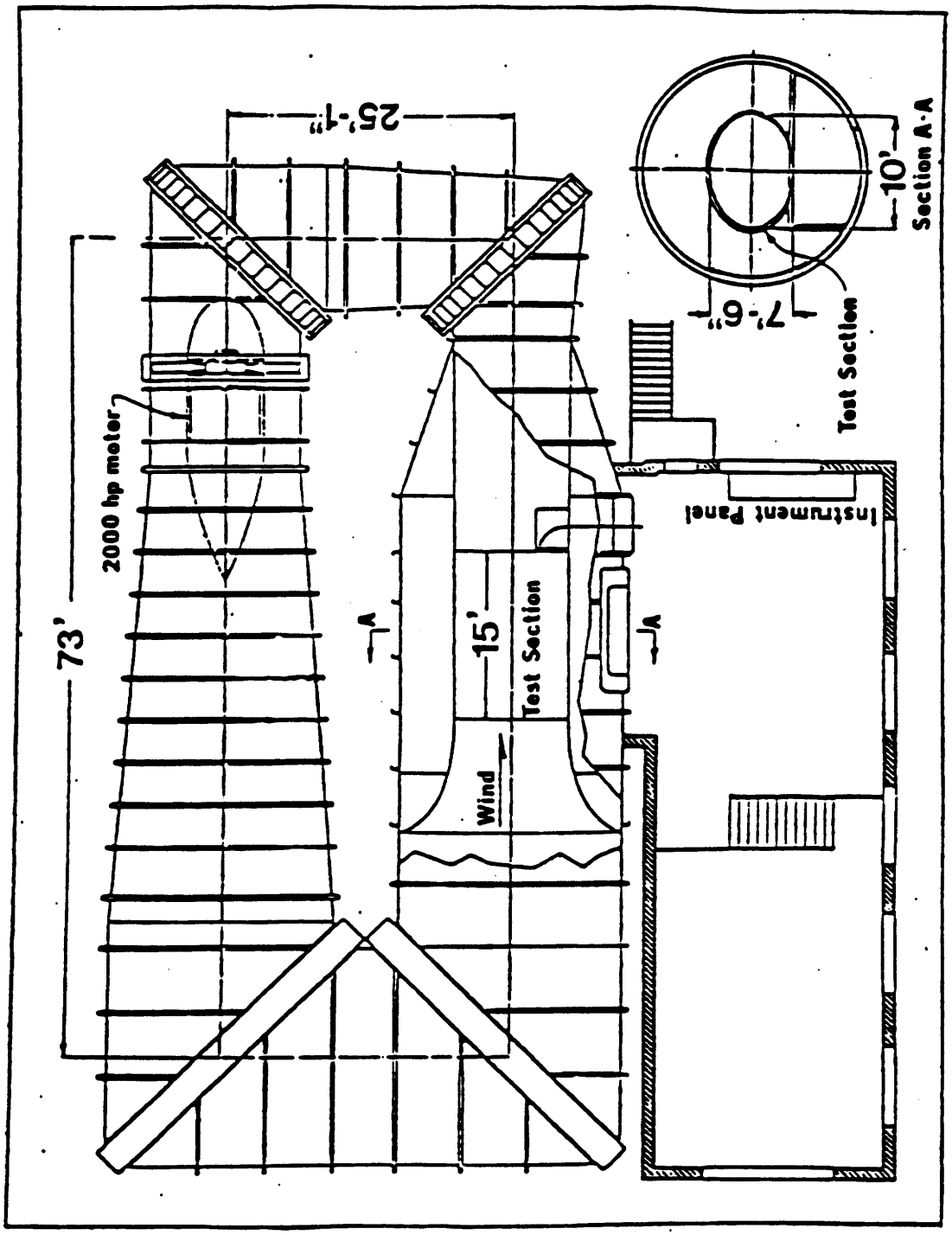

Figure B-2: Schematic diagram of the Wright Brothers Facility.

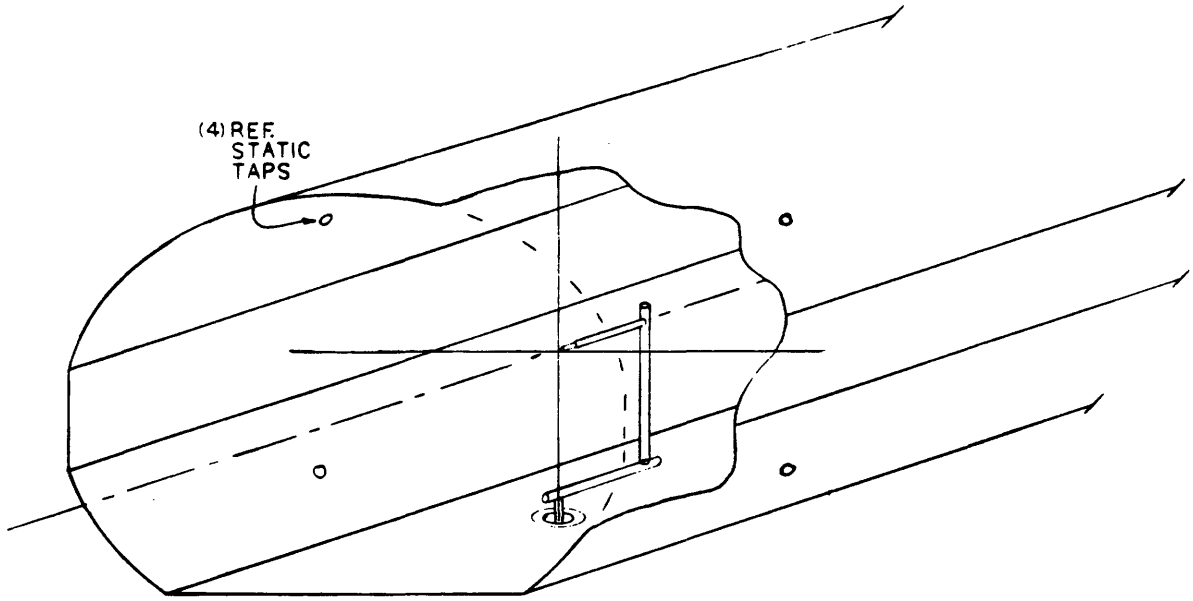

Figure B-3: Drawing of single five-hole probe calibration setup.

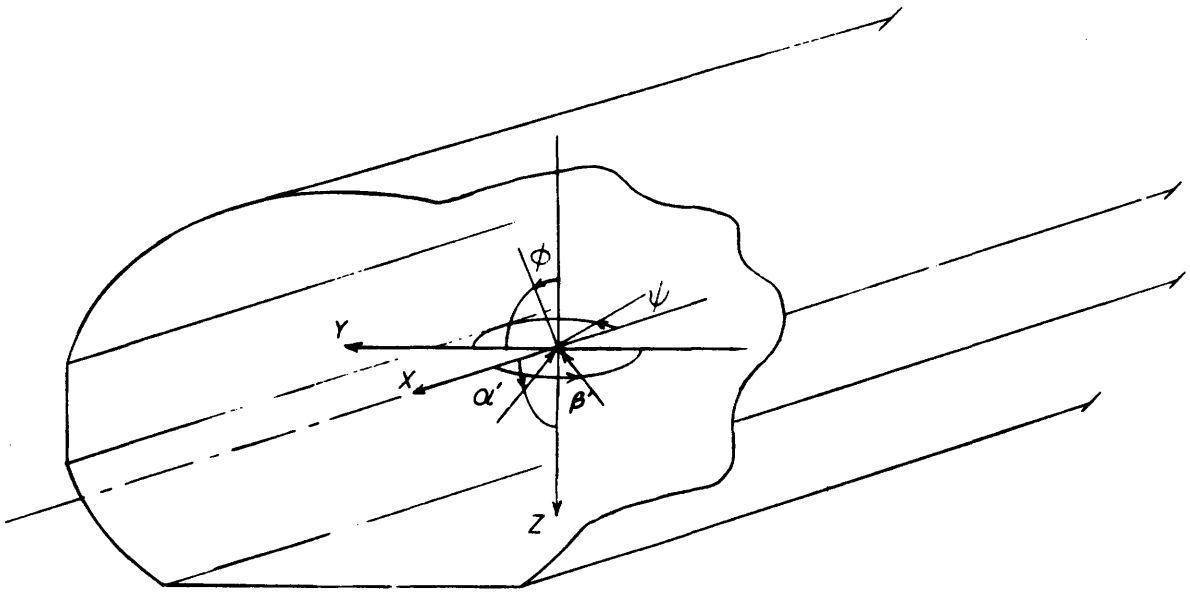

Figure B-4: Coordinate axes for single five-hole probe calibration.

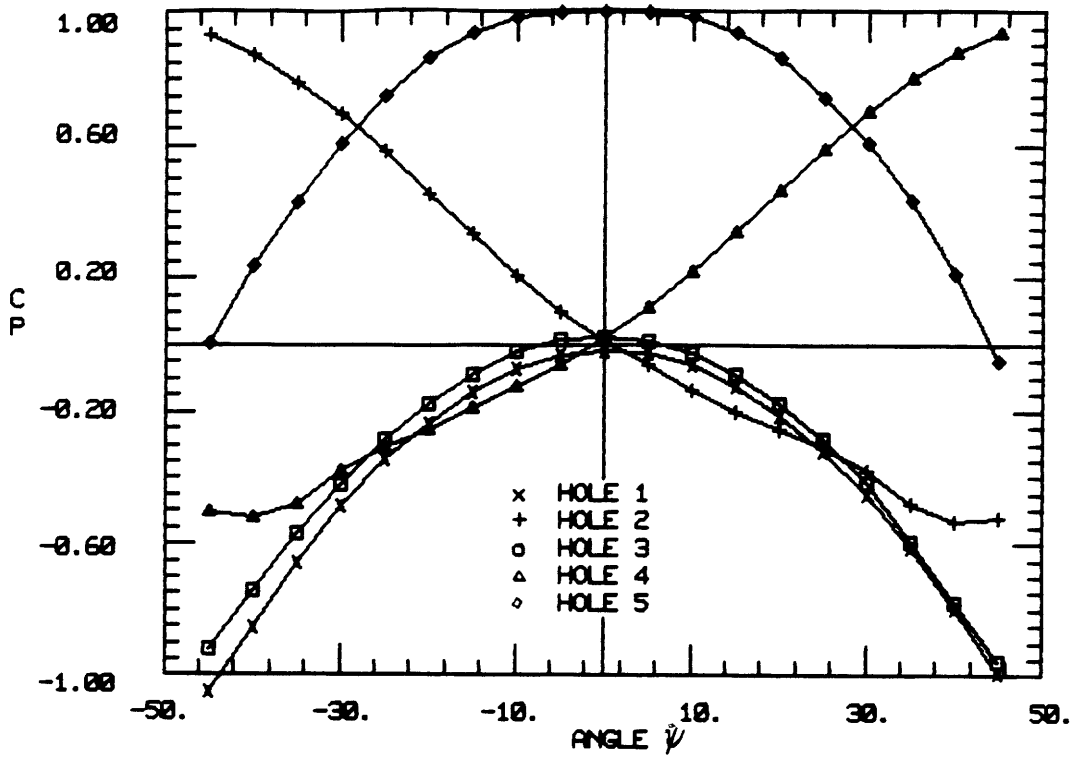

Figure B-5: Pressure coefficients from individual probe holes; ϕ=0°.

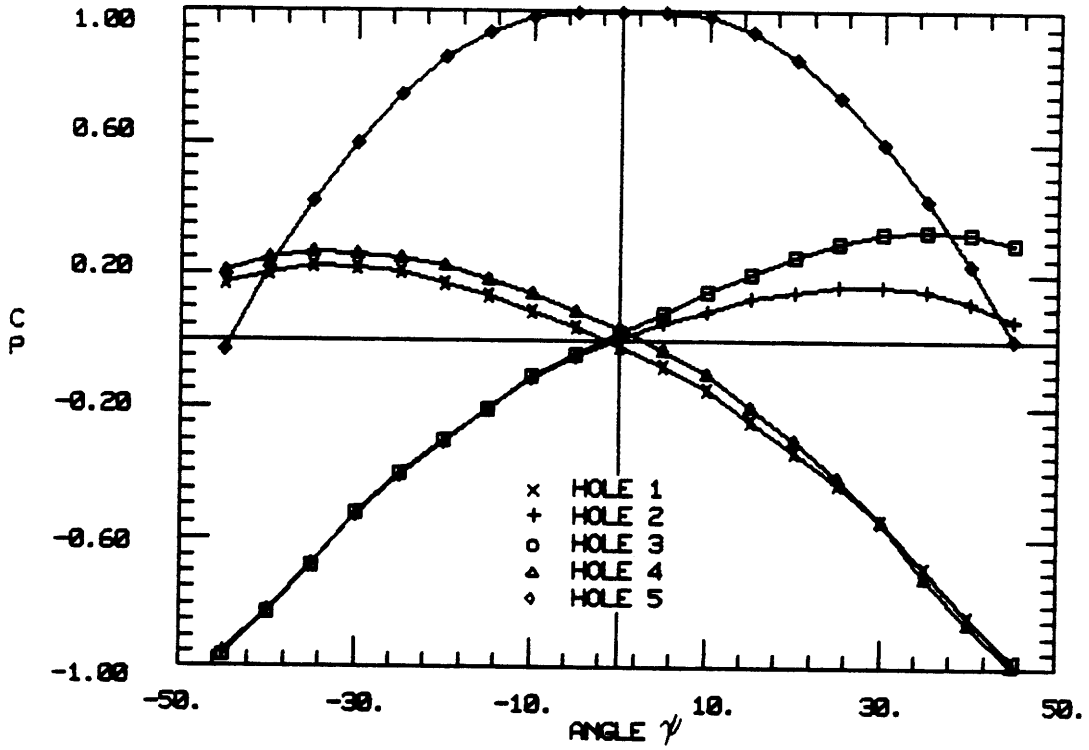

Figure B-6: Pressure coefficients from individual probe holes; ϕ=45°.

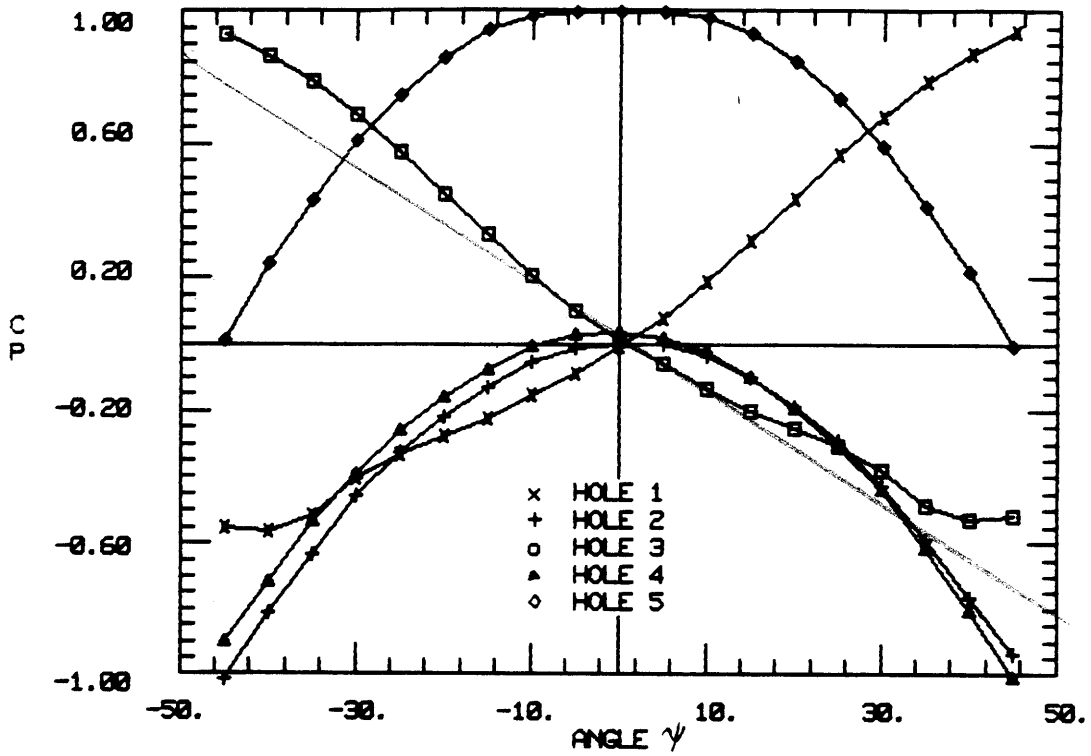

Figure B-7: Pressure coefficients from individual probe holes; ϕ=90°.

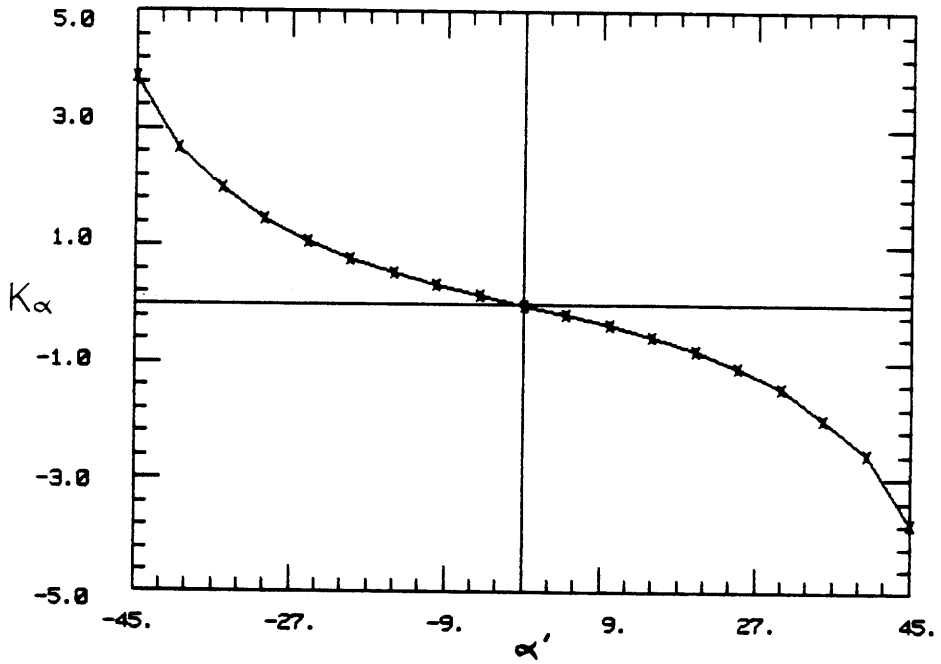

Figure B-8: Plot of K_α *vs* α'.

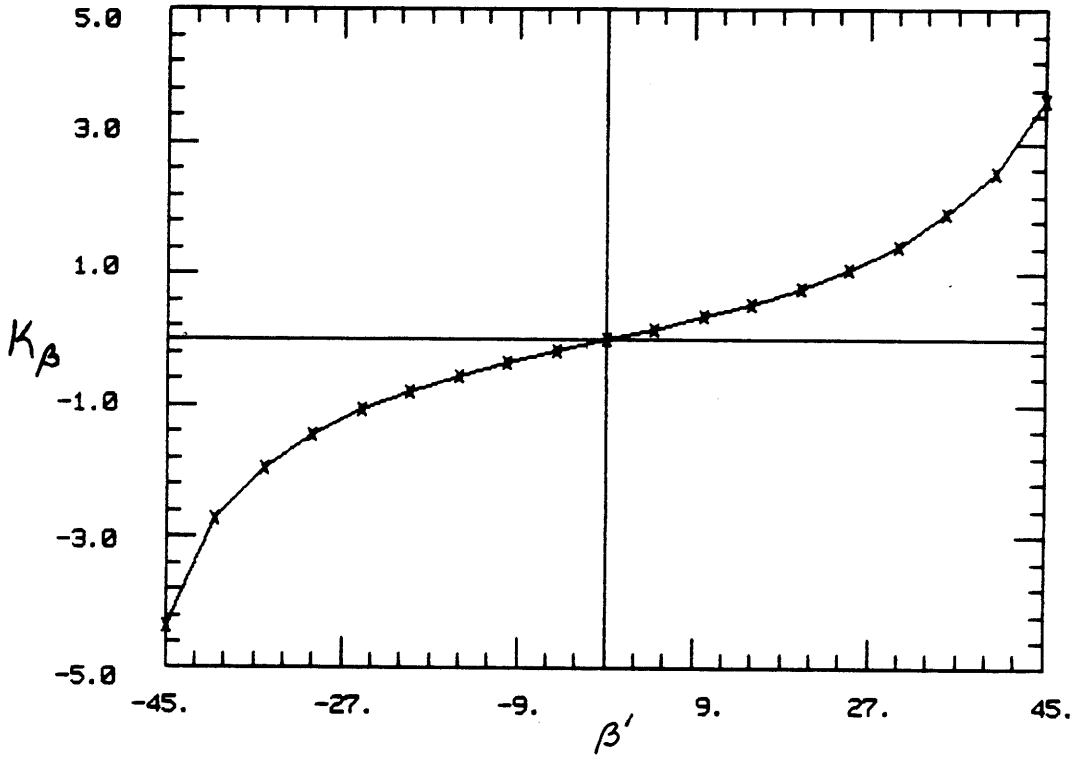

Figure B-9: Plot of K_β *vs* β'.

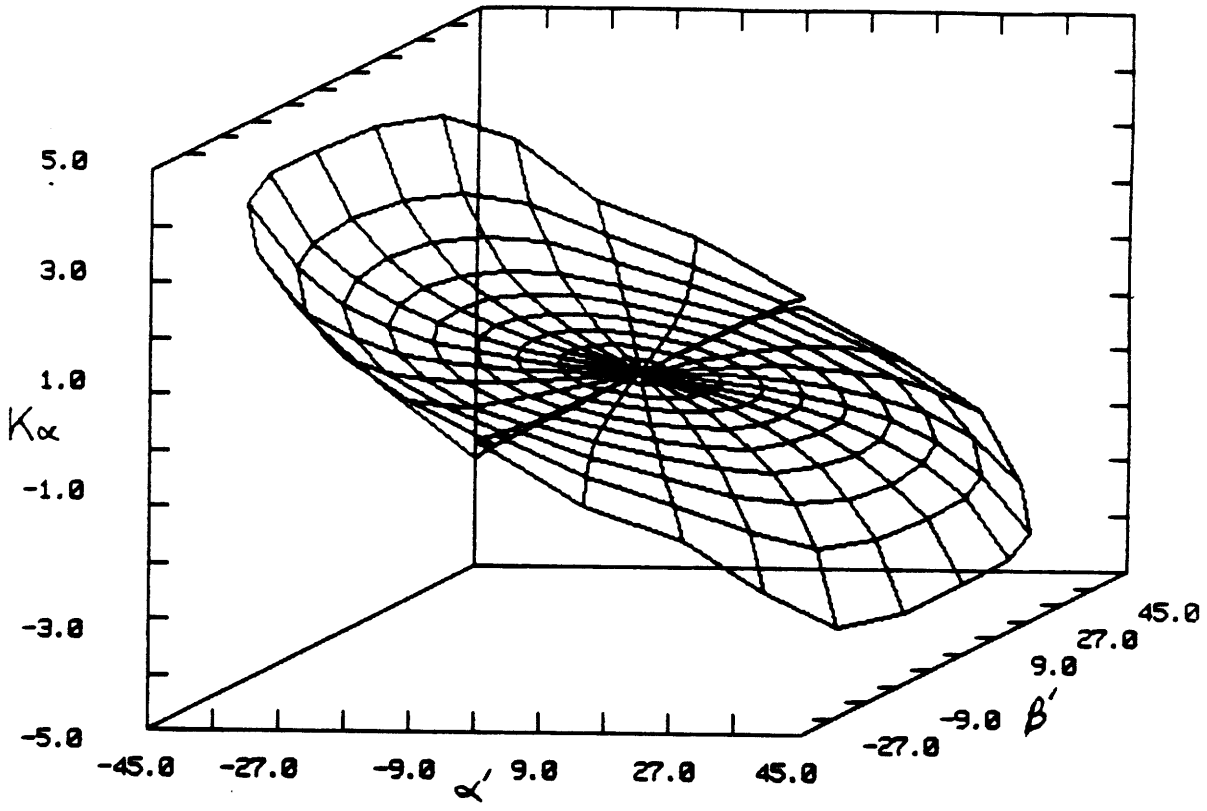

Figure B-10: Carpet plot of K_α *vs* α',β'.

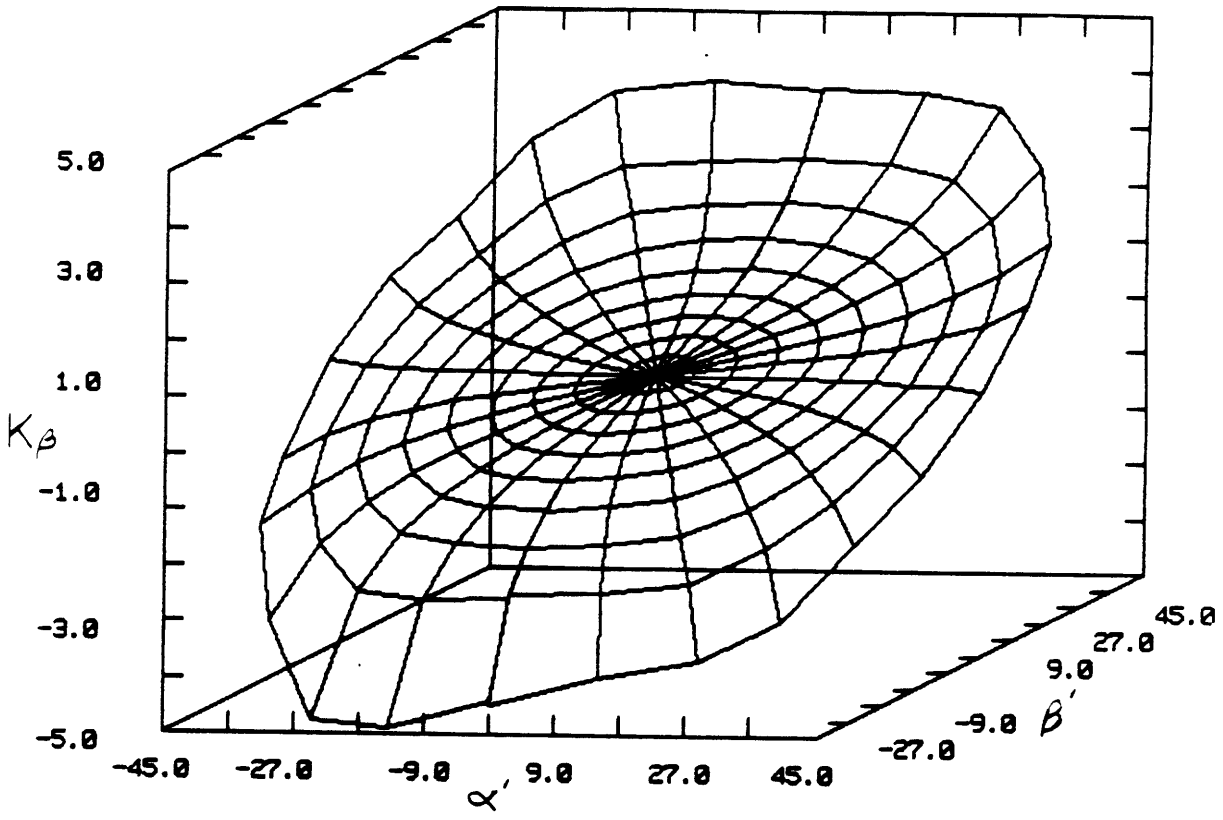

Figure B-11: Carpet plot of K_β *vs* α',β'.

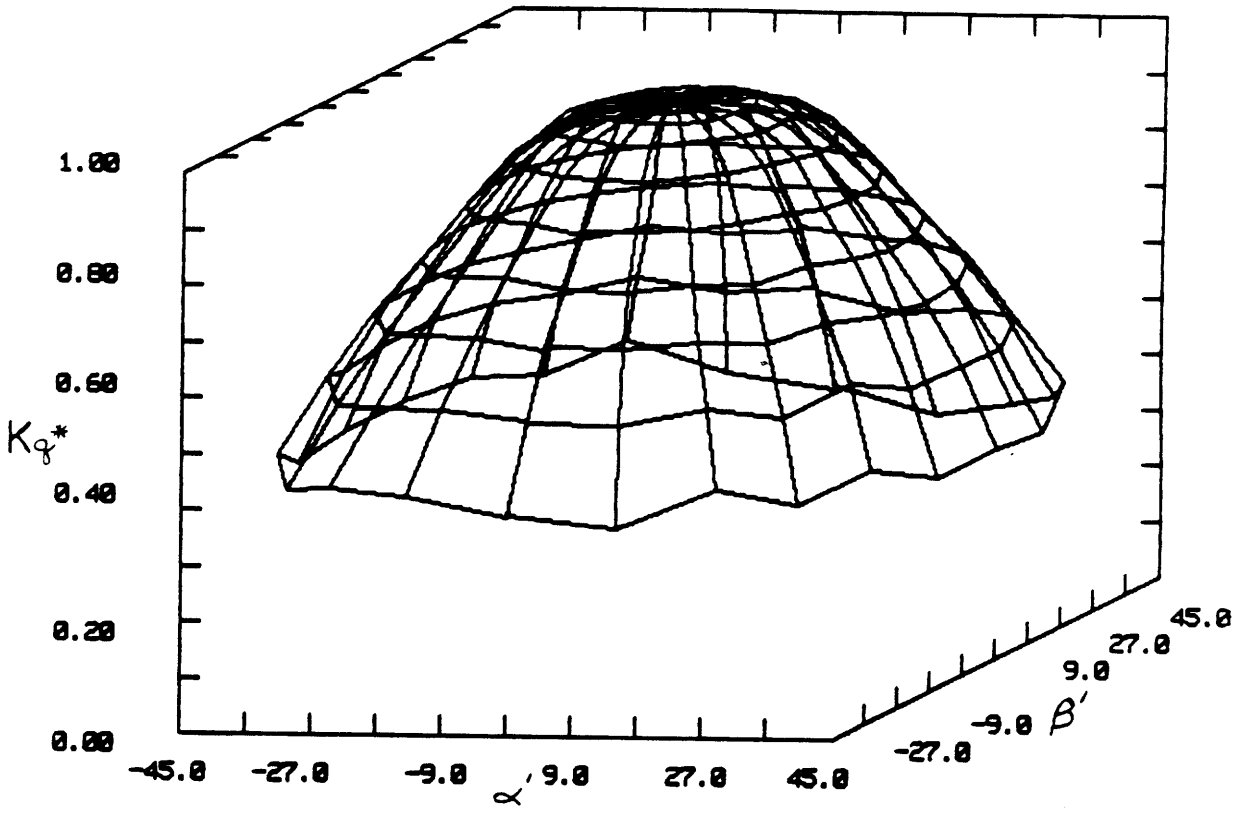

Figure B-12: Carpet plot of K_q* *vs* α',β'.

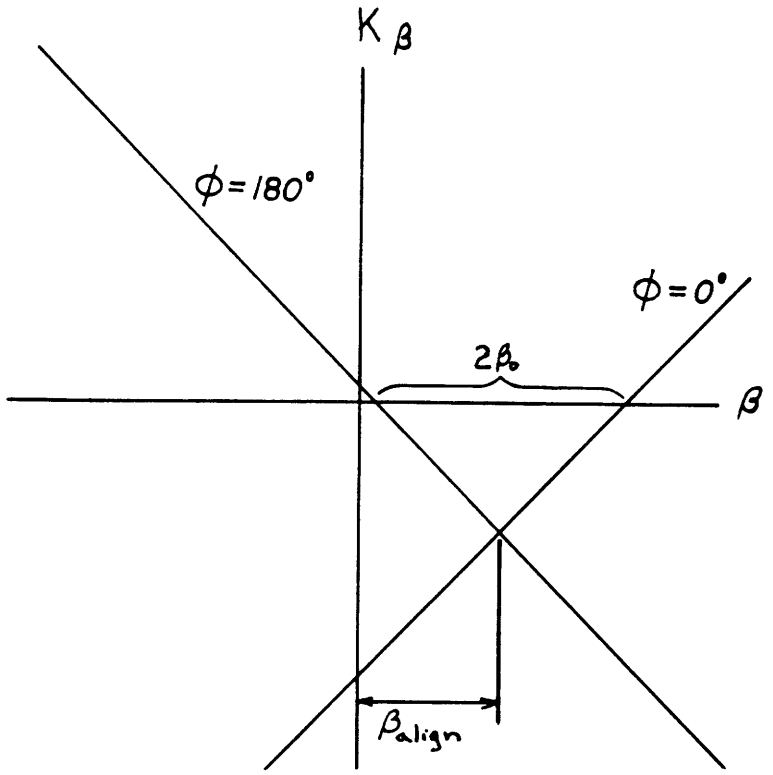

Figure B-13: Plot illustrating flow alignment and probe machining errors.

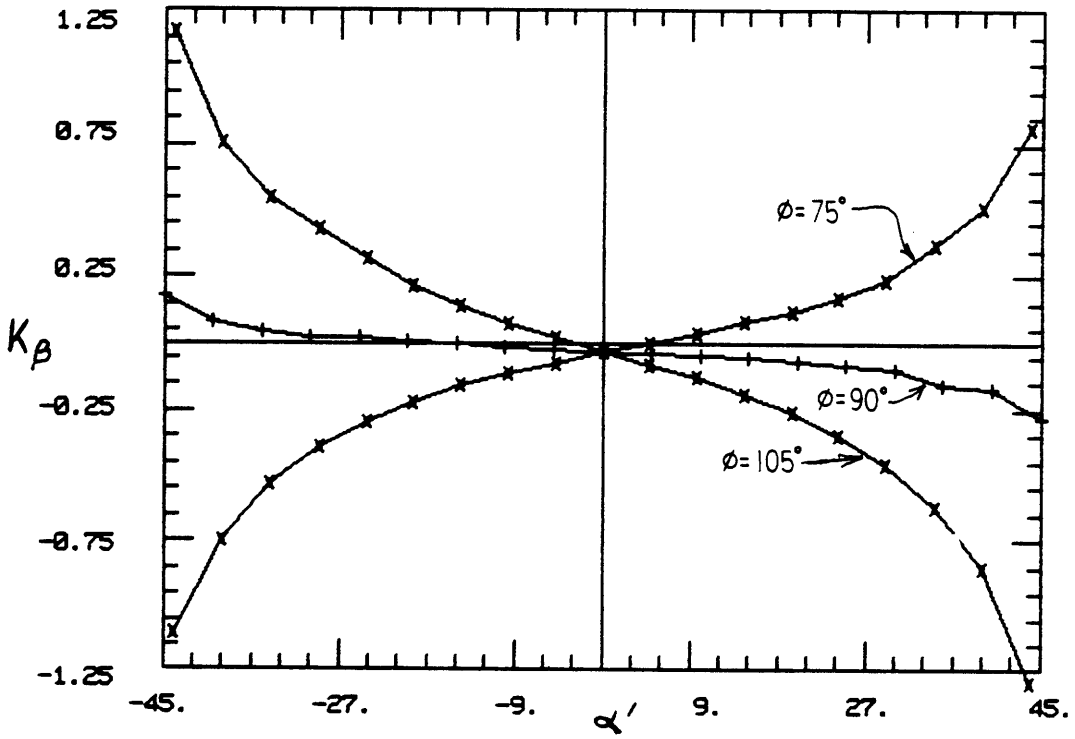

Figure B-14: Plot used to determine error in roll angle.

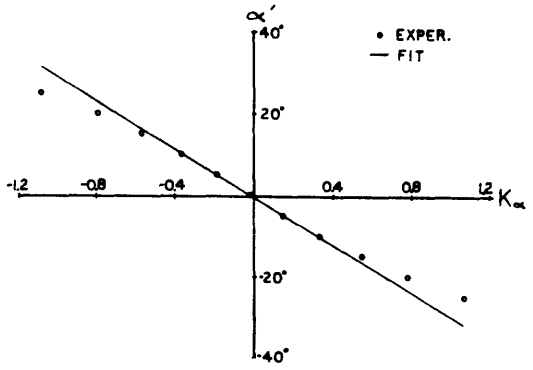

Figure B-15: 1st order fit to calibration data, α' *vs* K_α.

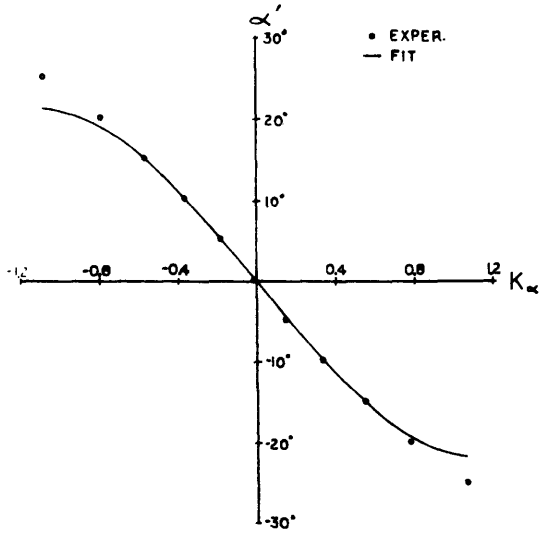

Figure B-16: 3rd order fit to calibration data, α' *vs* K_α.

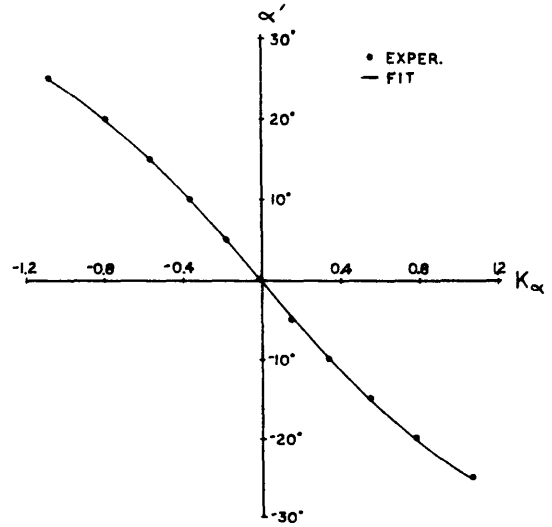

Figure B-17: 5th order fit to calibration data, α' *vs* K_α.

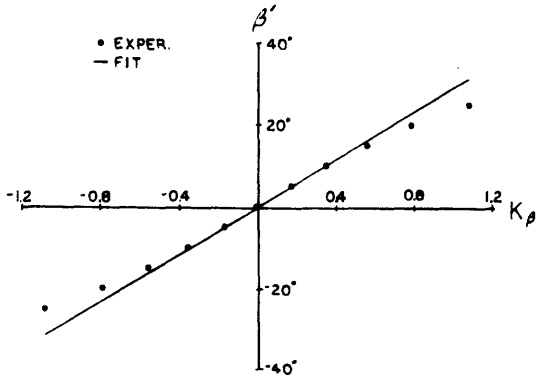

Figure B-18: 1st order fit to calibration data, β' *vs* K_β.

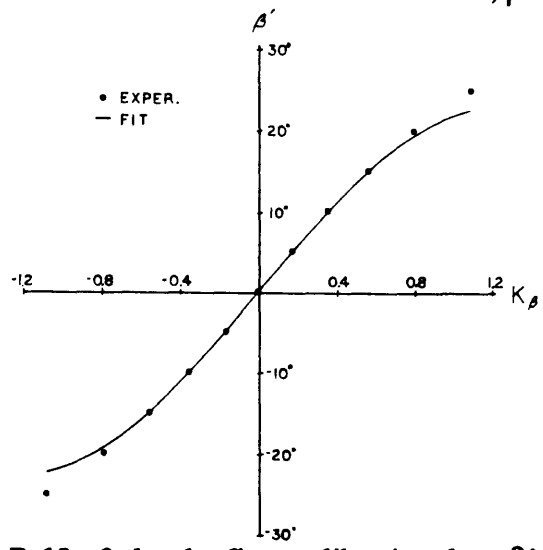

Figure B-19: 3rd order fit to calibration data, β' *vs* K_β.

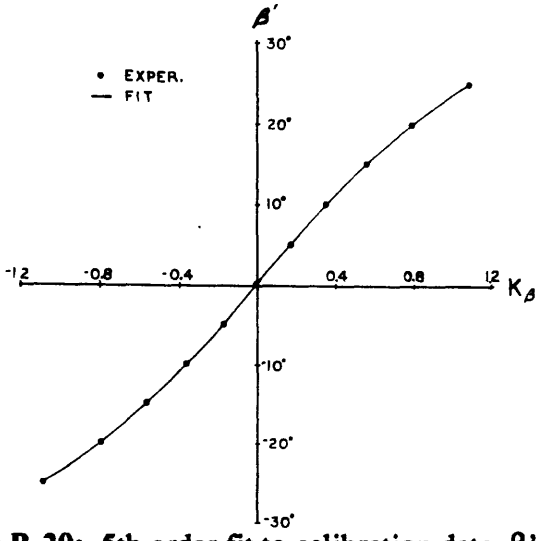

Figure B-20: 5th order fit to calibration data, β' *vs* K_β.

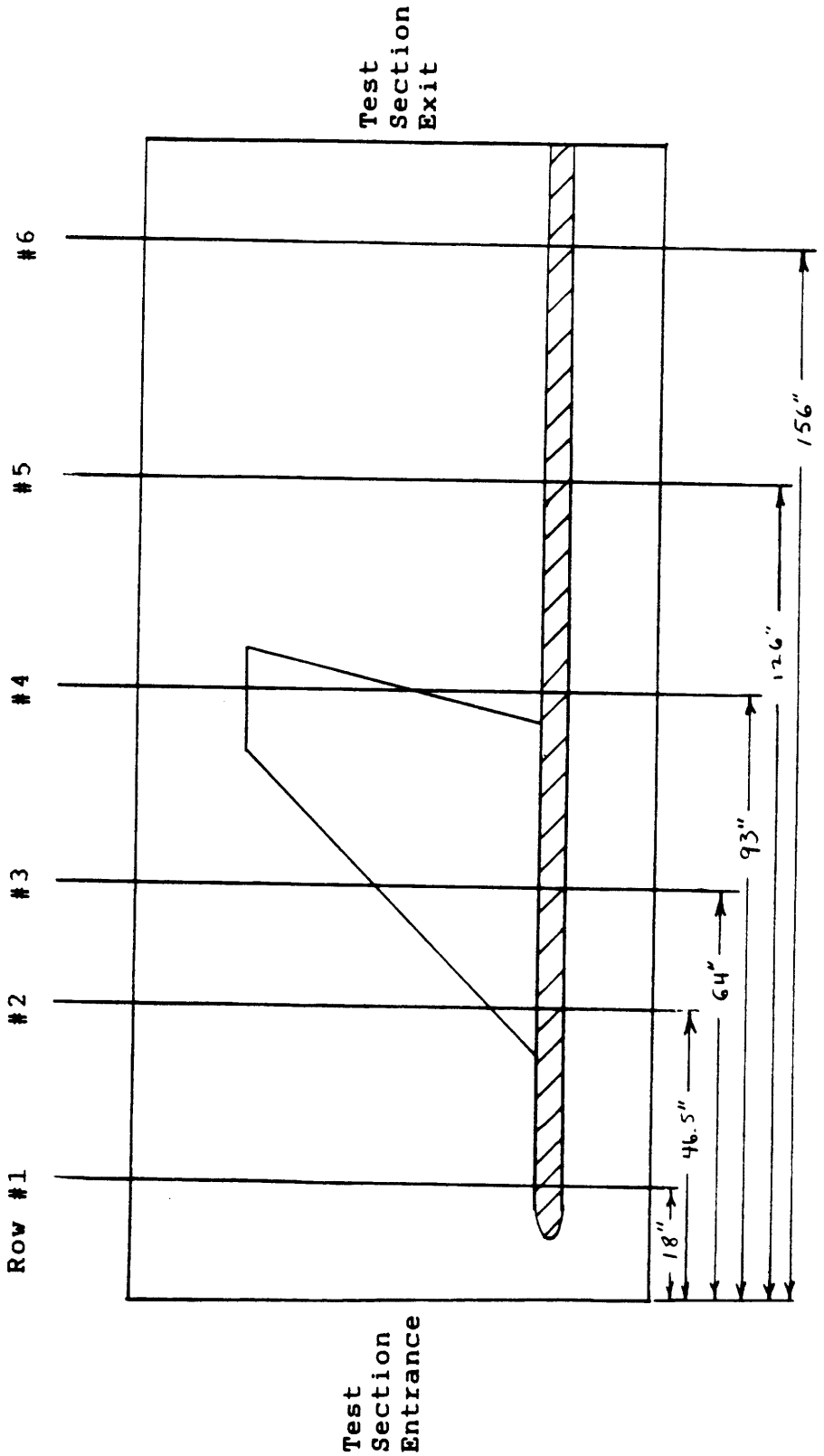

Figure B-21: Locations of wall static pressure tap rows.

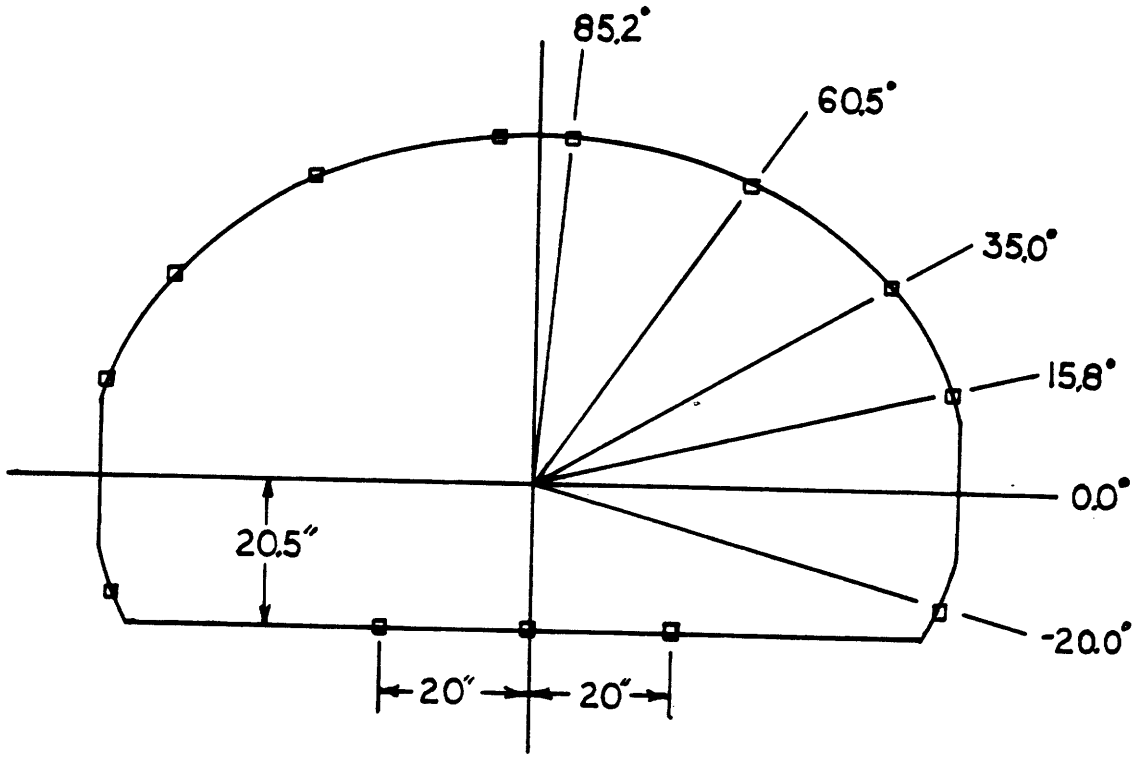

Figure B-22: Cross-sectional view of wall static pressure tap locations.

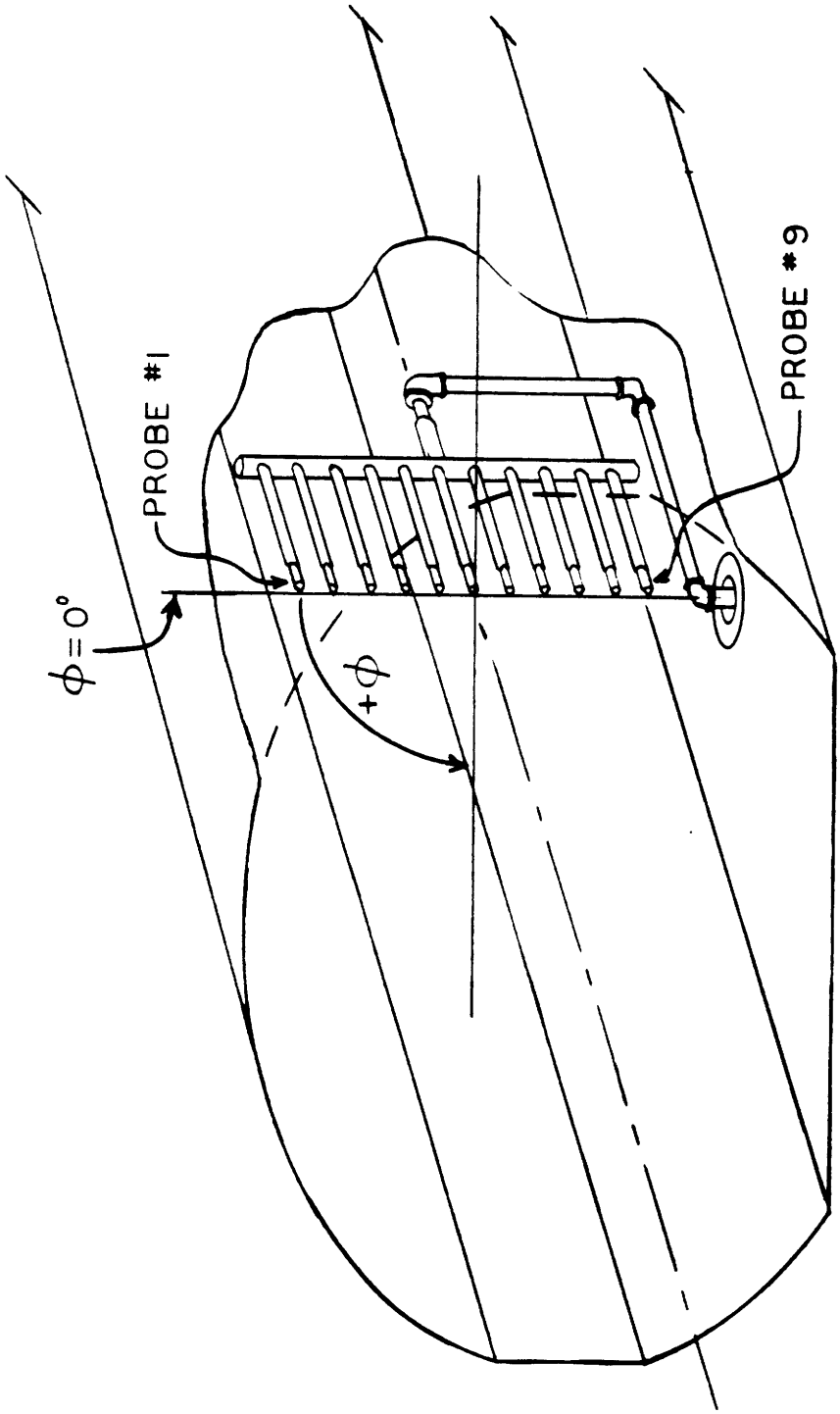

Figure B-23: Rake calibration setup in tunnel.

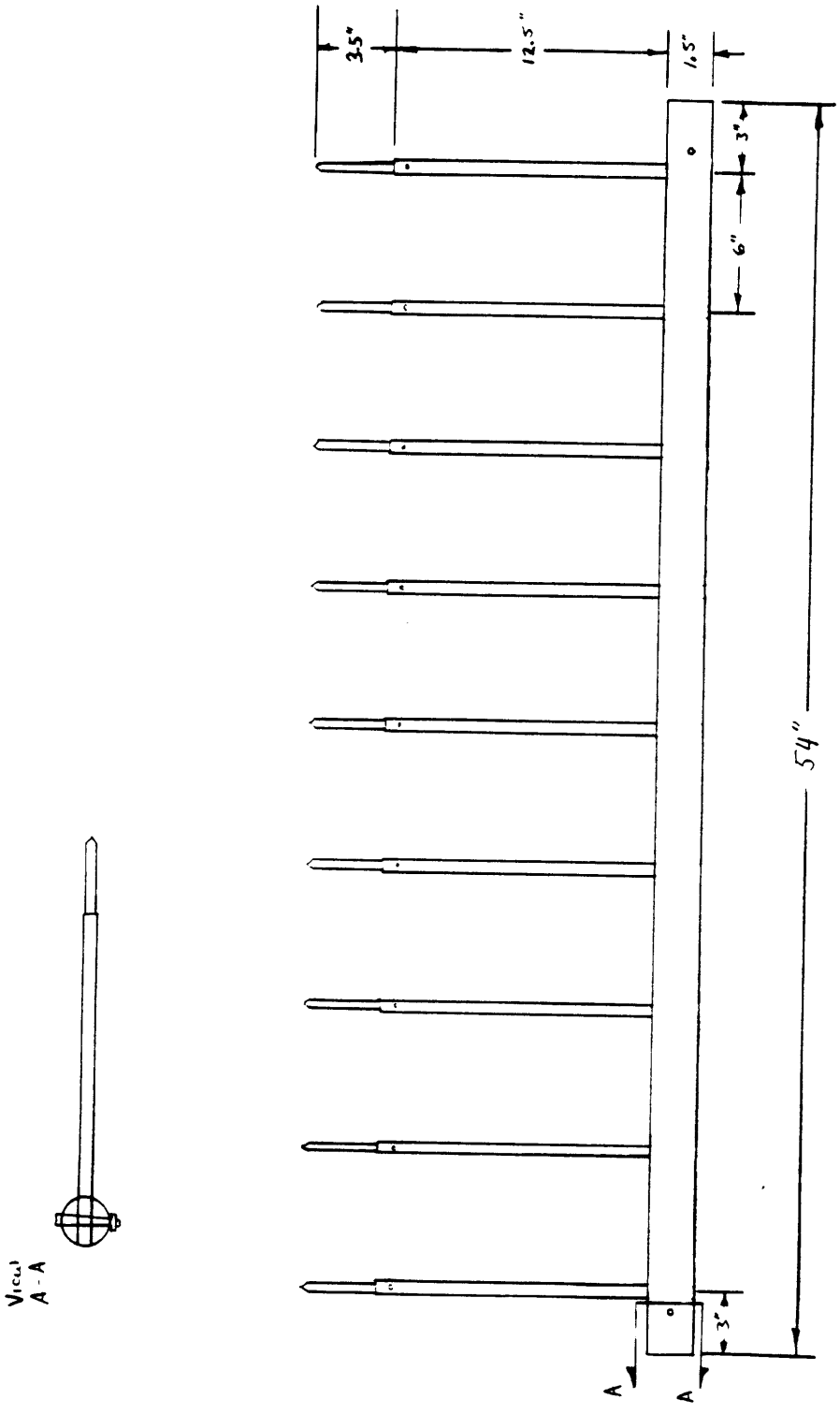

Figure B-24: Diagram of five-hole probe rake.

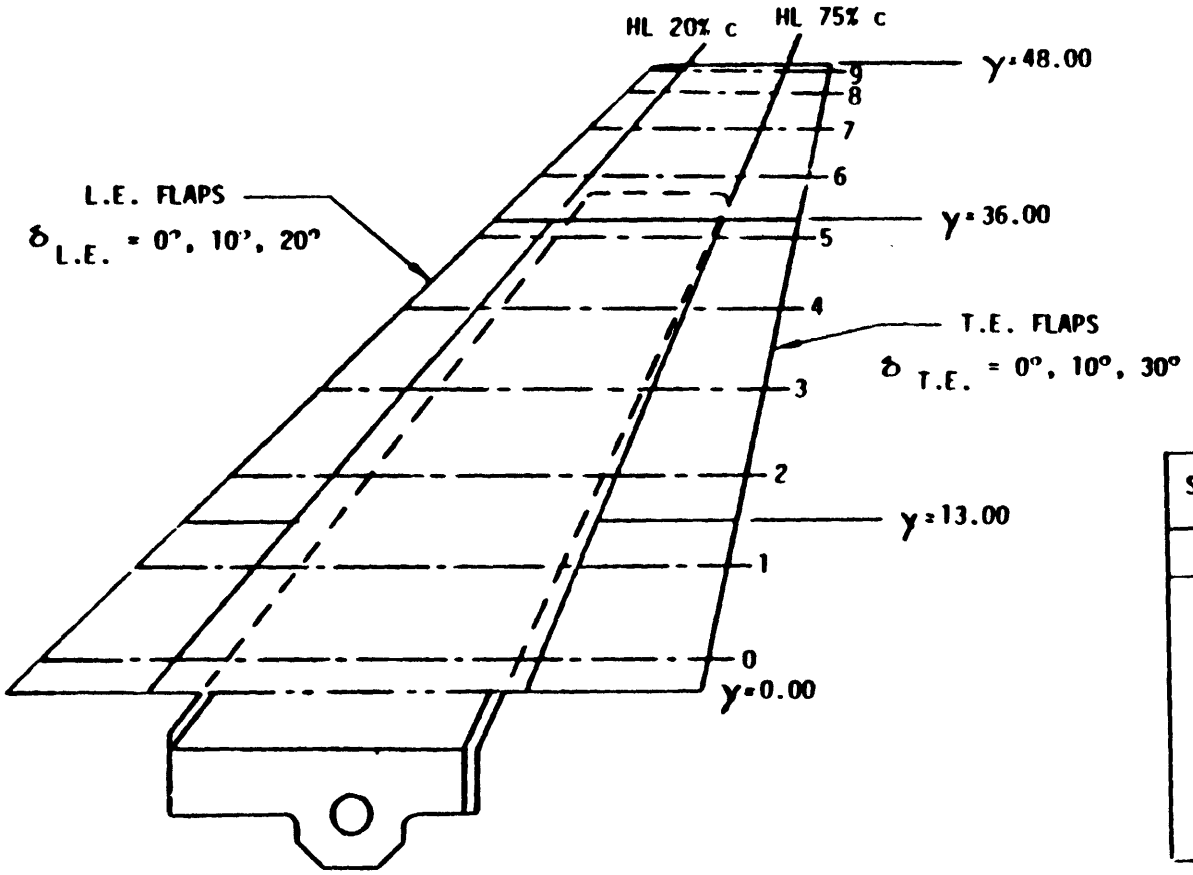

WING CHARACTERISTICS	
$\Lambda_{L.E.}$	45°
λ	.25
b/2	48.00 in
C_r	51.20 in
C_t	12.80 in
AR	3.0
S/2	1536 in^2

STATIC PRESSURE ROW LOCATION	
K	Y
0	2.40
1	9.53
2	16.49
3	23.10
4	29.20
5	34.65
6	39.29
7	43.03
8	45.79
9	47.44

SPANWISE LOCATION DERIVED FROM

$$\bar{y}_{K+1} = .05 + .95 \cos\left[\frac{\pi (10-k)}{20}\right]$$

WING TIP ~ 100 UPPER TAPS

WING SKIN ~ 54 UPPER TAPS

L.E. FLAPS ~ 60 UPPER TAPS

T.E. FLAPS ~ 36 UPPER TAPS

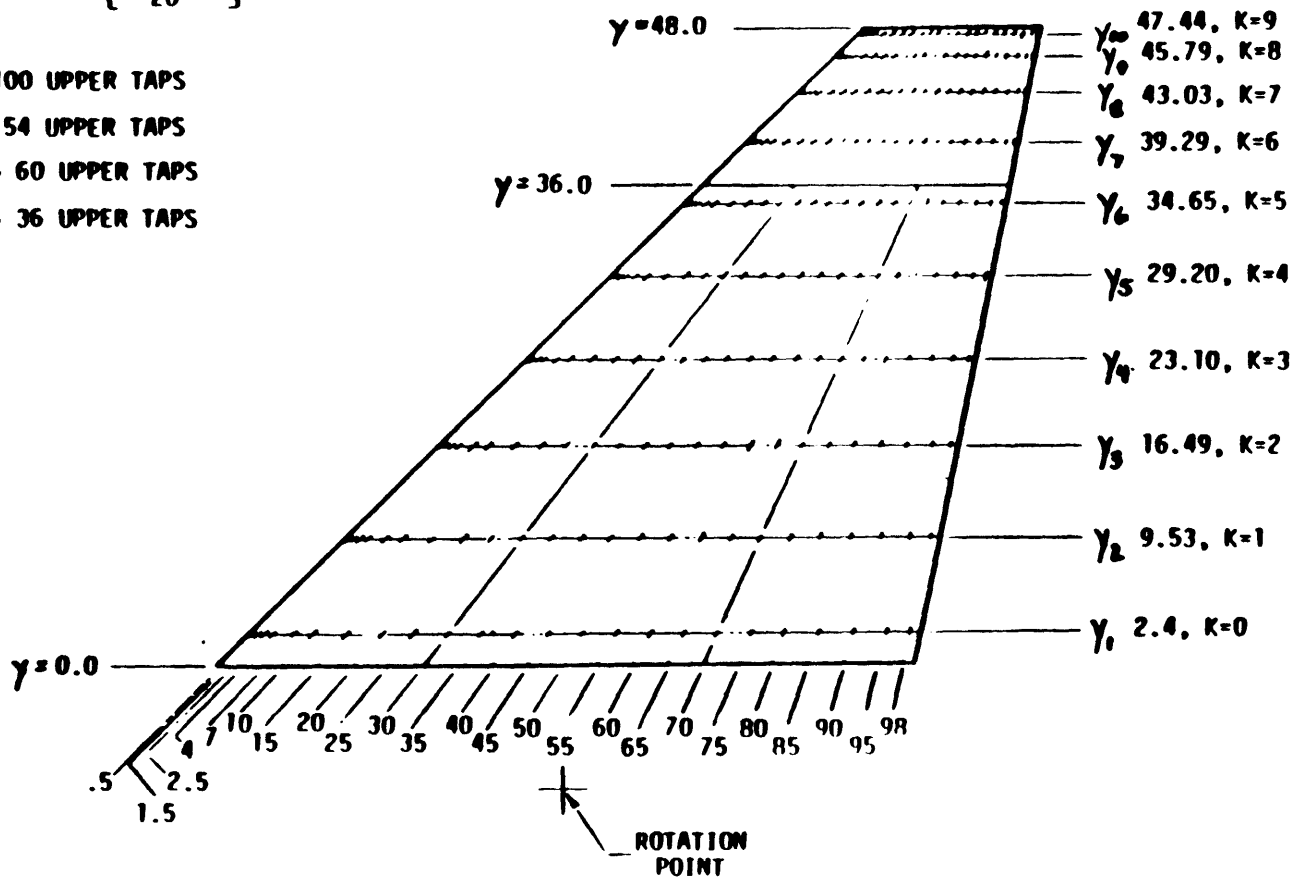

SPANWISE LOCATION DERIVED FROM

$$\bar{y}_{K+1} = .05 + .95 \cos\left[\frac{\pi (10-K)}{20}\right]$$

WING TIP ~ 48 LOWER TAPS

WING SKIN ~ 30 LOWER TAPS

L.E. FLAP ~ 24 LOWER TAPS

T.E. FLAP ~ 18 LOWER TAPS

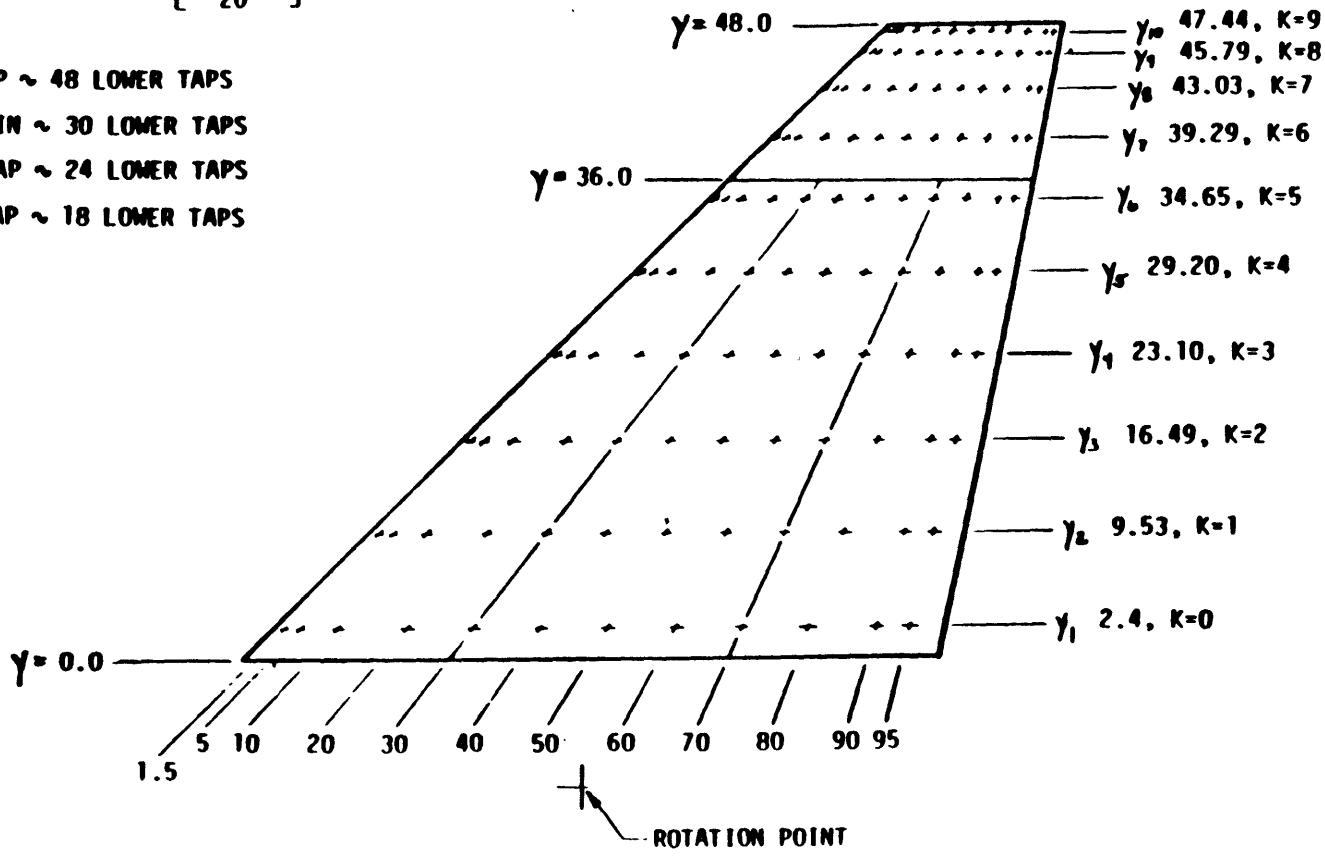

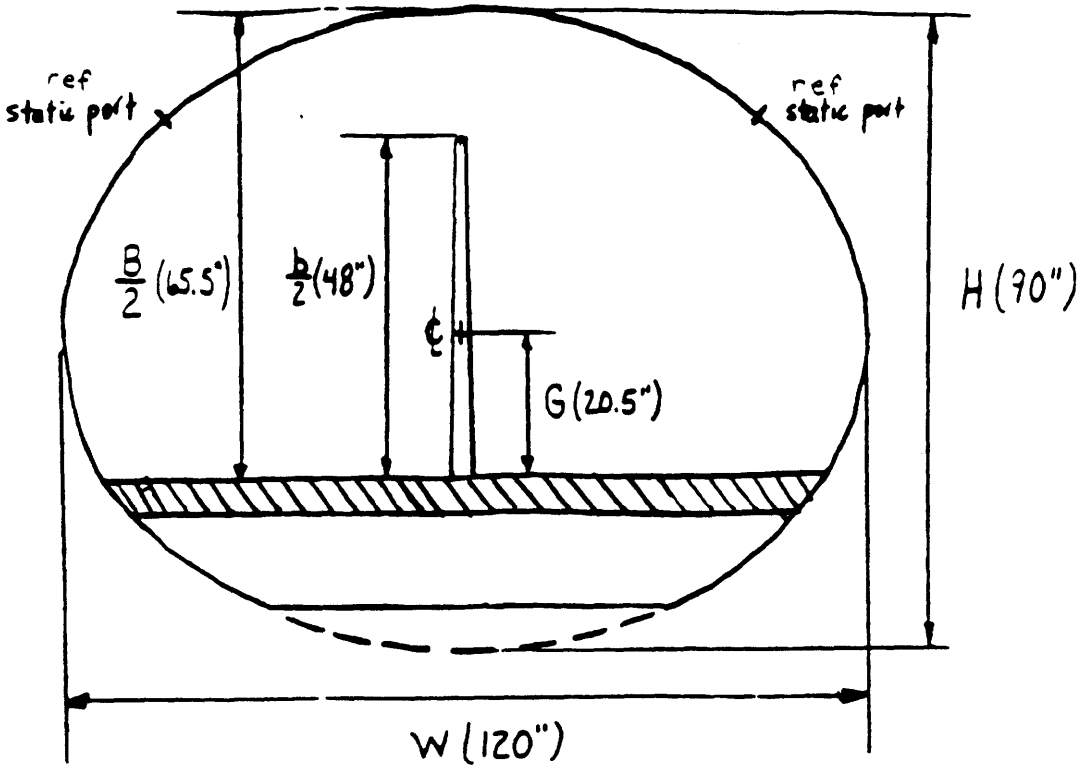

Figure B-28: Downstream view of wing and ground board installation.

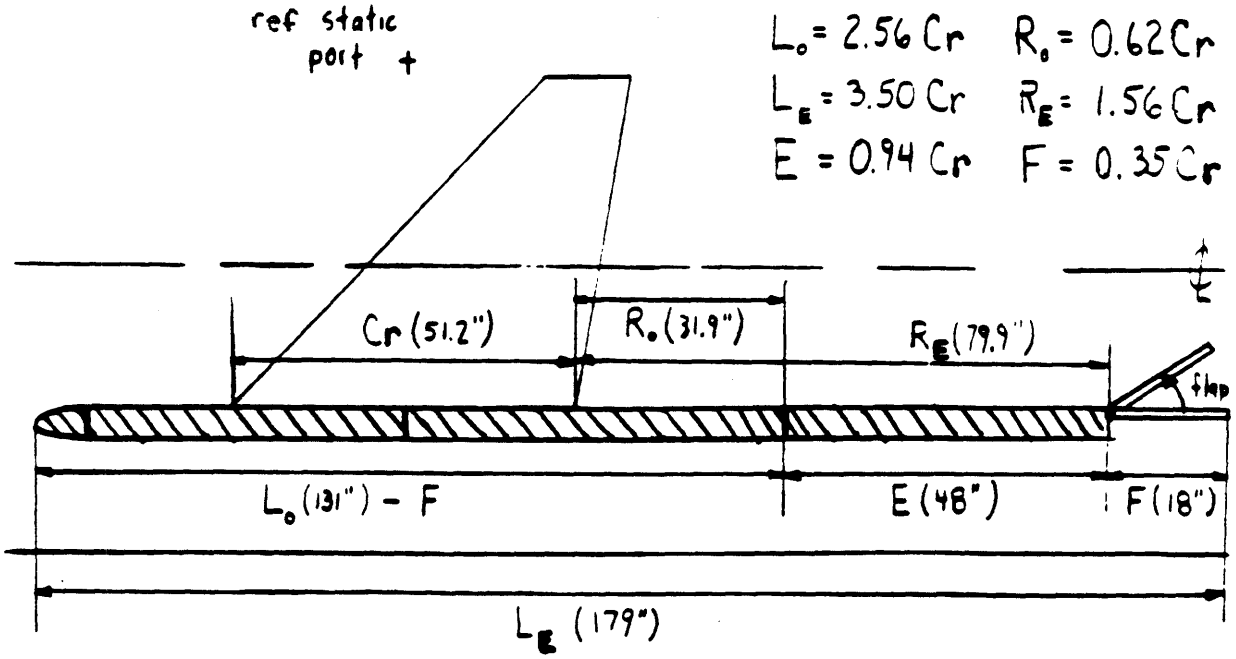

Figure B-29: Side view of wing and ground board installation.

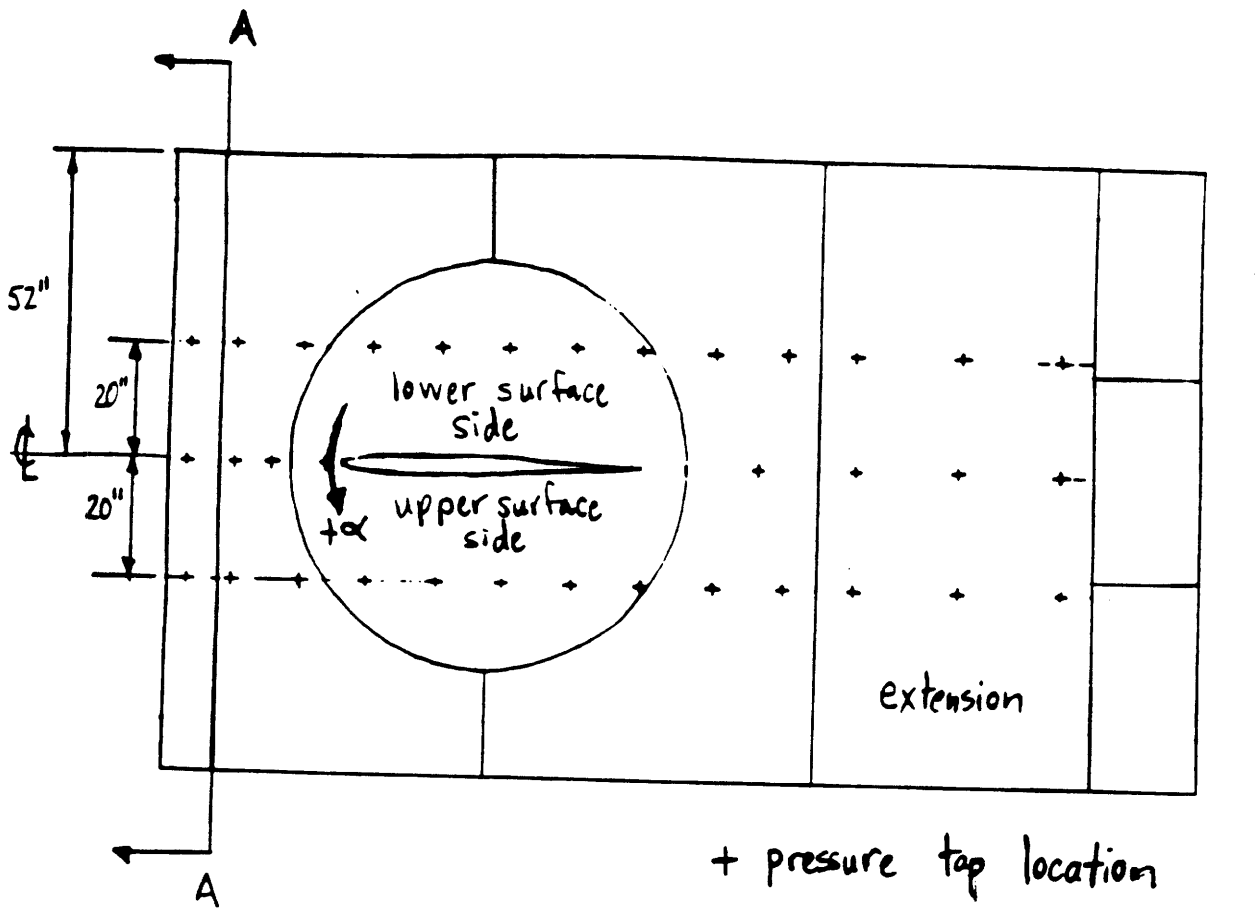

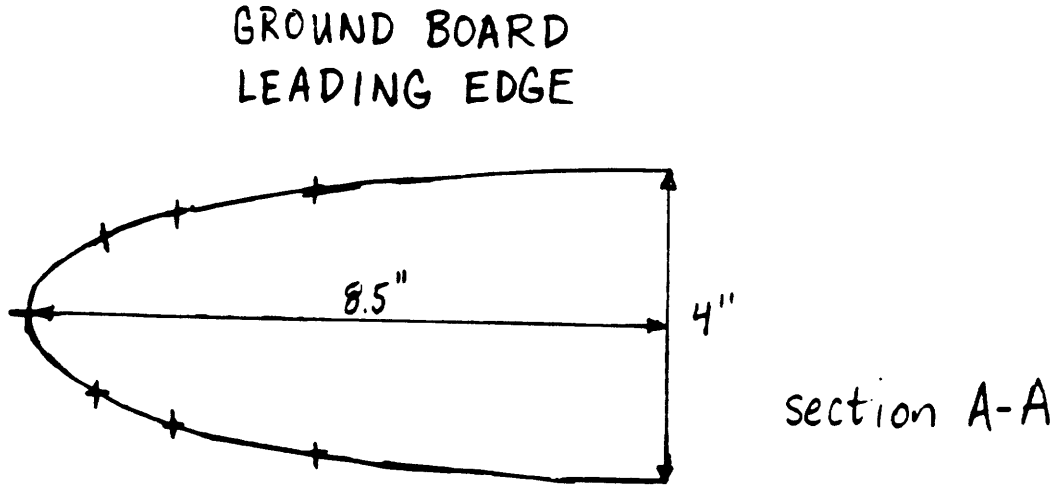

Figure B-30: Pressure tap locations on reflecting plane surface.

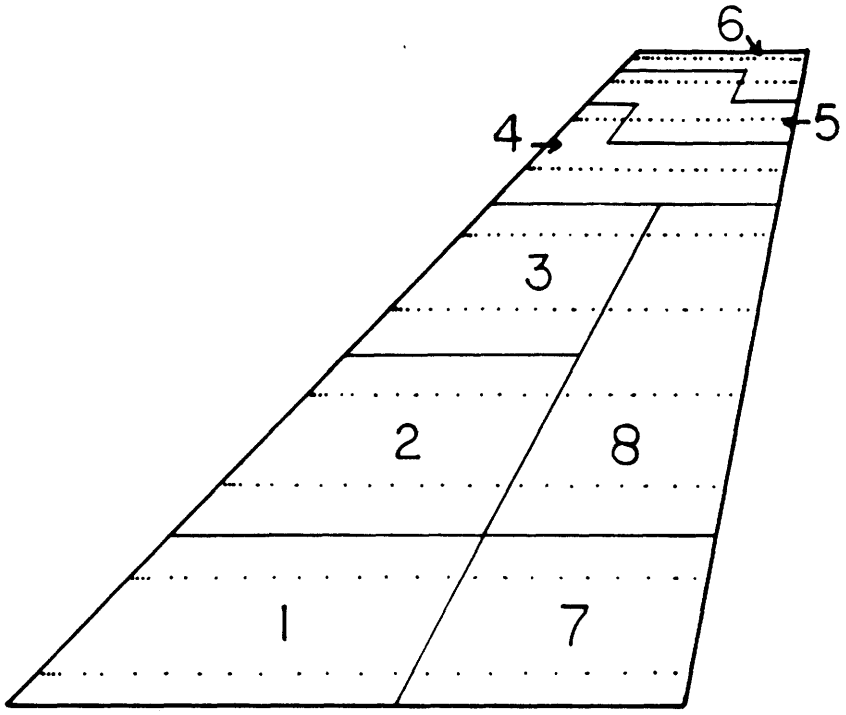

Figure B-31: Scanivalve map of wing upper surface.

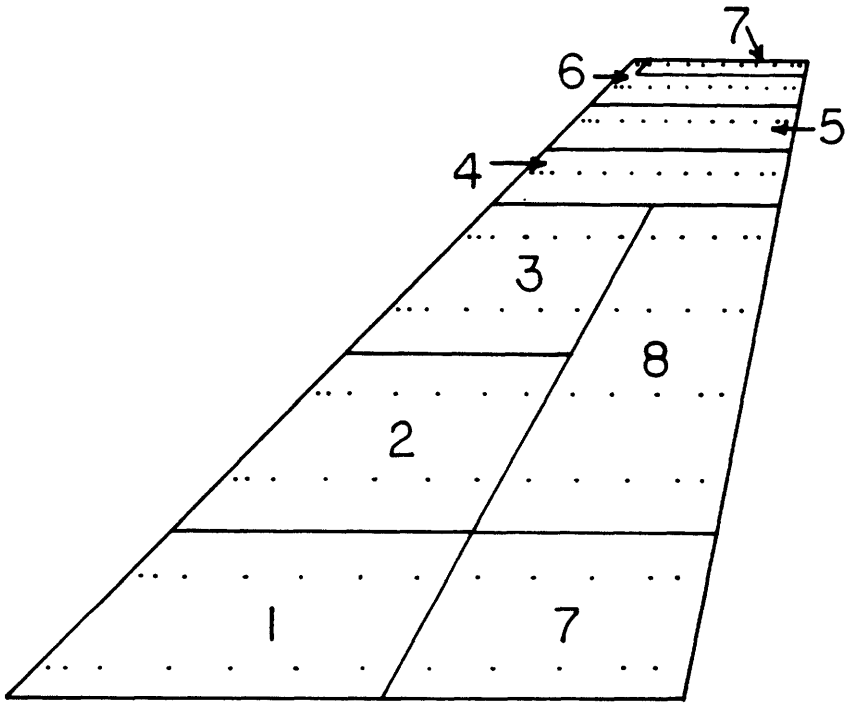

Figure B-32: Scanivalve map of wing lower surface.

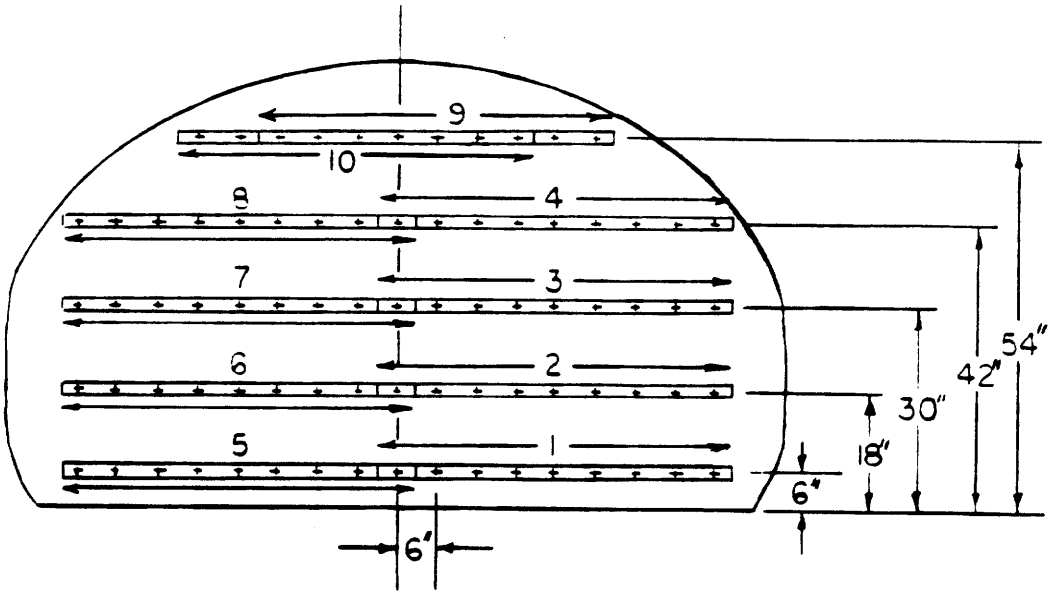

Figure B-33: Diagram of rake and tap locations.

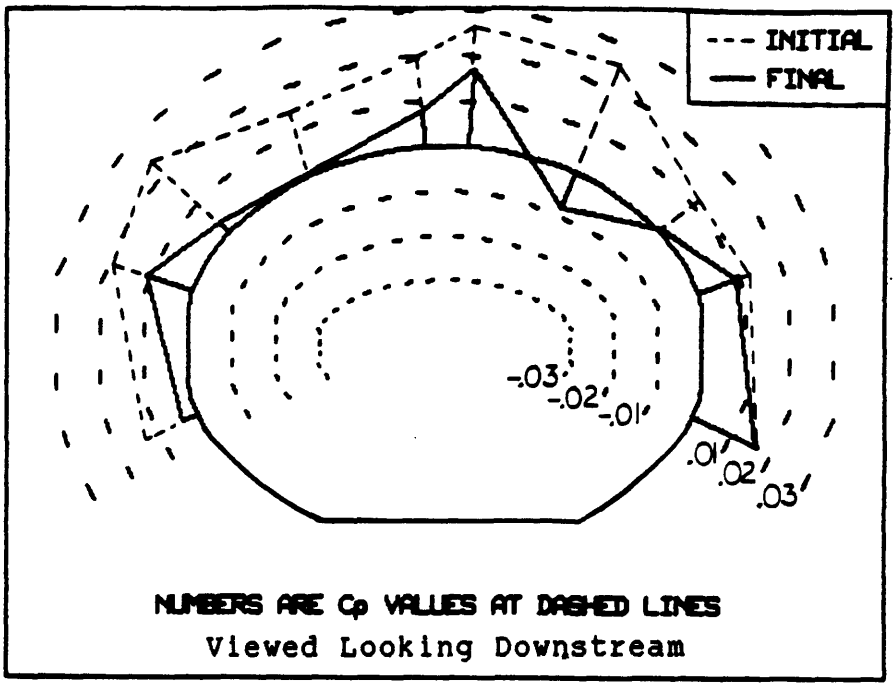

Figure B-34: Results of wall pressure tap tests; row 1.

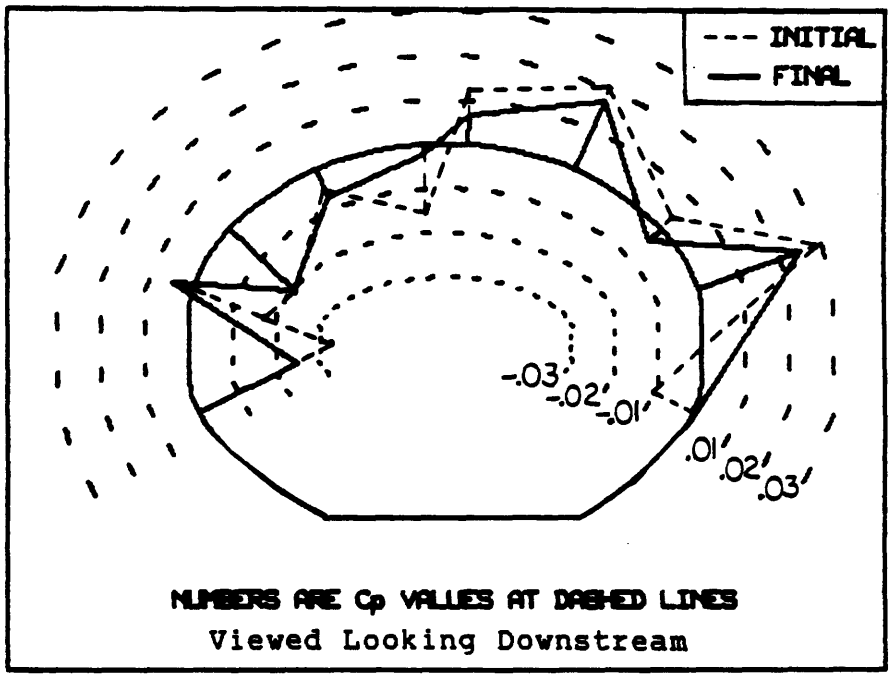

Figure B-35: Results of wall pressure tap tests; row 2.

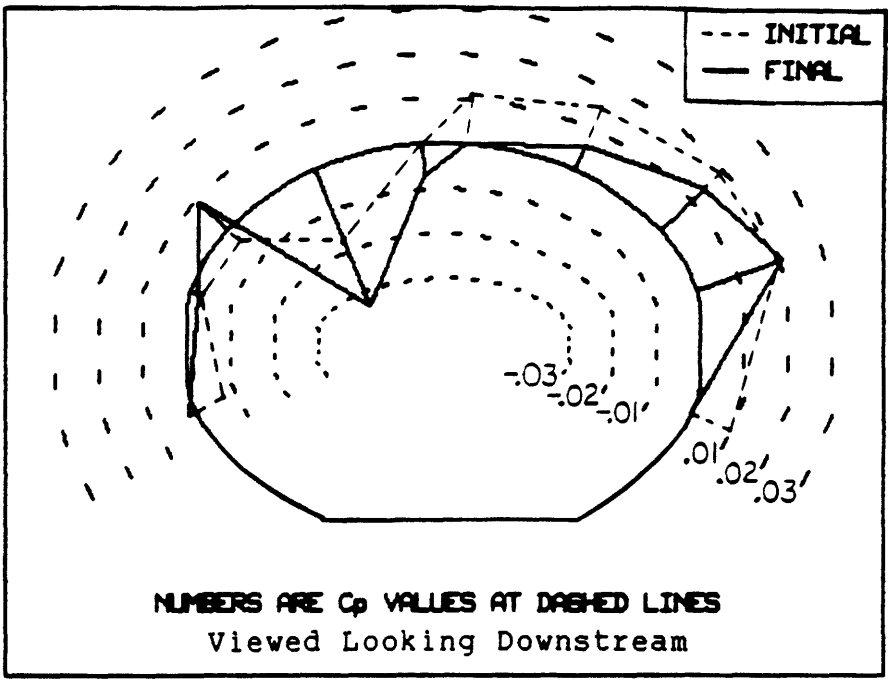

Figure B-36: Results of wall pressure tap tests; row 3.

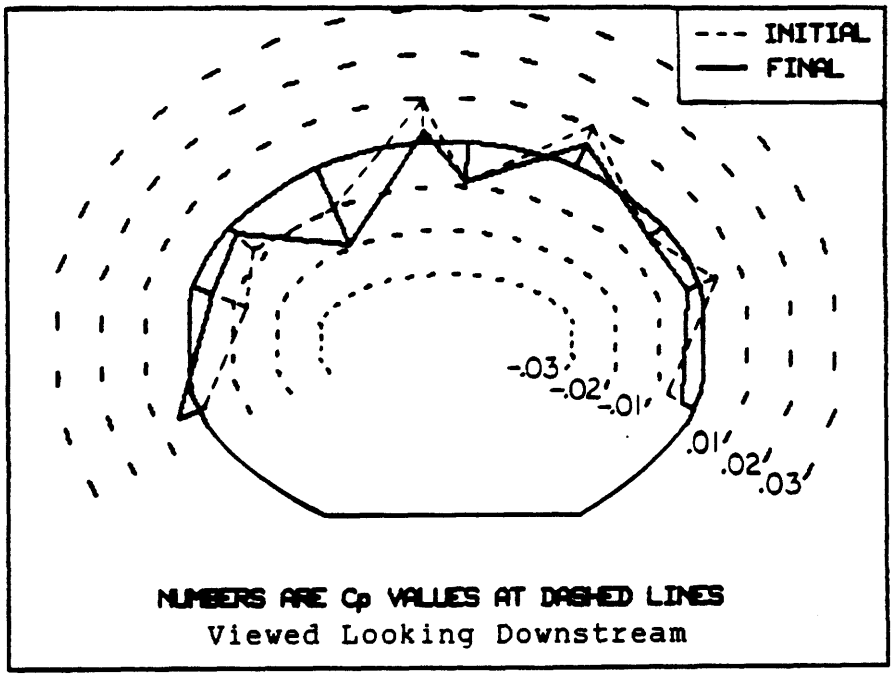

Figure B-37: Results of wall pressure tap tests; row 4.

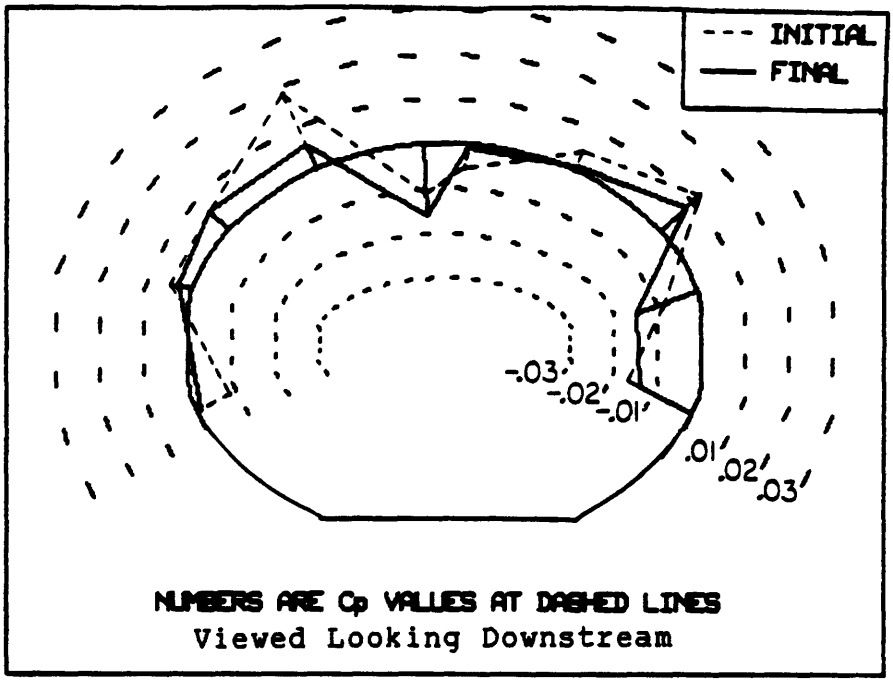

Figure B-38: Results of wall pressure tap tests; row 5.

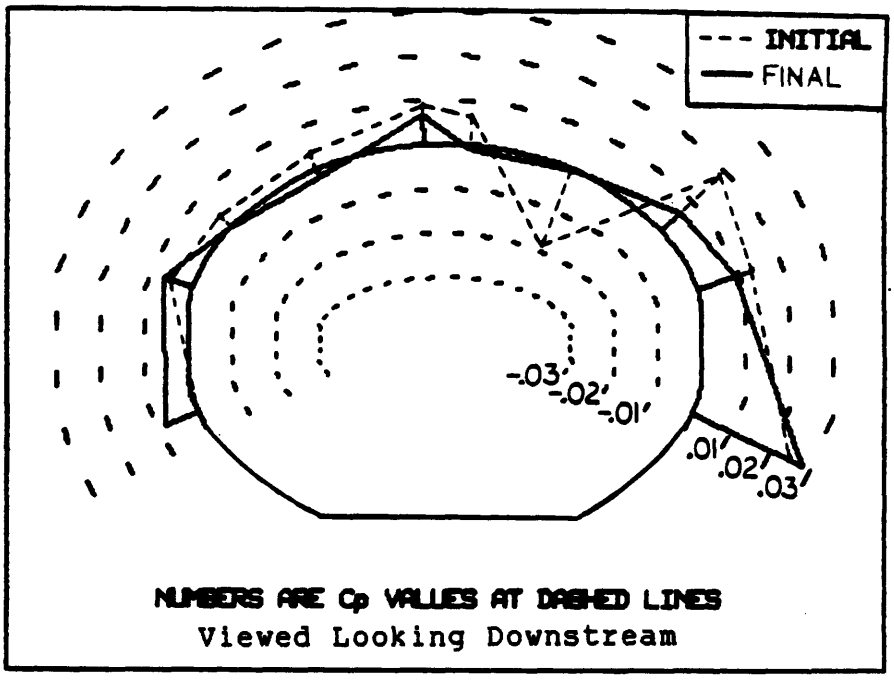

Figure B-39: Results of wall pressure tap tests; row 6.

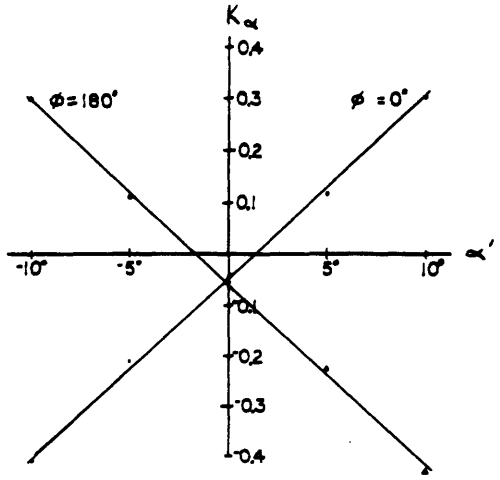

Figure B-40: Calibration data from probe #5; K_α *vs* α'.

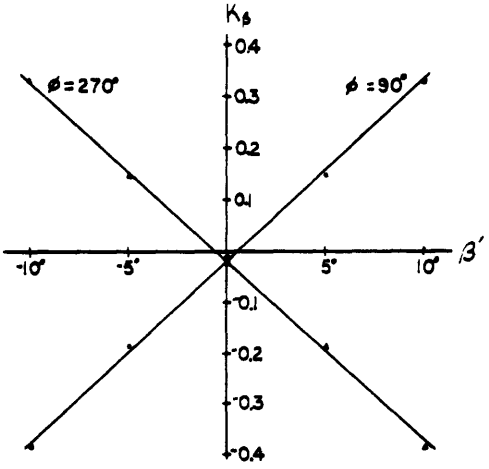

Figure B-41: Calibration data from probe #5; K_β *vs* β'.

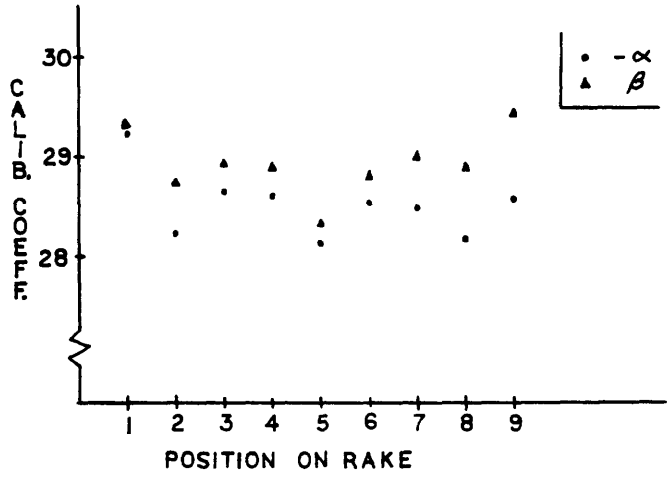

Figure B-42: Calibration slopes vs position on rake.

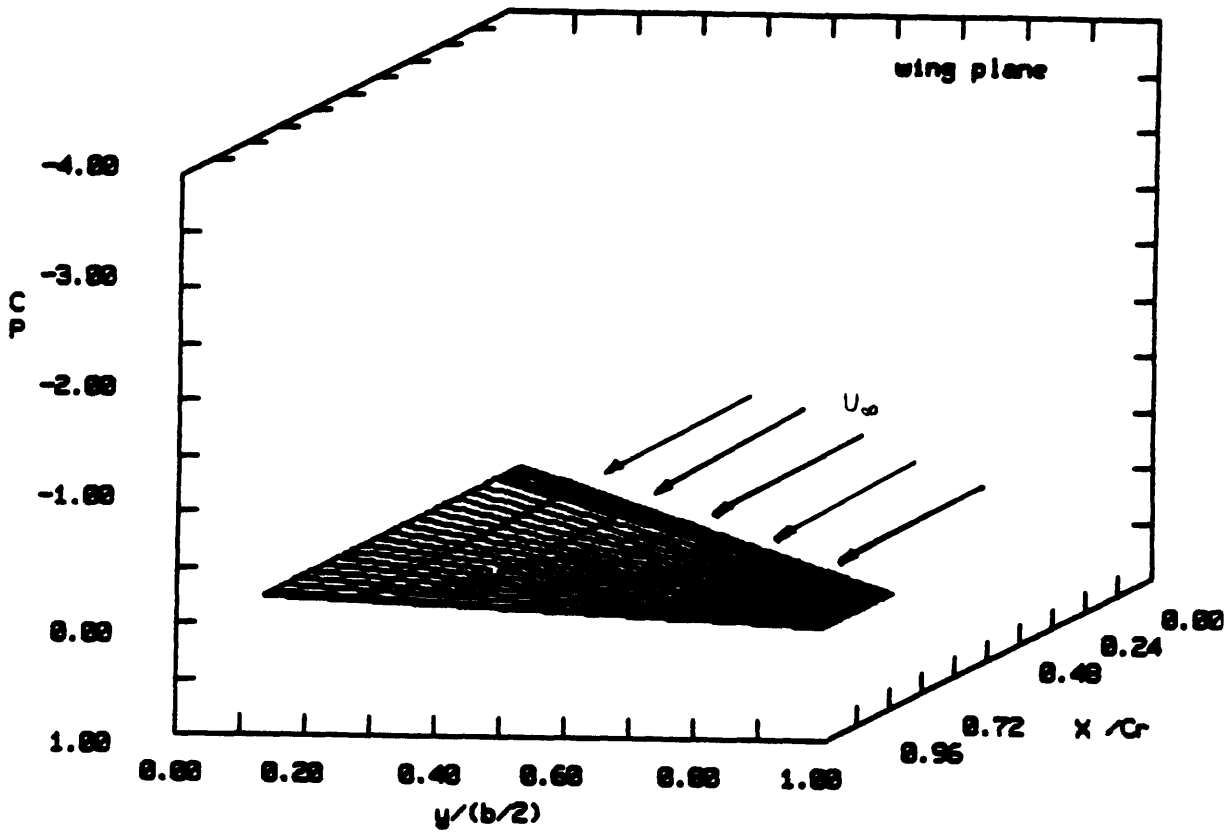

Figure B-43: Plane of zero pressure coefficients.

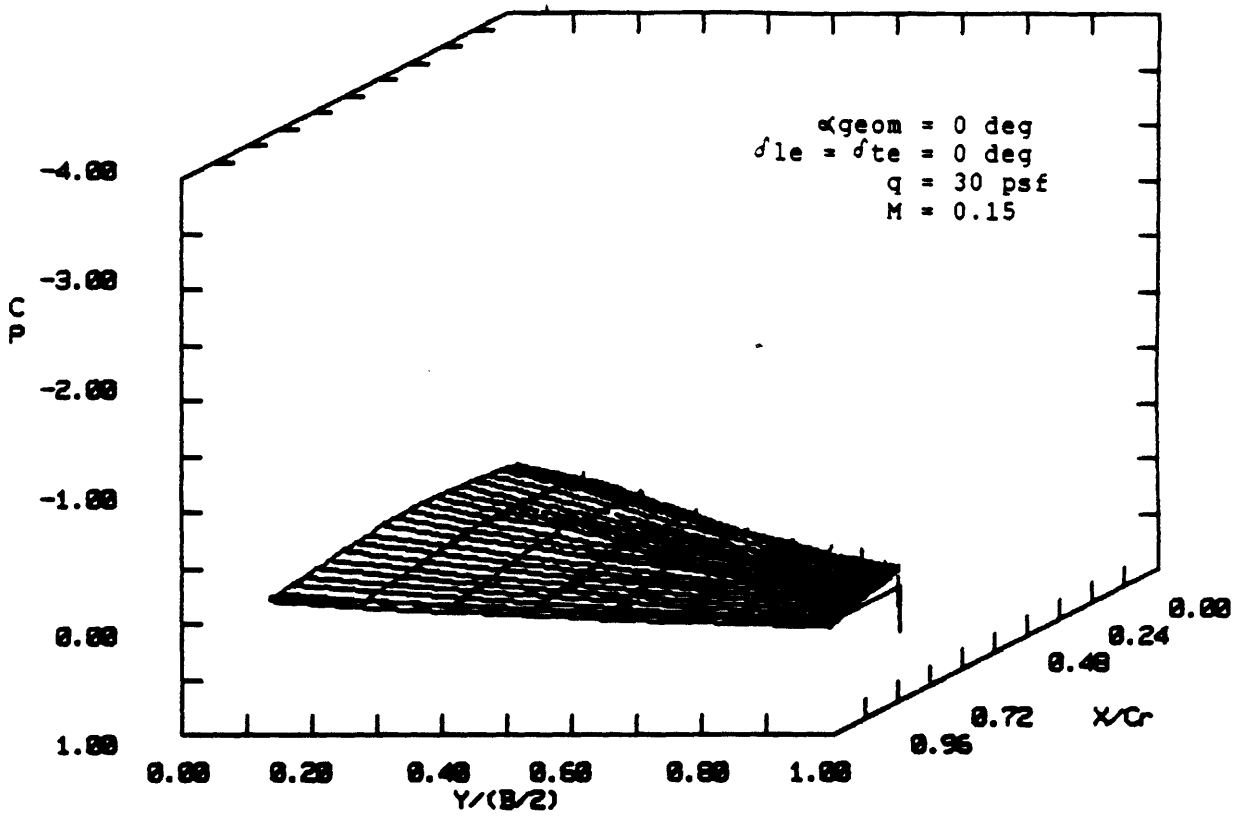

Figure B-44: Carpet plot of wing upper surface; α_{geom}=0°, δ_{le}=δ_{te}=0°.

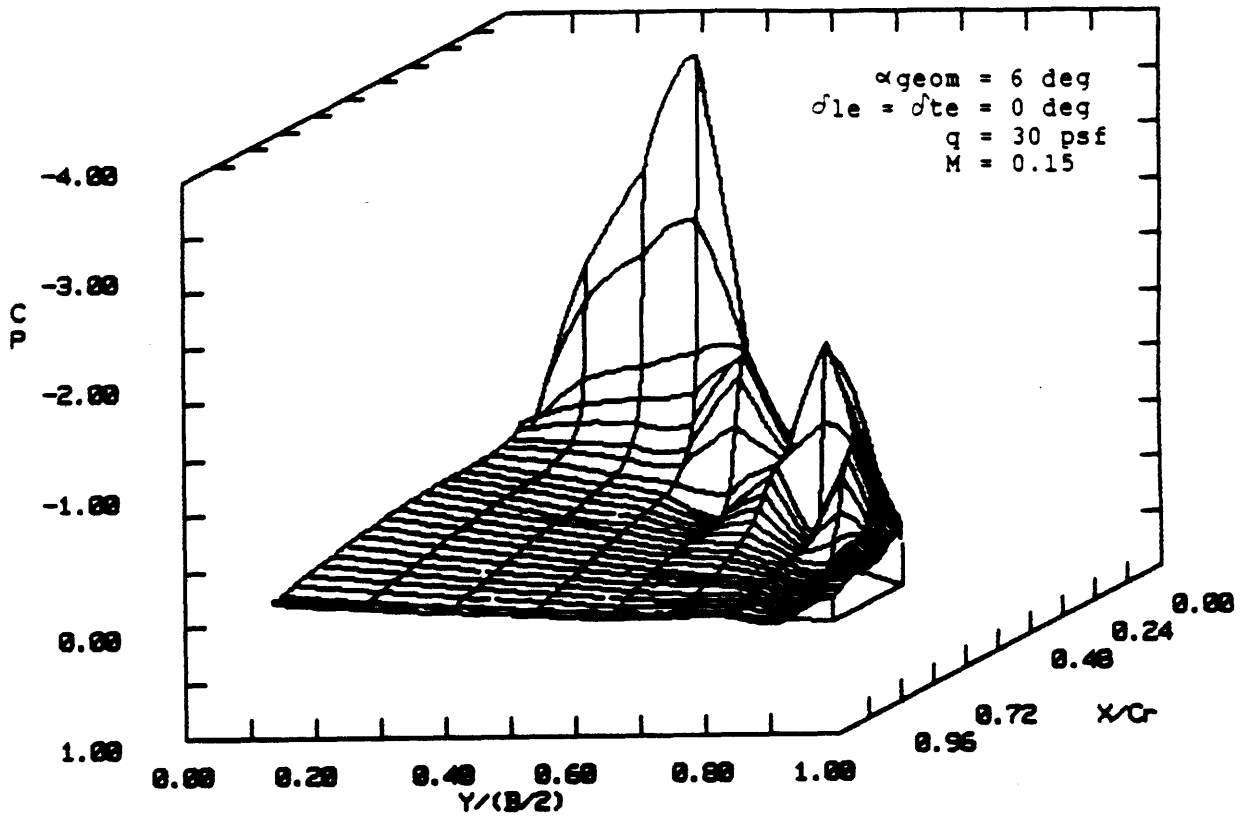

Figure B-45: Carpet plot of wing upper surface; α_{geom}=6°, δ_{le}=δ_{te}=0°.

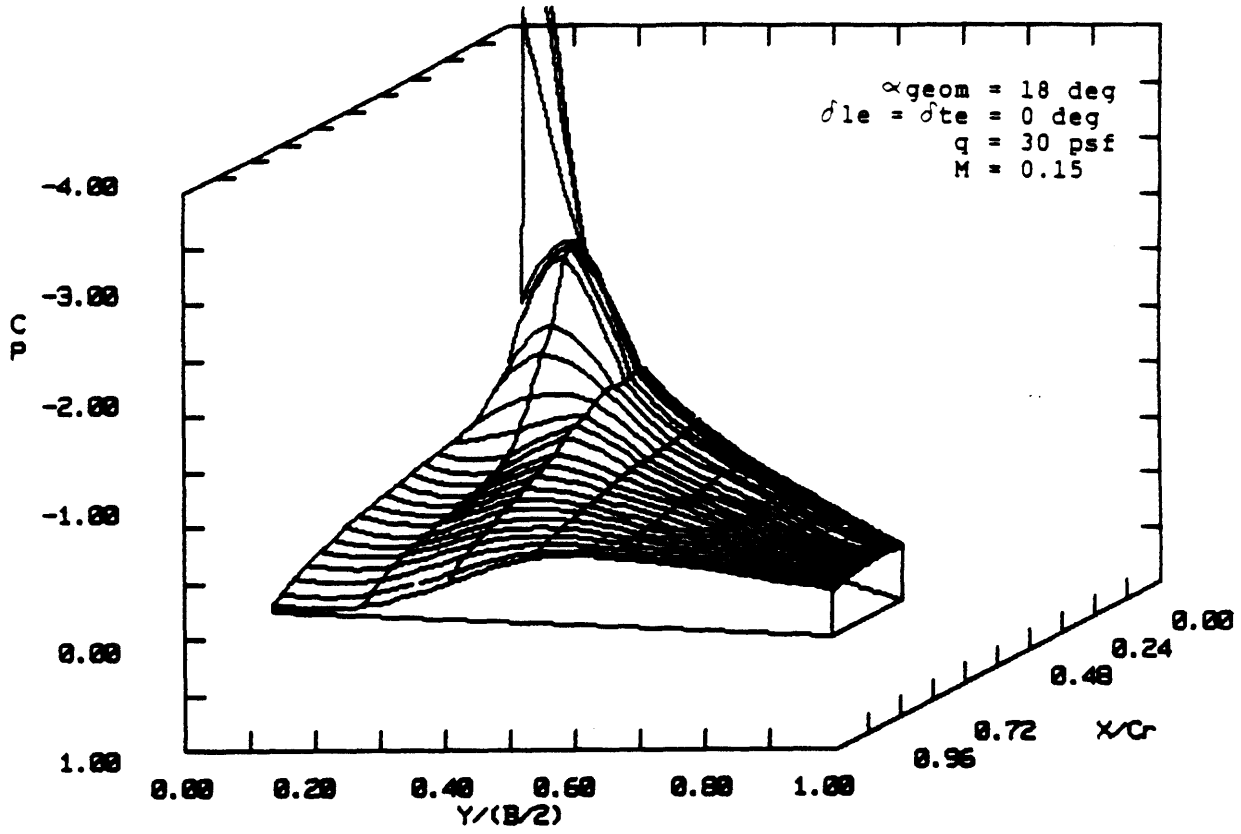

Figure B-46: Carpet plot of wing upper surface; α_{geom}=18°, δ_{le}=δ_{te}=0°.

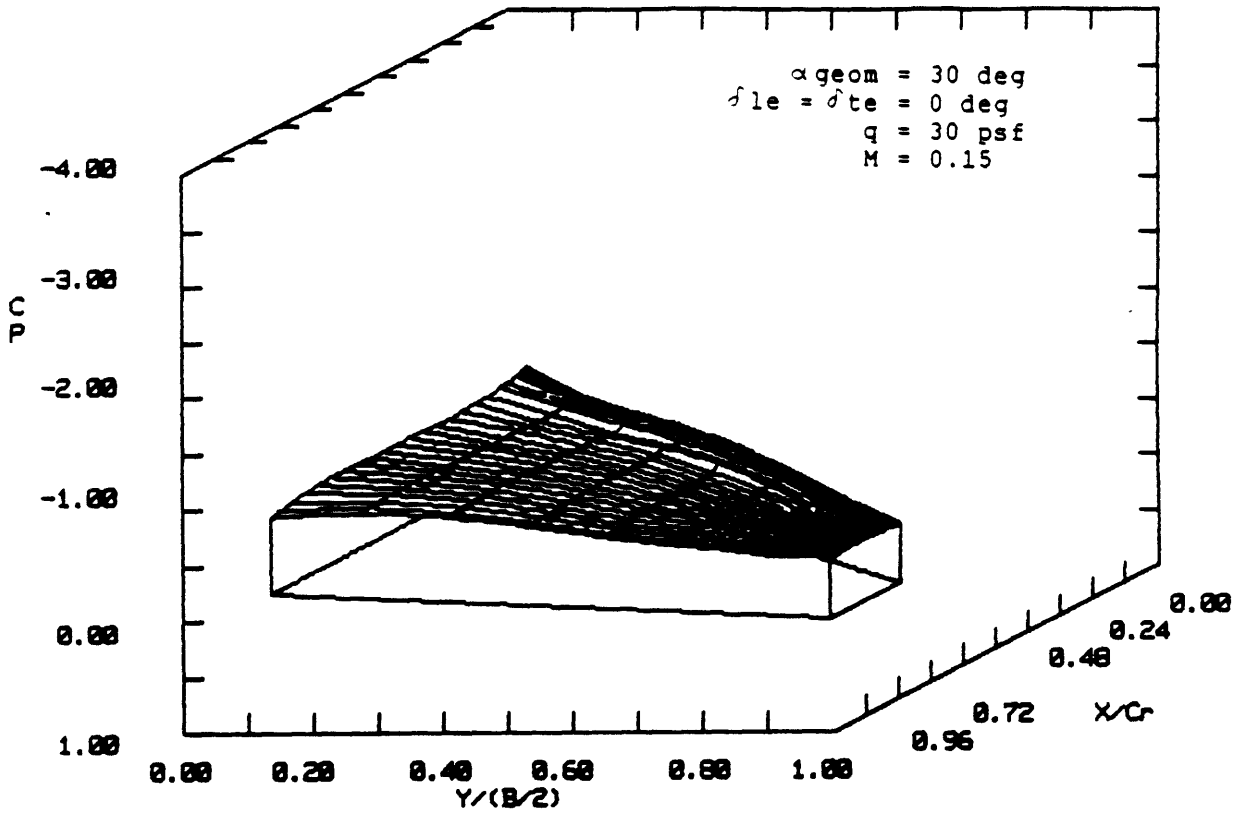

Figure B-47: Carpet plot of wing upper surface; α_{geom}=30°, δ_{le}=δ_{te}=0°.

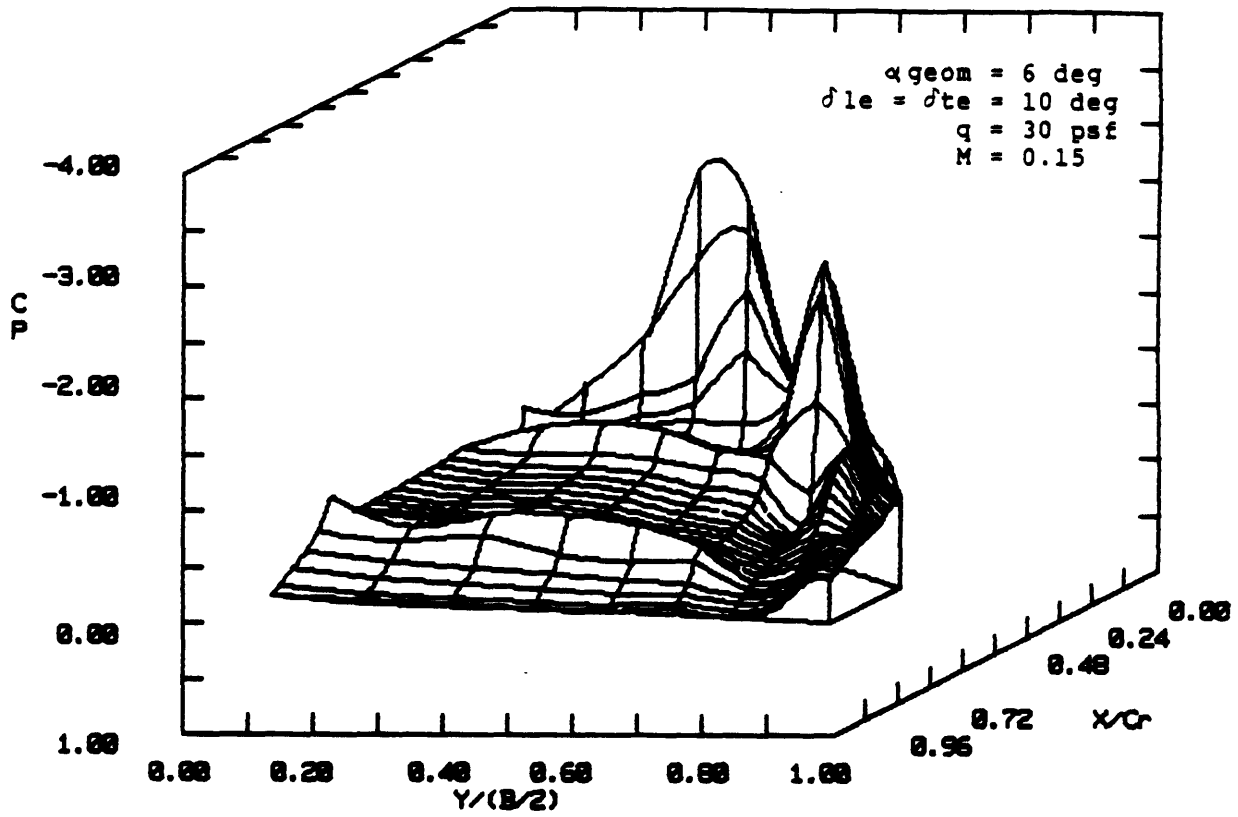

Figure B-48: Carpet plot of wing upper surface; α_{geom}=6°, δ_{le}=δ_{te}=10°.

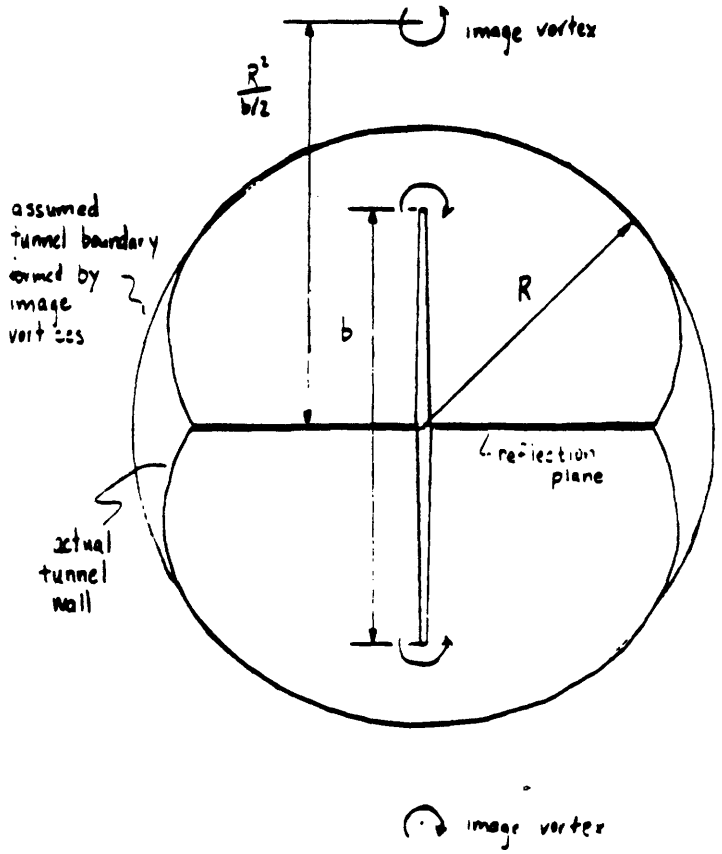

Figure B-49: Diagram showing tunnel approximated as a semi-circle.

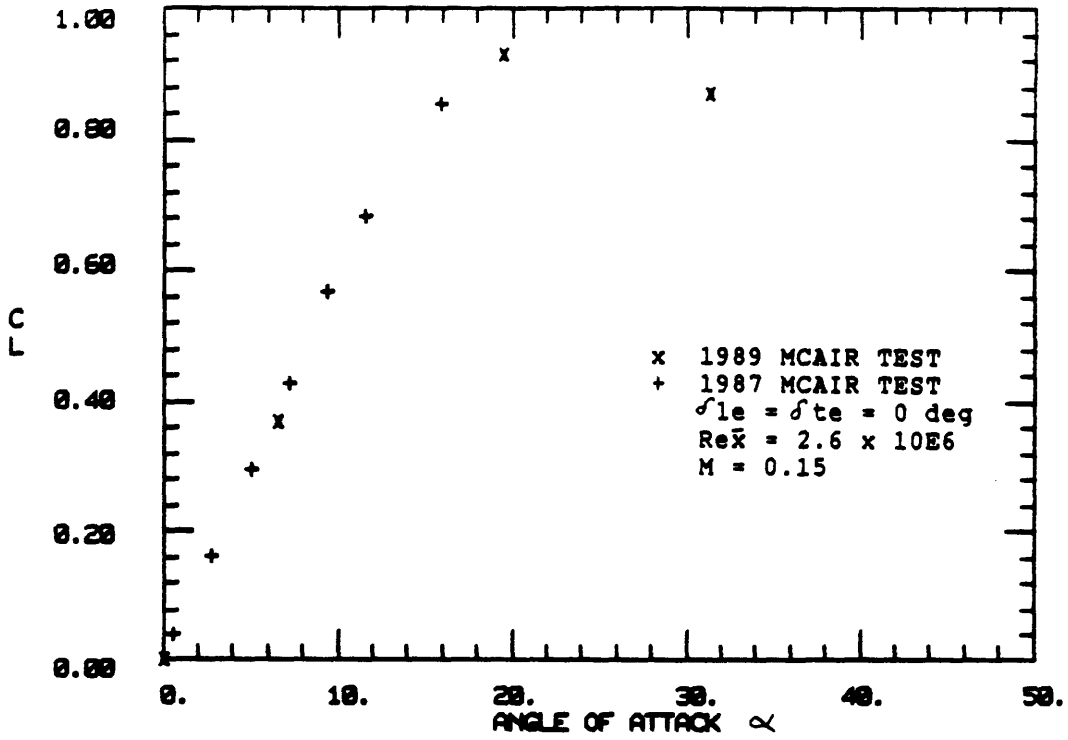

Figure B-50: Plot of MCAIR data; C_L *vs* α.

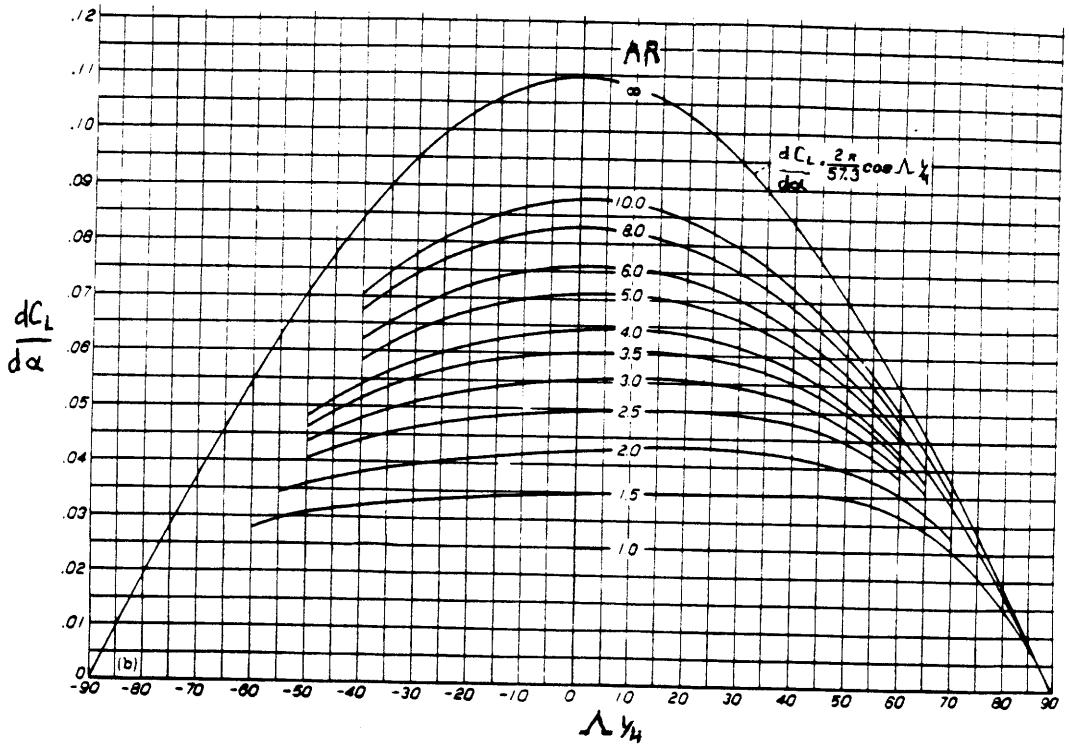

Figure B-51: Variation of lift curve slope with AR and $\Lambda_{1/4}$ for λ=0.25.

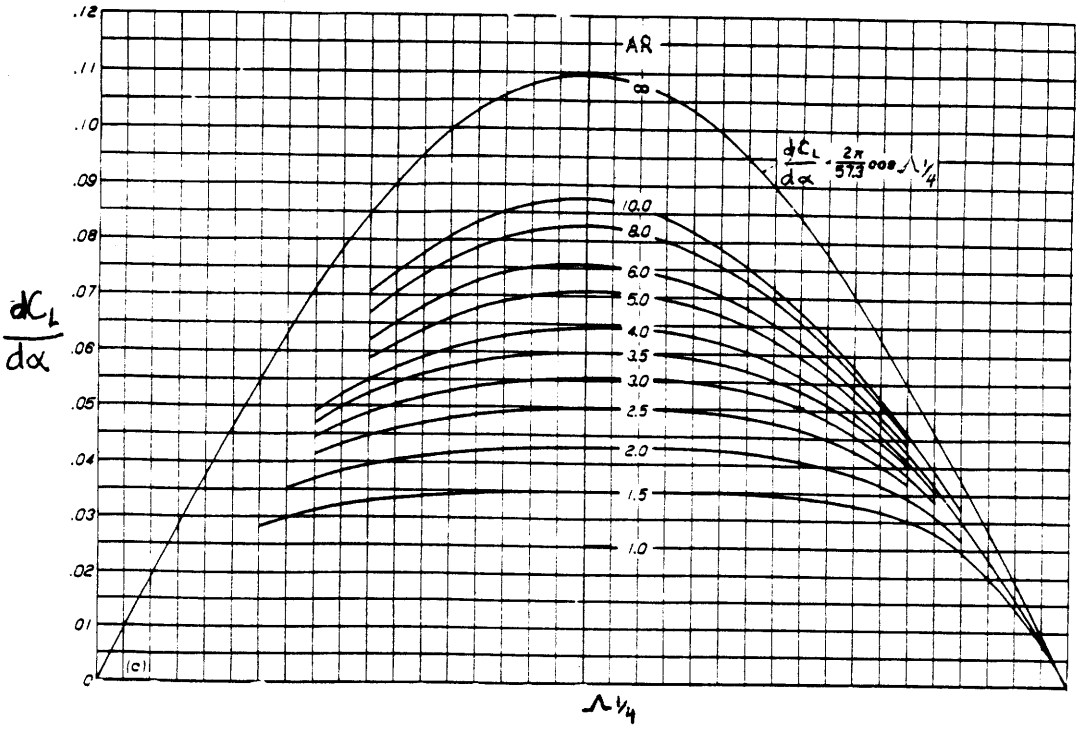

Figure B-52: Variation of lift curve slope with AR and $\Lambda_{1/4}$ for λ=0.50.

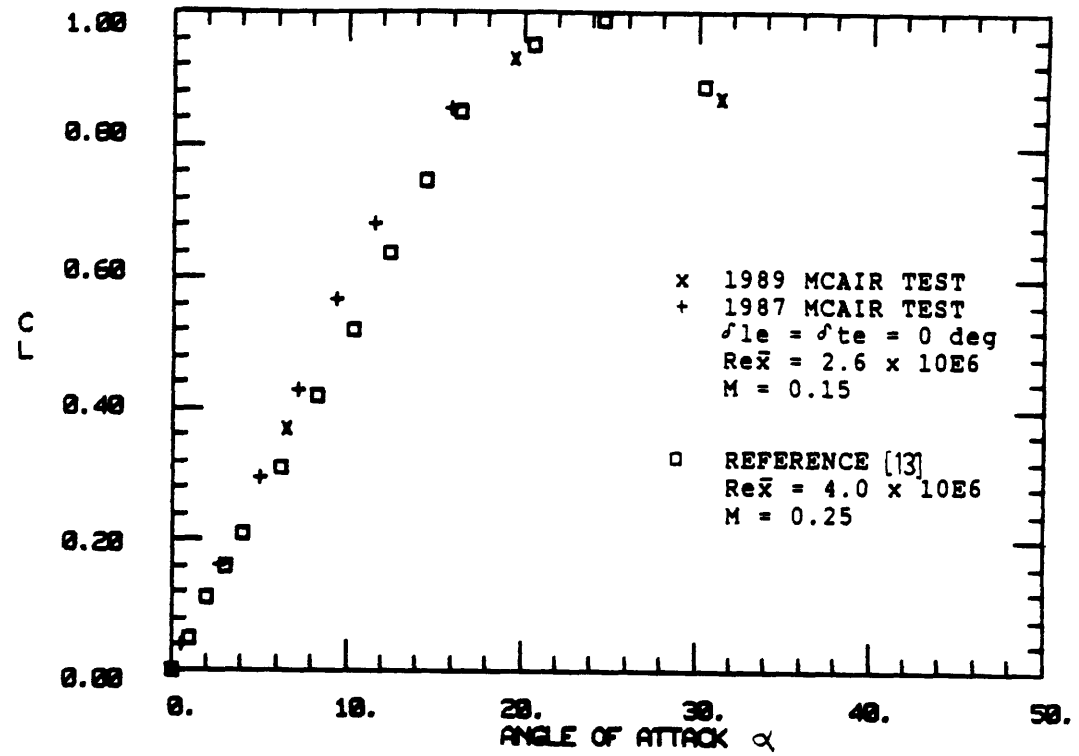

Figure B-53: Comparison of MCAIR data and reference 13; C_L *vs* α.

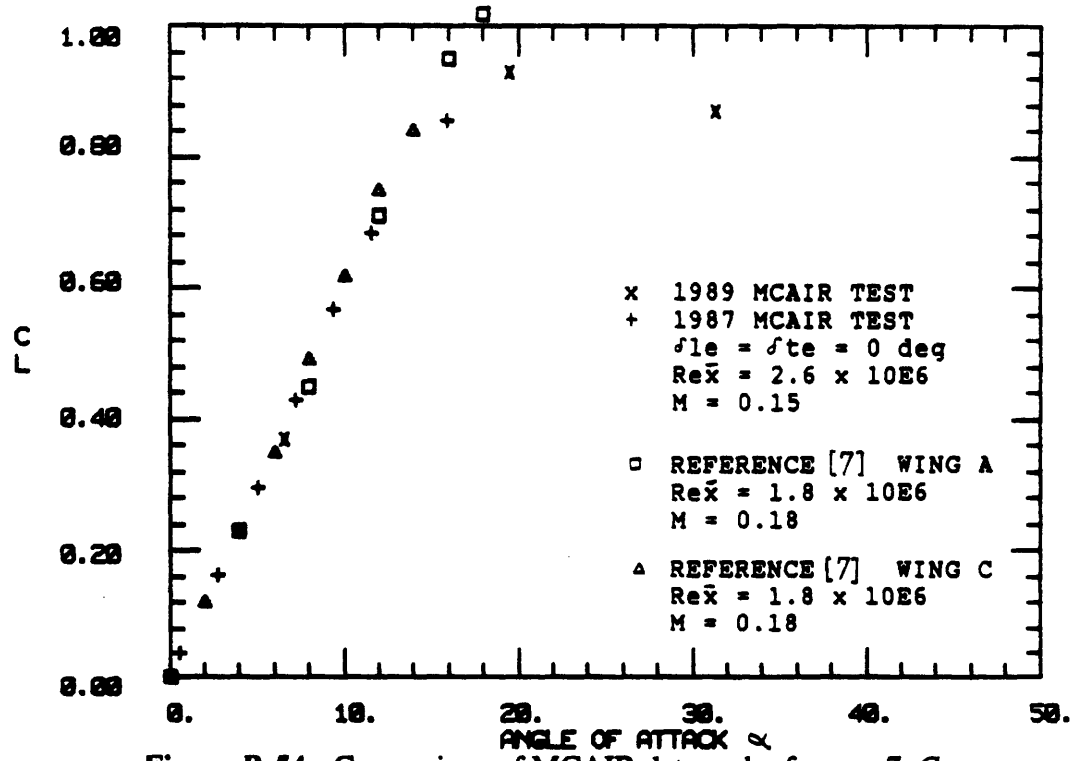

Figure B-54: Comparison of MCAIR data and reference 7; C_L *vs* α.

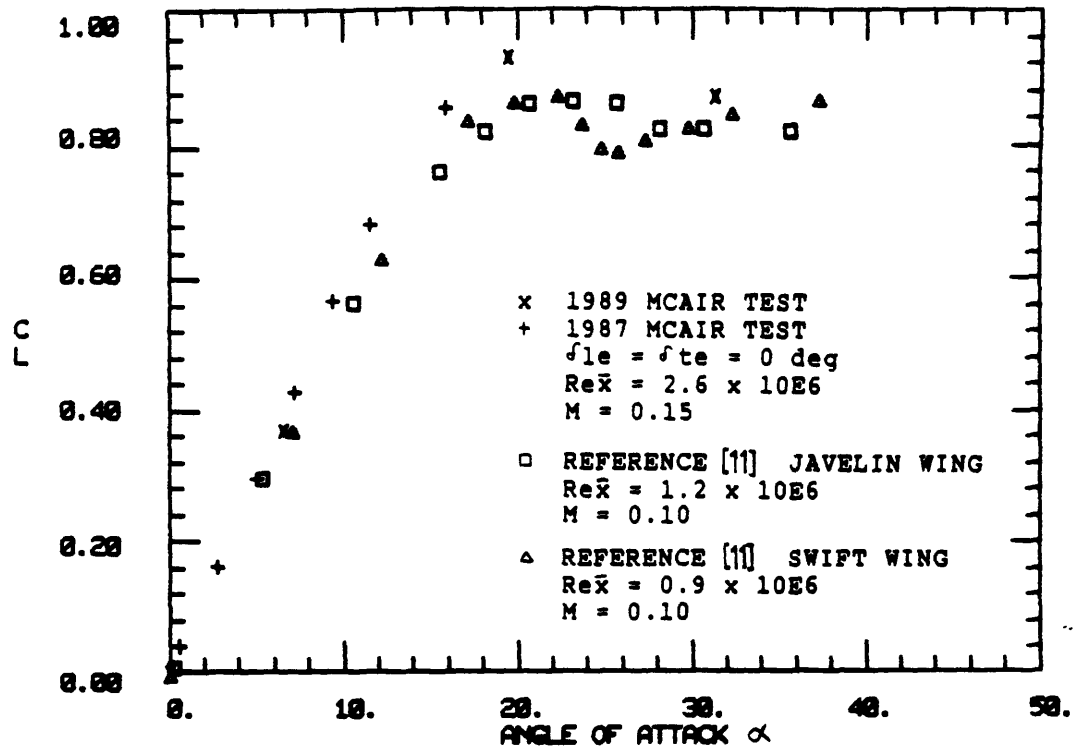

Figure B-55: Comparison of MCAIR data and reference 11; C_L *vs* α.

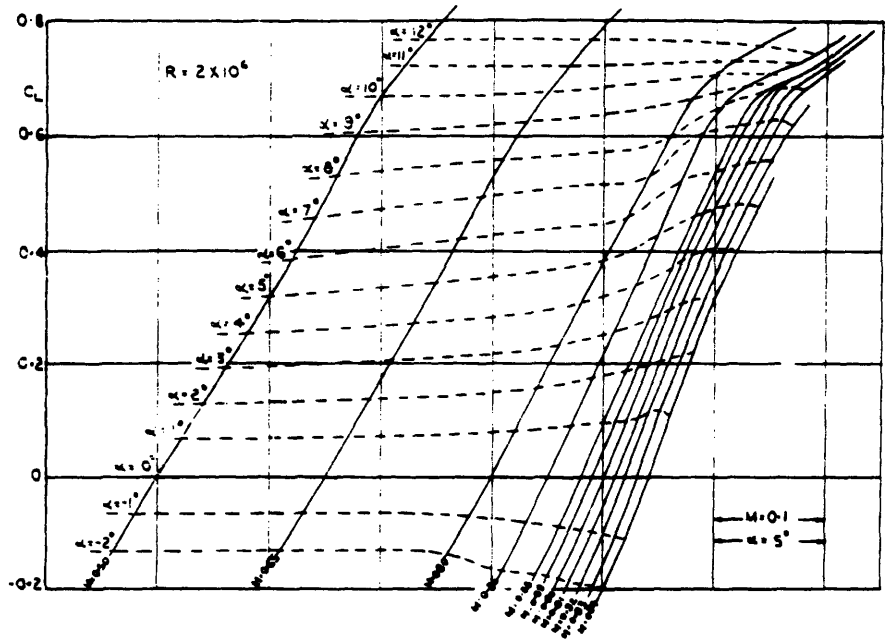

Figure B-56: Variation of C_L *vs* α with M, for RAE 101 airfoil of reference 9.

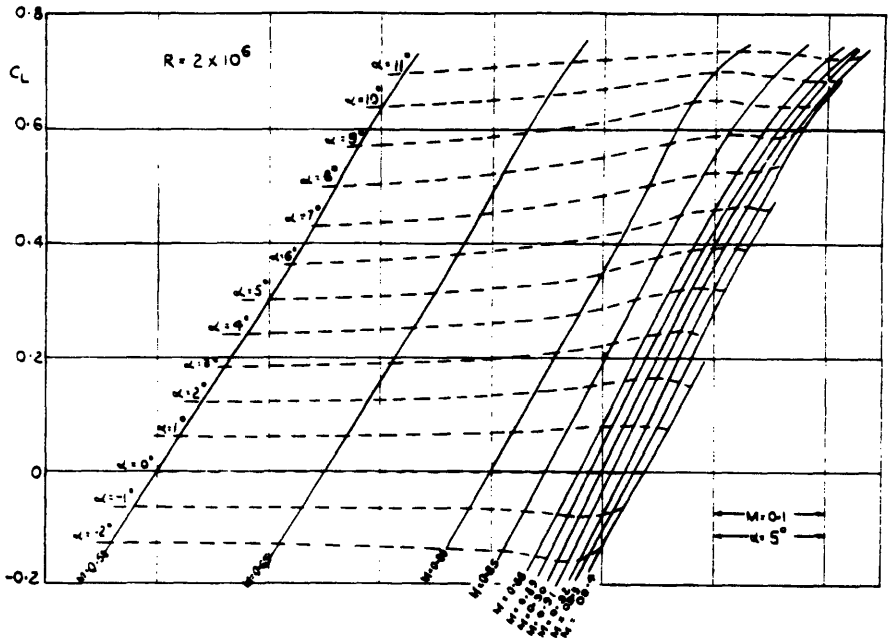

Figure B-57: Variation of C_L *vs* α with M, for RAE 104 airfoil of reference 9.

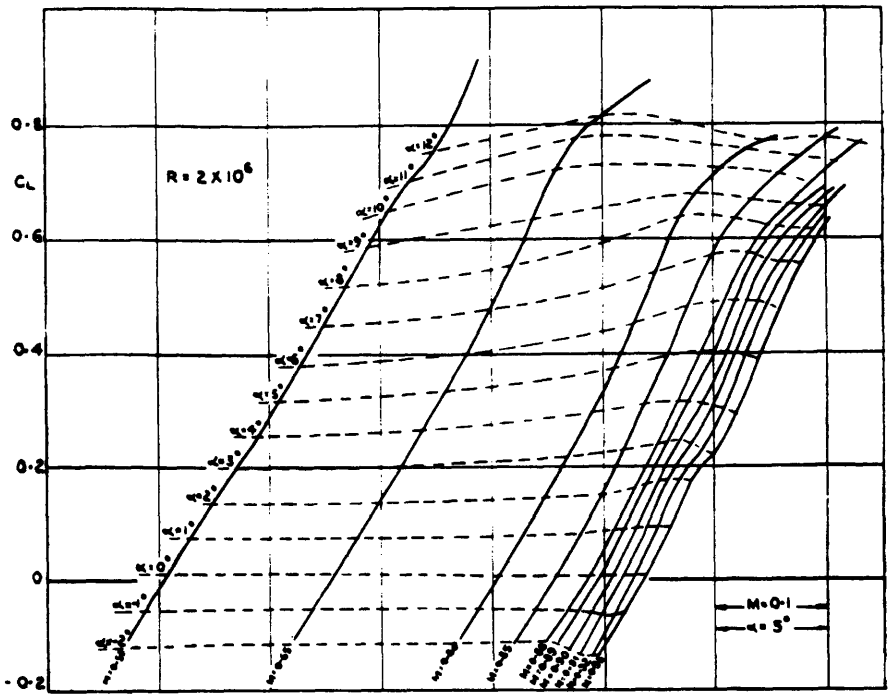

Figure B-58: Variation of C_L *vs* α with M, for HSA I airfoil of reference 9.

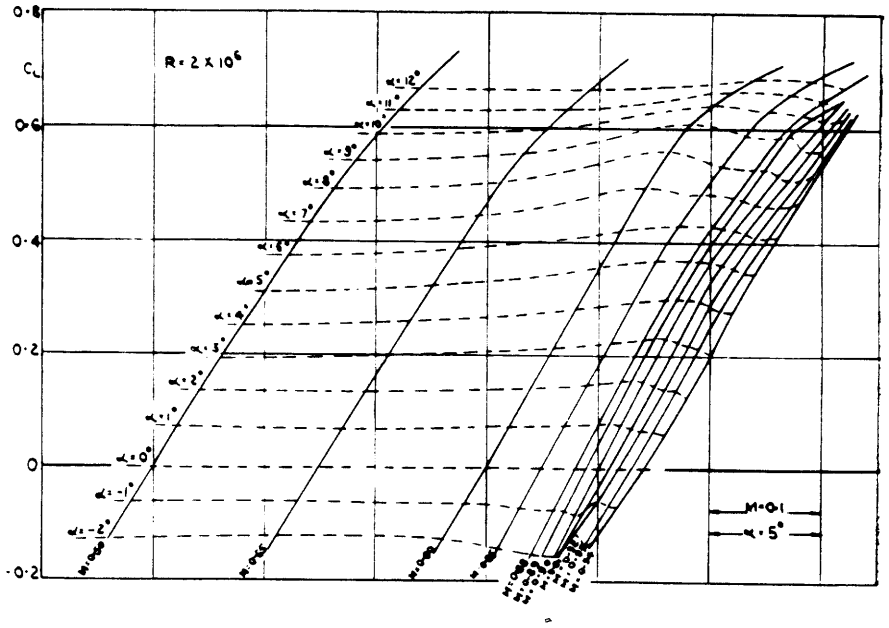

Figure B-59: Variation of C_L *vs* α with M, for NACA 64A010 airfoil of reference 9.

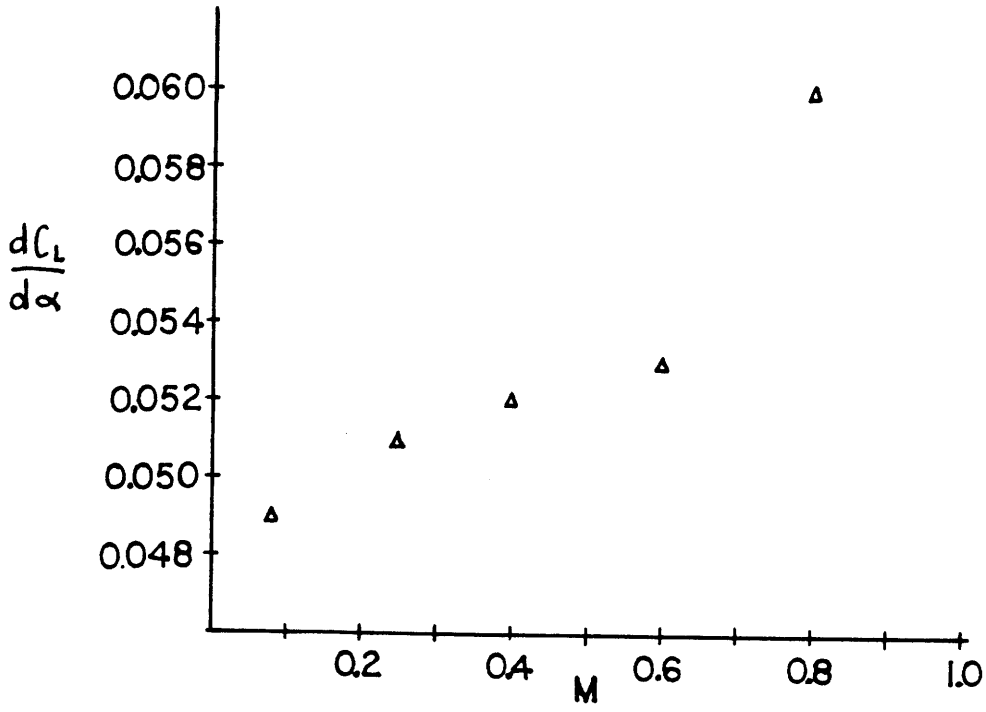

Figure B-60: Lift curve slope vs Mach number from reference 13.

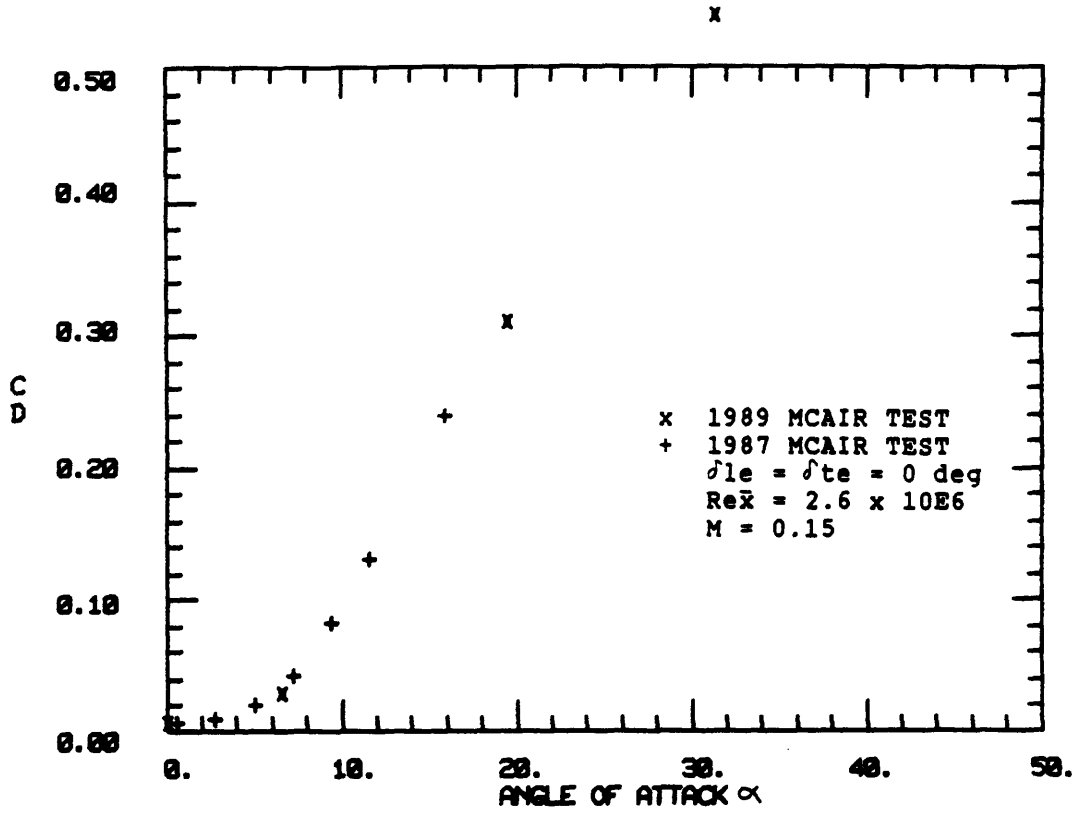

Figure B-61: Plot of MCAIR data; C_D *vs* α.

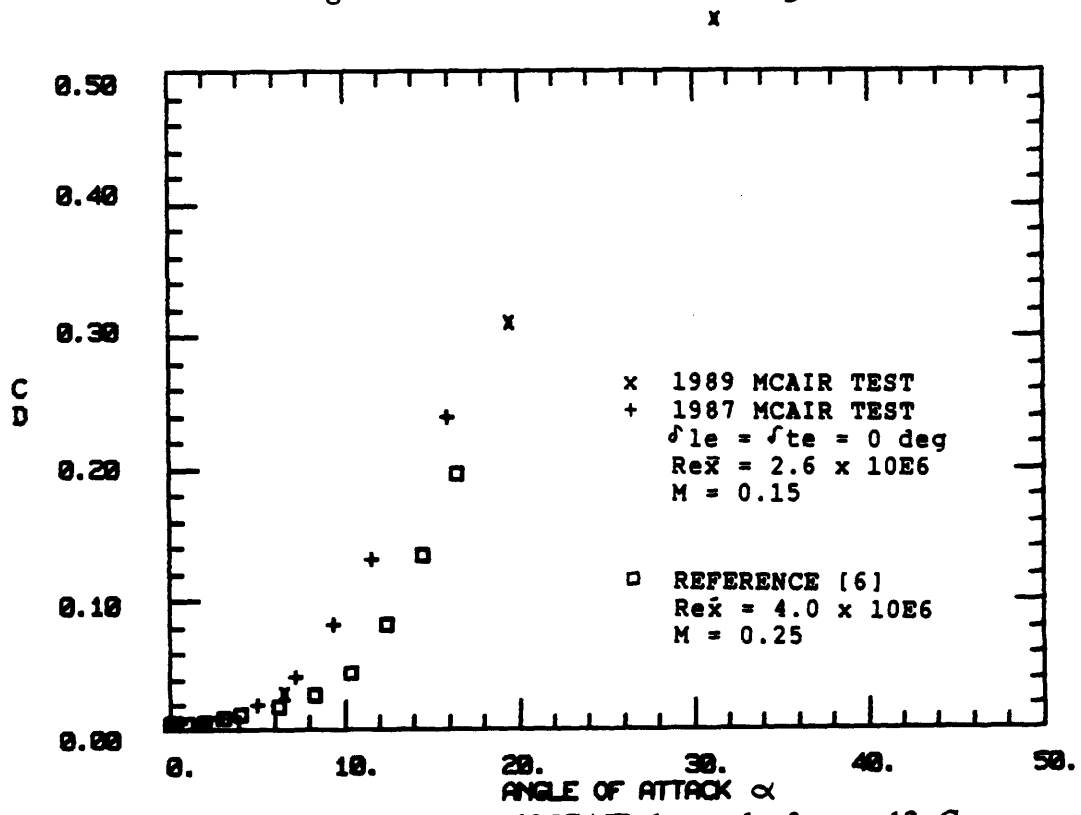

Figure B-62: Comparison of MCAIR data and reference 13; C_D *vs* α.

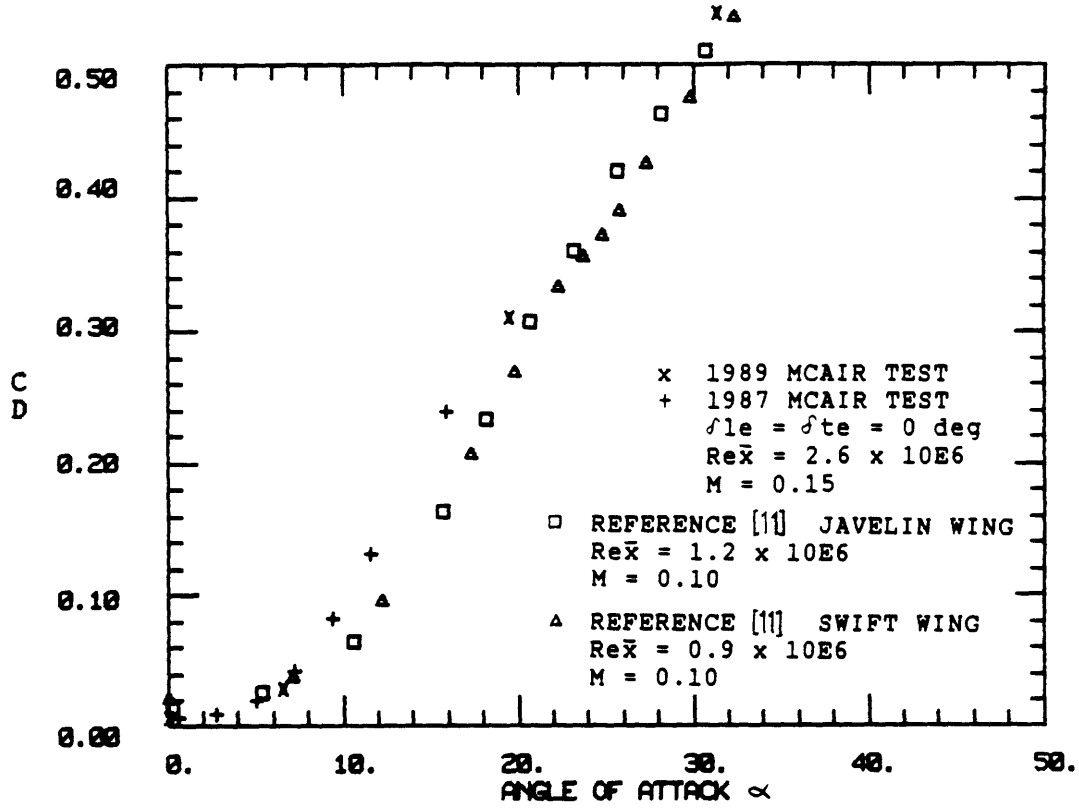

Figure B-63: Comparison of MCAIR data and reference 11; C_D *vs* α.

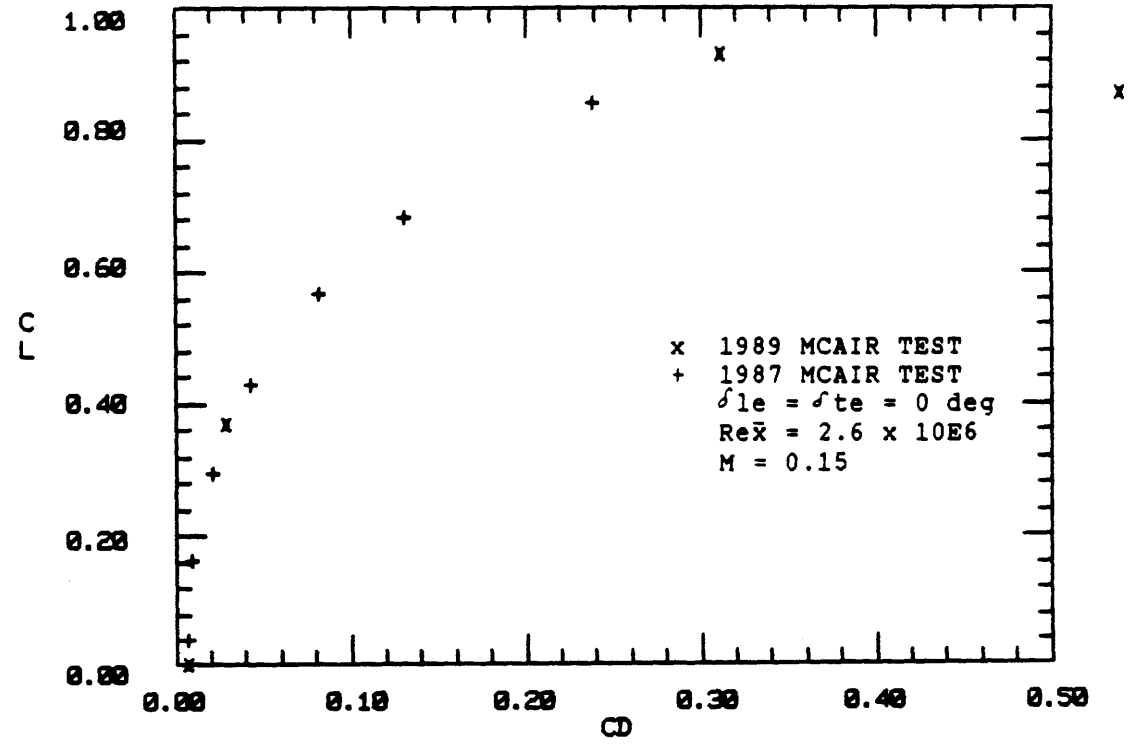

Figure B-64: Plot of MCAIR data; C_L *vs* C_D.

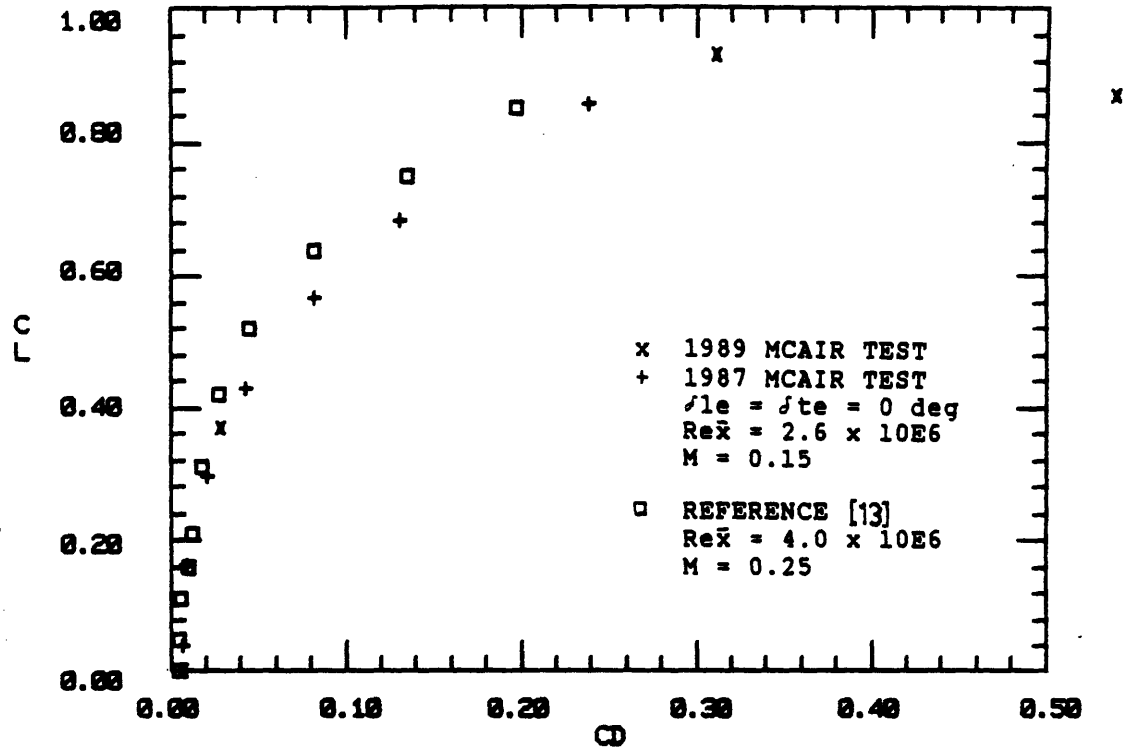

Figure B-65: Comparison of MCAIR data and reference 13; C_L *vs* C_D.

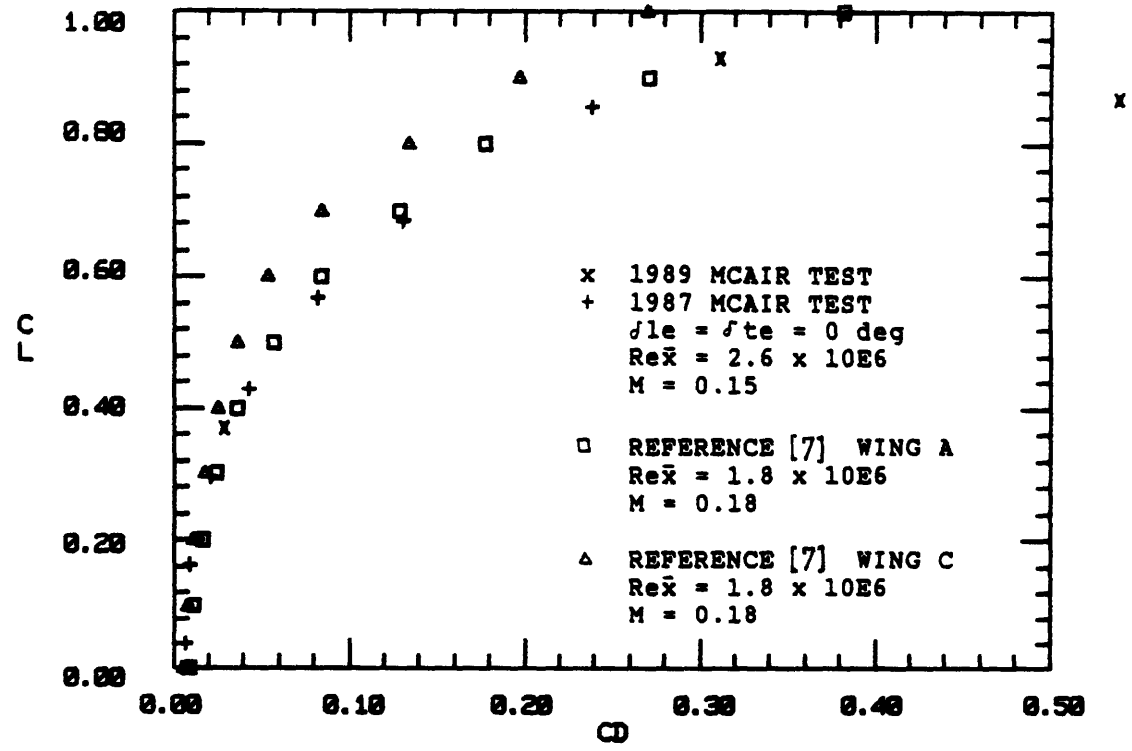

Figure B-66: Comparison of MCAIR data and reference 7; C_L *vs* C_D.

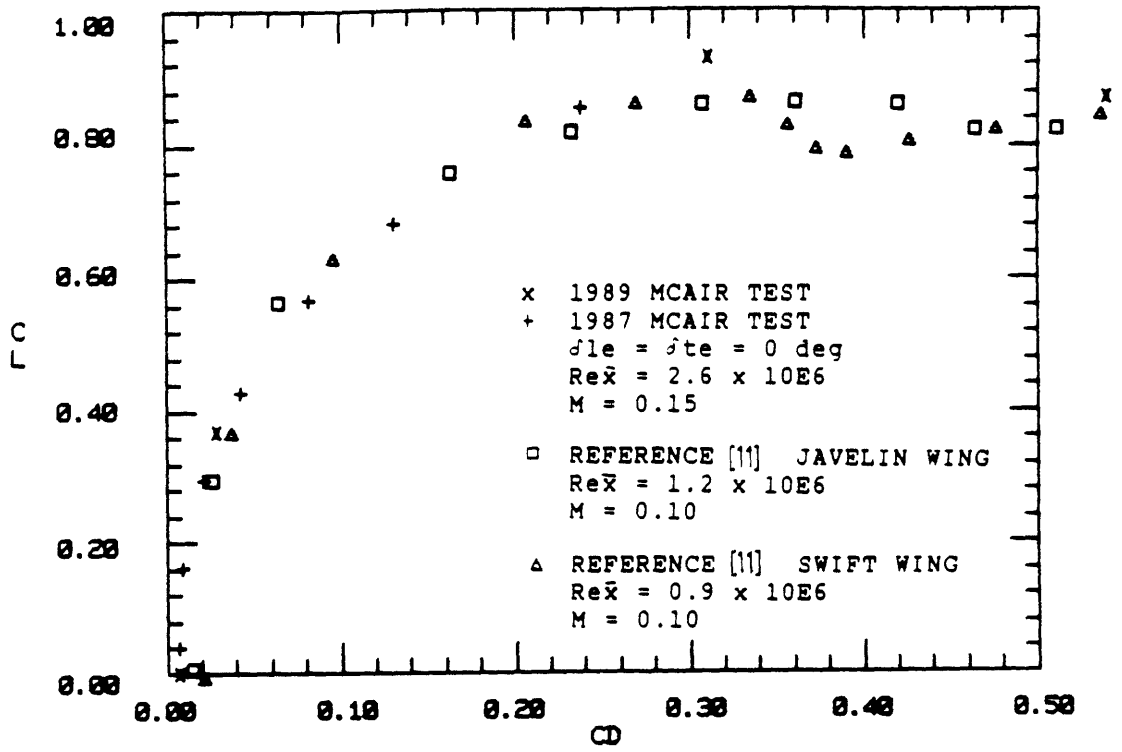

Figure B-67: Comparison of MCAIR data and reference 11: C_L *vs* C_D.

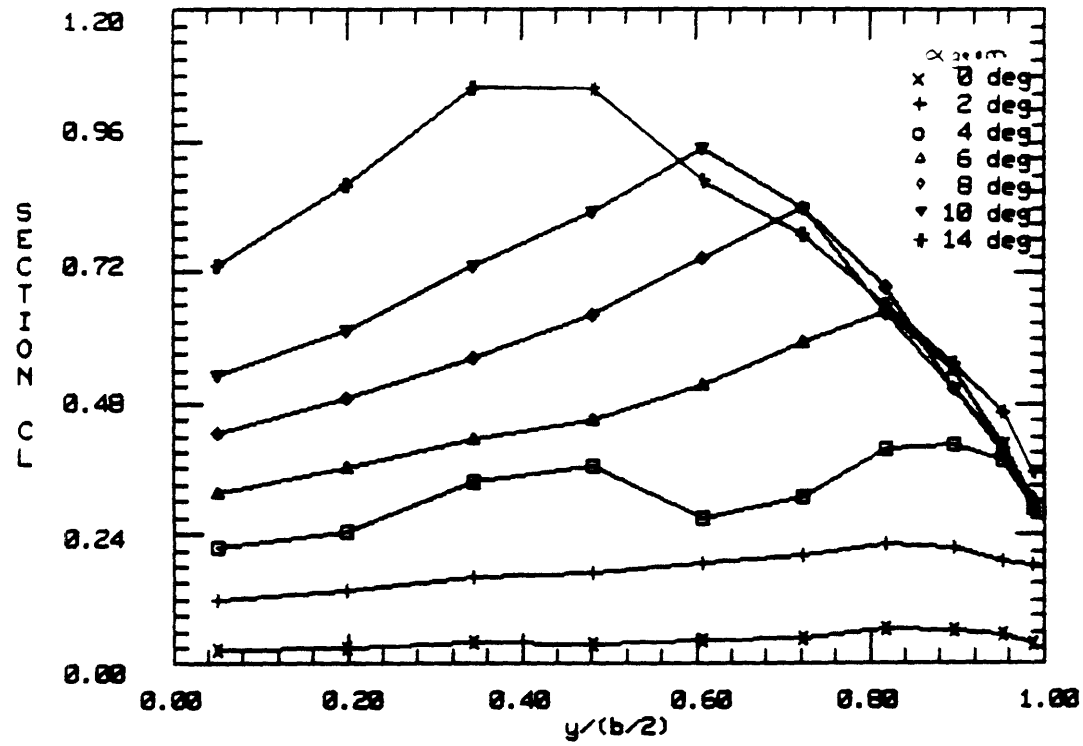

Figure B-68: Plot of 1987 MCAIR data; C_l *vs* $\bar{y}$.

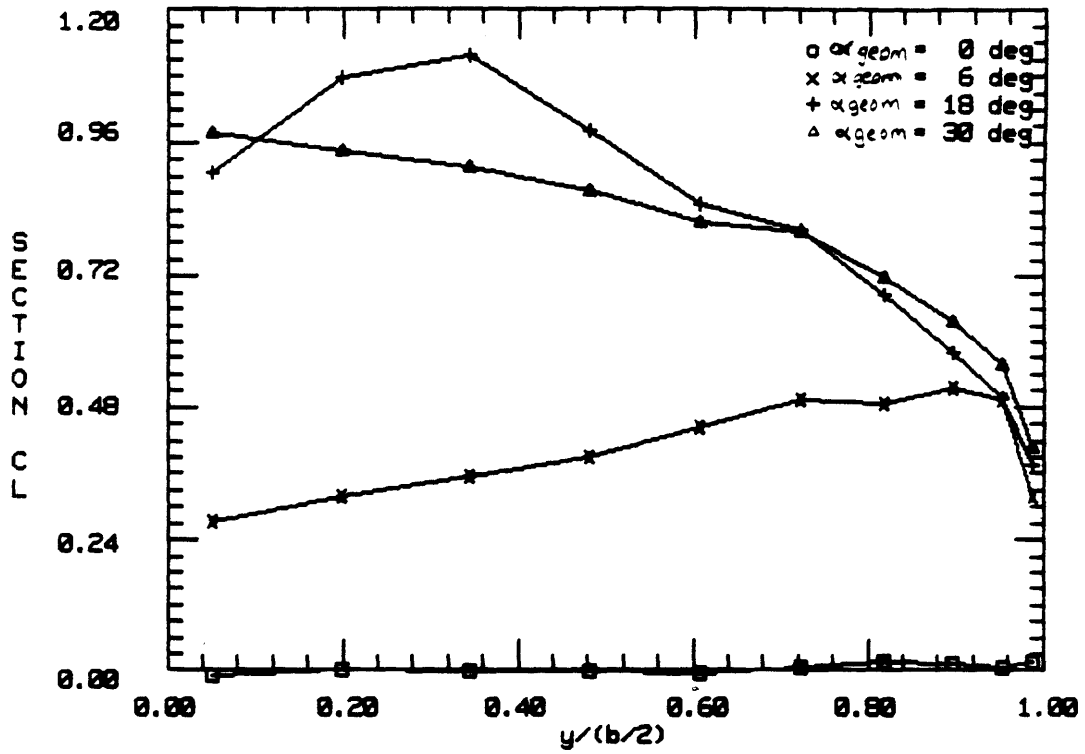

Figure B-69: Plot of 1989 MCAIR data; C_l *vs* $\bar{y}$.

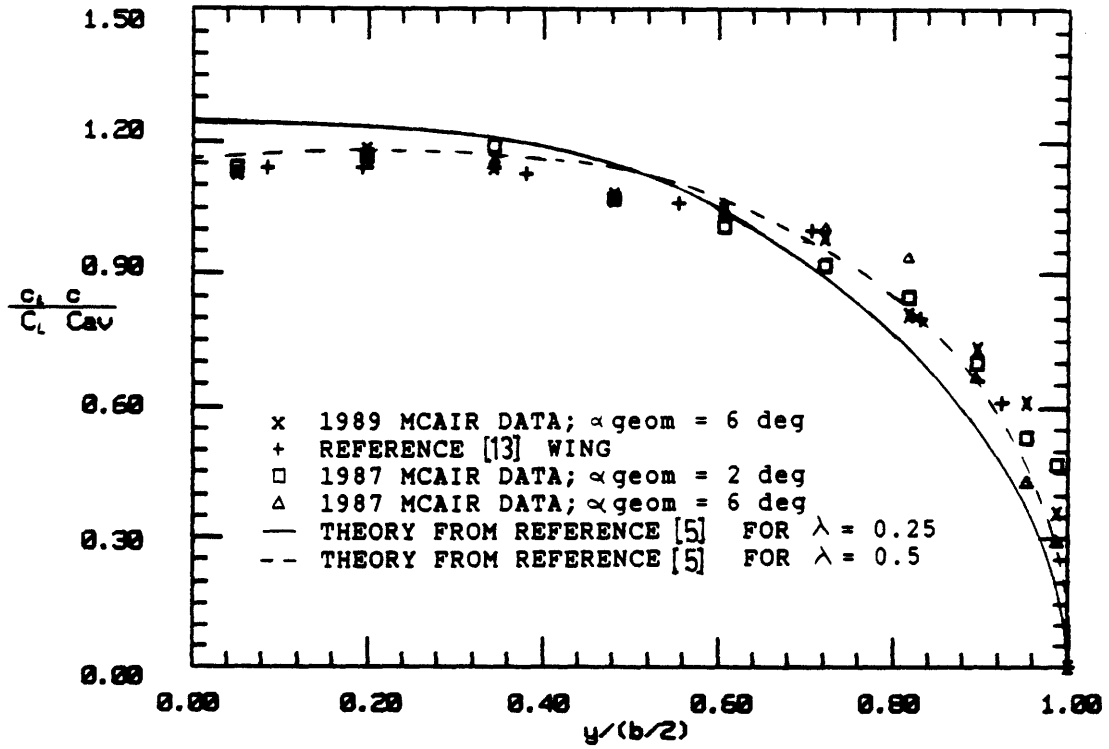

Figure B-70: Comparison of normalized wing loading with references 5 and 13.

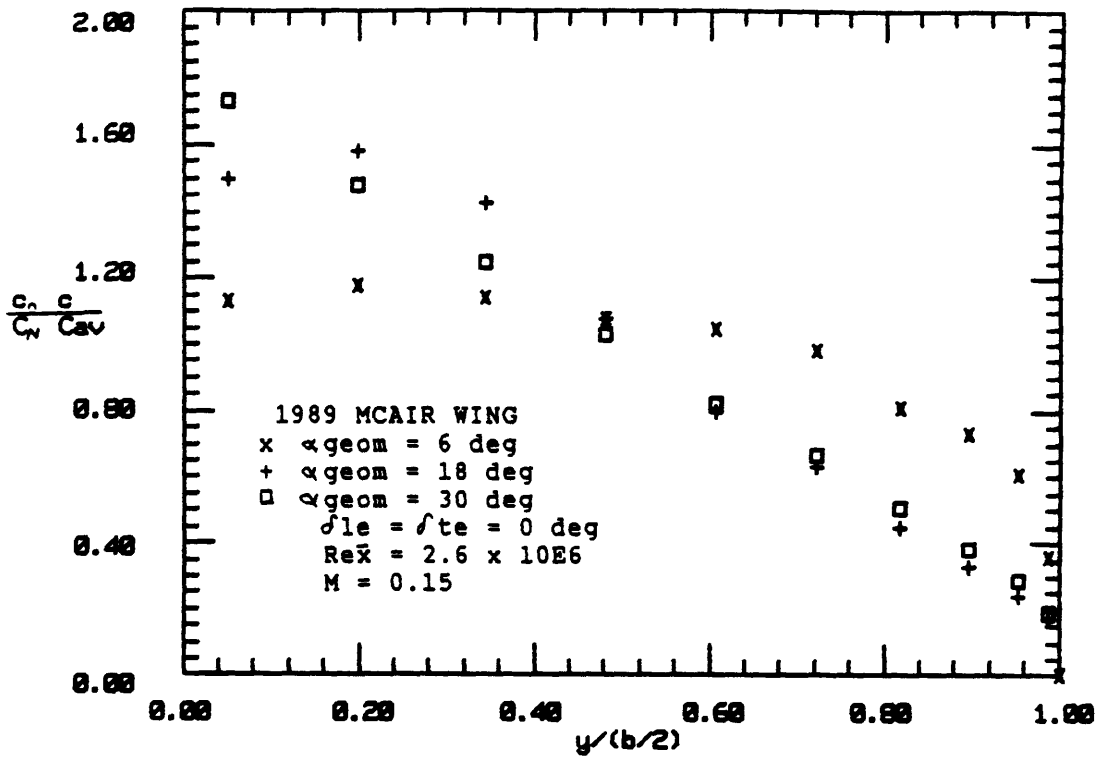

Figure B-71: Plot of normalized wing loading for MCAIR wing.

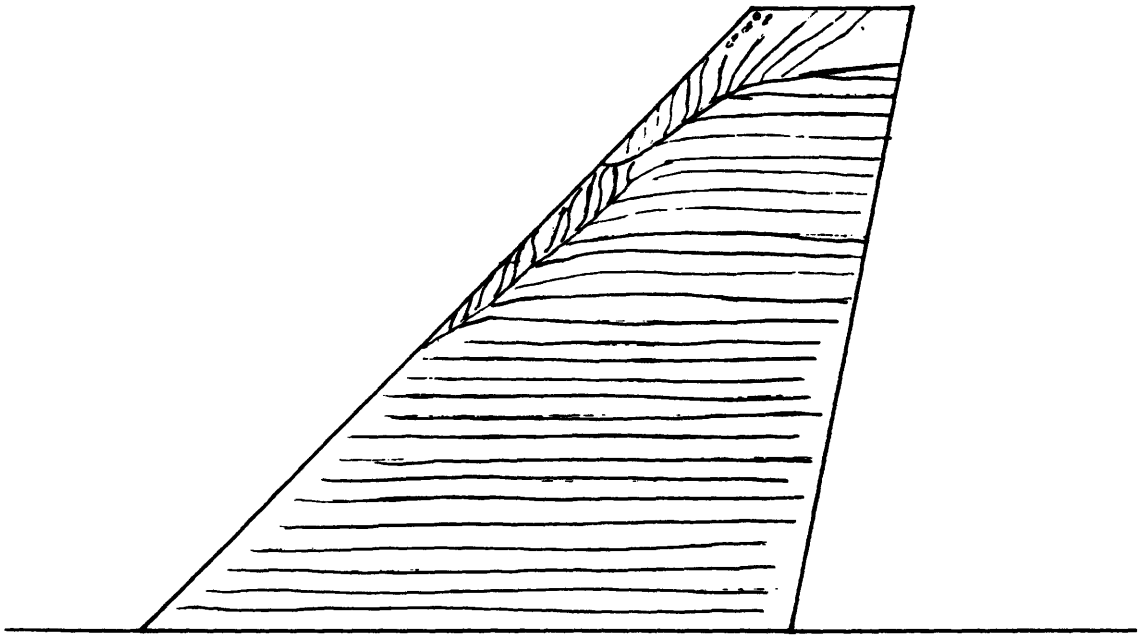

Figure B-72: Flow pattern sketch made from yarn tuft photos; α_{geom}=6°.

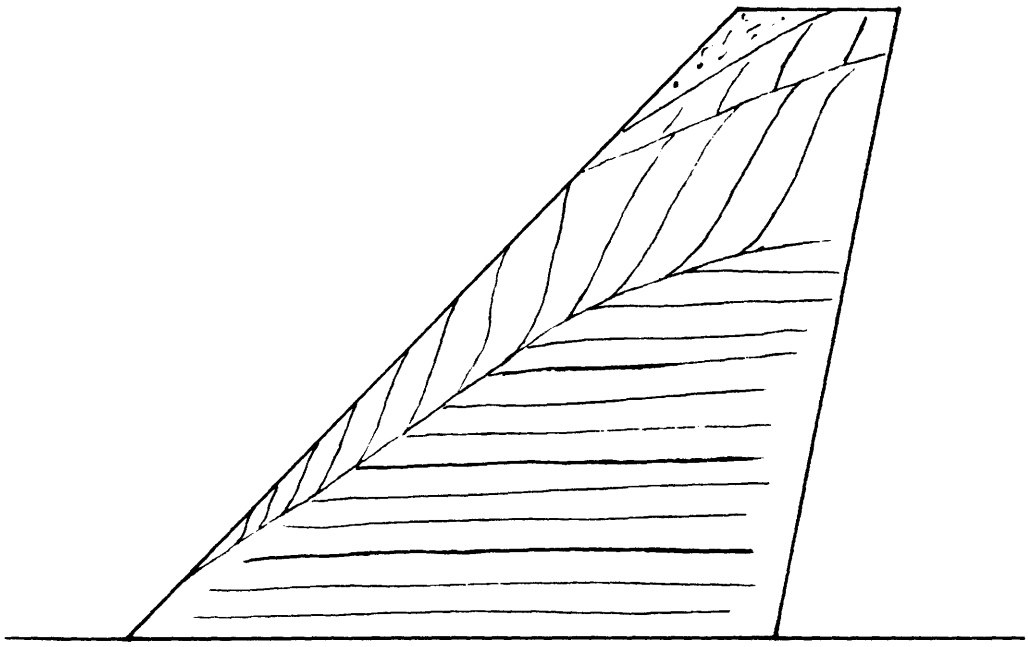

Figure B-73: Flow pattern sketch made from yarn tuft photos; α_{geom}=9°.

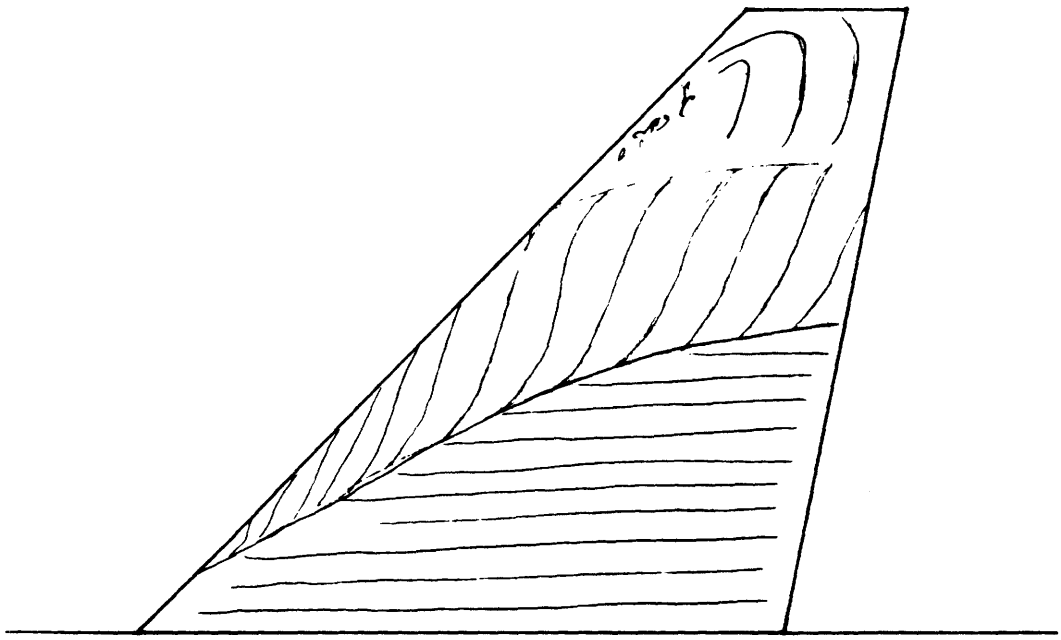

Figure B-74: Flow pattern sketch made from yarn tuft photos; α_{geom}=12°.

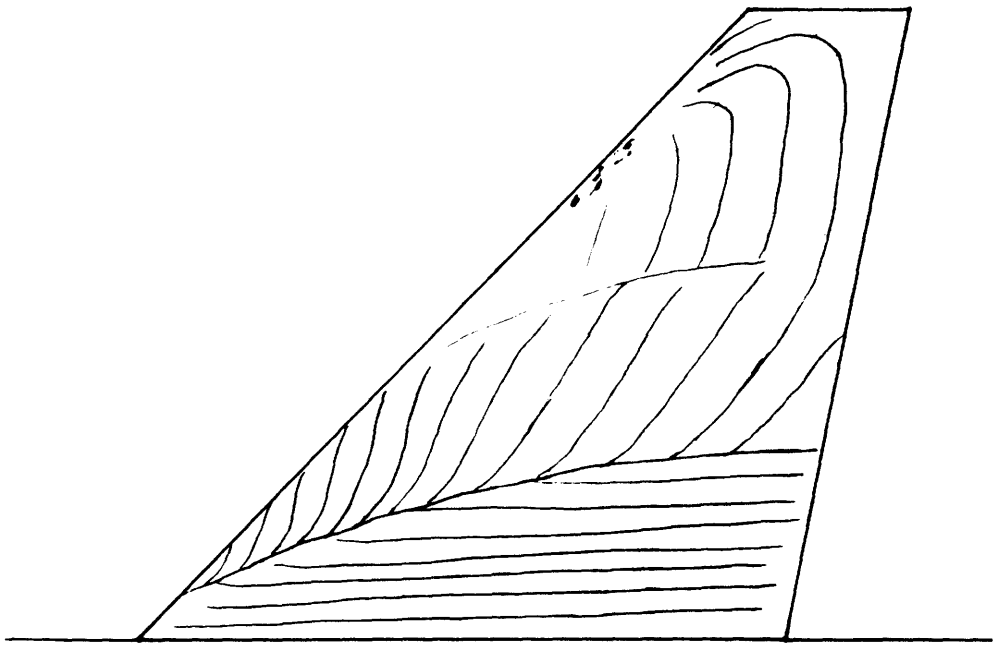

Figure B-75: Flow pattern sketch made from yarn tuft photos; α_{geom}=15°.

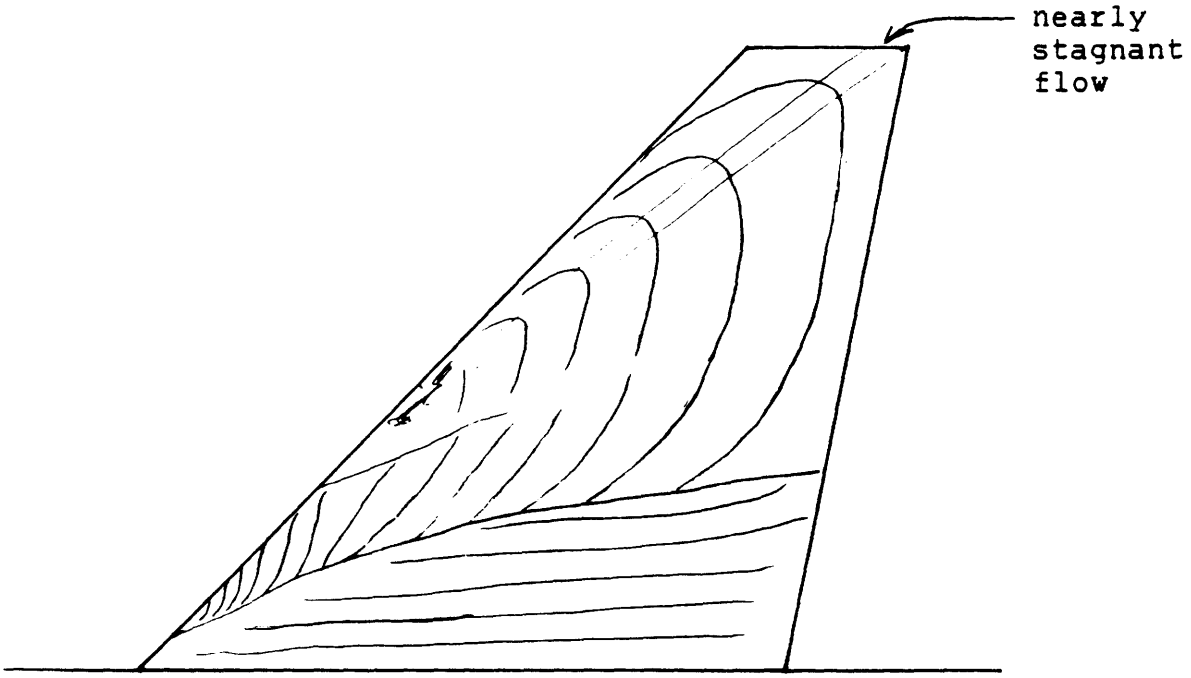

Figure B-76: Flow pattern sketch made from yarn tuft photos; α_{geom}=18°.

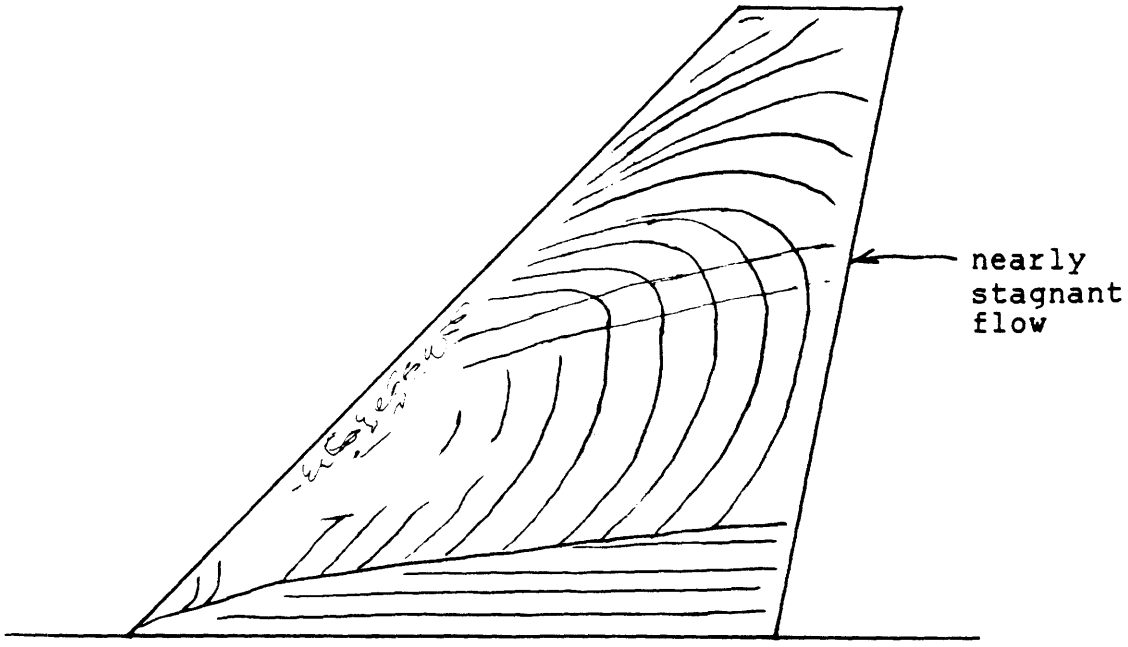

Figure B-77: Flow pattern sketch made from yarn tuft photos; α_{geom}=21°.

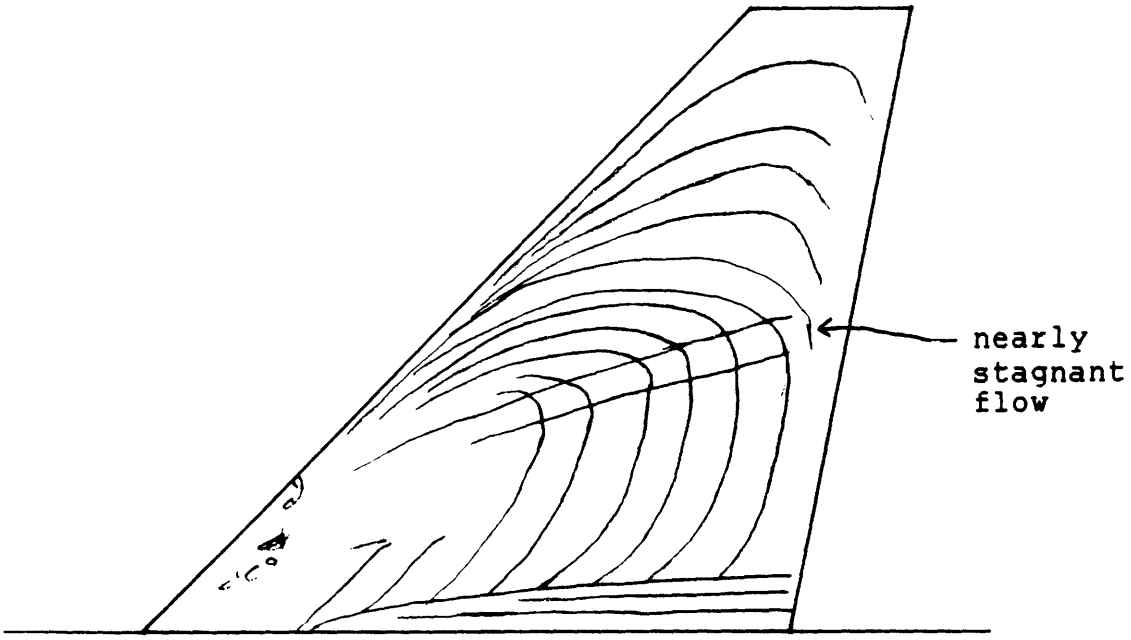

Figure B-78: Flow pattern sketch made from yarn tuft photos; α_{geom}=24°.

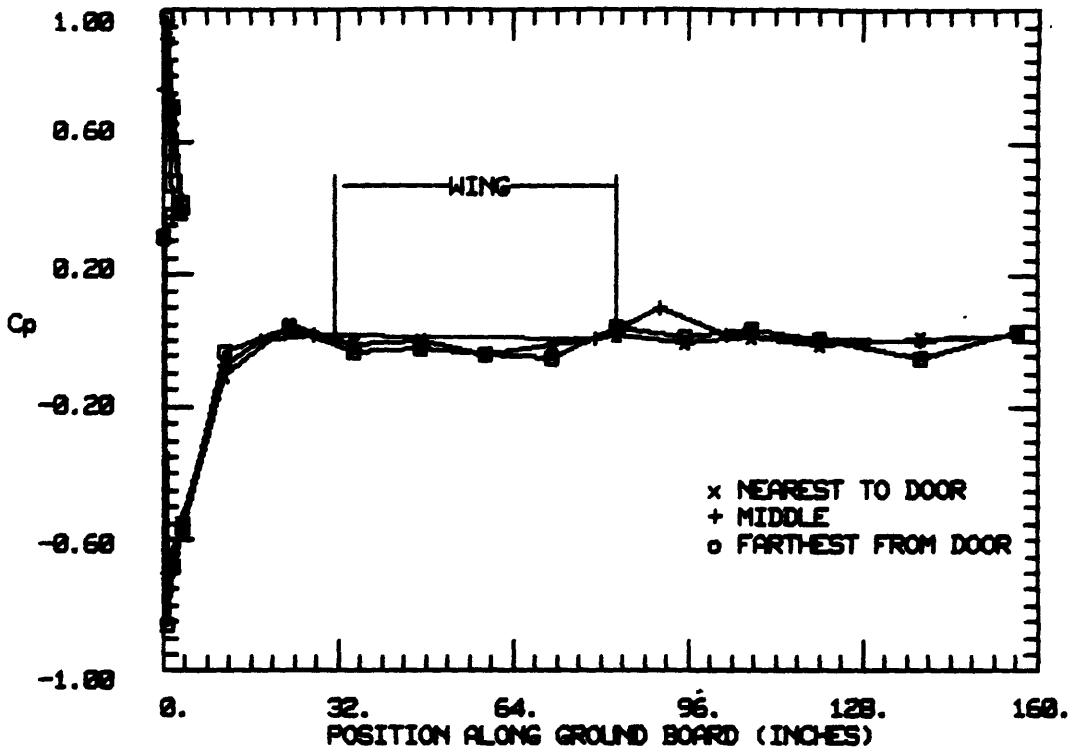

Figure B-79: Ground board data for α_{geom}=0°, δ_{le}=δ_{te}=0°.

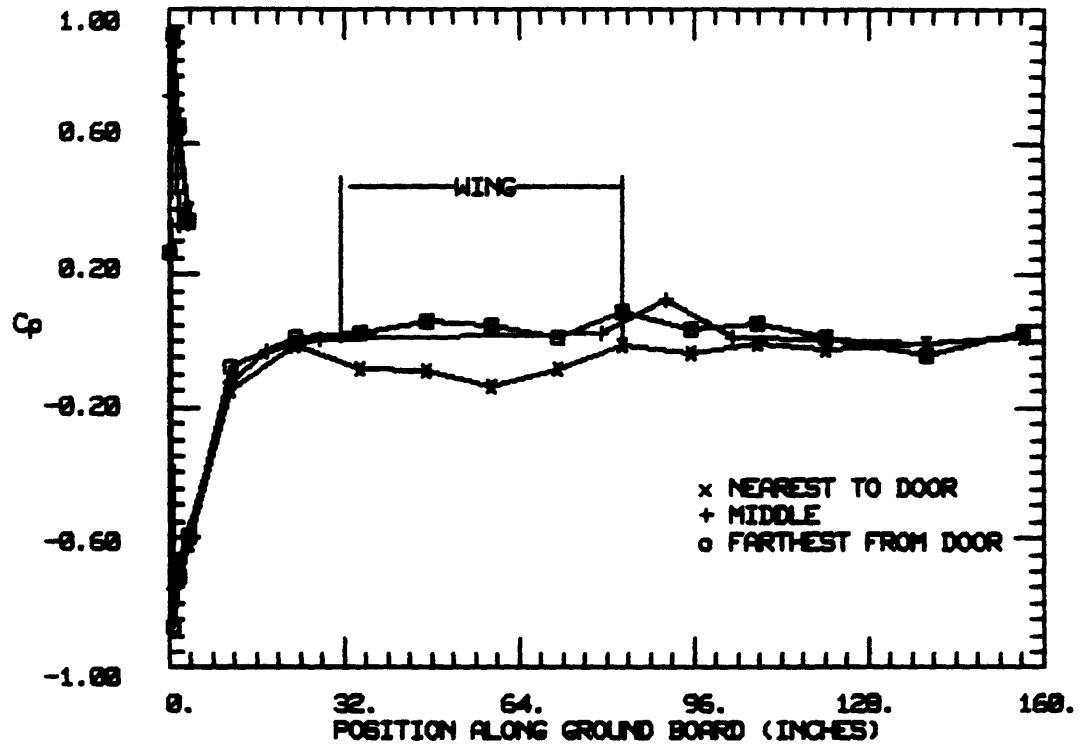

Figure B-80: Ground board data for α_{geom}=6°, δ_{le}=δ_{te}=0°.

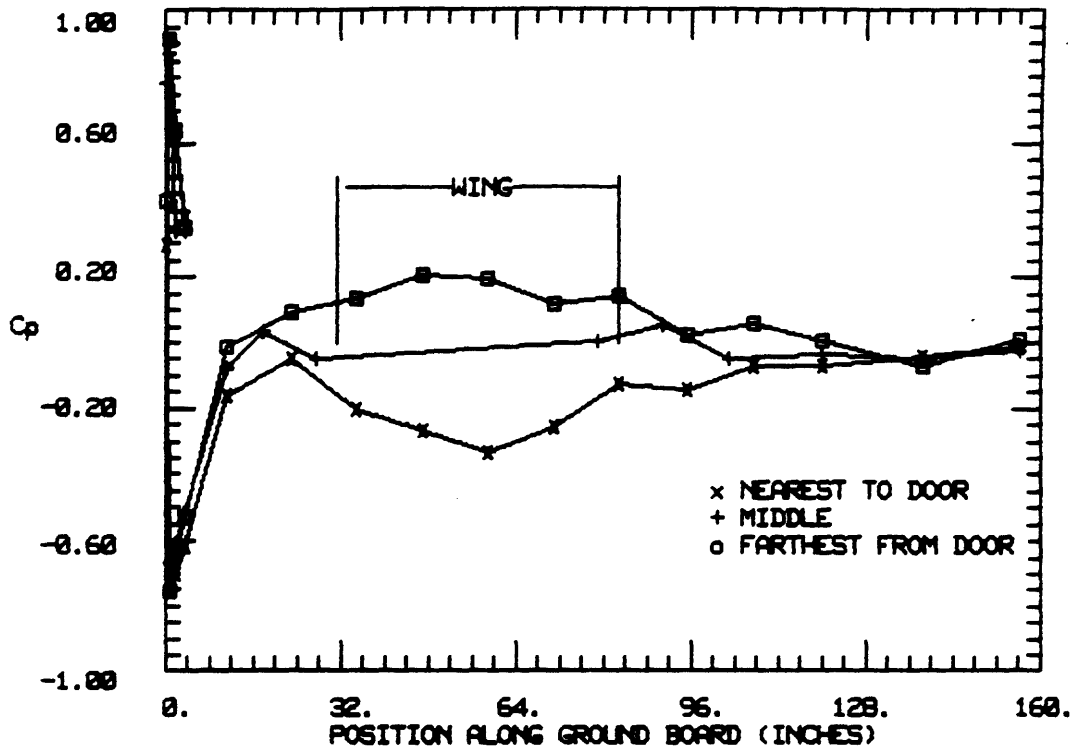

Figure B-81: Ground board data for α_{geom}=18°, δ_{le}=δ_{te}=0°.

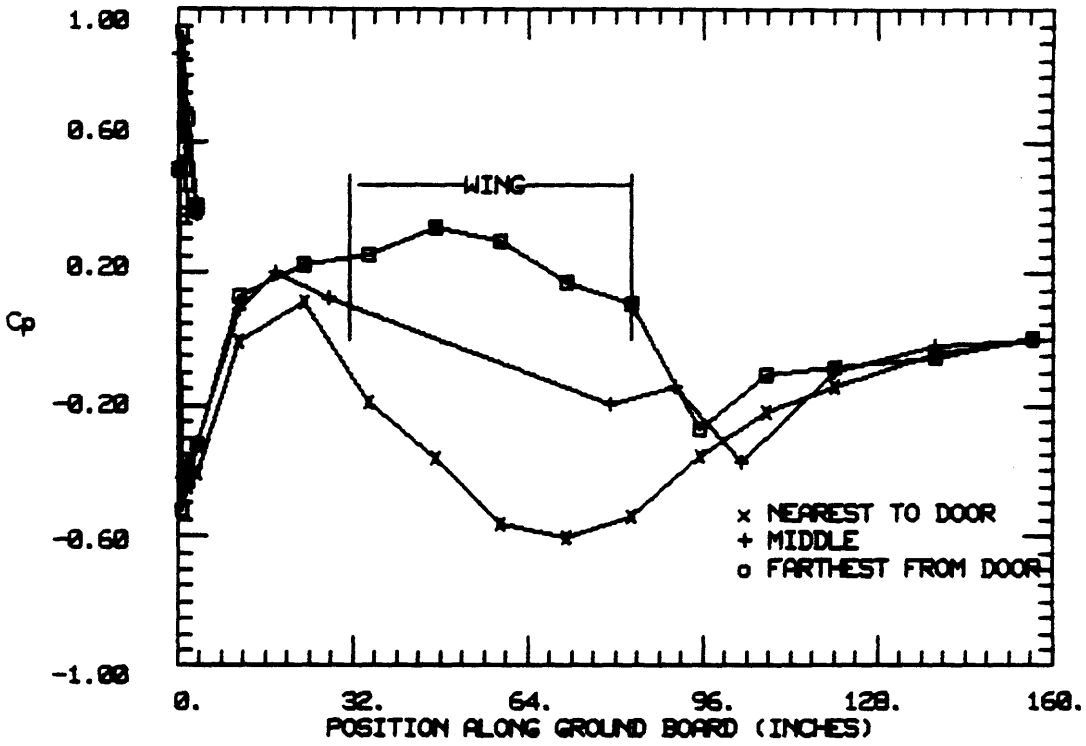

Figure B-82: Ground board data for α_{geom}=30°, δ_{le}=δ_{te}=0°.

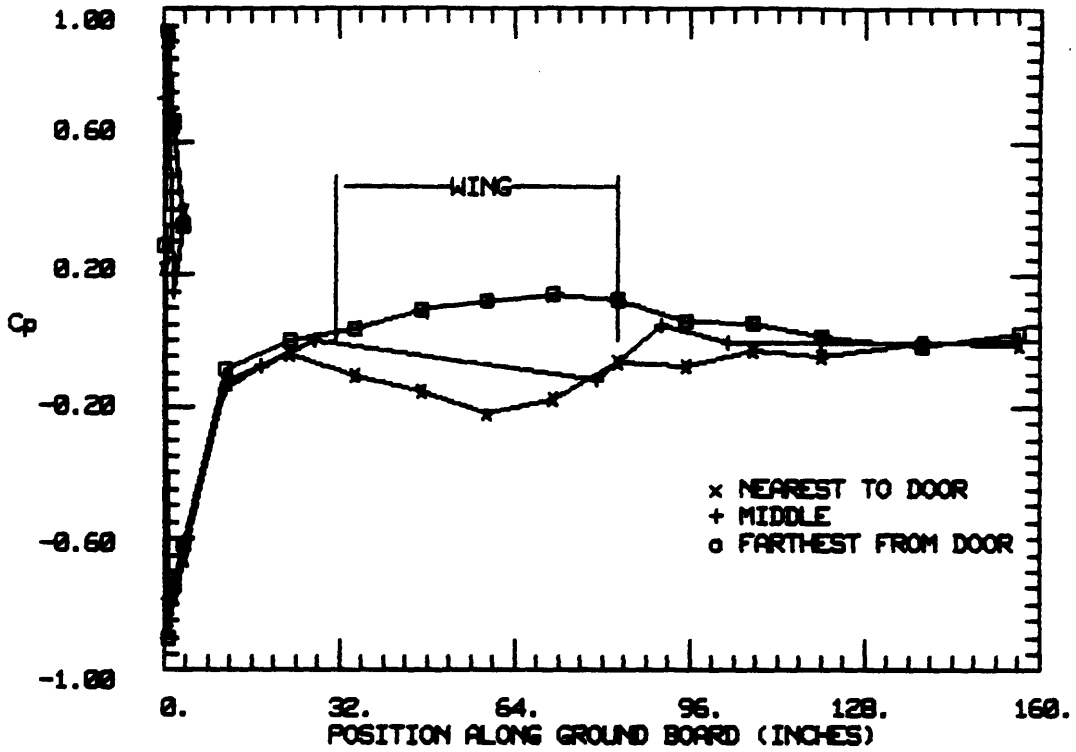

Figure B-83: Ground board data for α_{geom}=6°, δ_{le}=δ_{te}=10°.

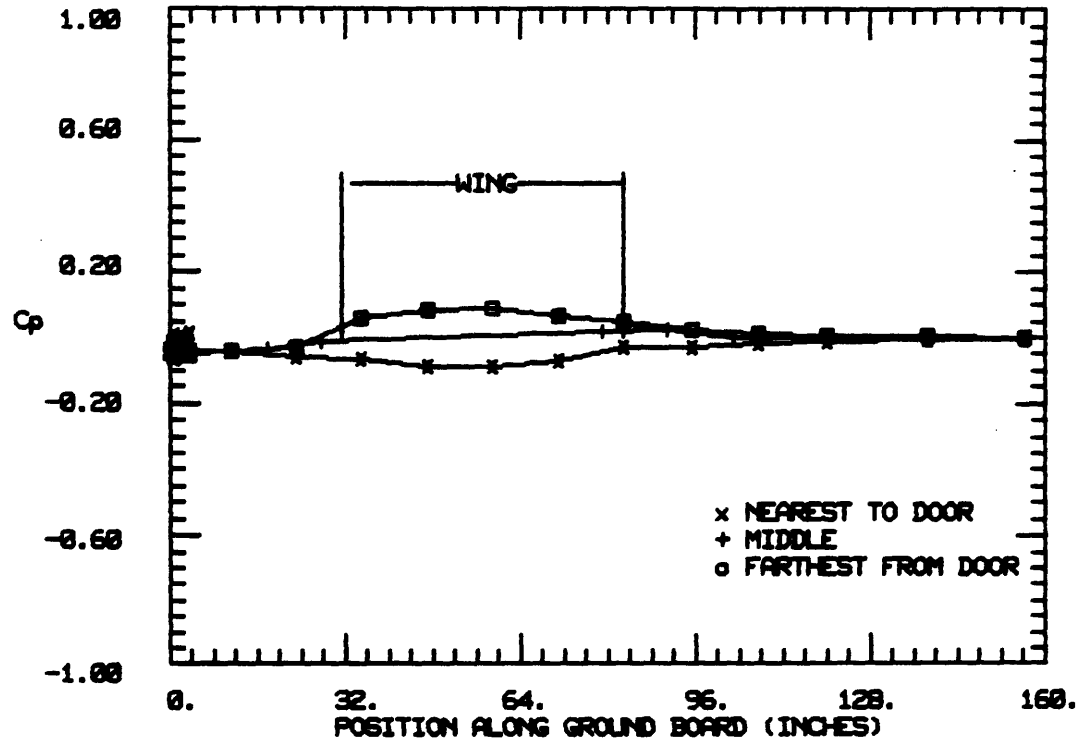

Figure B-84: Ground board data using α_{geom}=0° as datum; α_{geom}=6°.

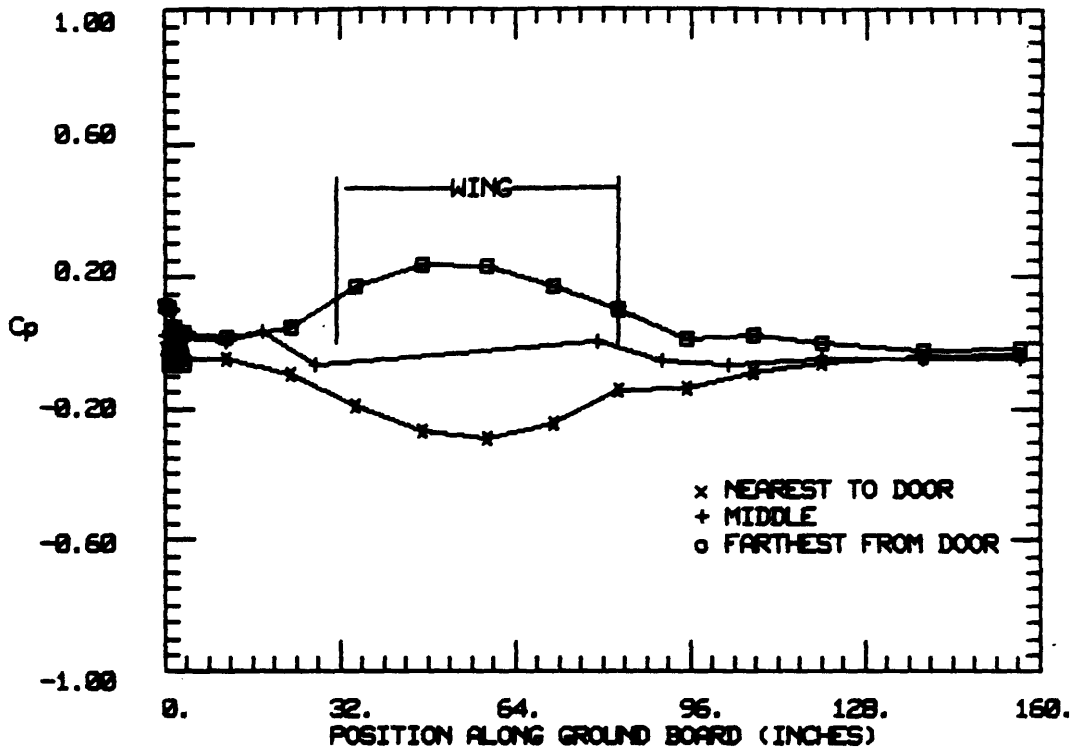

Figure B-85: Ground board data using α_{geom}=0° as datum; α_{geom}=18°.

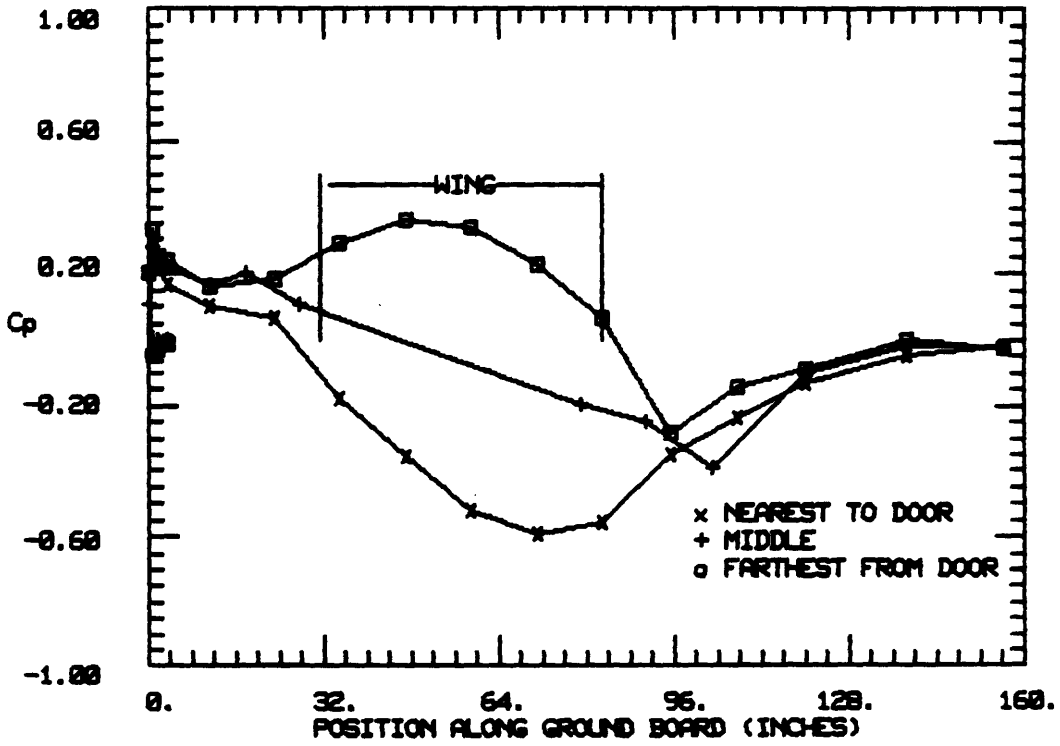

Figure B-86: Ground board data using α_{geom}=0° as datum; α_{geom}=30°.

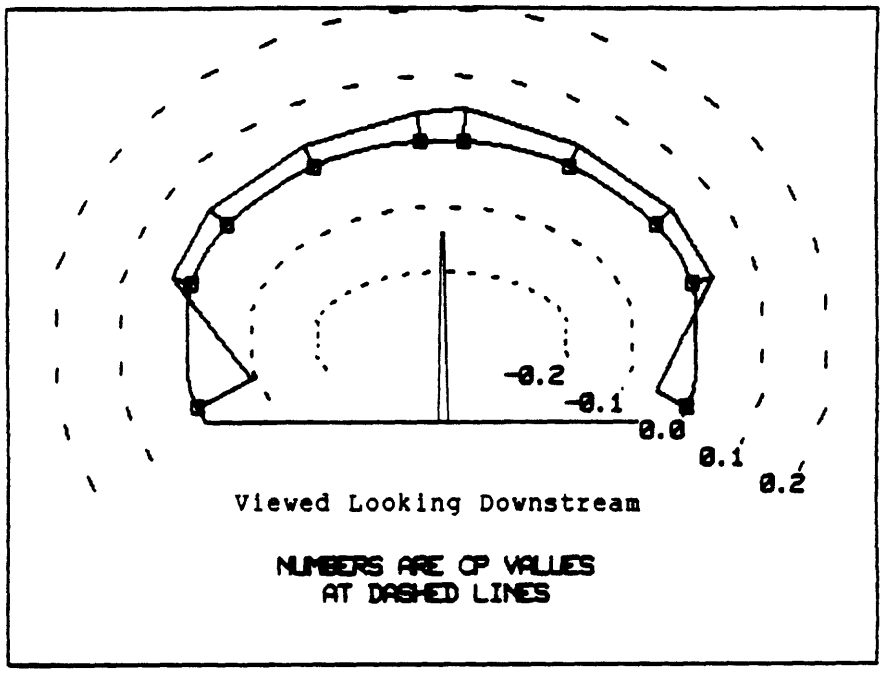

Figure B-87: Plot of wall pressure coefficients for α_{geom}=0°; row 1.

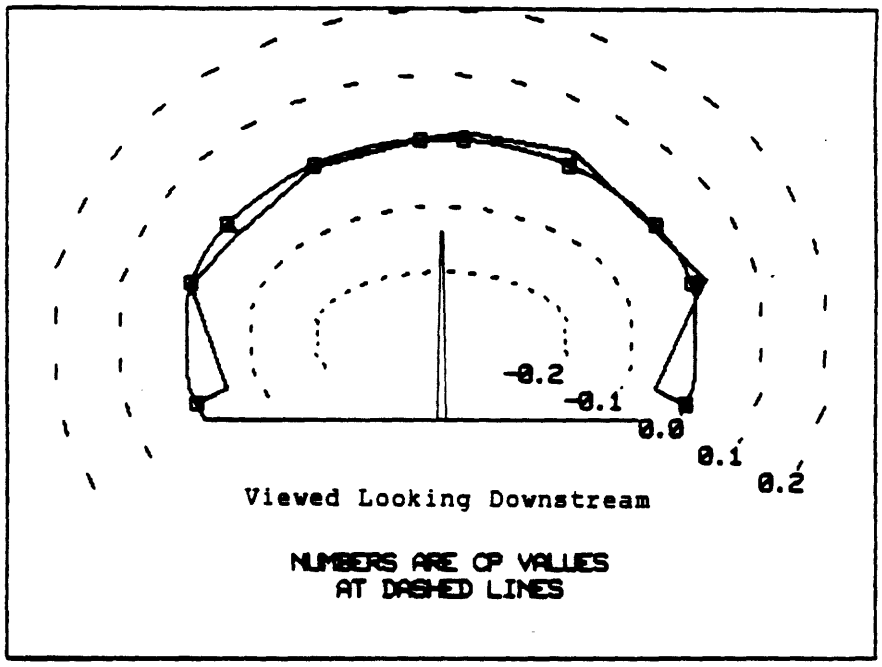

Figure B-88: Plot of wall pressure coefficients for α_{geom}=0°; row 2.

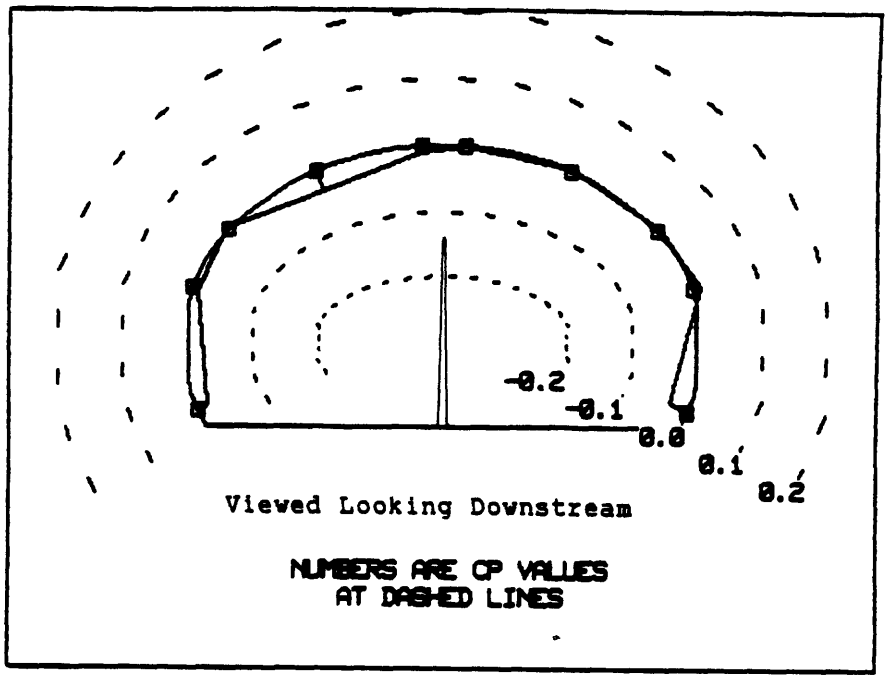

Figure B-89: Plot of wall pressure coefficients for α_{geom}=0°; row 3.

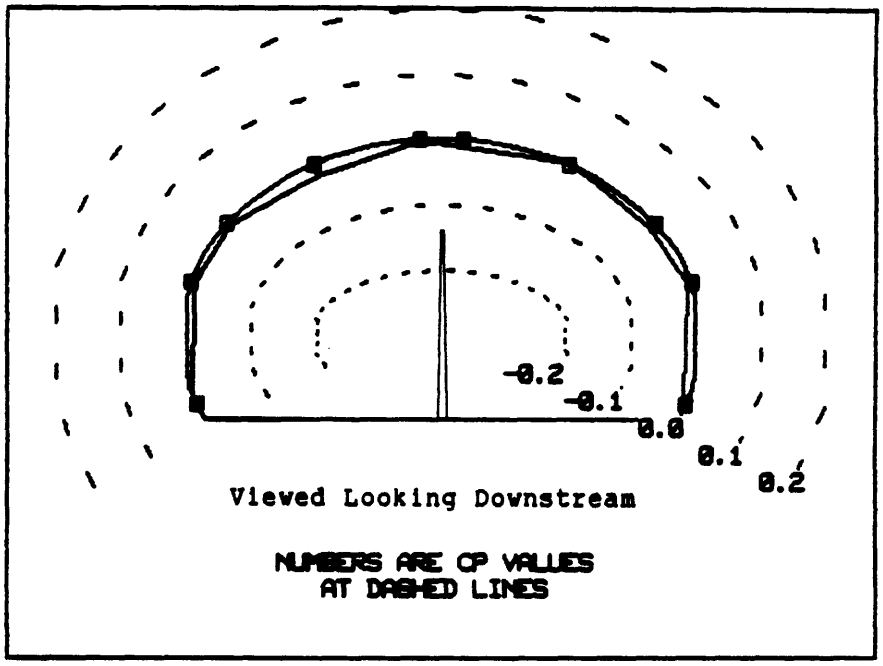

Figure B-90: Plot of wall pressure coefficients for α_{geom}=0°; row 4.

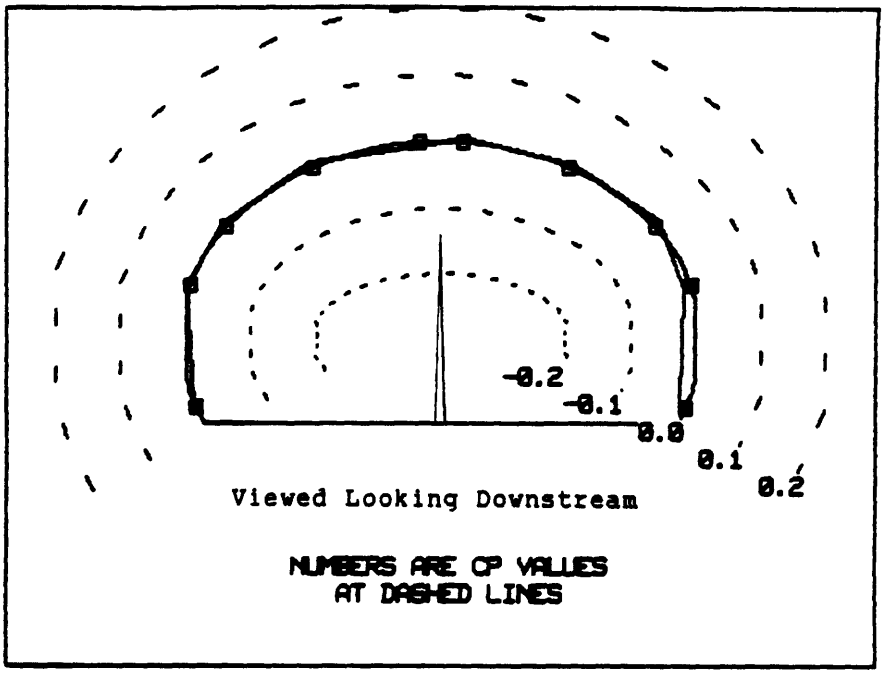

Figure B-91: Plot of wall pressure coefficients for α_{geom}=0°; row 5.

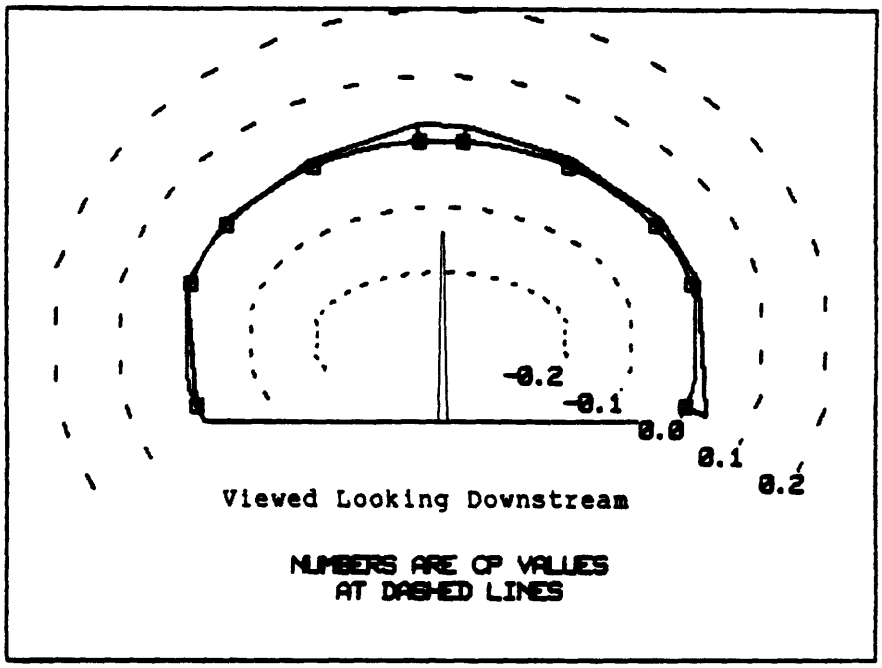

Figure B-92: Plot of wall pressure coefficients for α_{geom}=0°; row 6.

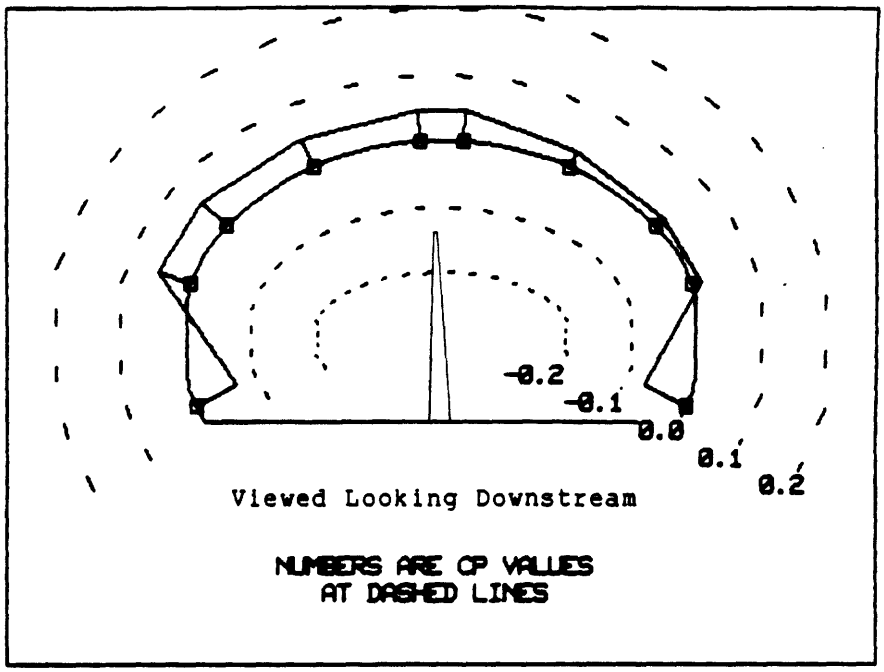

Figure B-93: Plot of wall pressure coefficients for α_{geom}=6°; row 1.

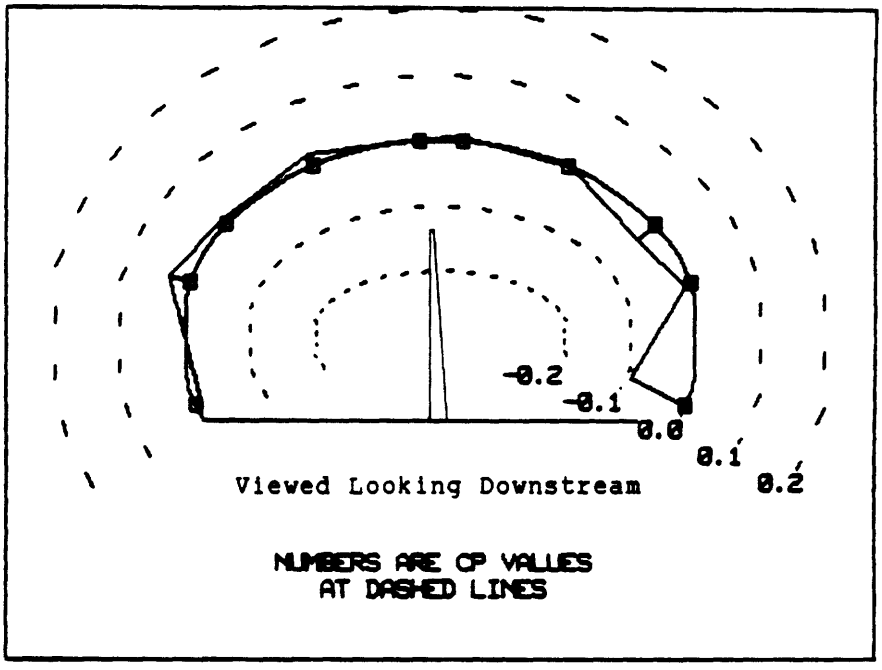

Figure B-94: Plot of wall pressure coefficients for α_{geom}=6°; row 2.

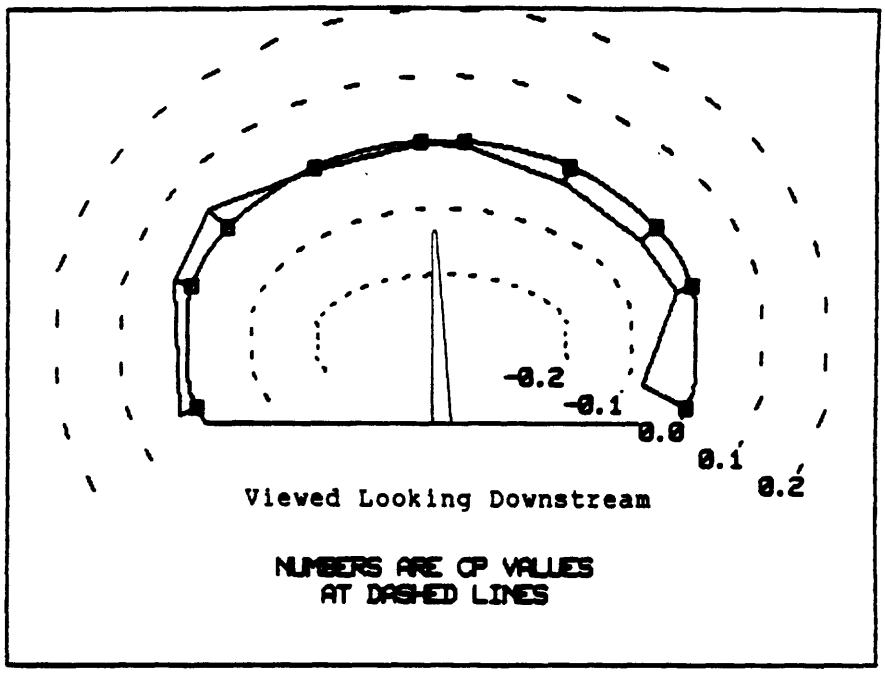

Figure B-95: Plot of wall pressure coefficients for α_{geom}=6°; row 3.

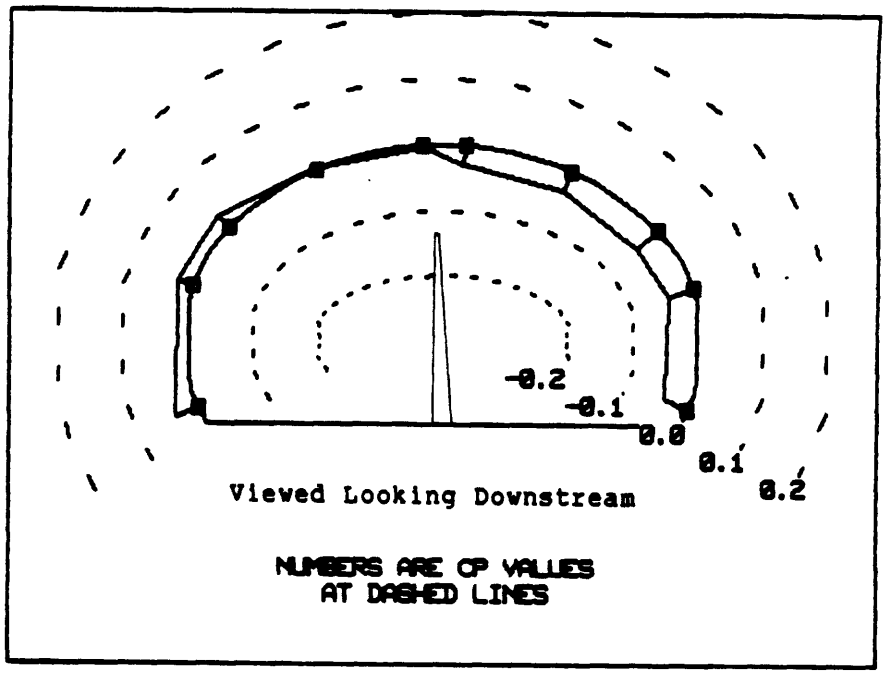

Figure B-96: Plot of wall pressure coefficients for α_{geom}=6°; row 4.

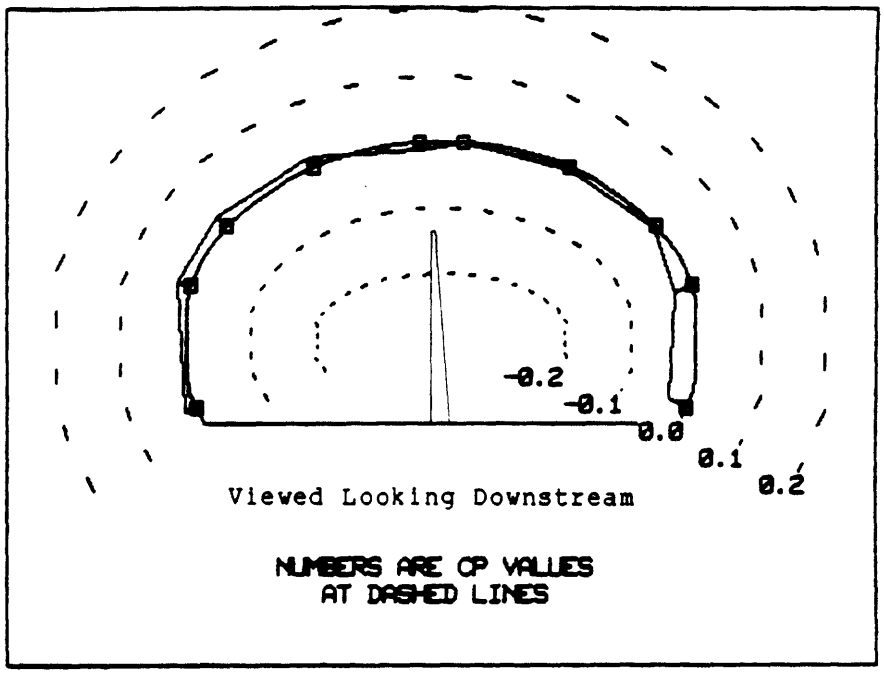

Figure B-97: Plot of wall pressure coefficients for α_{geom}=6°; row 5.

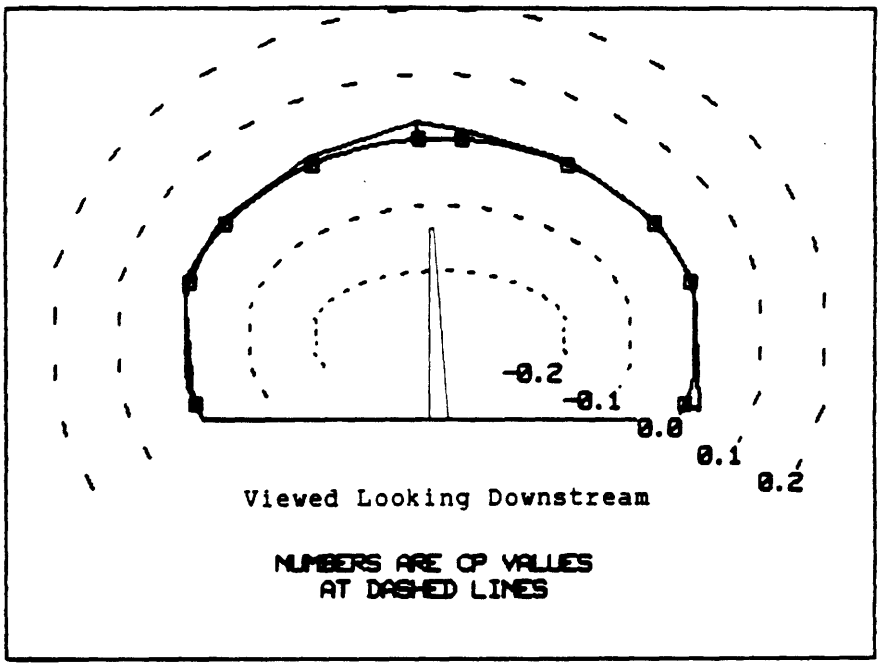

Figure B-98: Plot of wall pressure coefficients for α_{geom}=6°; row 6.

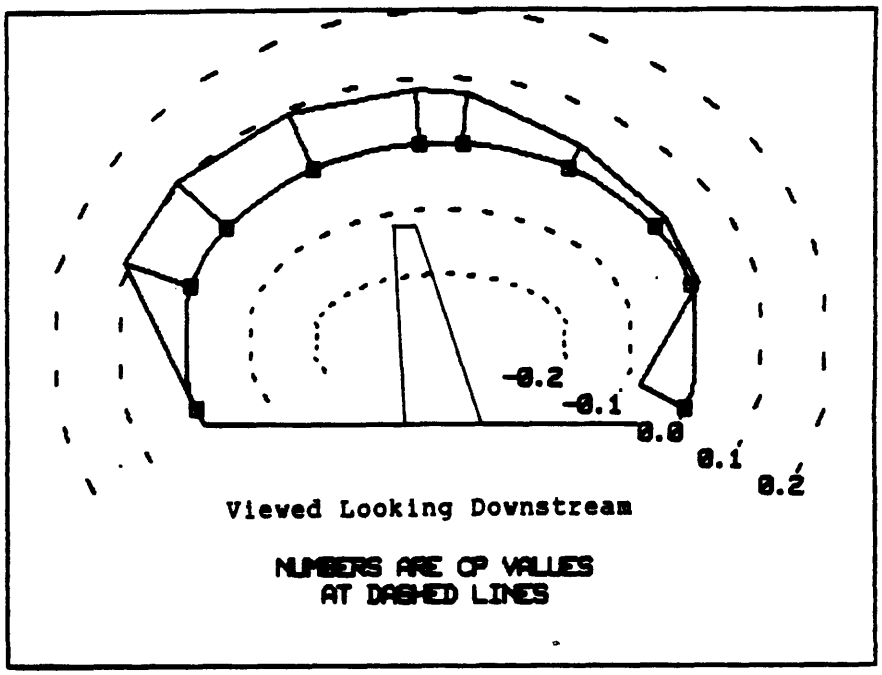

Figure B-99: Plot of wall pressure coefficients for α_{geom}=18°; row 1.

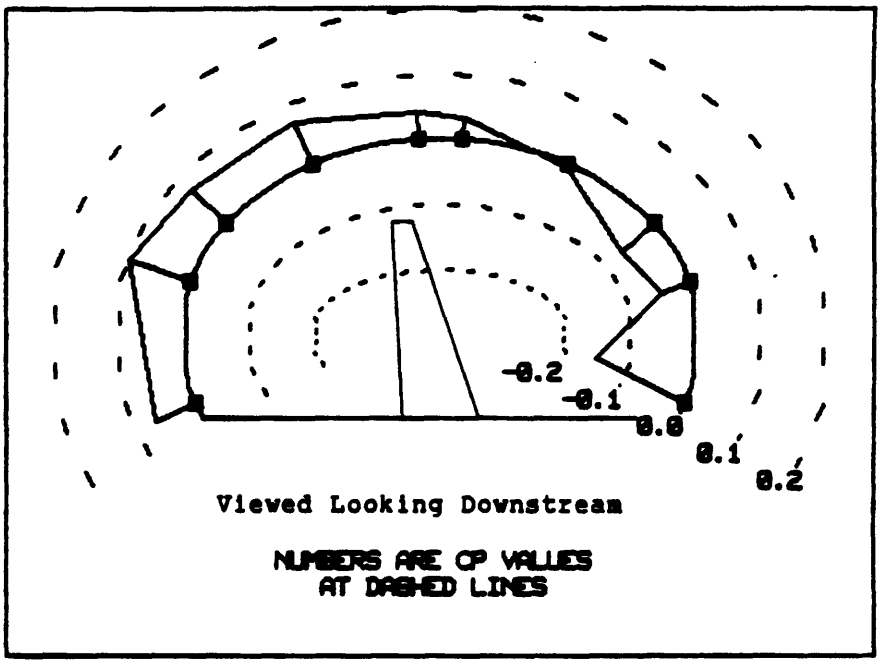

Figure B-100: Plot of wall pressure coefficients for α_{geom}=18°; row 2.

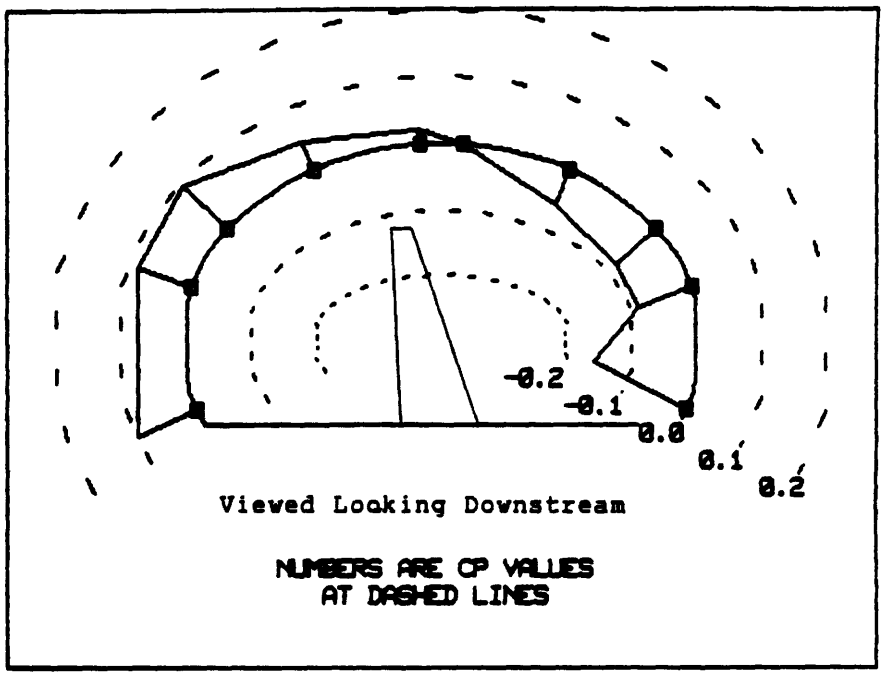

Figure B-101: Plot of wall pressure coefficients for α_{geom}=18°; row 3.

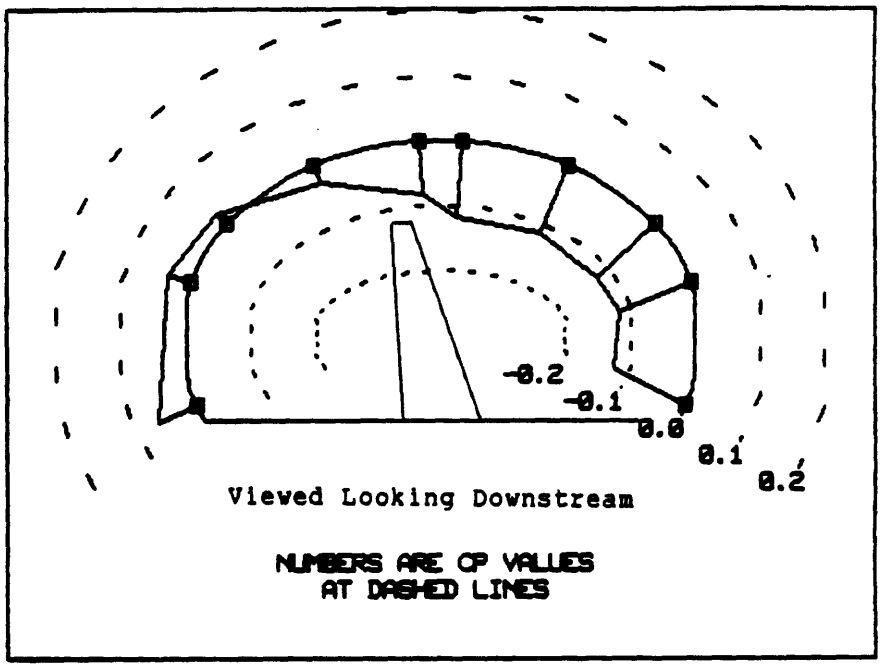

Figure B-102: Plot of wall pressure coefficients for α_{geom}=18°; row 4.

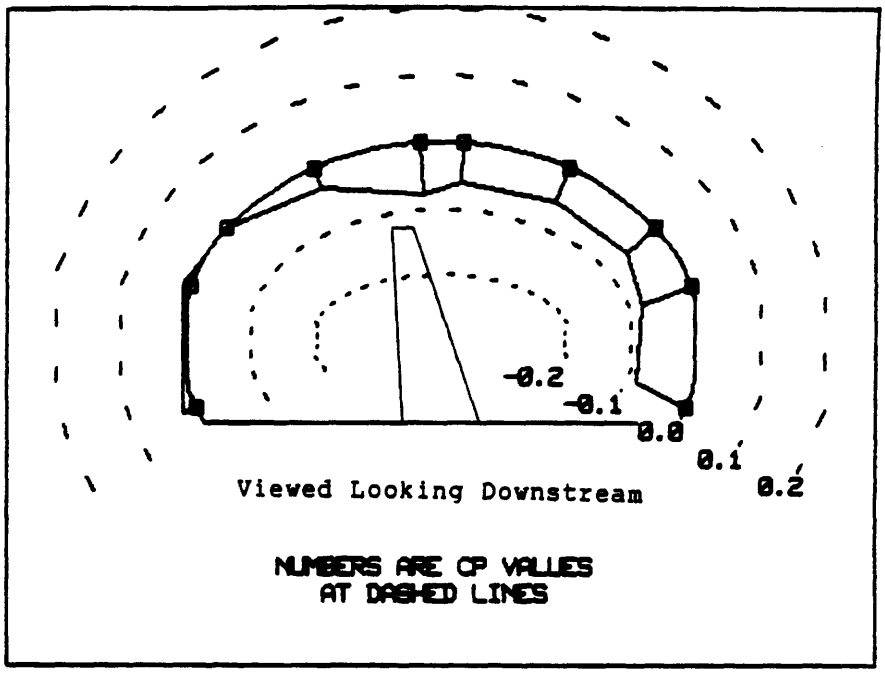

Figure B-103: Plot of wall pressure coefficients for α_{geom}=18°; row 5.

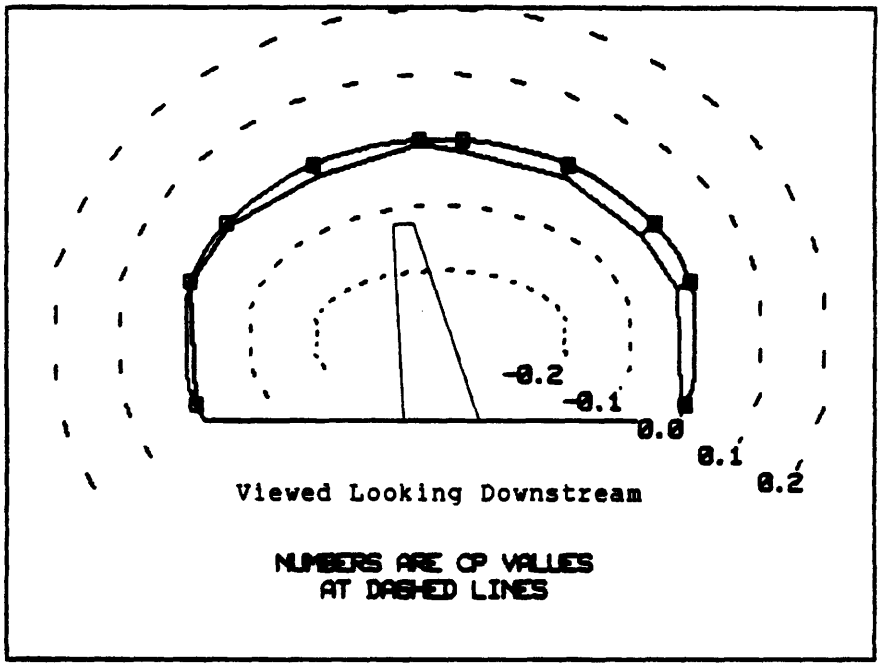

Figure B-104: Plot of wall pressure coefficients for α_{geom}=18°; row 6.

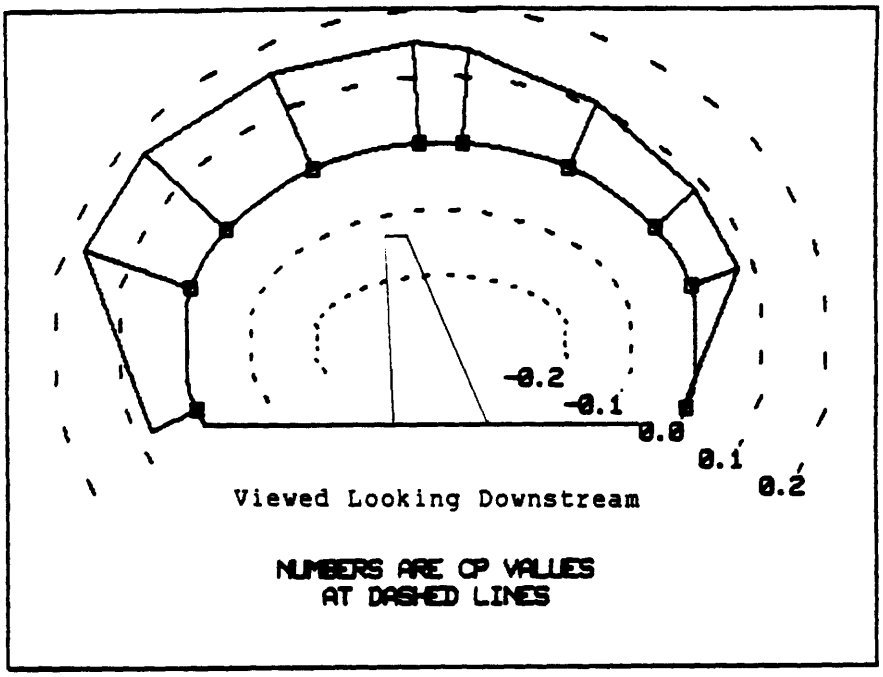

Figure B-105: Plot of wall pressure coefficients for α_{geom}=30°; row 1.

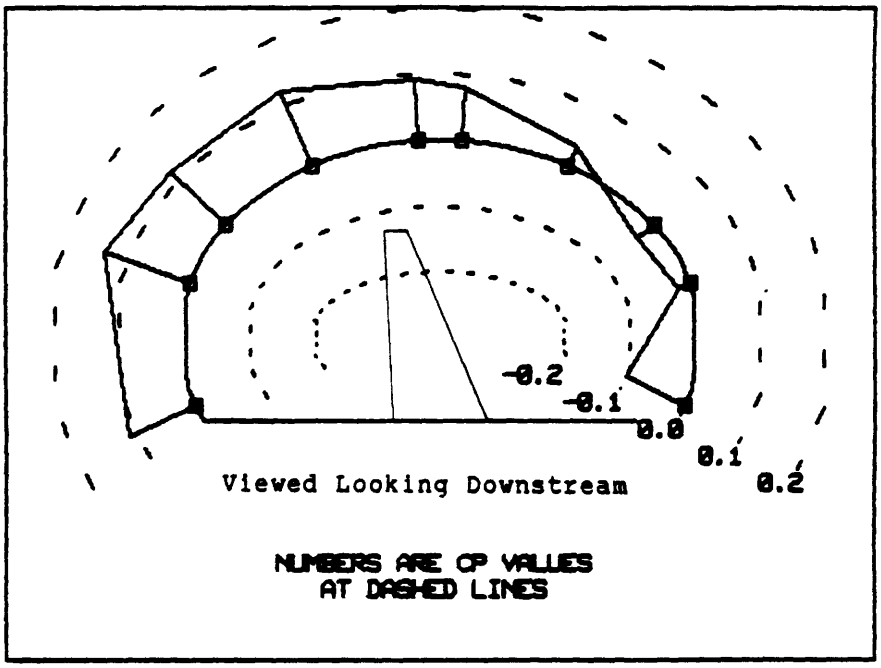

Figure B-106: Plot of wall pressure coefficients for α_{geom}=30°; row 2.

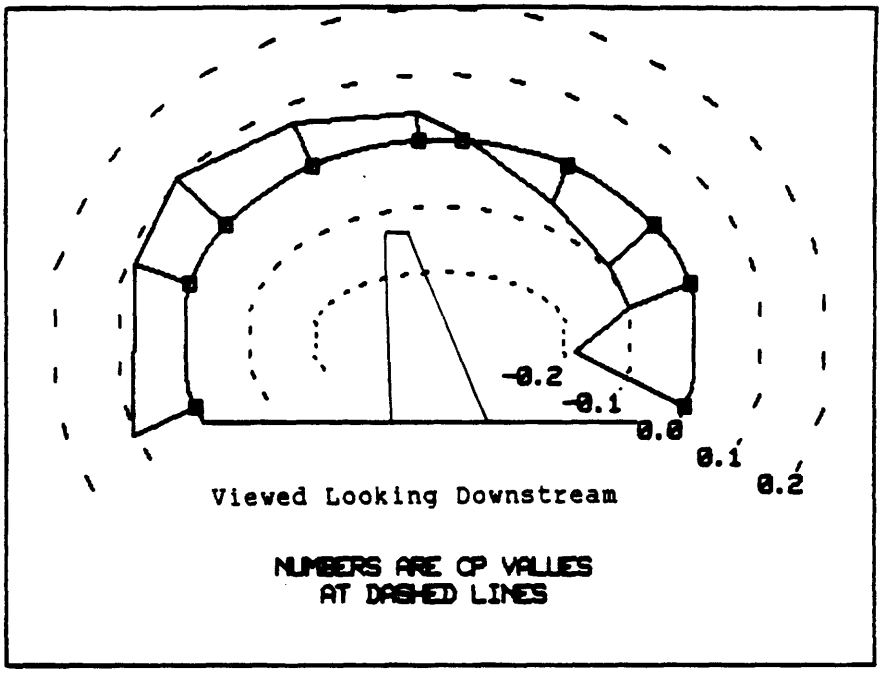

Figure B-107: Plot of wall pressure coefficients for α_{geom}=30°; row 3.

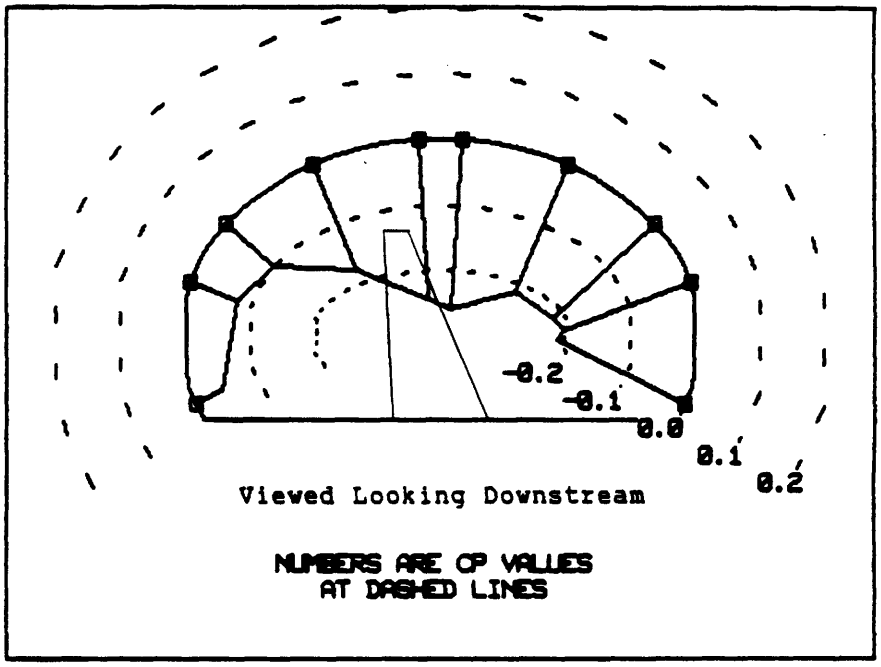

Figure B-108: Plot of wall pressure coefficients for α_{geom}=30°; row 4.

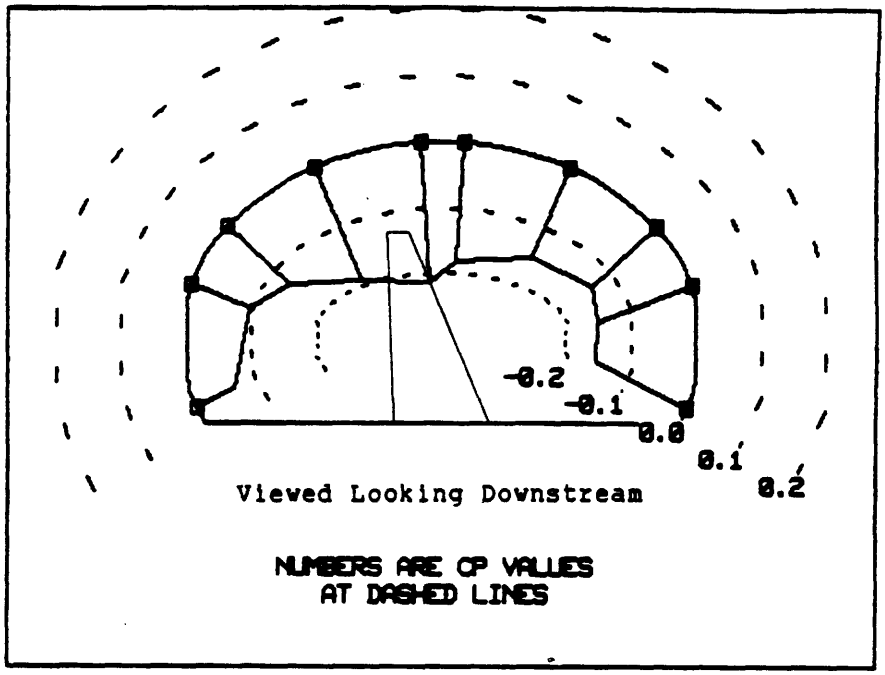

Figure B-109: Plot of wall pressure coefficients for α_{geom}=30°; row 5.

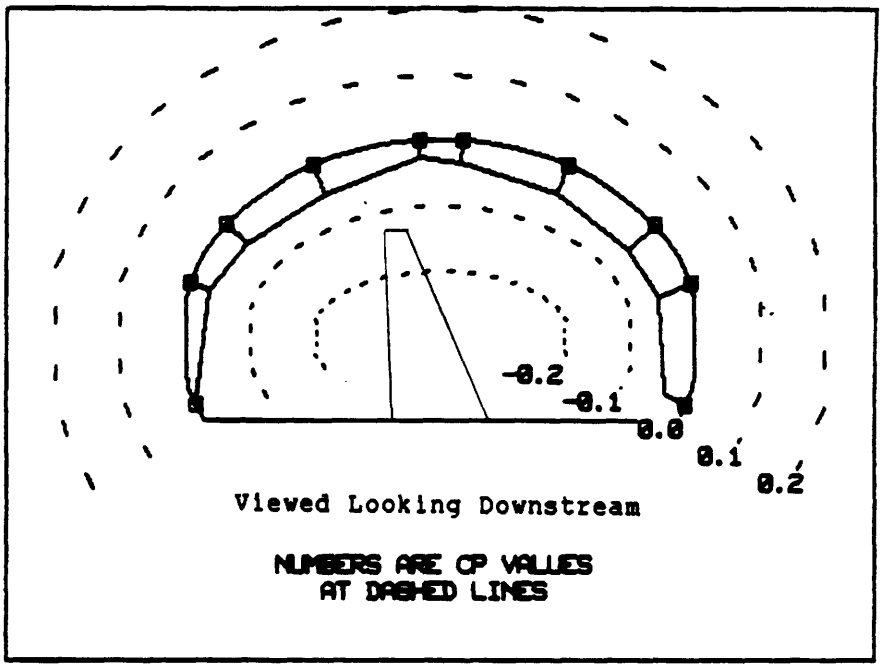

Figure B-110: Plot of wall pressure coefficients for α_{geom}=30°; row 6.

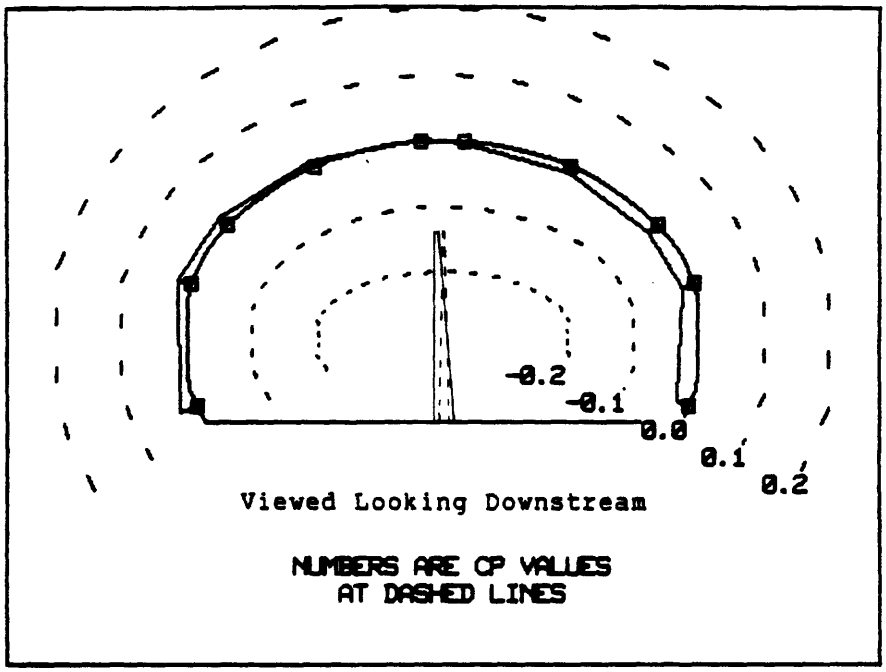

Figure B-111: Wall pressure coefficients with α_{geom}=0° as datum; α_{geom}=6°, row 1.

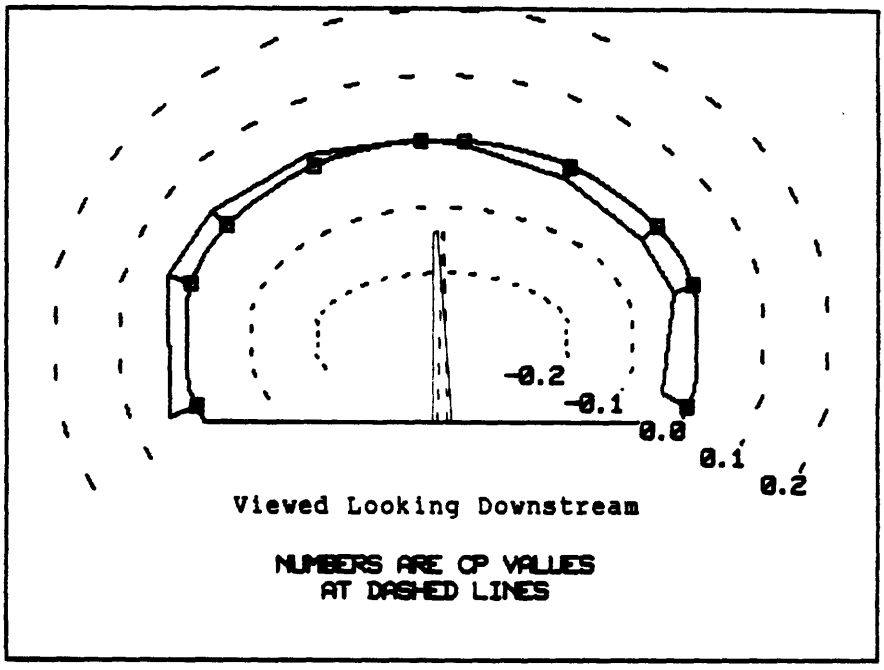

Figure B-112: Wall pressure coefficients with α_{geom}=0° as datum; α_{geom}=6°, row 2.

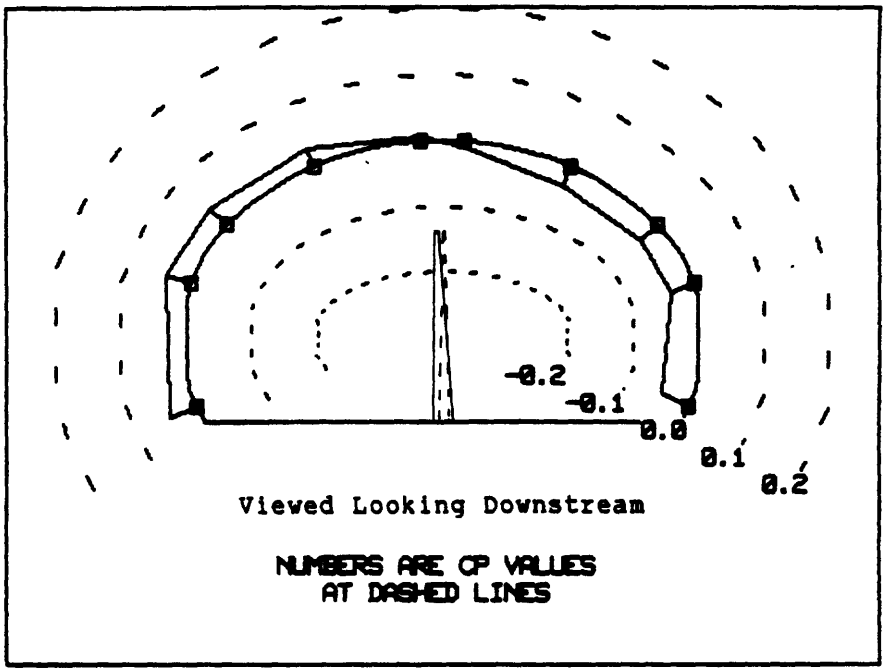

Figure B-113: Wall pressure coefficients with α_{geom}=0° as datum; α_{geom}=6°, row 3.

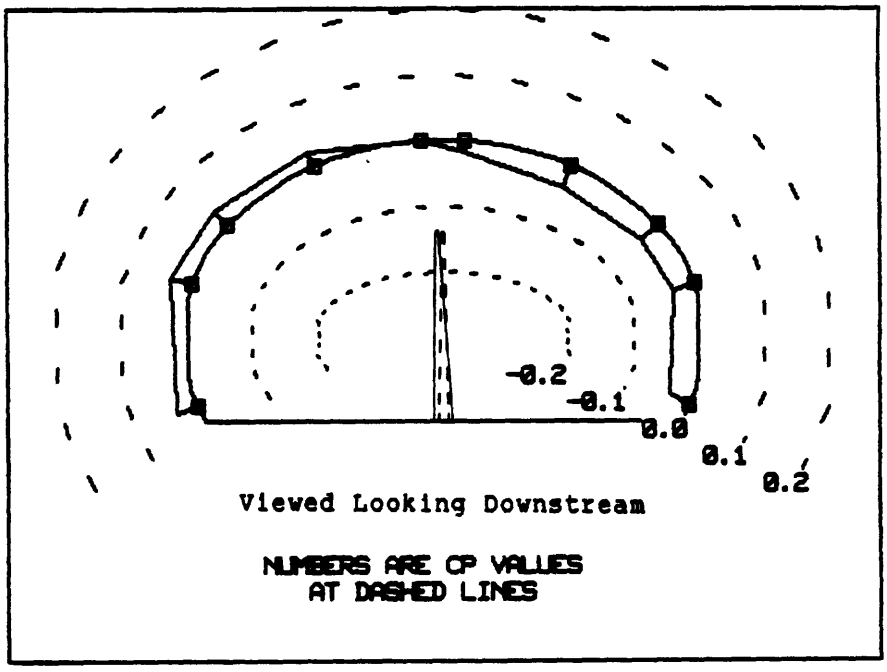

Figure B-114: Wall pressure coefficients with α_{geom}=0° as datum; α_{geom}=6°, row 4.

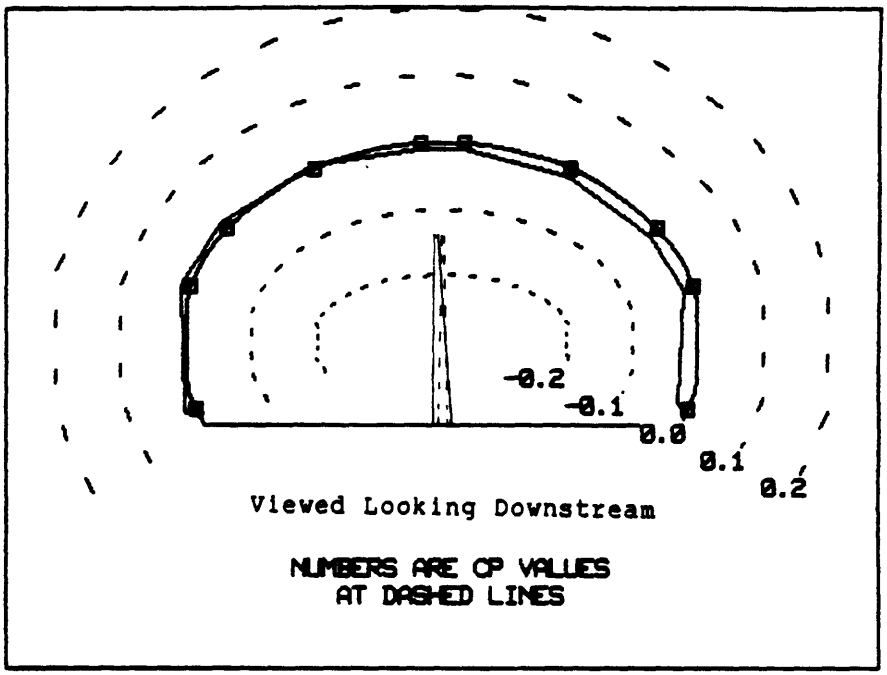

Figure B-115: Wall pressure coefficients with α_{geom}=0° as datum; α_{geom}=6°, row 5.

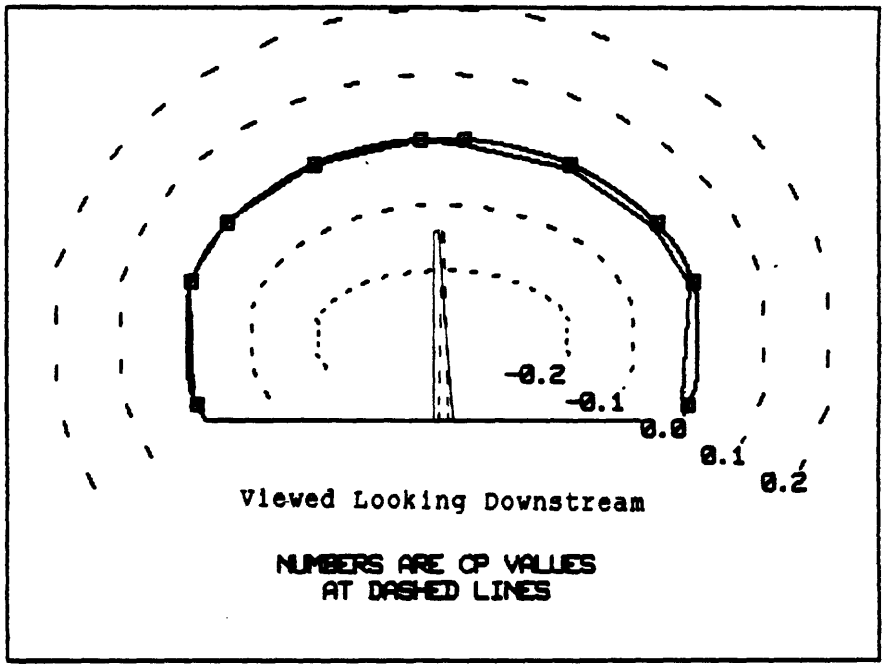

Figure B-116: Wall pressure coefficients with α_{geom}=0° as datum; α_{geom}=6°, row 6.

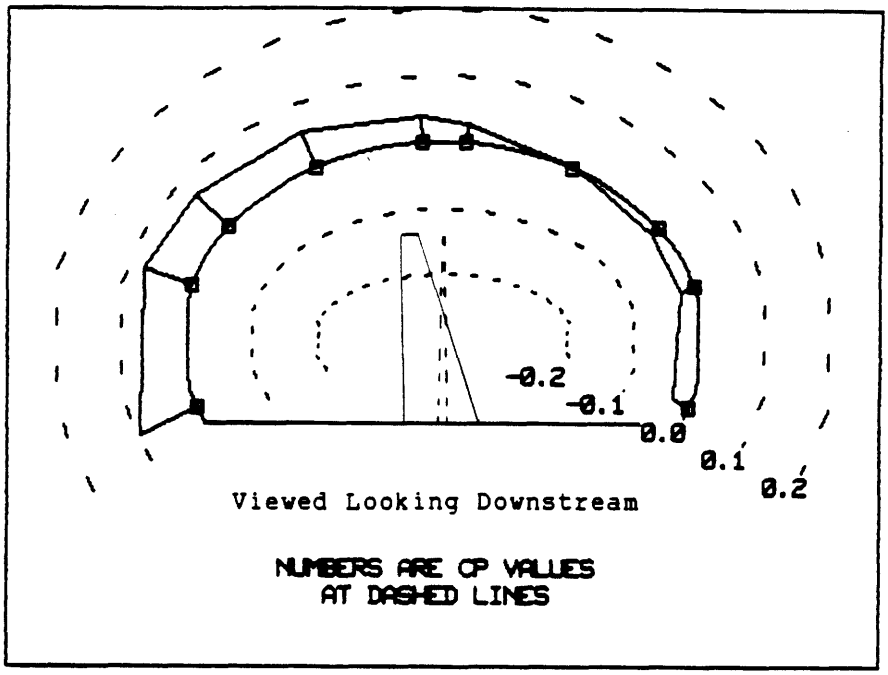

Figure B-117: Wall pressure coefficients with α_{geom}=0° as datum; α_{geom}=18°, row 1.

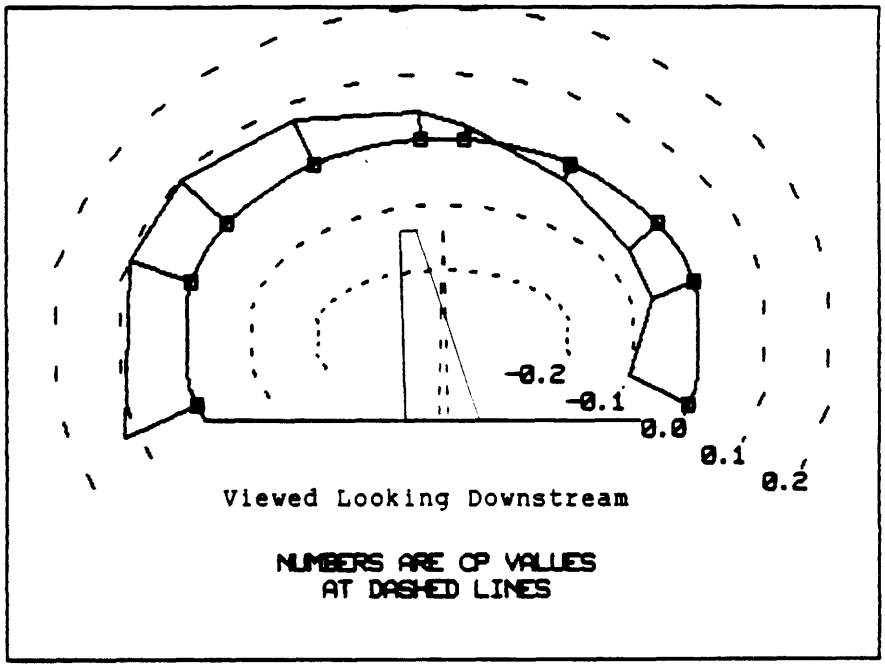

Figure B-118: Wall pressure coefficients with α_{geom}=0° as datum; α_{geom}=18°, row 2.

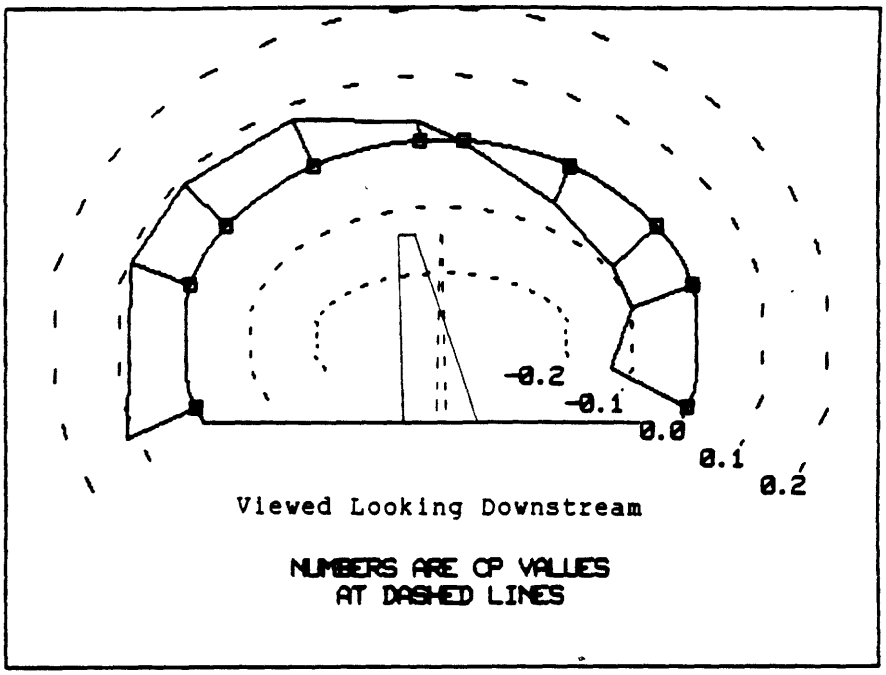

Figure B-119: Wall pressure coefficients with α_{geom}=0° as datum; α_{geom}=18°, row 3.

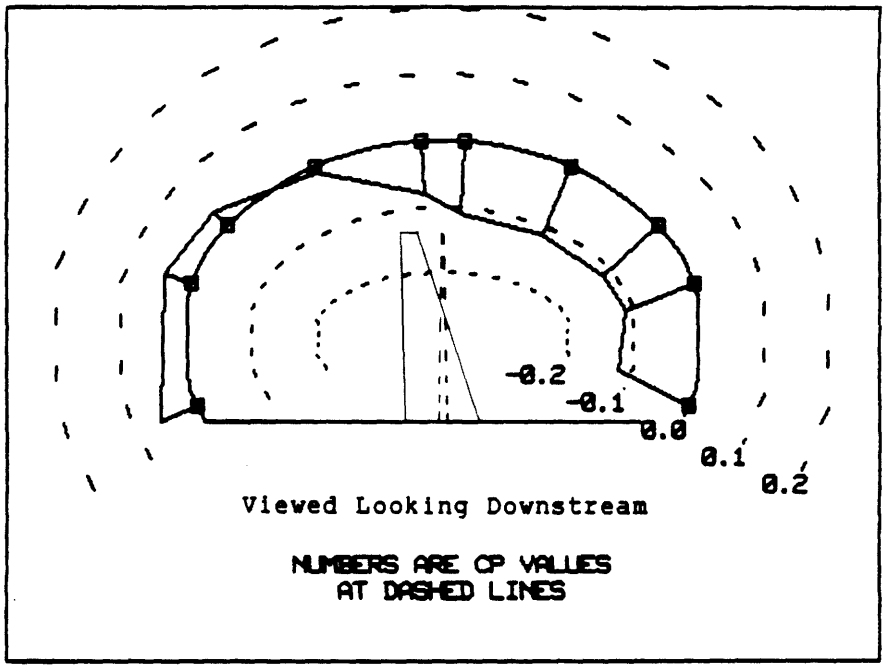

Figure B-120: Wall pressure coefficients with α_{geom}=0° as datum; α_{geom}=18°, row 4.

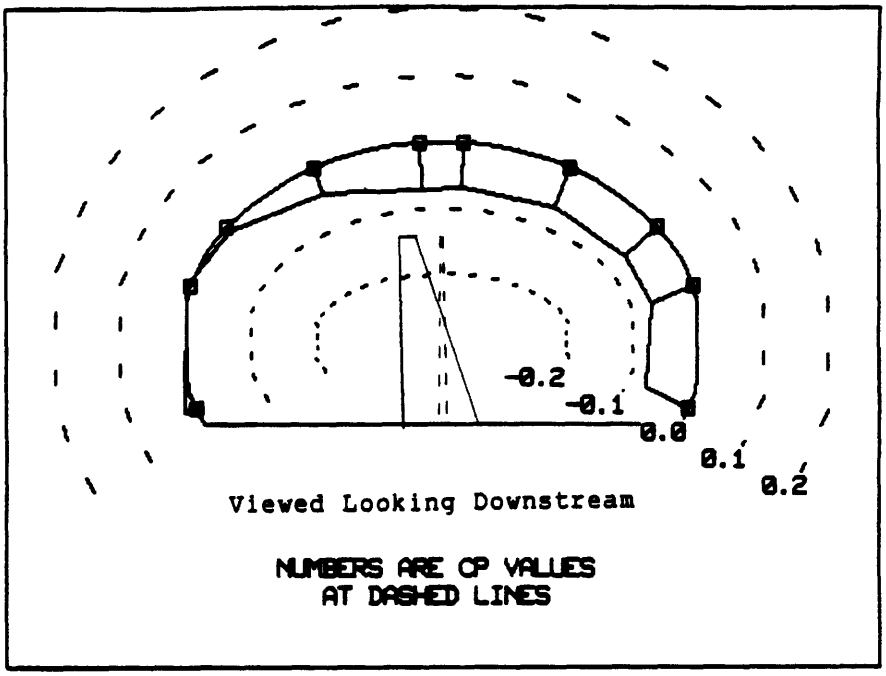

Figure B-121: Wall pressure coefficients with α_{geom}=0° as datum; α_{geom}=18°, row 5.

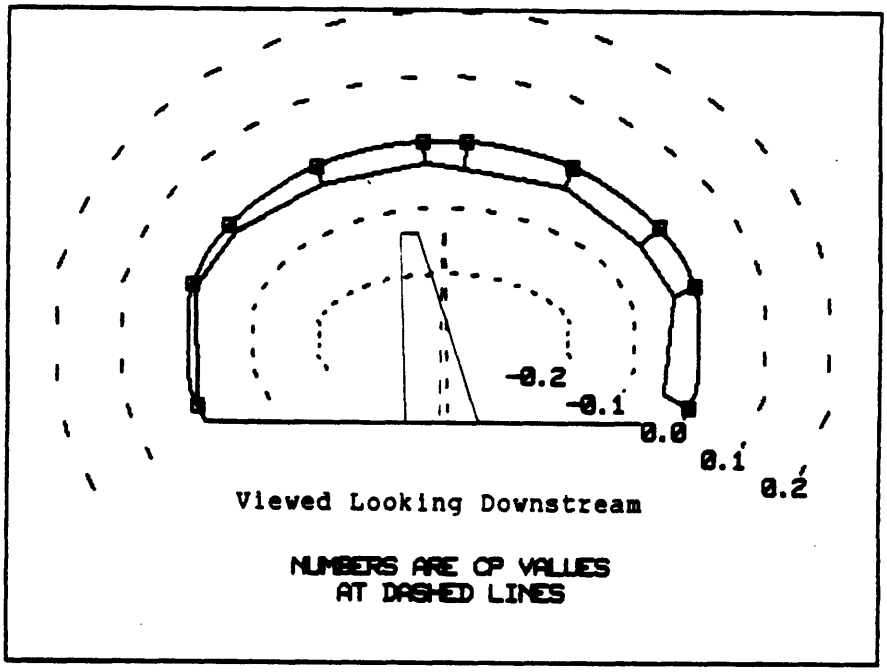

Figure B-122: Wall pressure coefficients with α_{geom}=0° as datum; α_{geom}=18°, row 6.

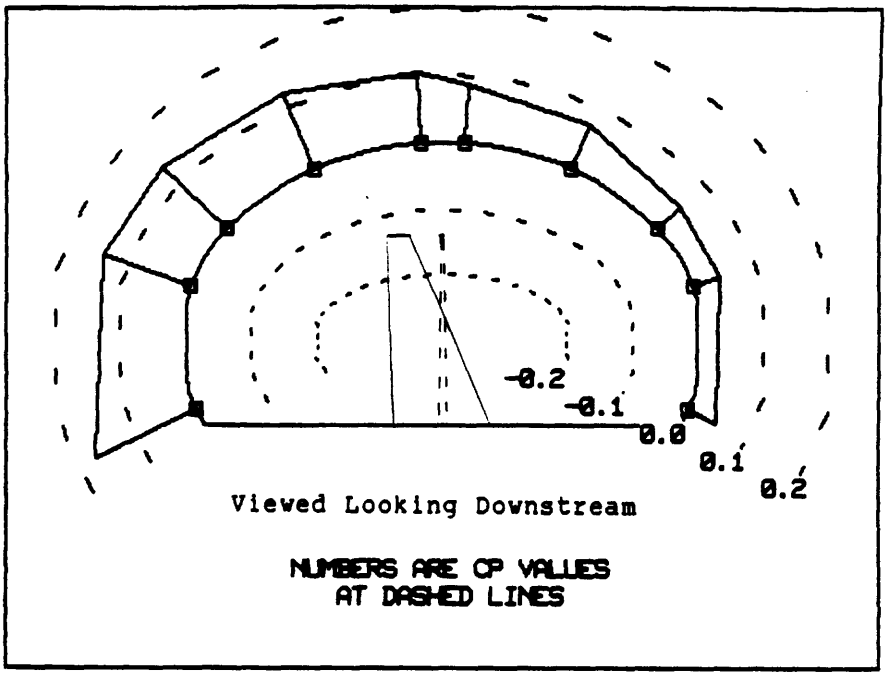

Figure B-123: Wall pressure coefficients with α_{geom}=0° as datum; α_{geom}=30°, row 1.

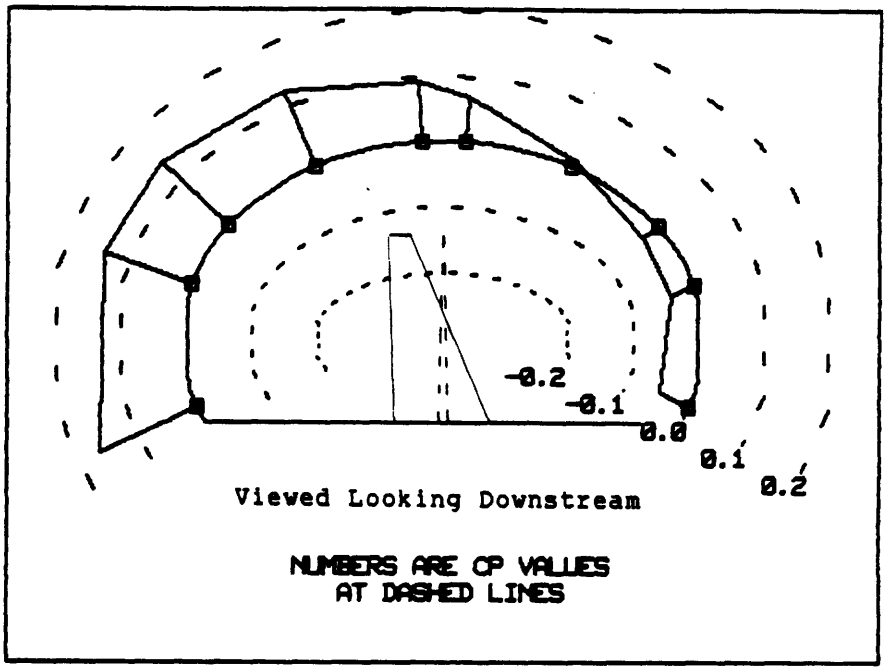

Figure B-124: Wall pressure coefficients with α_{geom}=0° as datum; α_{geom}=30°, row 2.

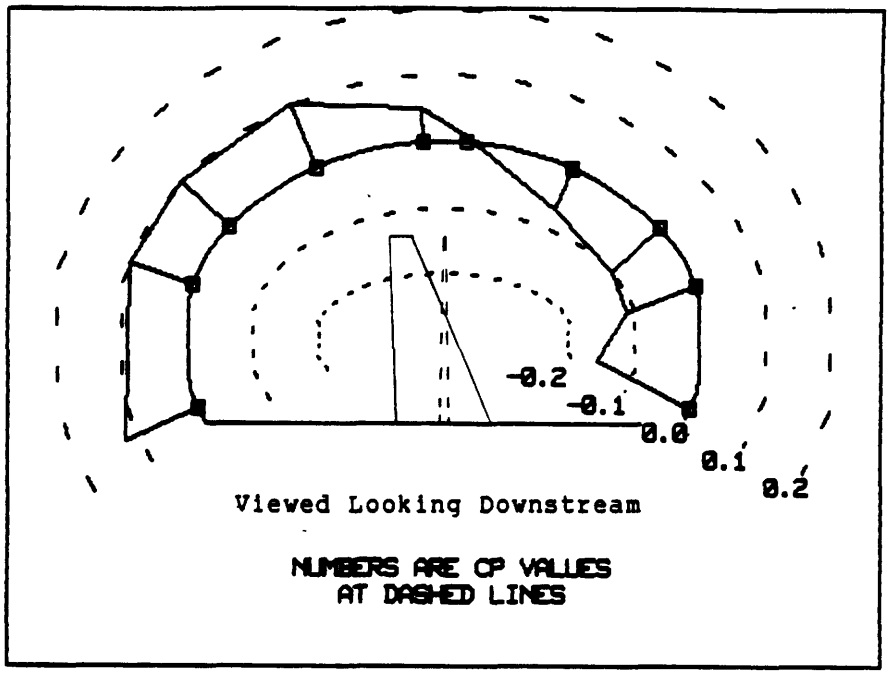

Figure B-125: Wall pressure coefficients with α_{geom}=0° as datum; α_{geom}=30°, row 3.

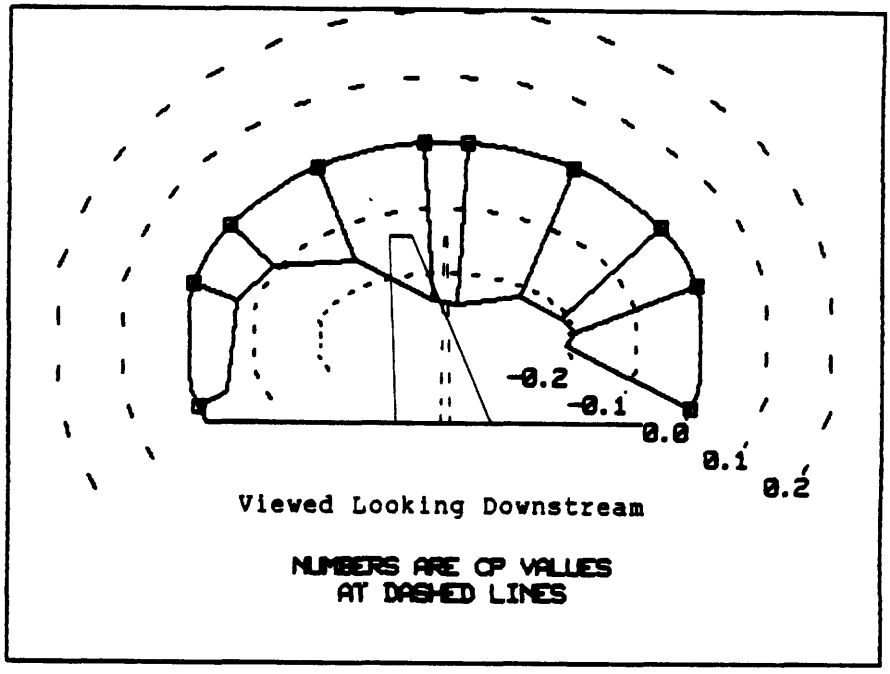

Figure B-126: Wall pressure coefficients with α_{geom}=0° as datum; α_{geom}=30°, row 4.

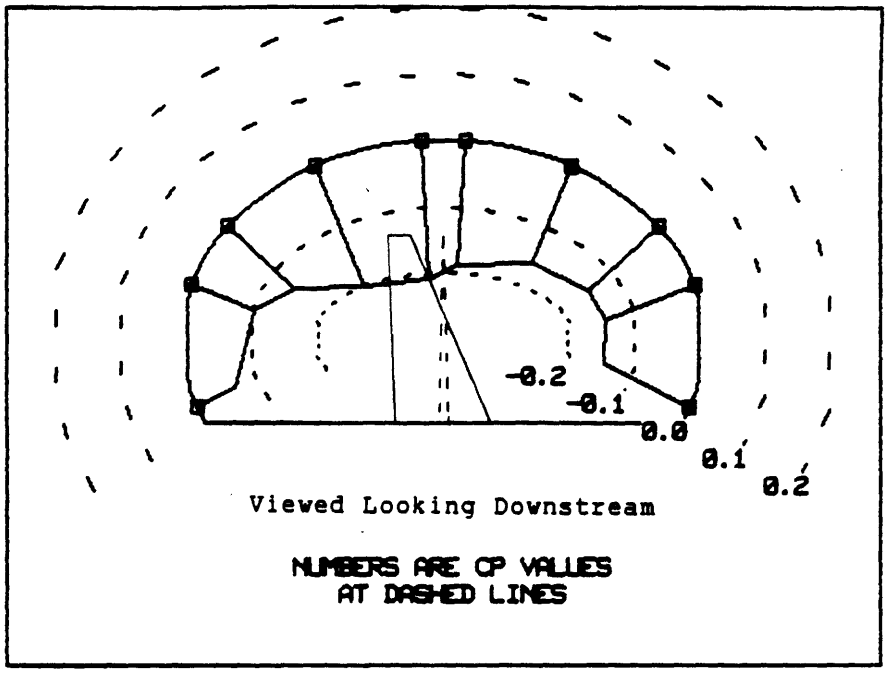

Figure B-127: Wall pressure coefficients with α_{geom}=0° as datum; α_{geom}=30°, row 5.

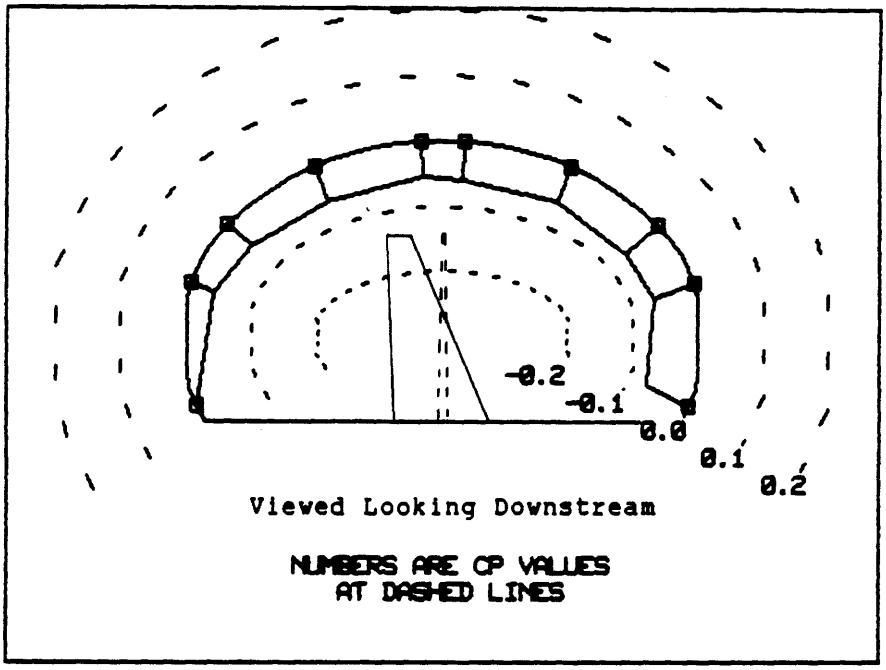

Figure B-128: Wall pressure coefficients with α_{geom}=0° as datum; α_{geom}=30°, row 6.

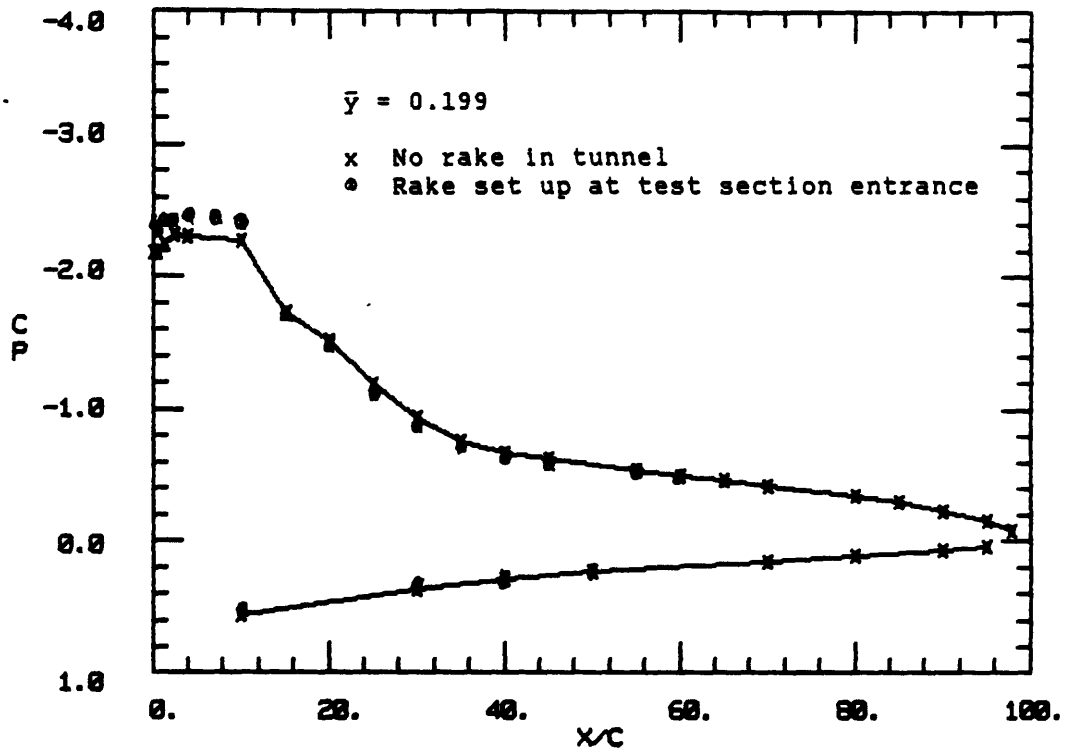

Figure B-129: Plot showing effect of rake wake on wing pressures.

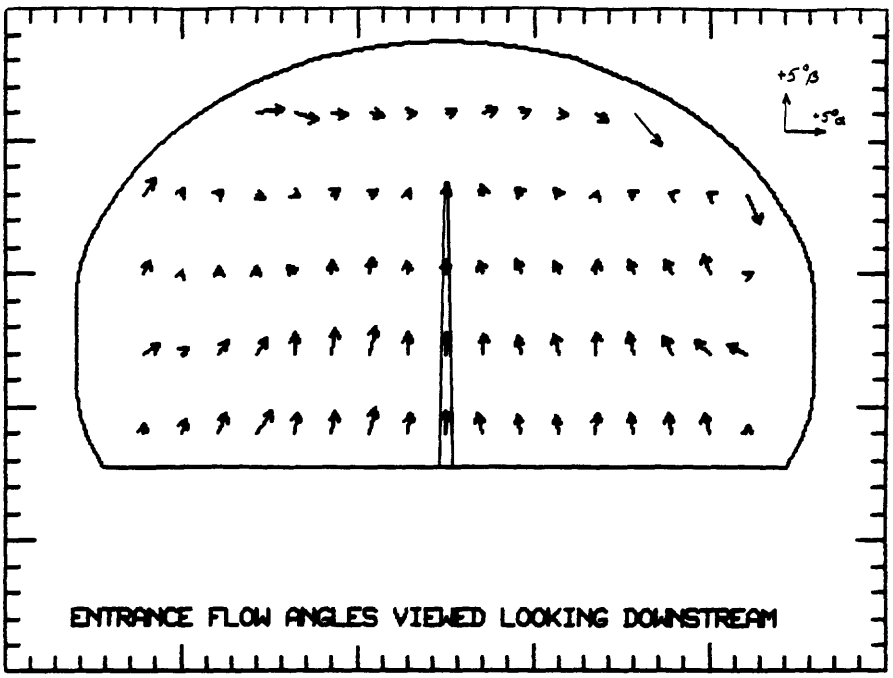

Figure B-130: Flow angle plot at test section entrance; $\alpha_{geom}=0°$, $\delta_{le}=\delta_{te}=0°$.

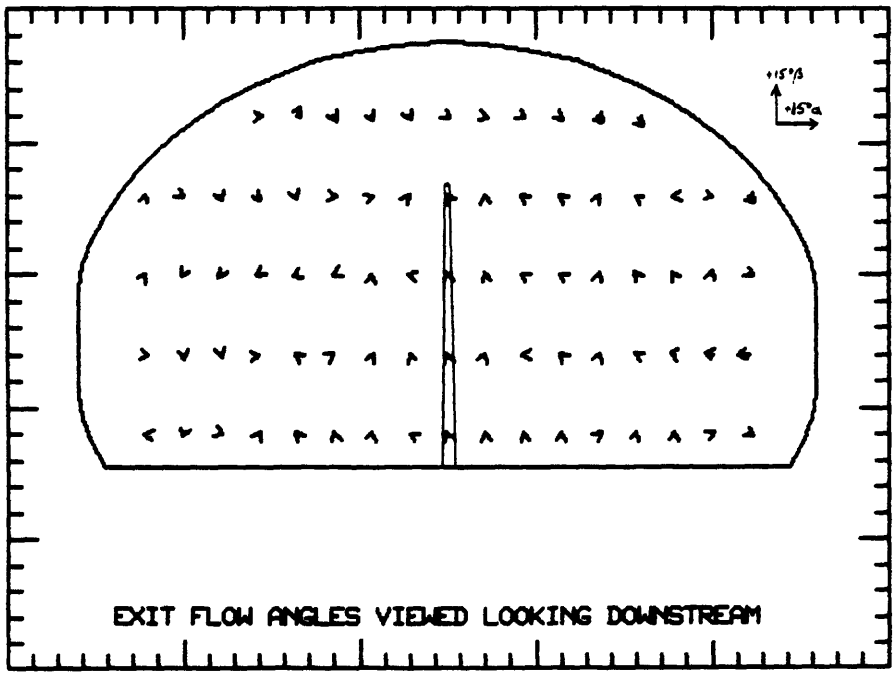

Figure B-131: Flow angle plot at test section exit; $\alpha_{geom}=0°$, $\delta_{le}=\delta_{te}=0°$.

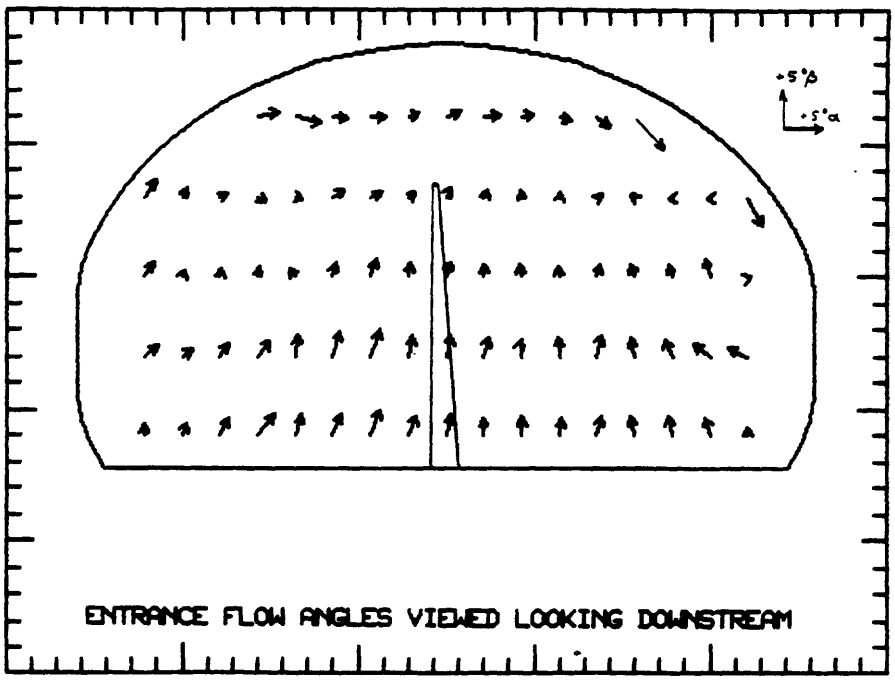

Figure B-132: Flow angle plot at test section entrance; α_{geom}=6°, δ_{le}=δ_{te}=0°.

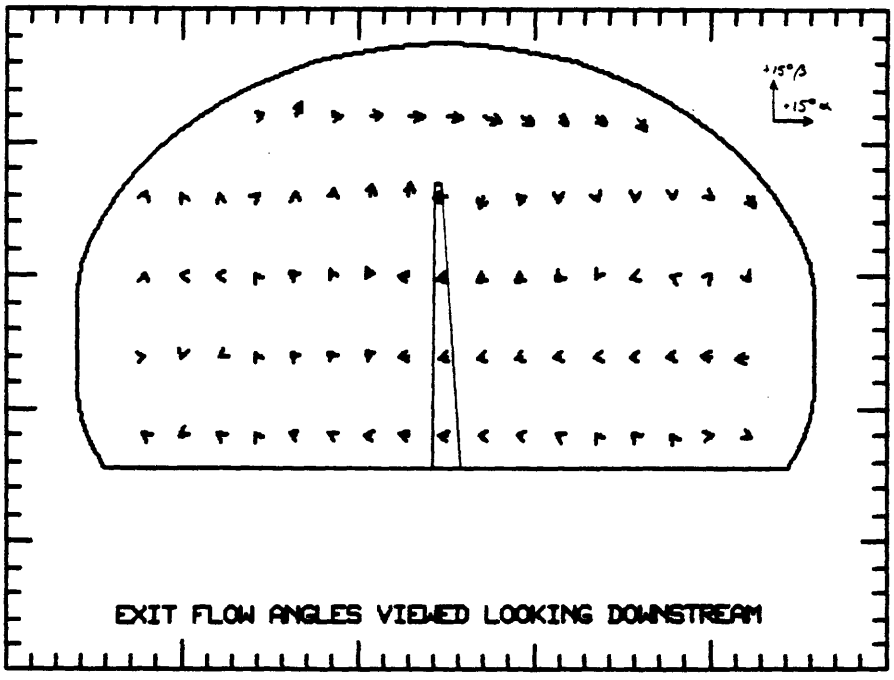

Figure B-133: Flow angle plot at test section exit; α_{geom}=6°, δ_{le}=δ_{te}=0°.

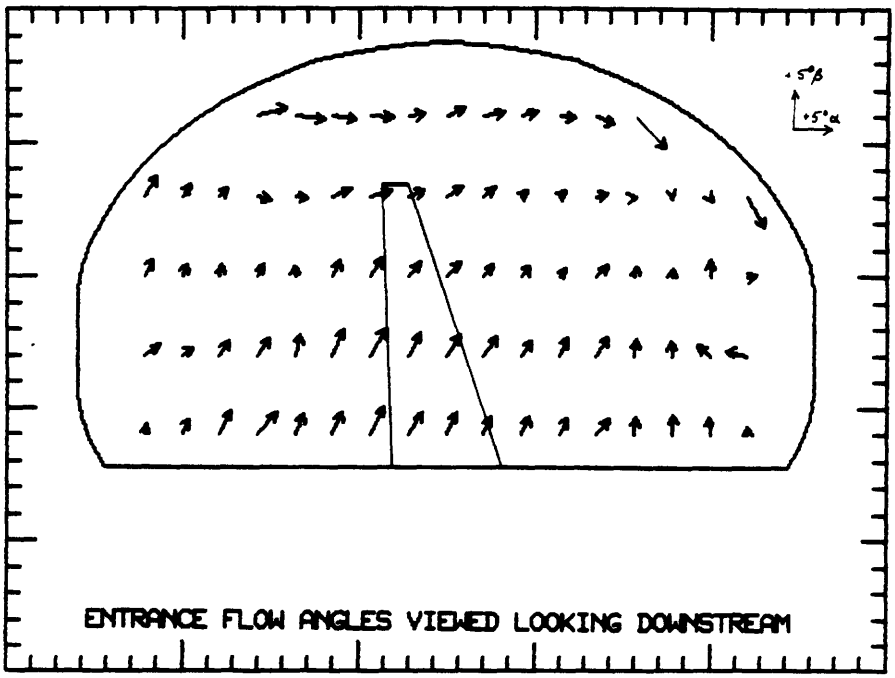

Figure B-134: Flow angle plot at test section entrance; α_{geom}=18°, δ_{le}=δ_{te}=0°.

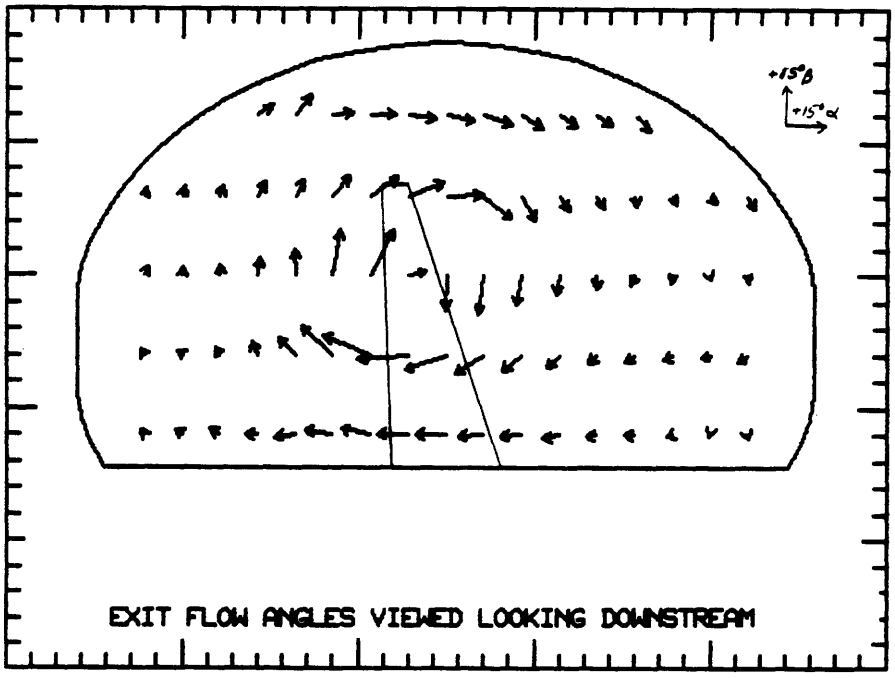

Figure B-135: Flow angle plot at test section exit; α_{geom}=18°, δ_{le}=δ_{te}=0°.

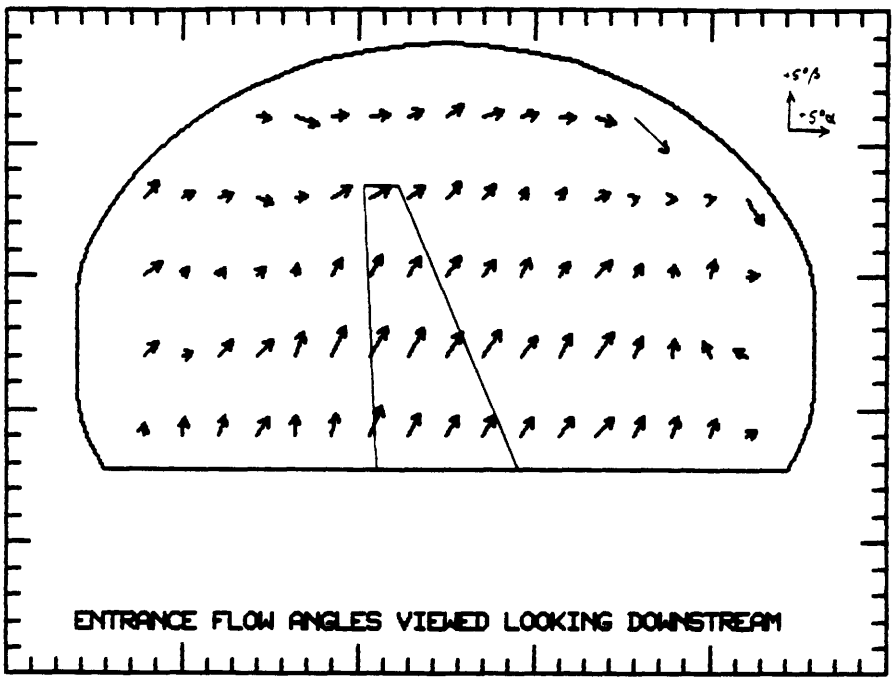

Figure B-136: Flow angle plot at test section entrance; α_{geom}=30°, δ_{le}=δ_{te}=0°.

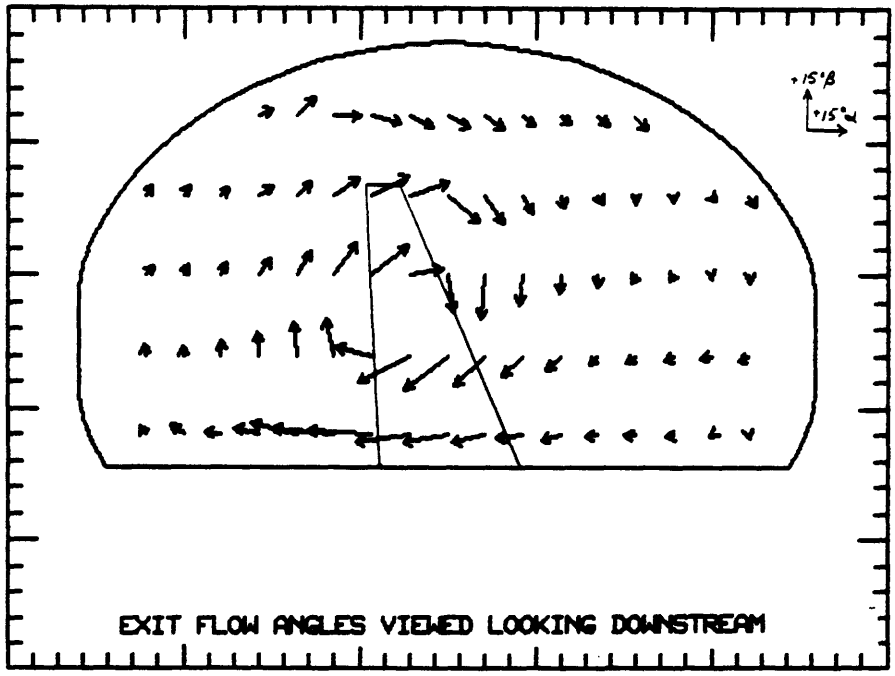

Figure B-137: Flow angle plot at test section exit; α_{geom}=30°, δ_{le}=δ_{te}=0°.

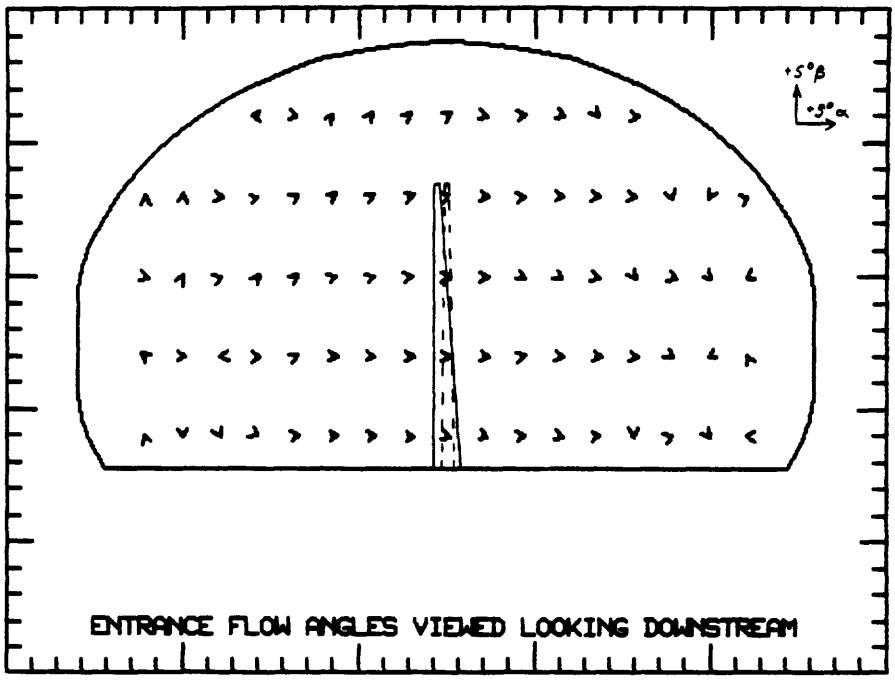

Figure B-138: Flow angle plot at entrance with α_{geom}=0° as datum; α_{geom}=6°.

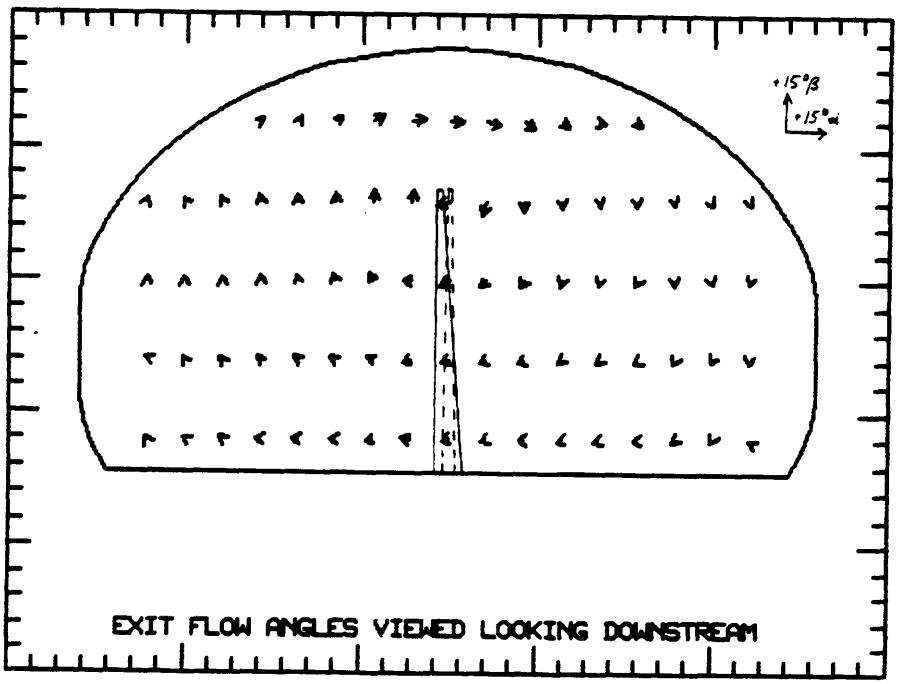

Figure B-139: Flow angle plot at exit with α_{geom}=0° as datum; α_{geom}=6°.

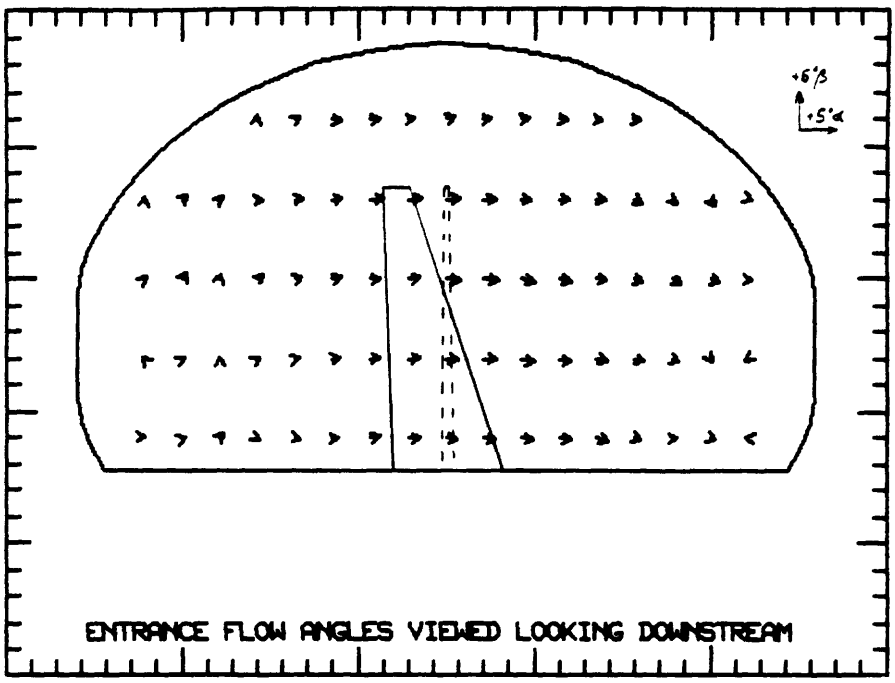

Figure B-140: Flow angle plot at entrance with α_{geom}=0° as datum; α_{geom}=18°.

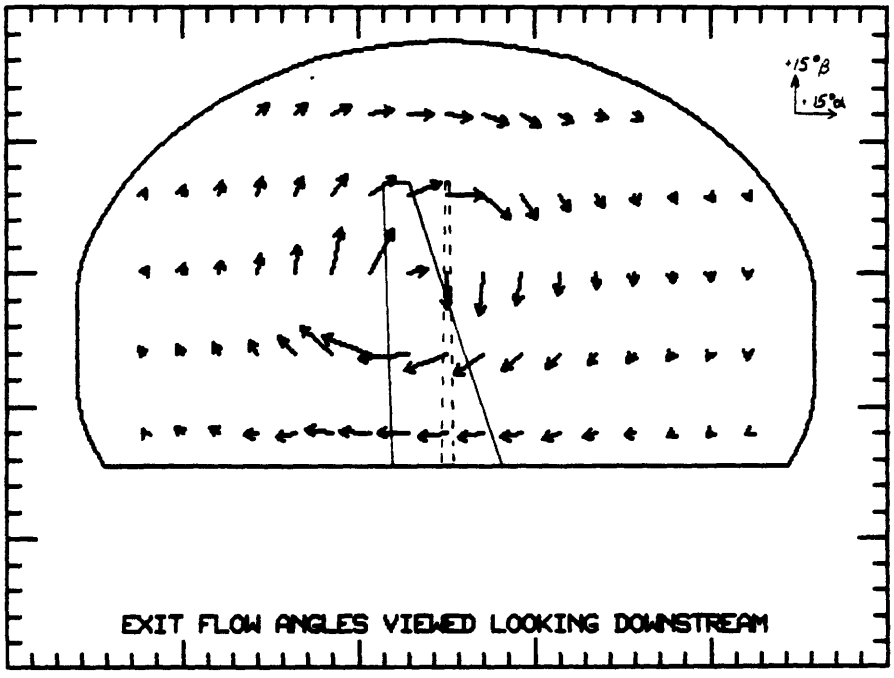

Figure B-141: Flow angle plot at exit with α_{geom}=0° as datum; α_{geom}=18°.

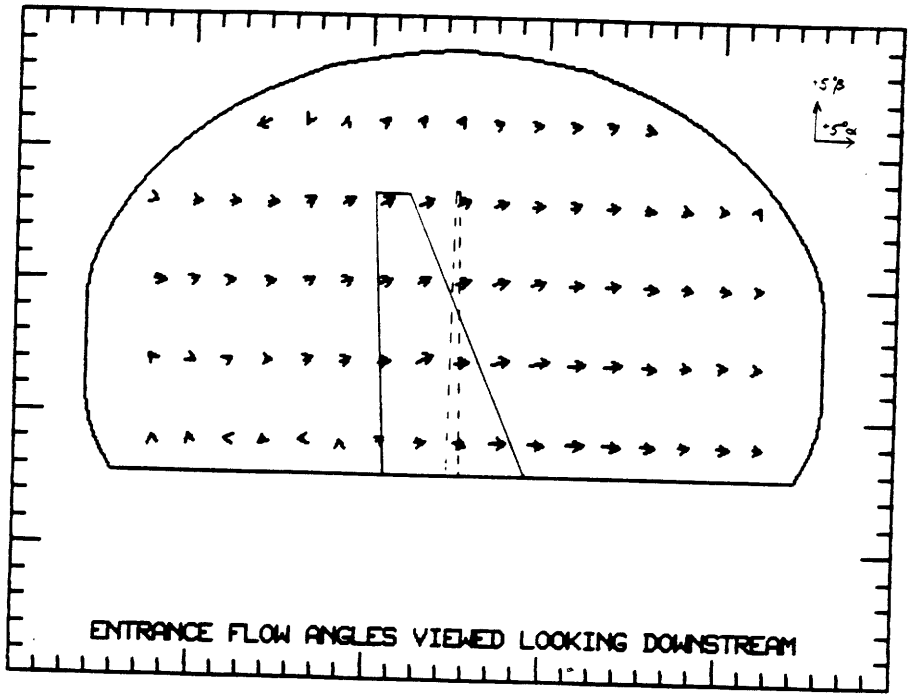

Figure B-142: Flow angle plot at entrance with α_{geom}=0° as datum; α_{geom}=30°.

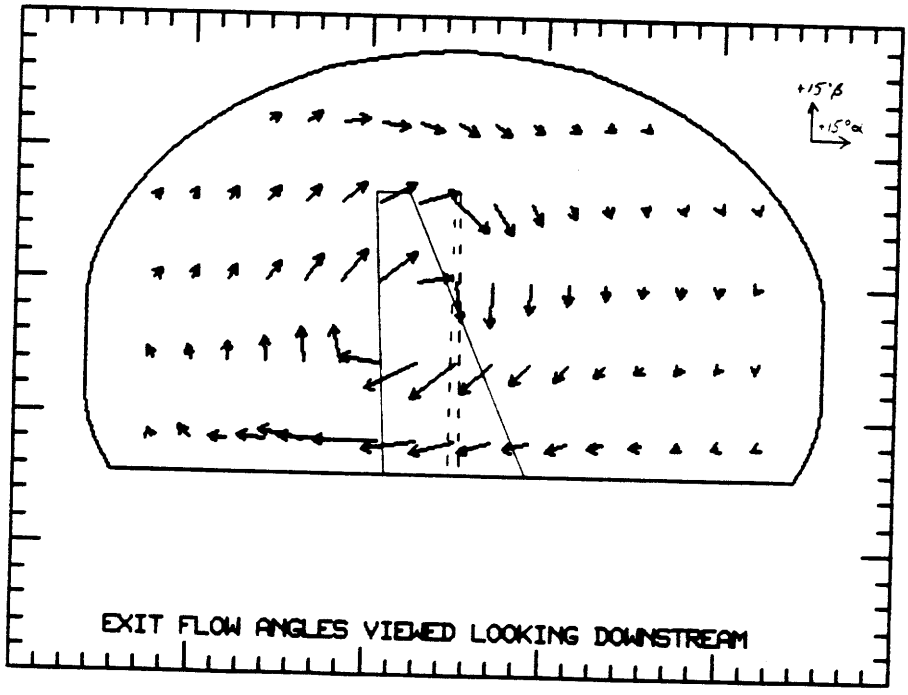

Figure B-143: Flow angle plot at exit with α_{geom}=0° as datum; α_{geom}=30°.

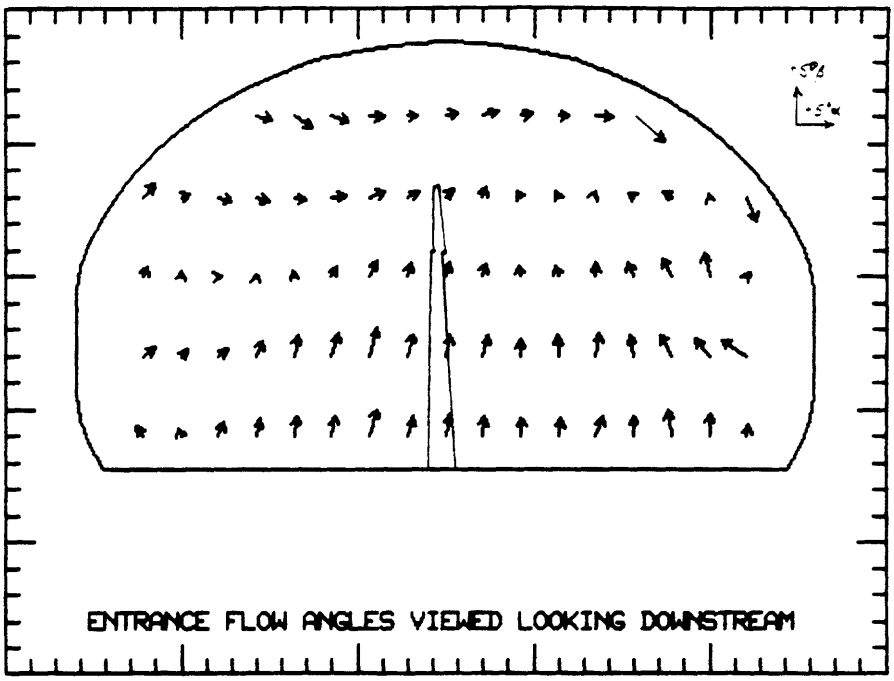

Figure B-144: Flow angle plot at test section entrance; α_{geom}=6°, δ_{le}=δ_{te}=10°.

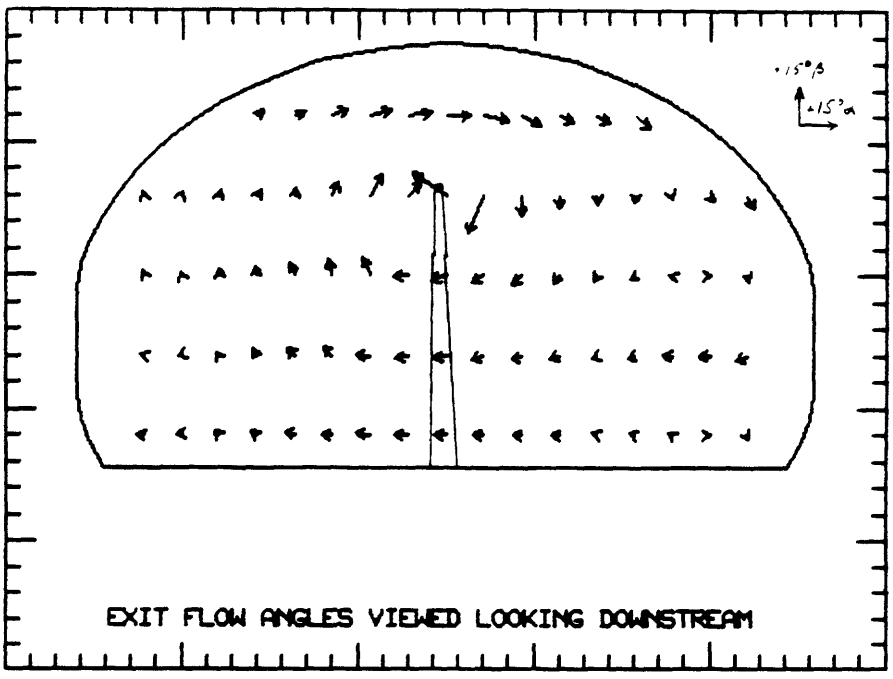

Figure B-145: Flow angle plot at test section exit; α_{geom}=6°, δ_{le}=δ_{te}=10°.

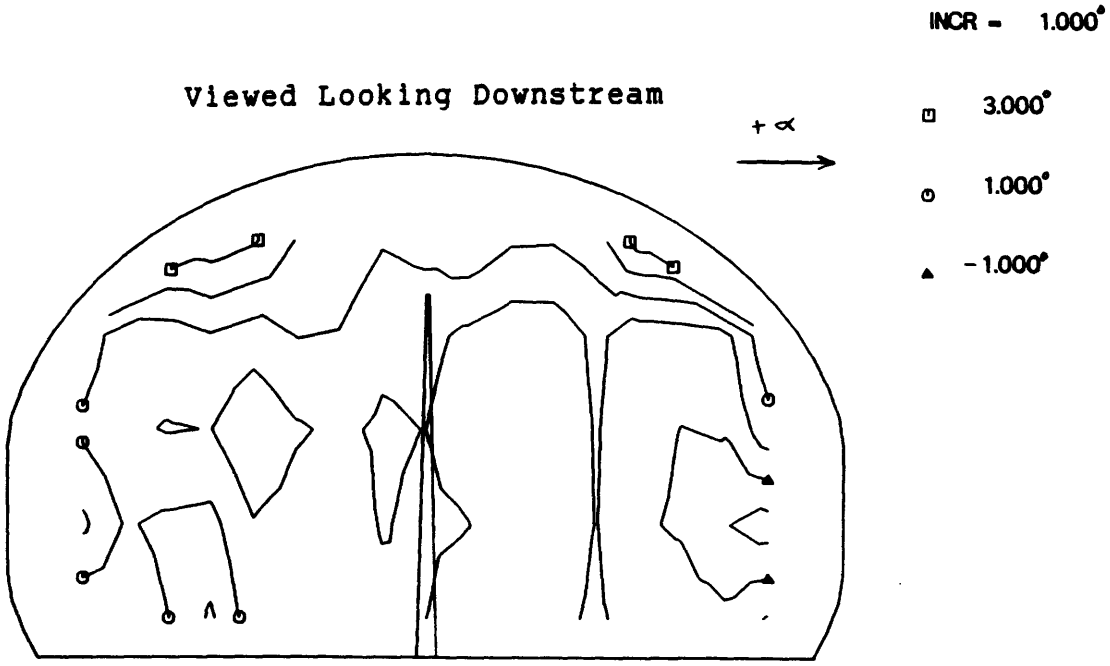

Figure B-146: Pitch angle contours at test section entrance; α_{geom}=0°, δ_{le}=δ_{te}=0°.

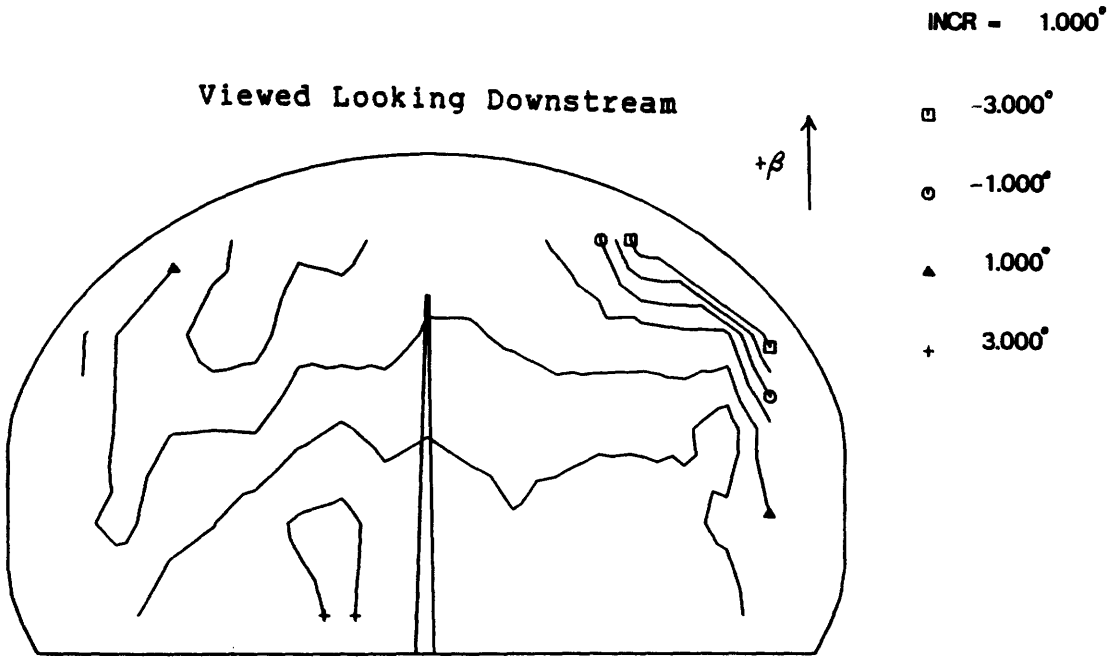

Figure B-147: Yaw angle contours at test section entrance; α_{geom}=0°, δ_{le}=δ_{te}=0°.

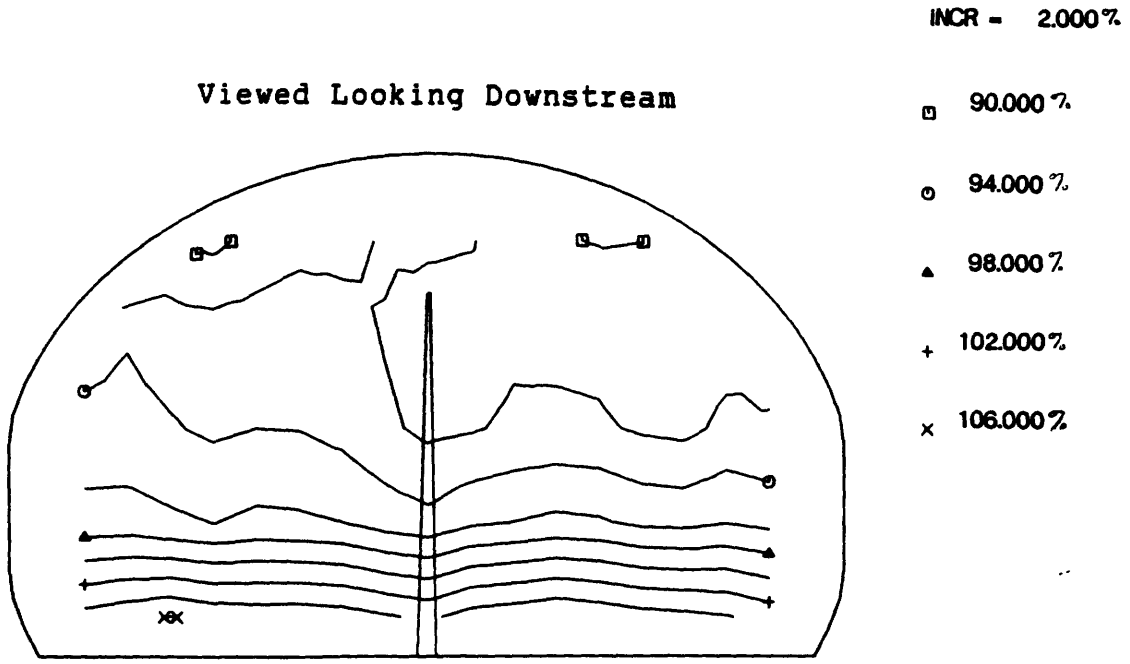

Figure B-148: Dynamic pressure contours at test section entrance; $\alpha_{geom}=0°$, $\delta_{le}=\delta_{te}=0°$.

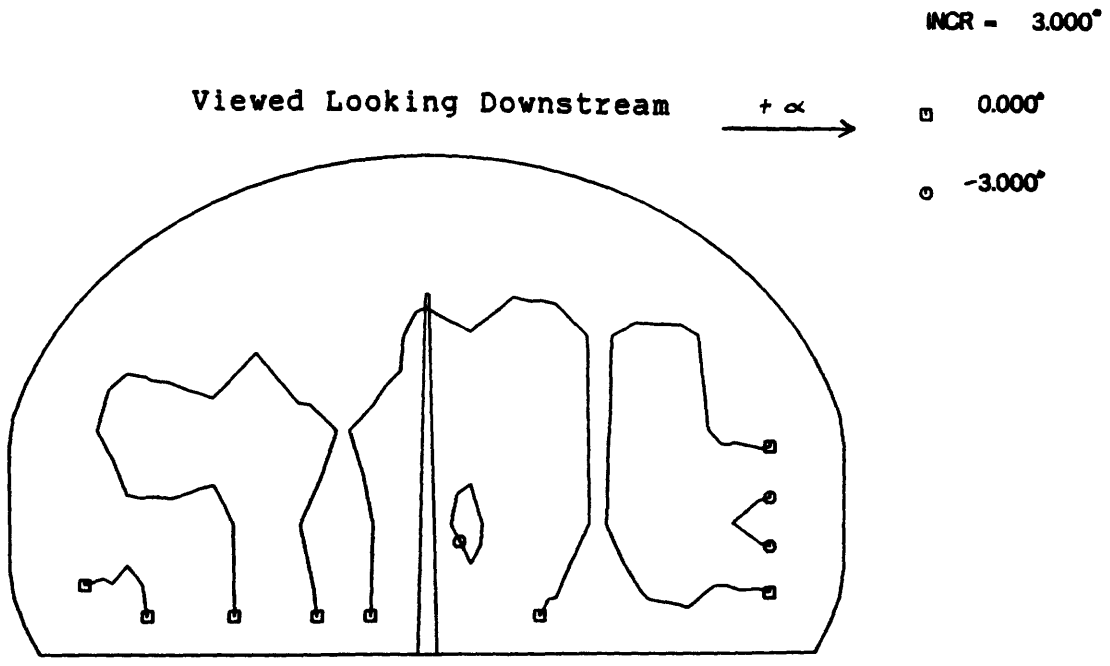

Figure B-149: Pitch angle contours at test section exit; $\alpha_{geom}=0°$, $\delta_{le}=\delta_{te}=0°$.

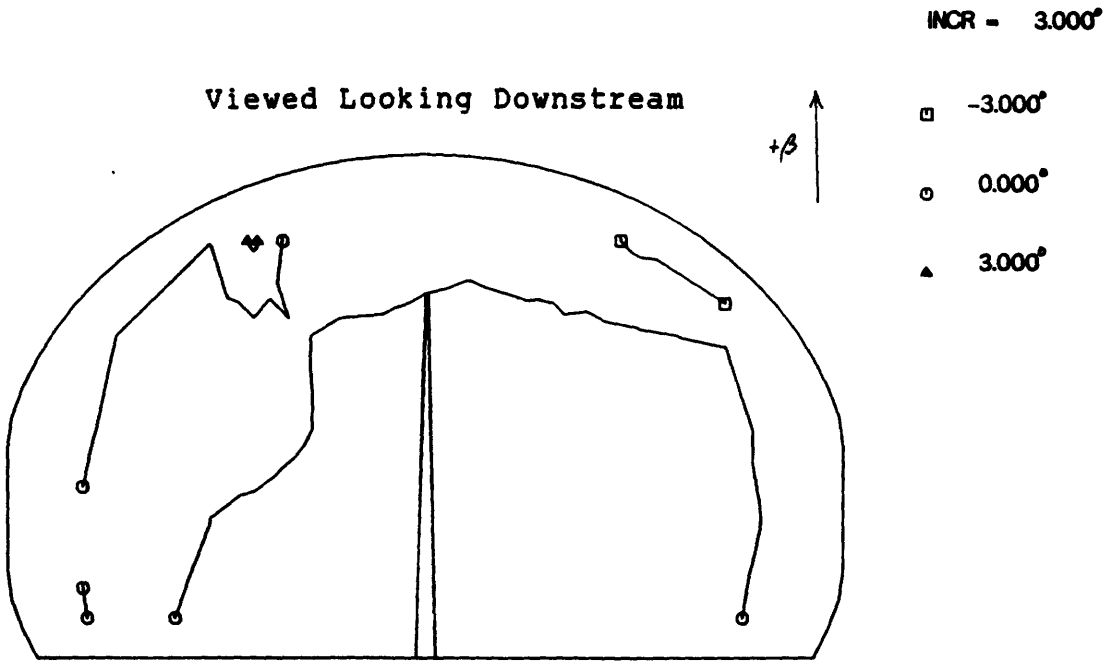

Figure B-150: Yaw angle contours at test section exit; α_{geom}=0°, δ_{le}=δ_{te}=0°.

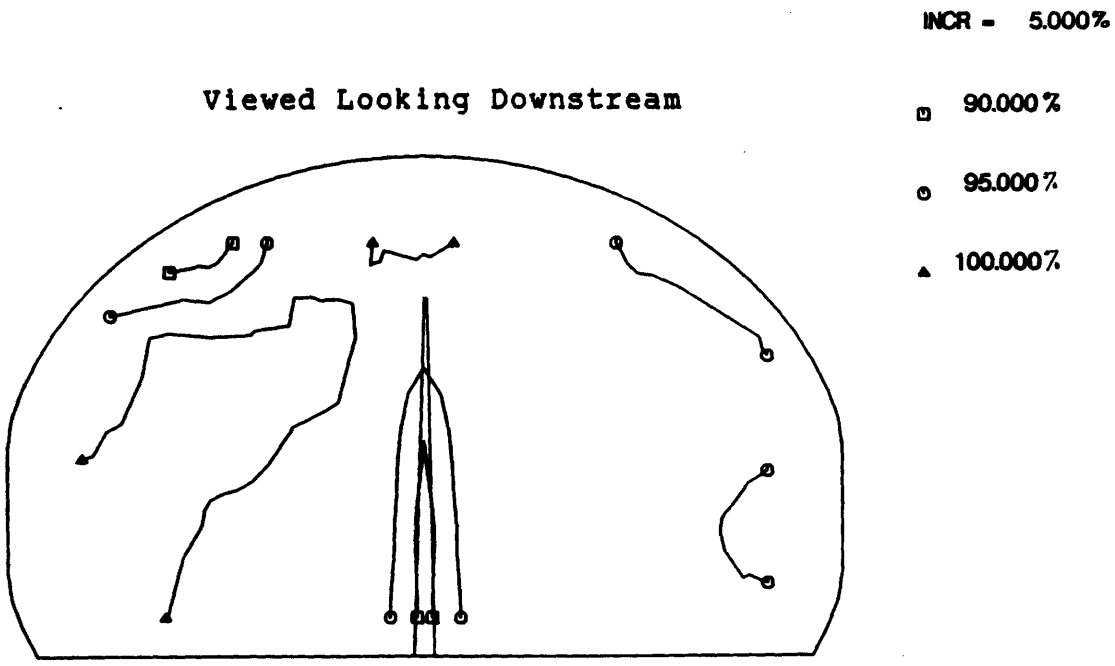

Figure B-151: Dynamic pressure contours at test section exit; α_{geom}=0°, δ_{le}=δ_{te}=0°.

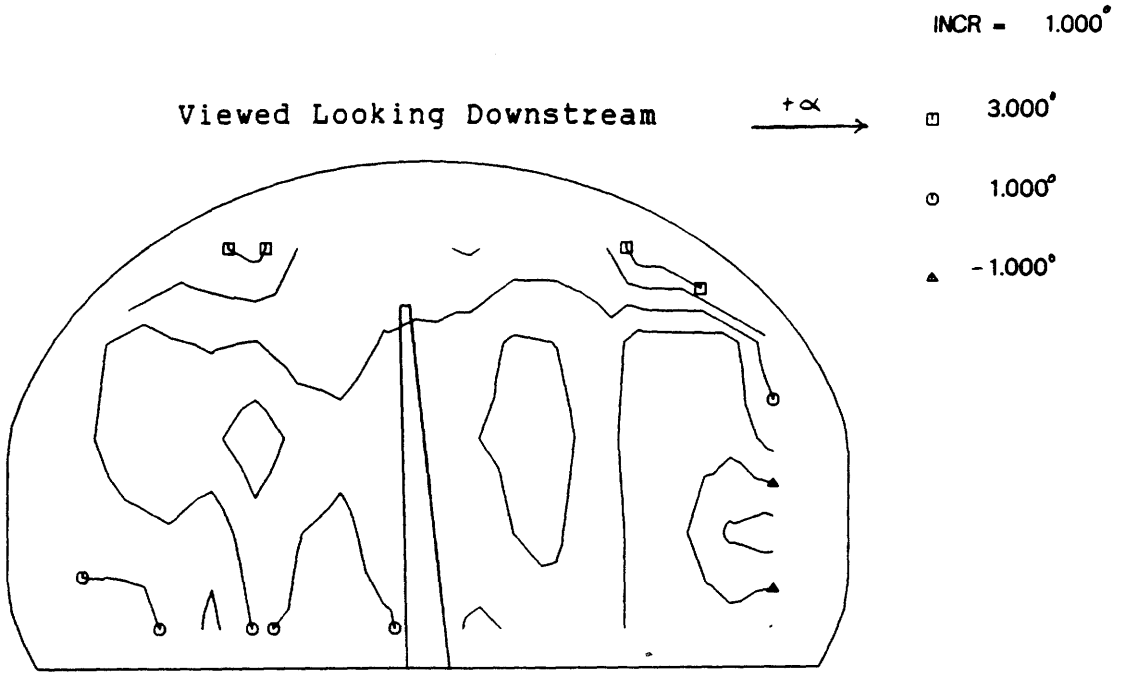

Figure B-152: Pitch angle contours at test section entrance; α_{geom}=6°, δ_{le}=δ_{te}=0°.

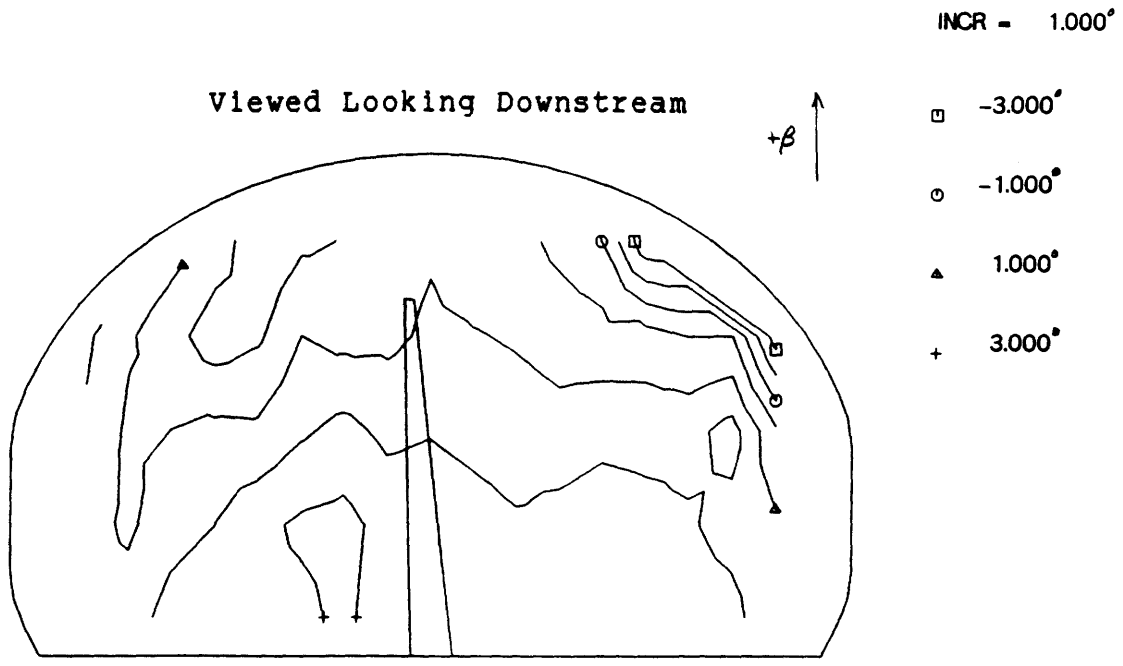

Figure B-153: Yaw angle contours at test section entrance; α_{geom}=6°, δ_{le}=δ_{te}=0°.

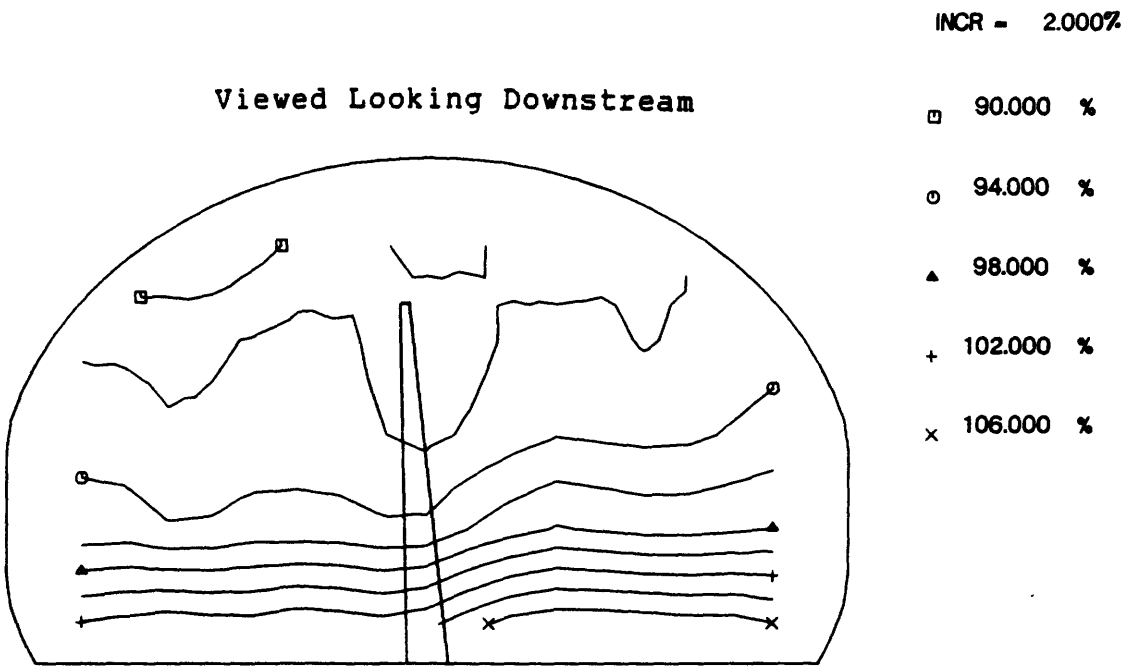

Figure B-154: Dynamic pressure contours at test section entrance; α_{geom}=6°, δ_{le}=δ_{te}=0°.

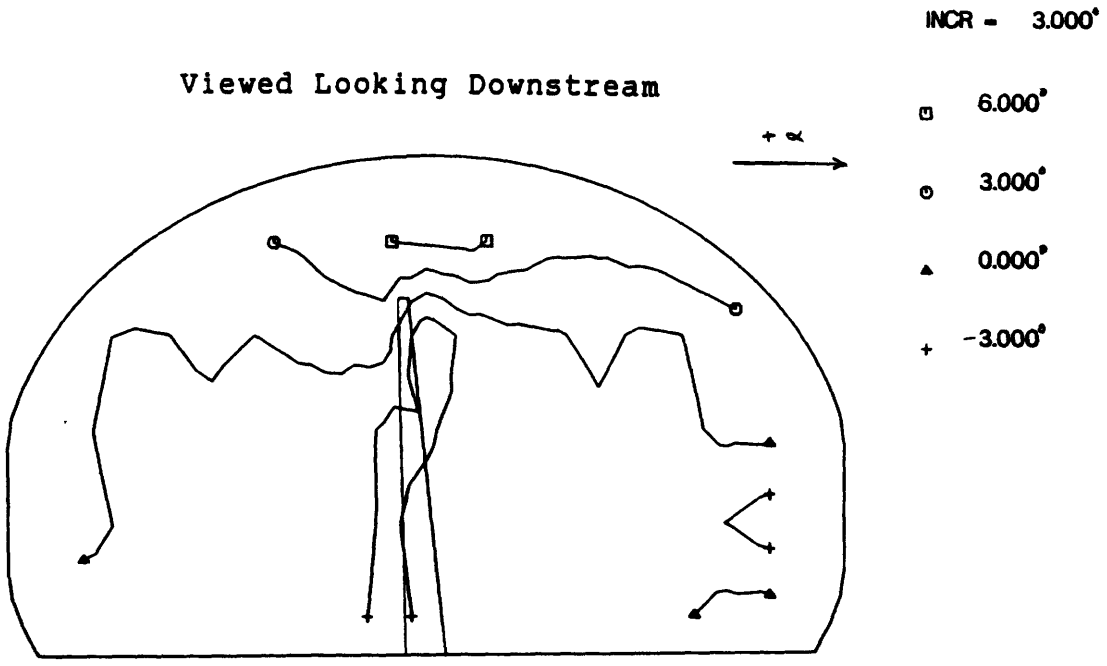

Figure B-155: Pitch angle contours at test section exit; α_{geom}=6°, δ_{le}=δ_{te}=0°.

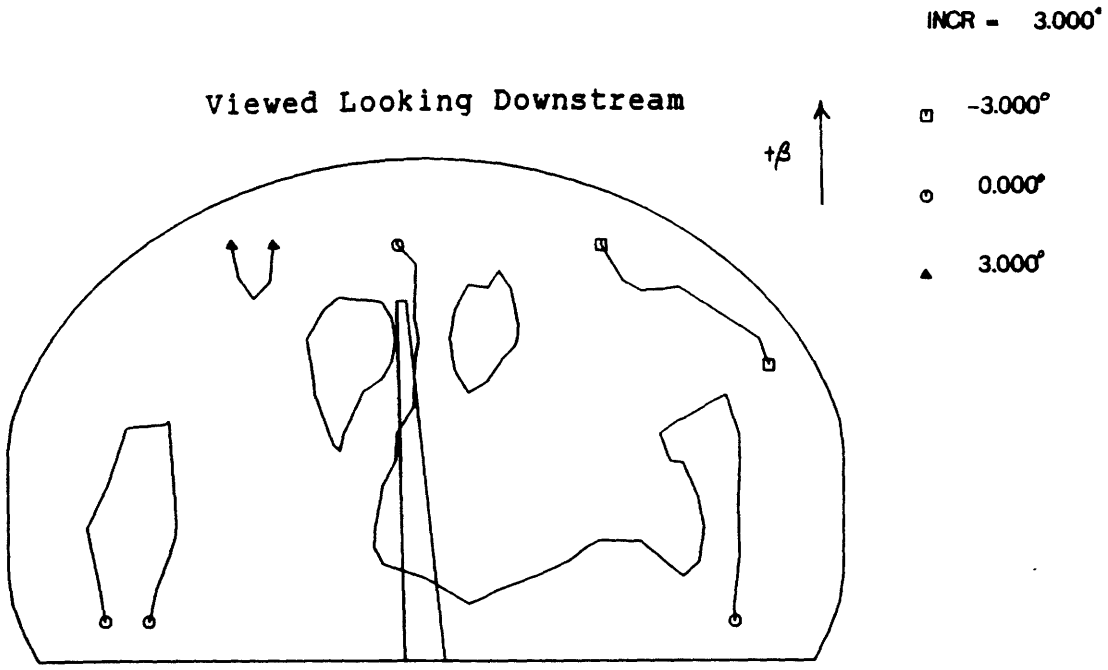

Figure B-156: Yaw angle contours at test section exit; α_{geom}=6°, δ_{le}=δ_{te}=0°.

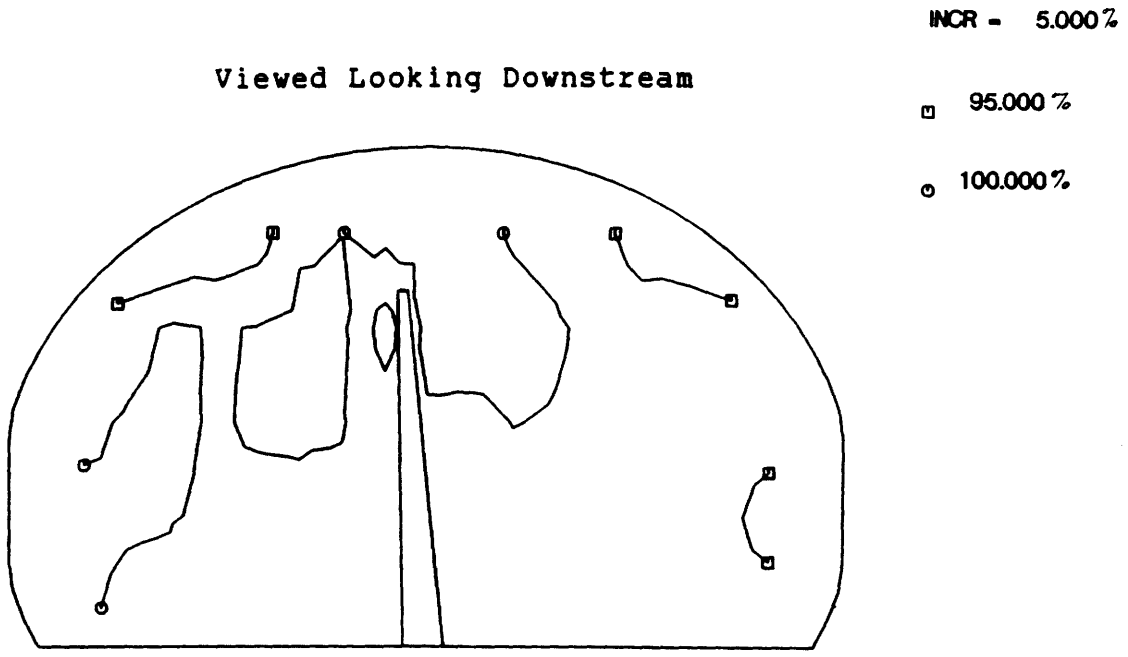

Figure B-157: Dynamic pressure contours at test section exit; α_{geom}=6°, δ_{le}=δ_{te}=0°.

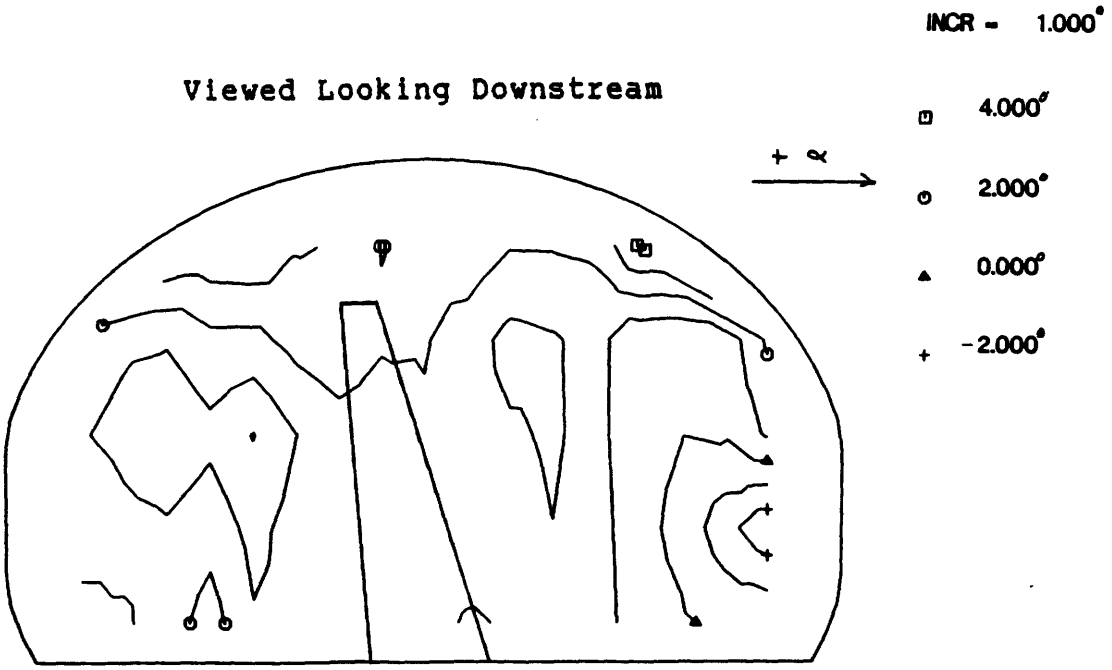

Figure B-158: Pitch angle contours at test section entrance; α_{geom}=18°, δ_{le}=δ_{te}=0°.

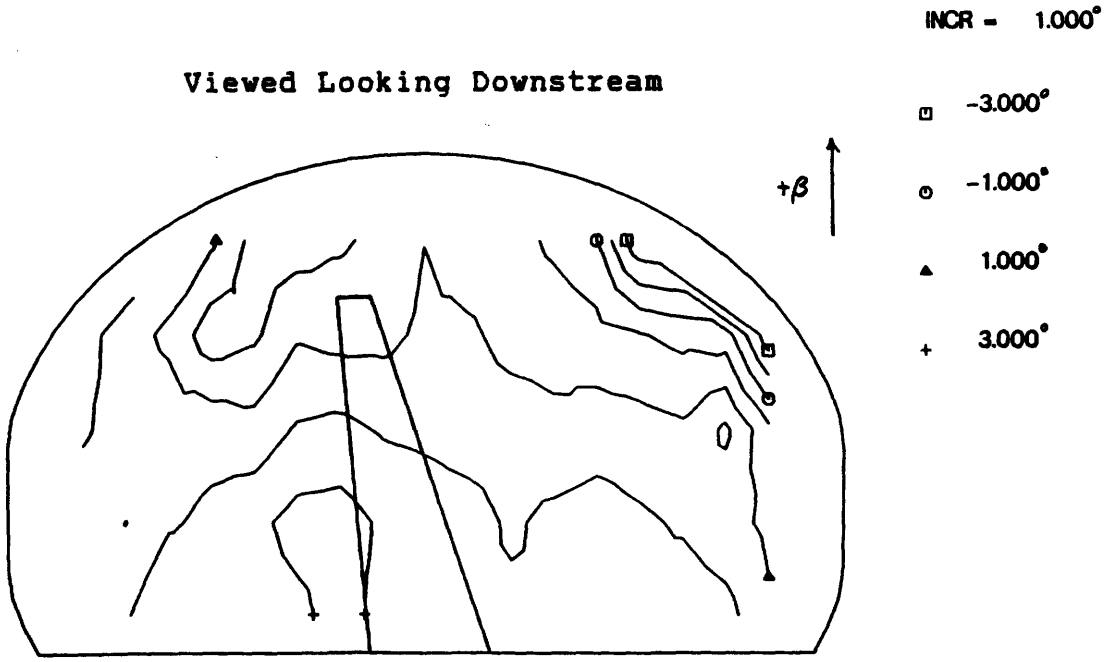

Figure B-159: Yaw angle contours at test section entrance; α_{geom}=18°, δ_{le}=δ_{te}=0°.

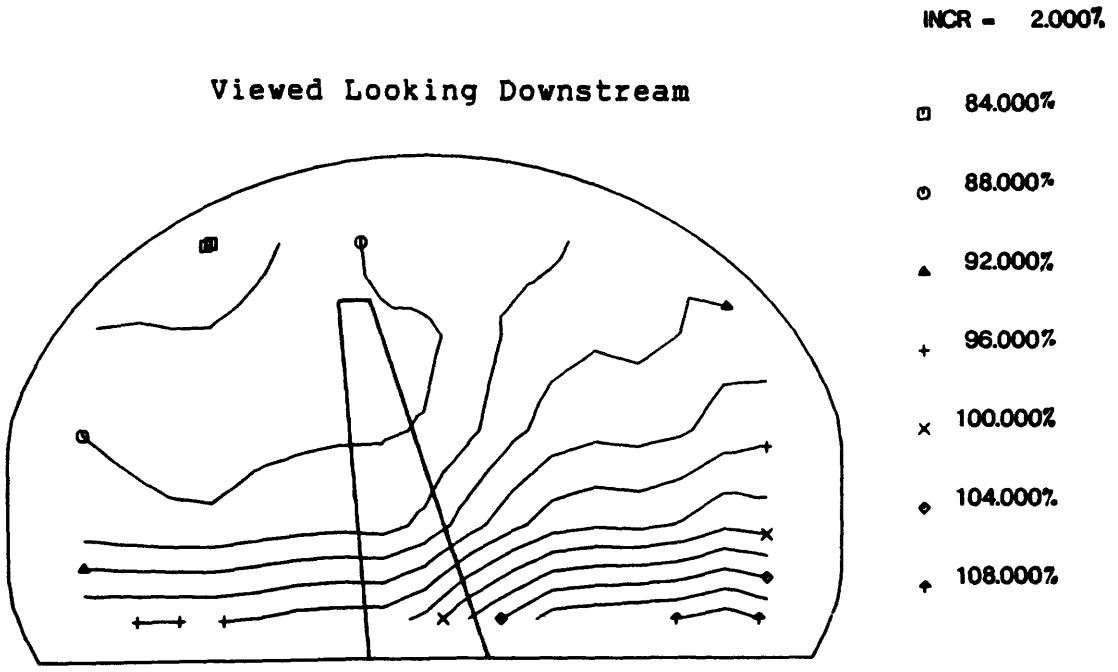

Figure B-160: Dynamic pressure contours at test section entrance; α_{geom}=18°, δ_{le}=δ_{te}=0°.

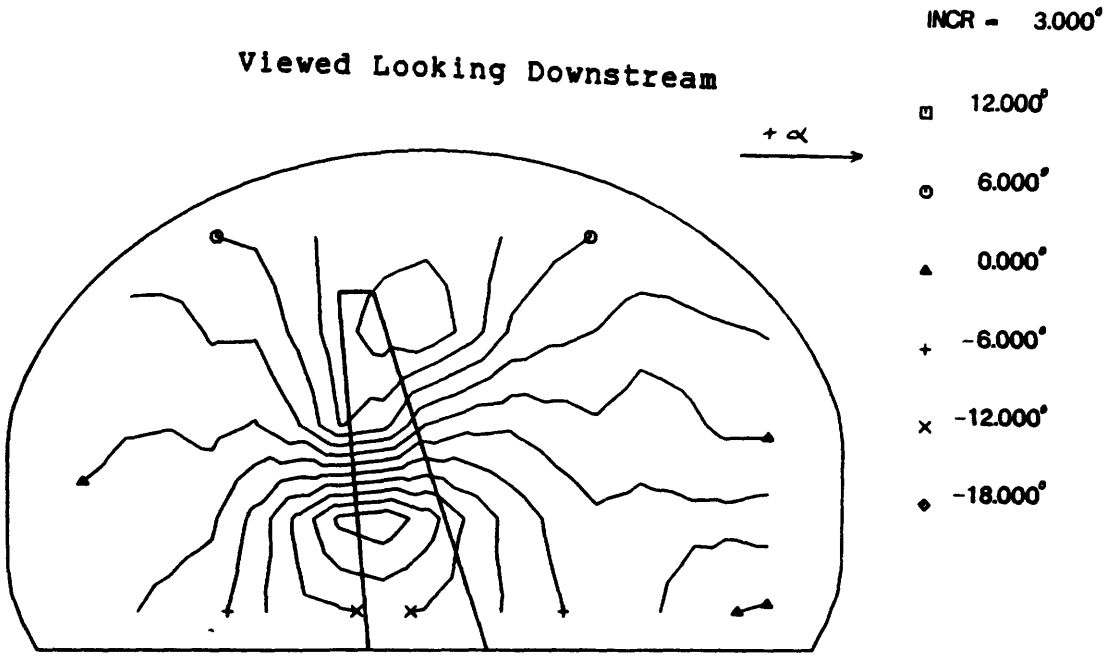

Figure B-161: Pitch angle contours at test section exit; α_{geom}=18°, δ_{le}=δ_{te}=0°.

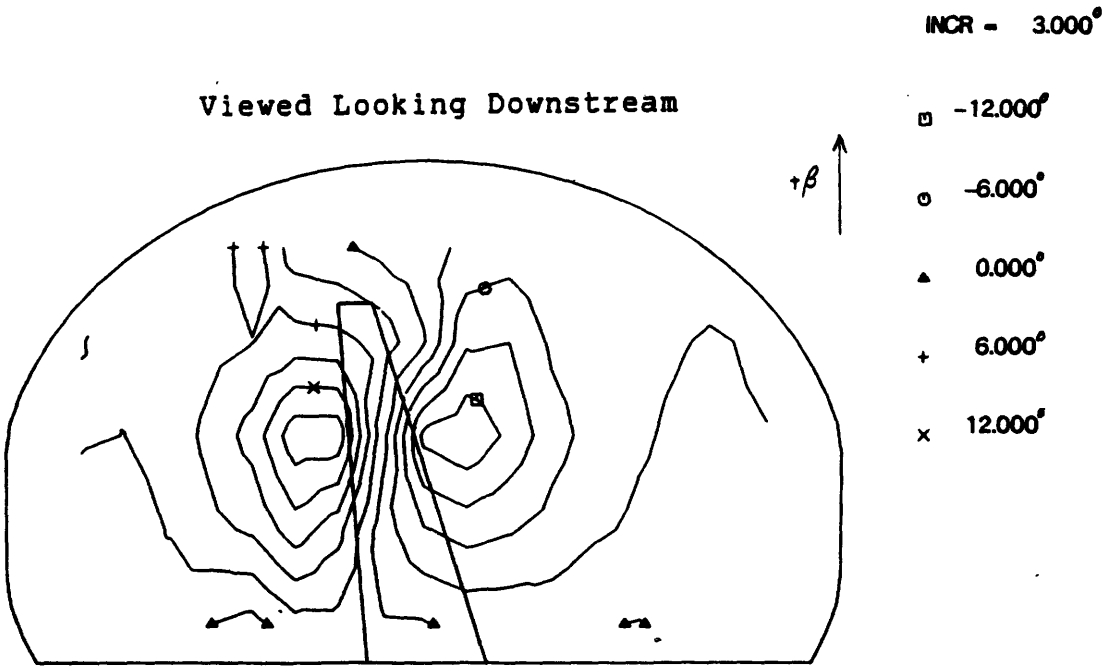

Figure B-162: Yaw angle contours at test section exit; α_{geom}=18°, δ_{le}=δ_{te}=0°.

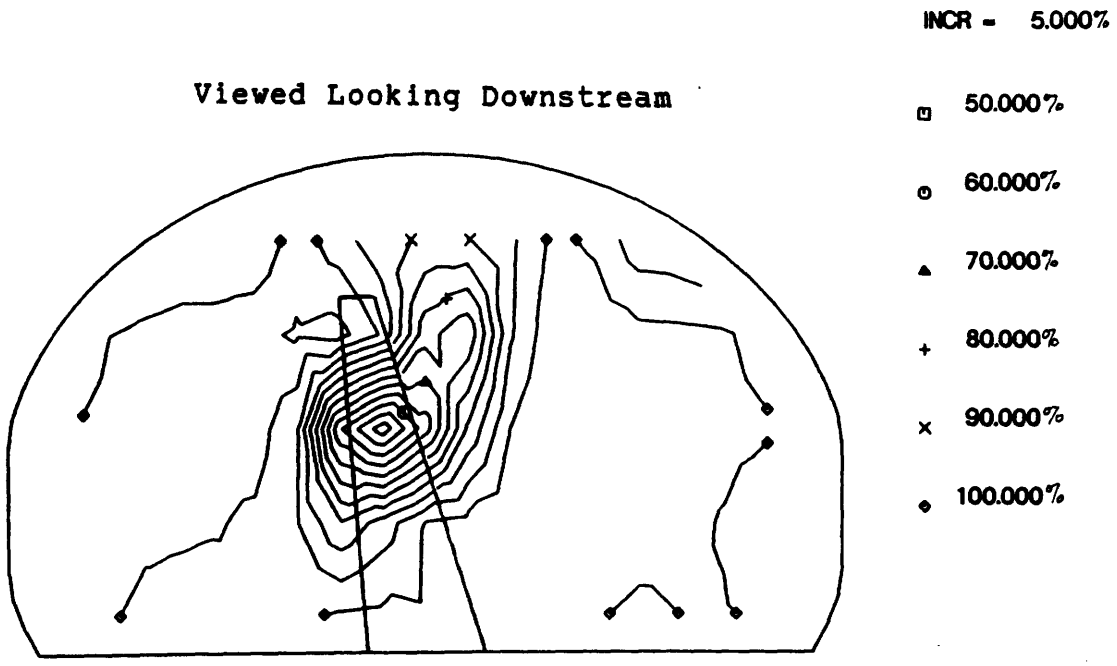

Figure B-163: Dynamic pressure contours at test section exit; α_{geom}=18°, δ_{le}=δ_{te}=0°.

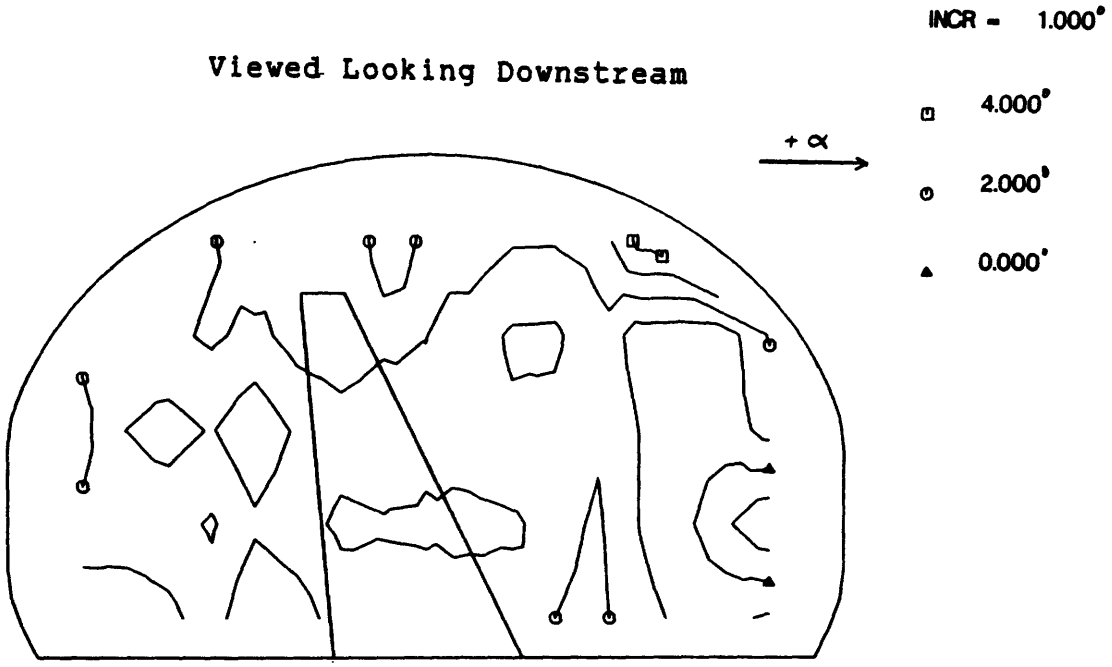

Figure B-164: Pitch angle contours at test section entrance; α_{geom}=30°, δ_{le}=δ_{te}=0°.

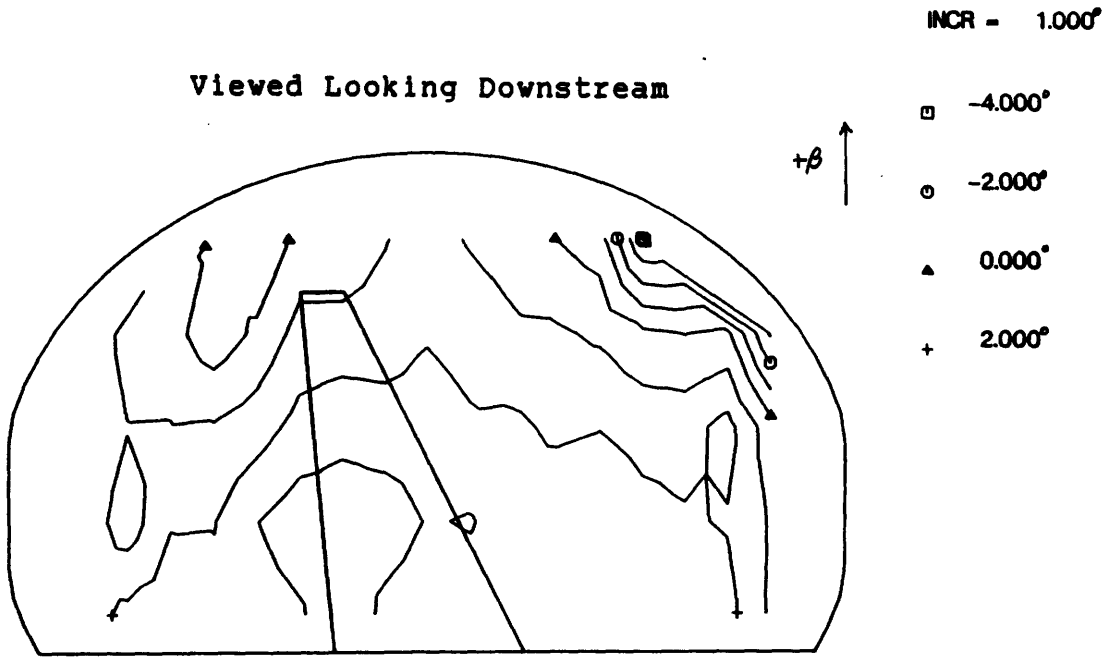

Figure B-165: Yaw angle contours at test section entrance; α_{geom}=30°, δ_{le}=δ_{te}=0°.

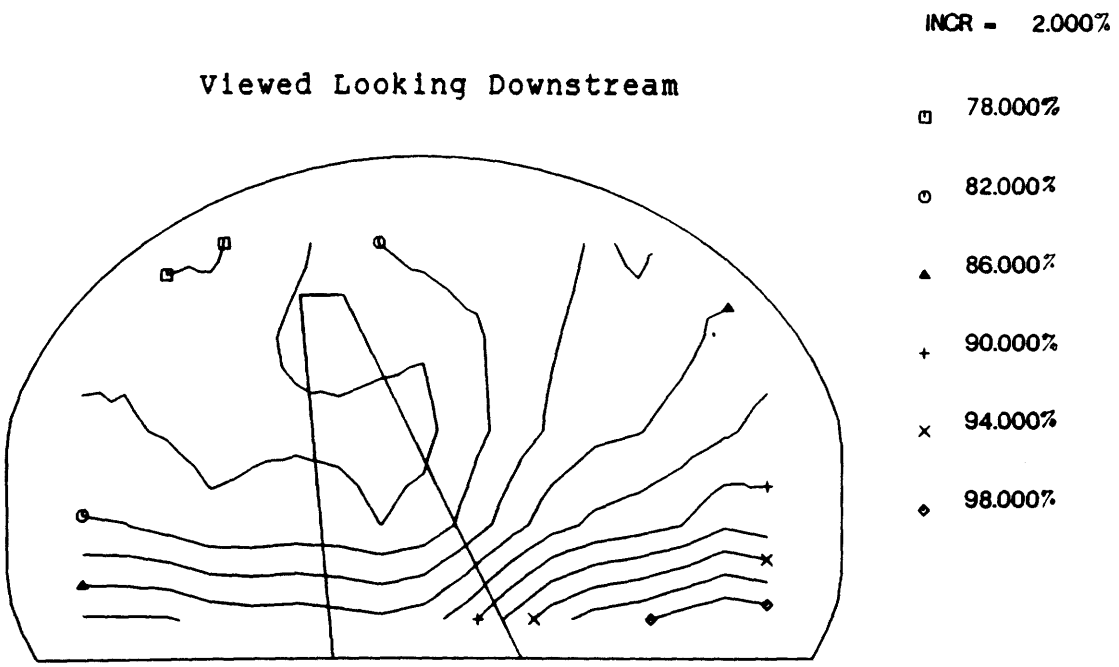

Figure B-166: Dynamic pressure contours at test section entrance; α_{geom}=30°, δ_{le}=δ_{te}=0°.

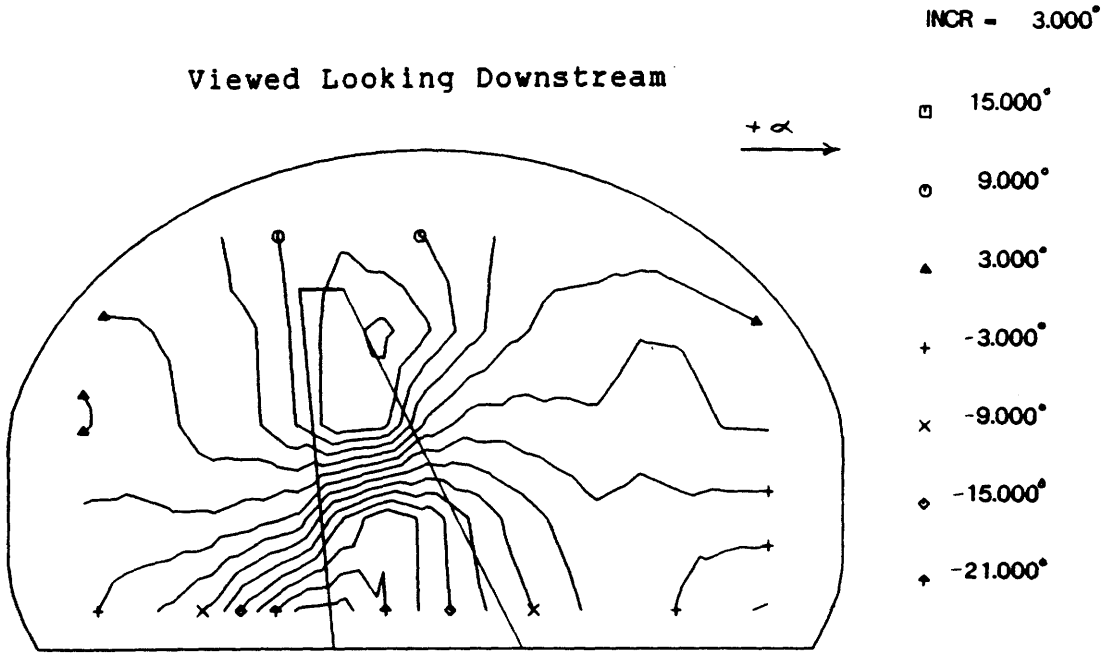

Figure B-167: Pitch angle contours at test section exit; α_{geom}=30°, δ_{le}=δ_{te}=0°.

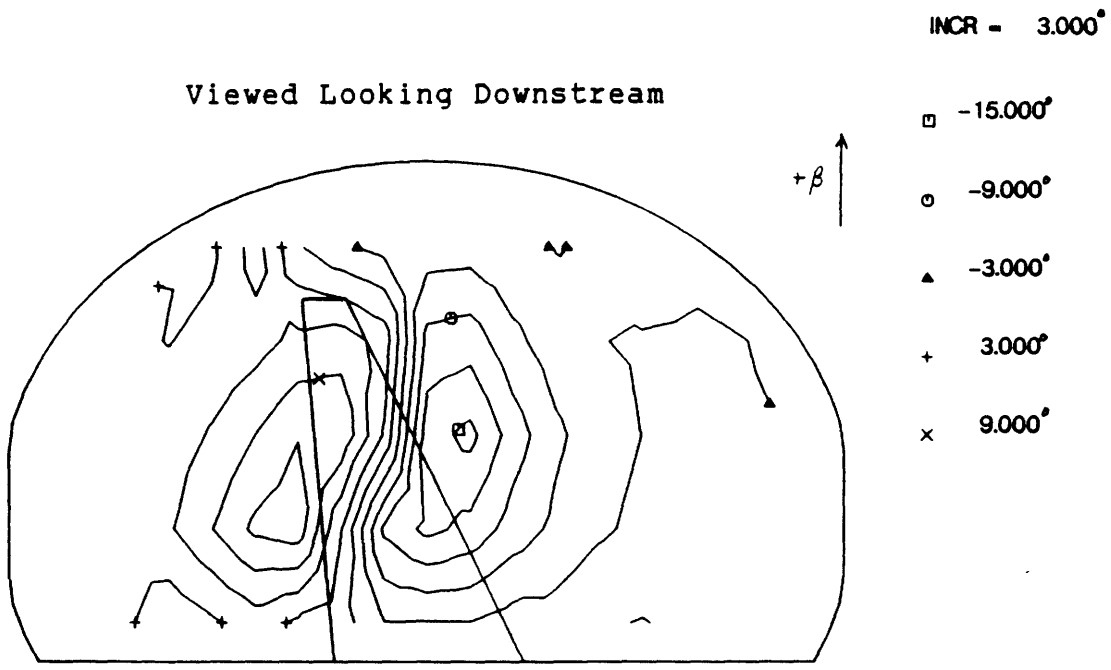

Figure B-168: Yaw angle contours at test section exit; α_{geom}=30°, δ_{le}=δ_{te}=0°.

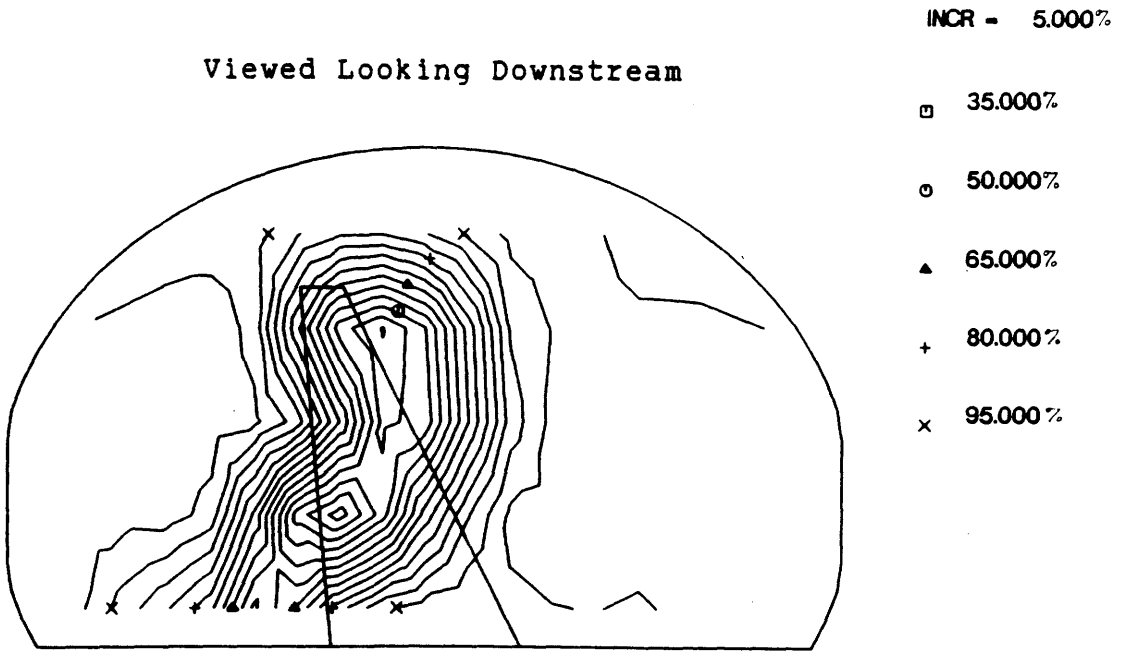

Figure B-169: Dynamic pressure contours at test section exit; α_{geom}=30°, δ_{le}=δ_{te}=0°.

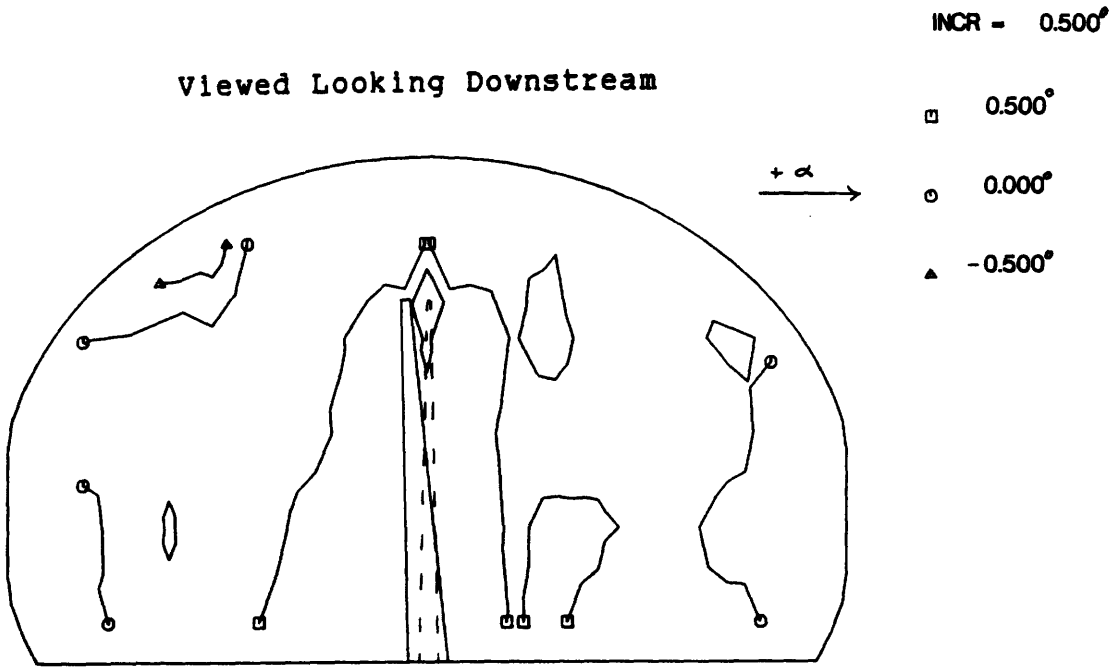

Figure B-170: Pitch angle contours at entrance with α_{geom}=0° as datum; α_{geom}=6°.

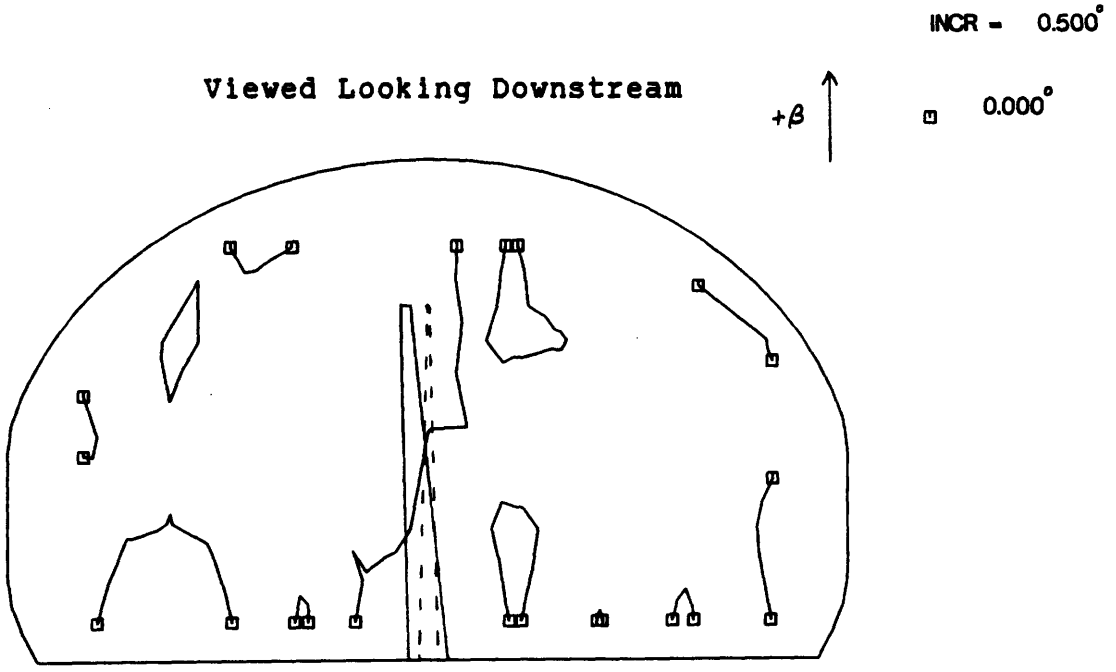

Figure B-171: Yaw angle contours at entrance with α_{geom}=0° as datum; α_{geom}=6°.

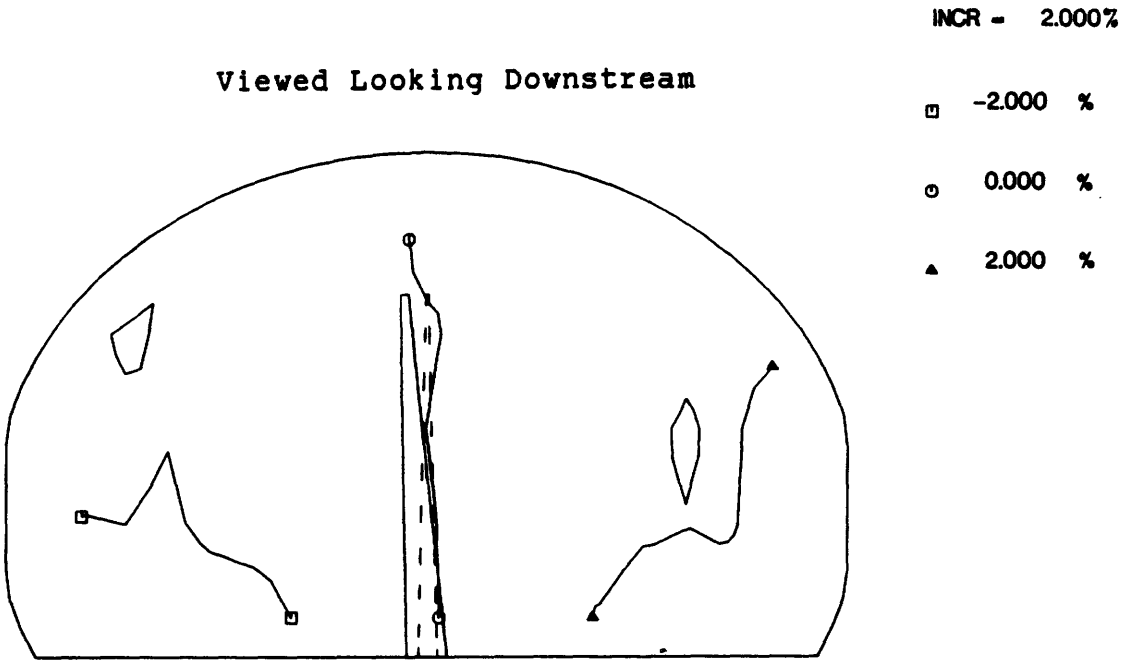

Figure B-172: Dynamic pressure contours at entrance with α_{geom}=0° as datum; α_{geom}=6°.

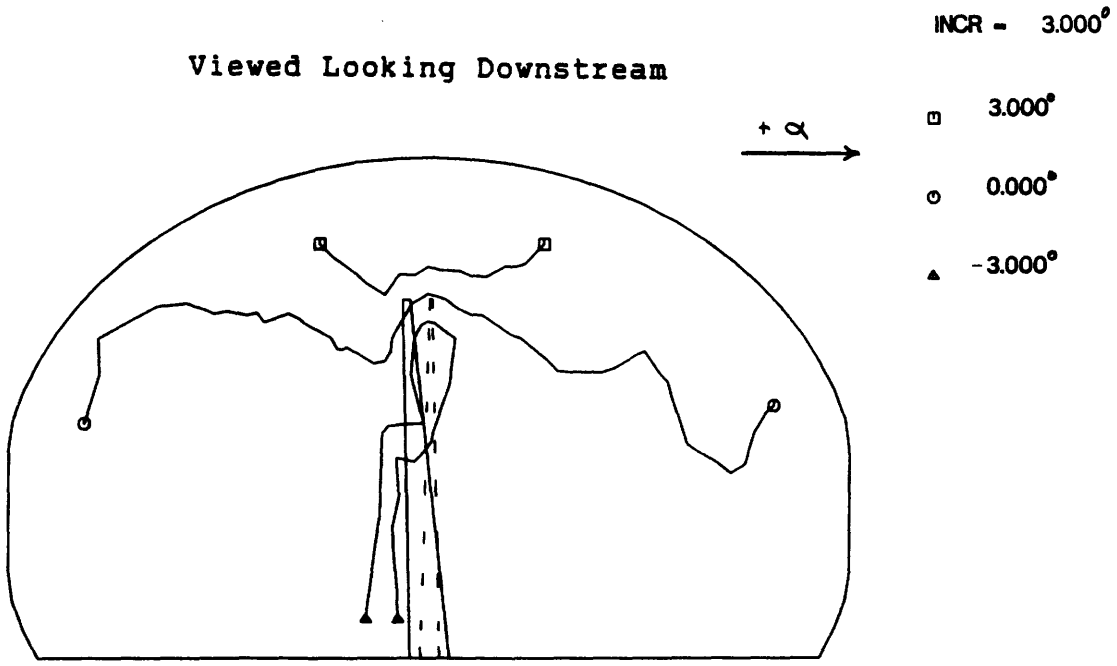

Figure B-173: Pitch angle contours at exit with α_{geom}=0° as datum; α_{geom}=6°.

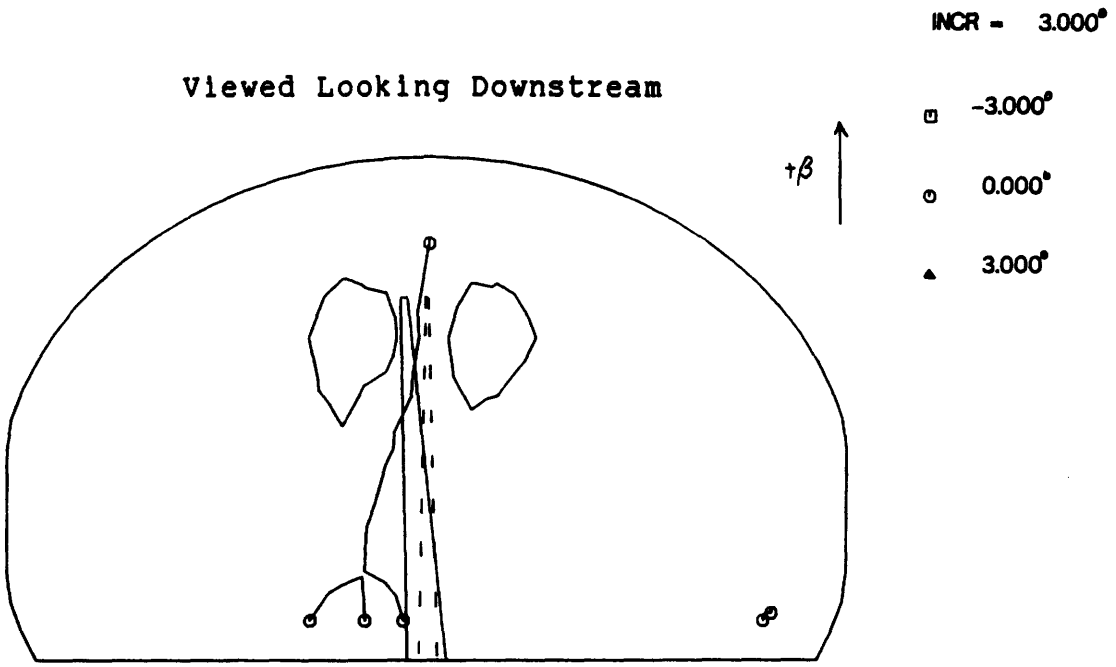

Figure B-174: Yaw angle contours at exit with α_{geom}=0° as datum; α_{geom}=6°.

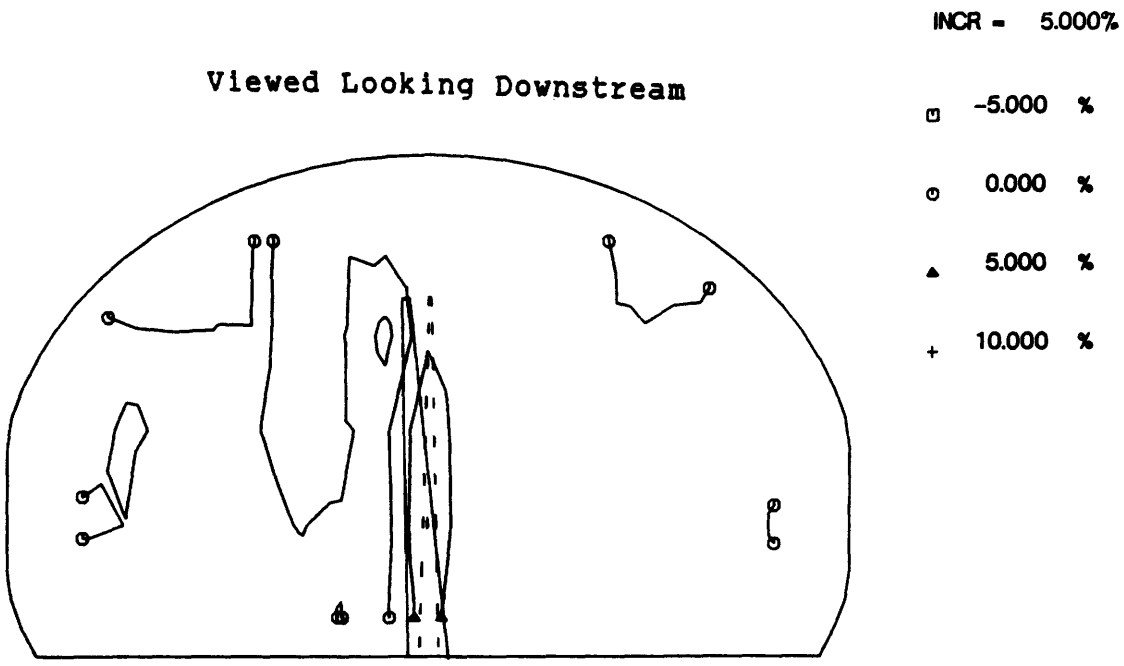

Figure B-175: Dynamic pressure contours at exit with α_{geom}=0° as datum; α_{geom}=6°.

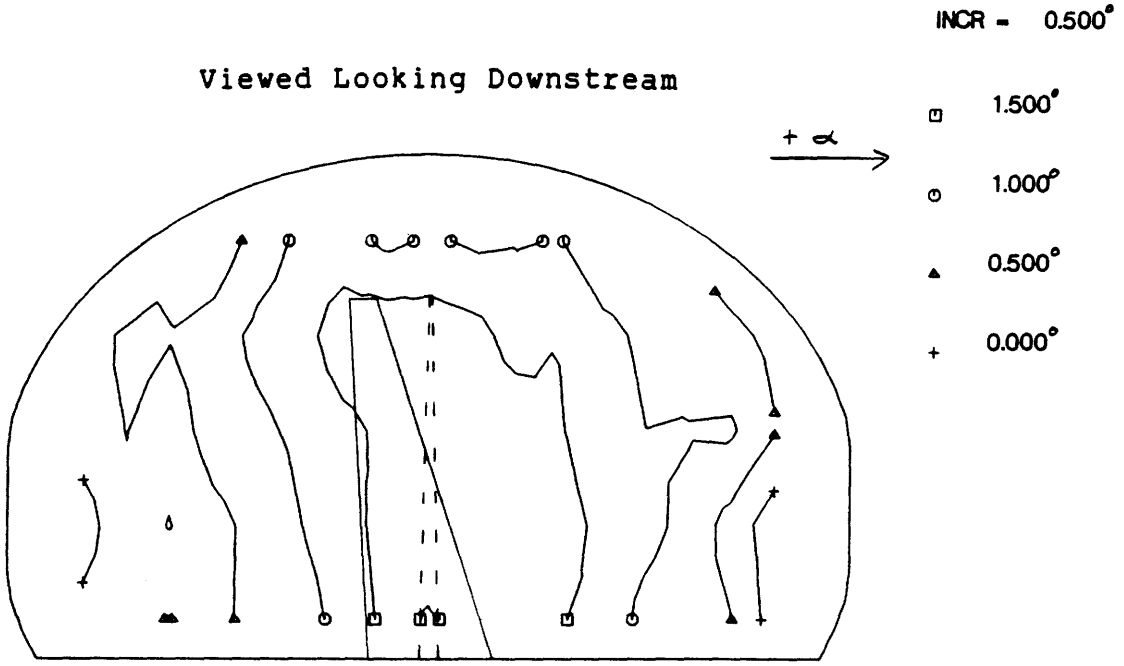

Figure B-176: Pitch angle contours at entrance with α_{geom}=0° as datum; α_{geom}=18°.

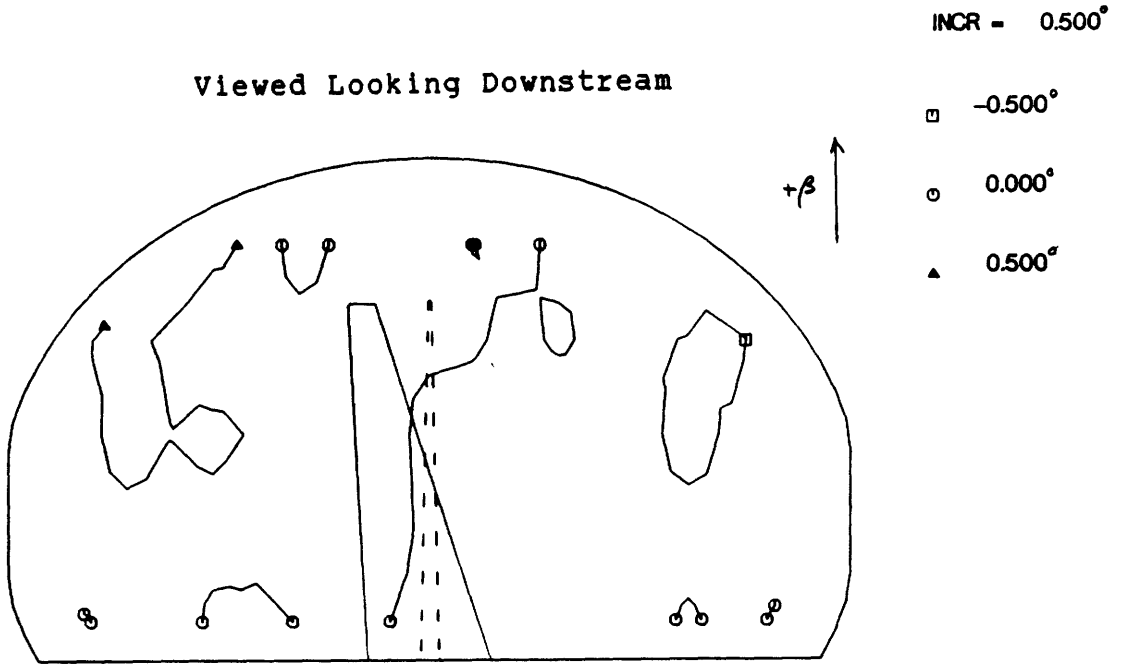

Figure B-177: Yaw angle contours at entrance with α_{geom}=0° as datum; α_{geom}=18°.

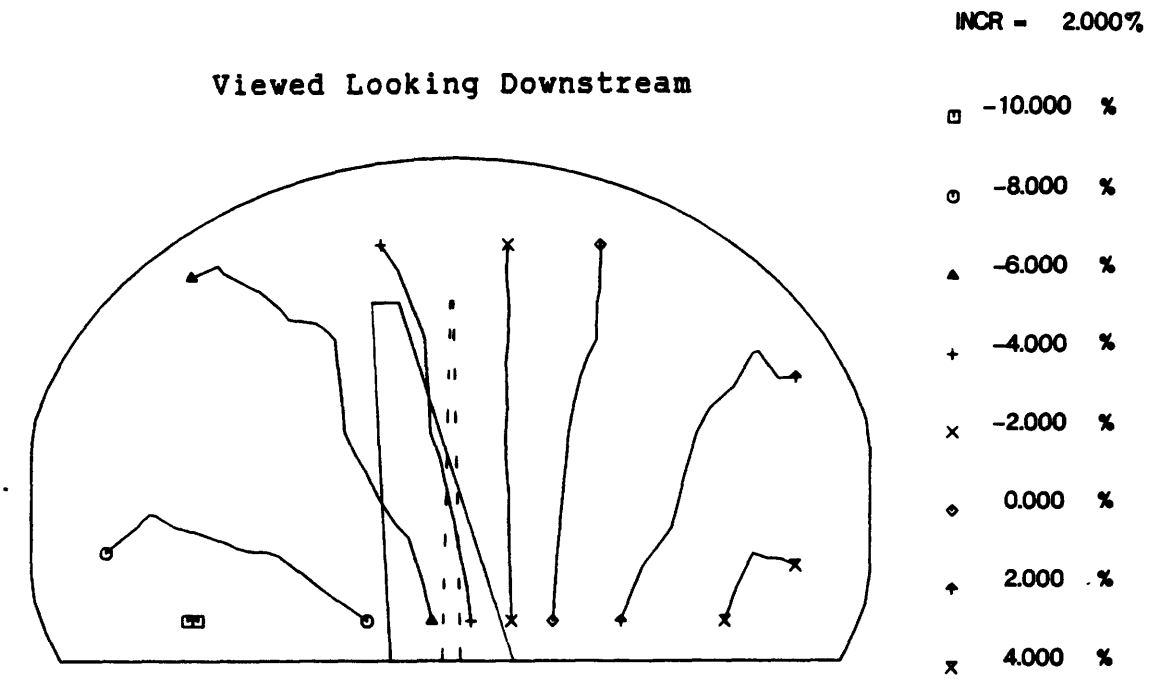

Figure B-178: Dynamic pressure contours at entrance with α_{geom}=0° as datum; α_{geom}=18°.

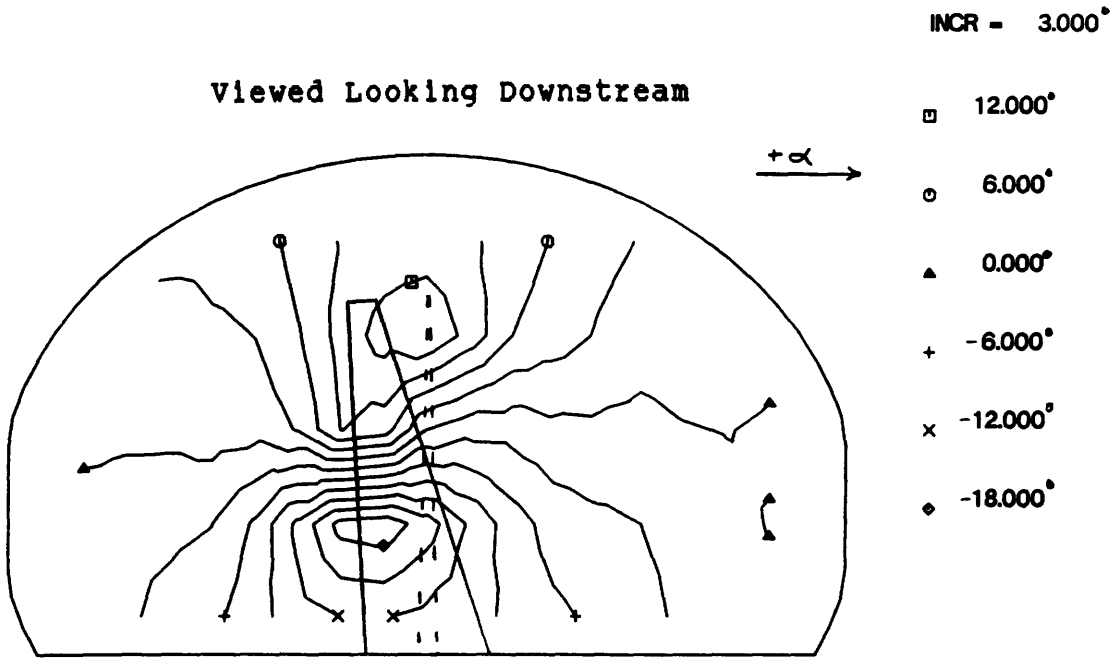

Figure B-179: Pitch angle contours at exit with α_{geom}=0° as datum; α_{geom}=18°.

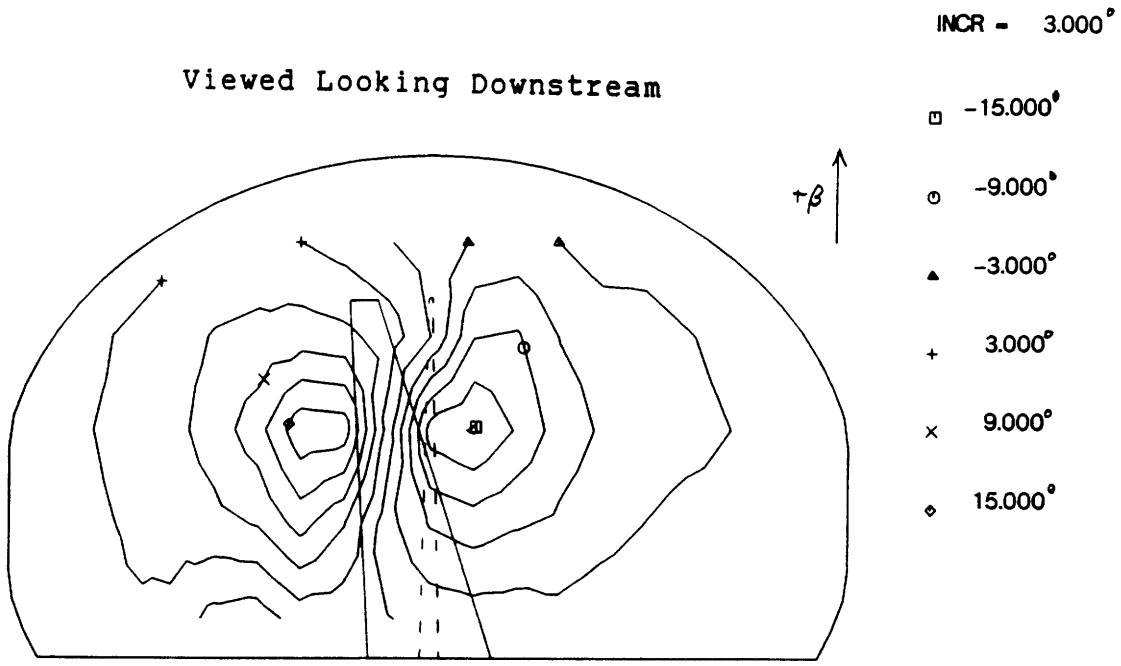

Figure B-180: Yaw angle contours at exit with α_{geom}=0° as datum; α_{geom}=18°.

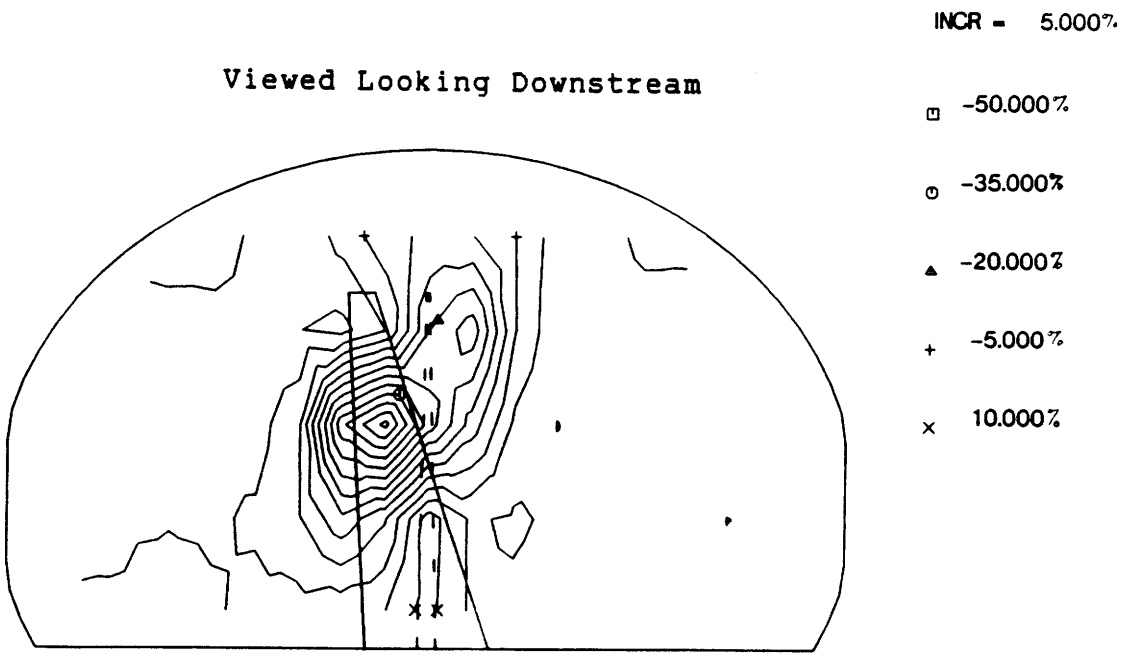

Figure B-181: Dynamic pressure contours at exit with α_{geom}=0° as datum; α_{geom}=18°.

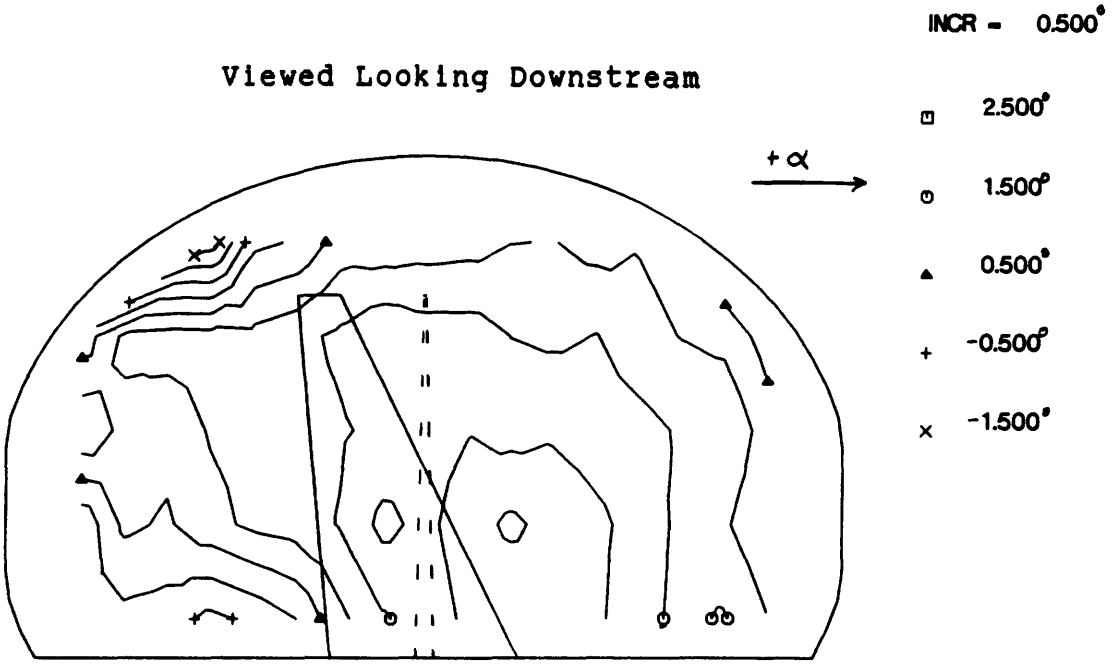

Figure B-182: Pitch angle contours at entrance with α_{geom}=0° as datum; α_{geom}=30°.

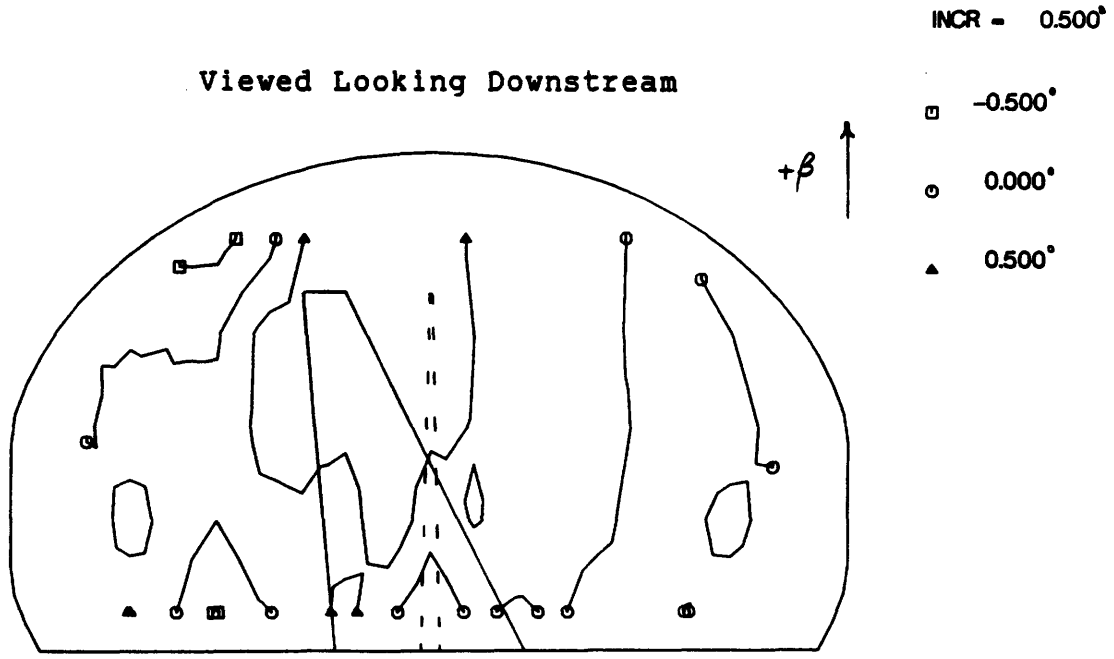

Figure B-183: Yaw angle contours at entrance with α_{geom}=0° as datum; α_{geom}=30°.

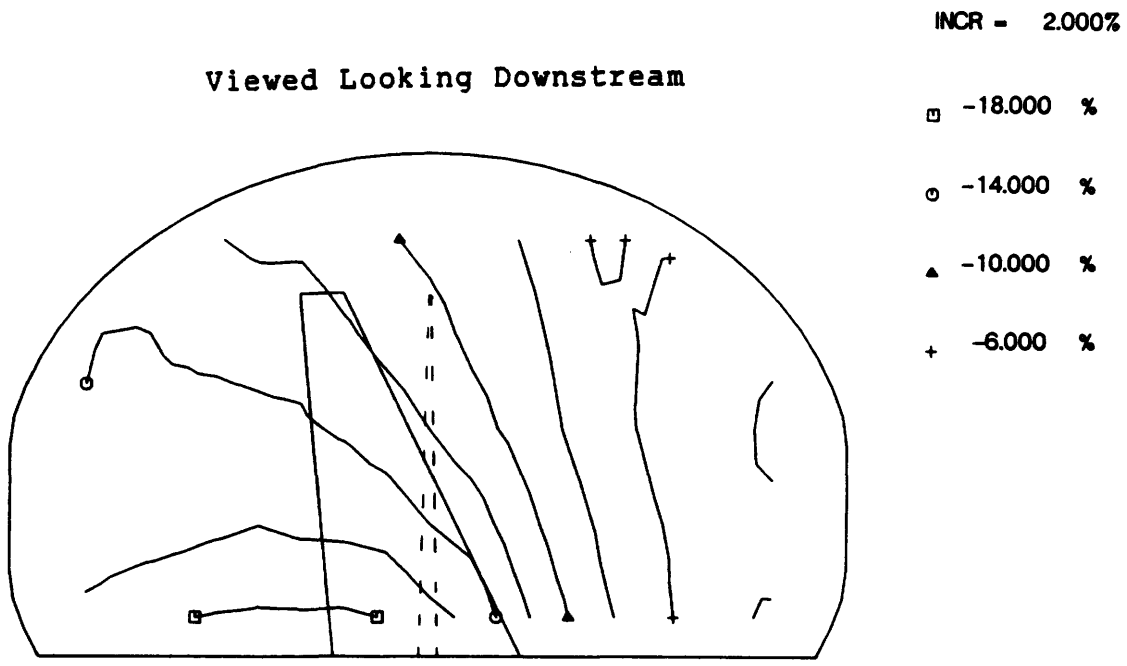

Figure B-184: Dynamic pressure contours at entrance with α_{geom}=0° as datum; α_{geom}=30°.

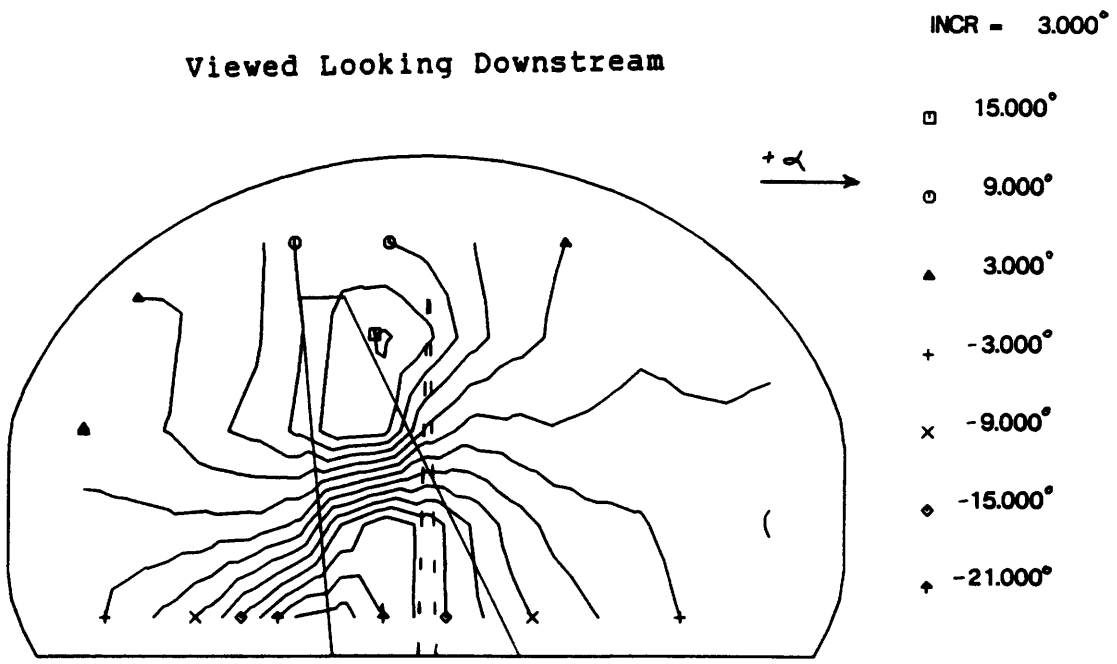

Figure B-185: Pitch angle contours at exit with α_{geom}=0° as datum; α_{geom}=30°.

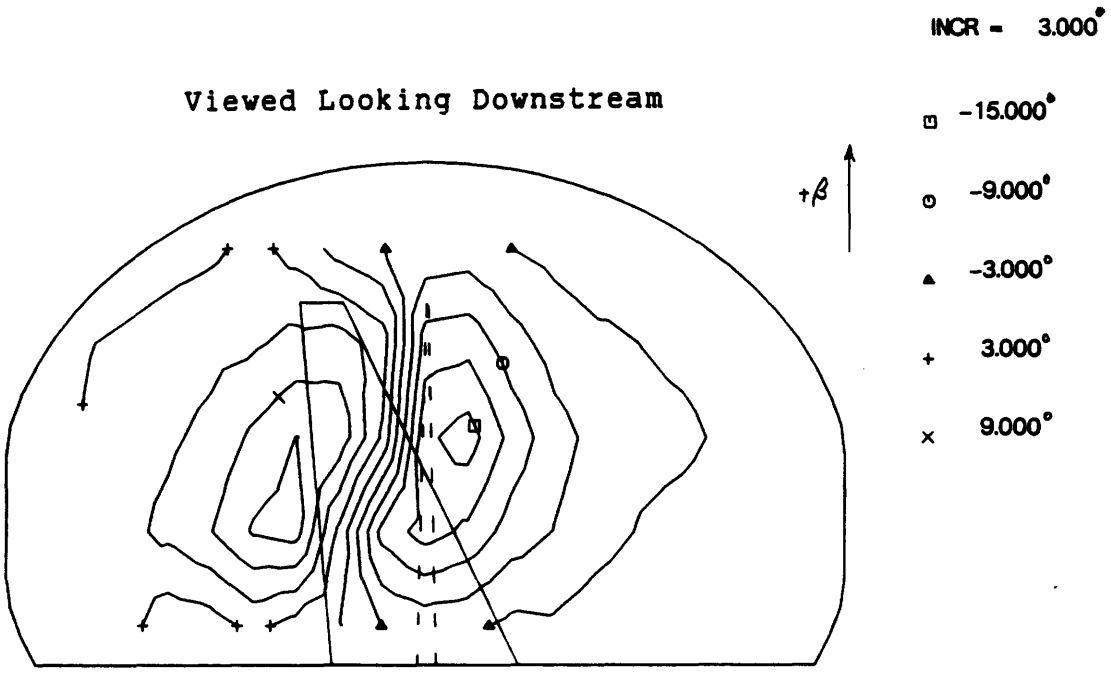

Figure B-186: Yaw angle contours at exit with α_{geom}=0° as datum; α_{geom}=30°.

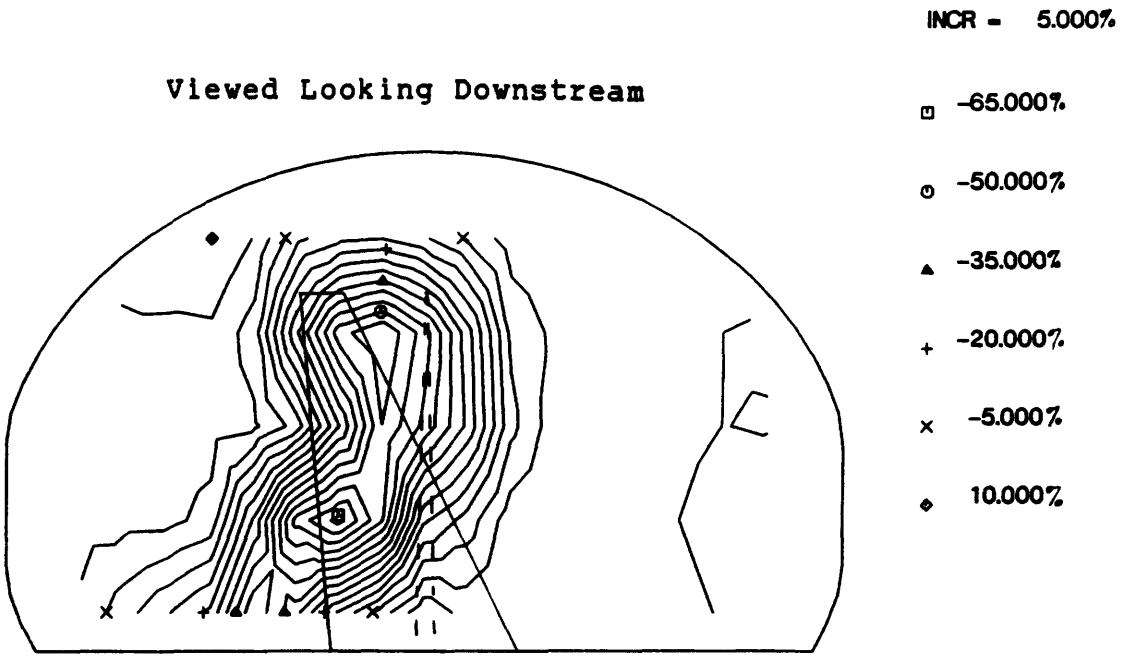

Figure B-187: Dynamic pressure contours at exit with α_{geom}=0° as datum; α_{geom}=30°.

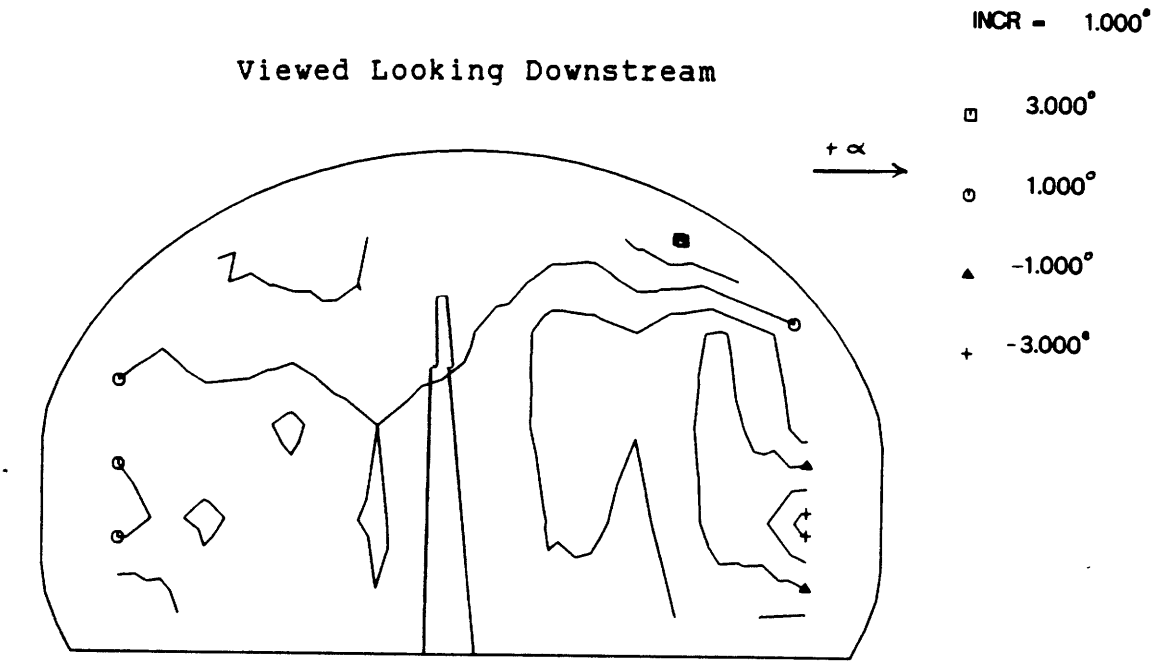

Figure B-188: Pitch angle contours at test section entrance; α_{geom}=6°, δ_{le}=δ_{te}=10°.

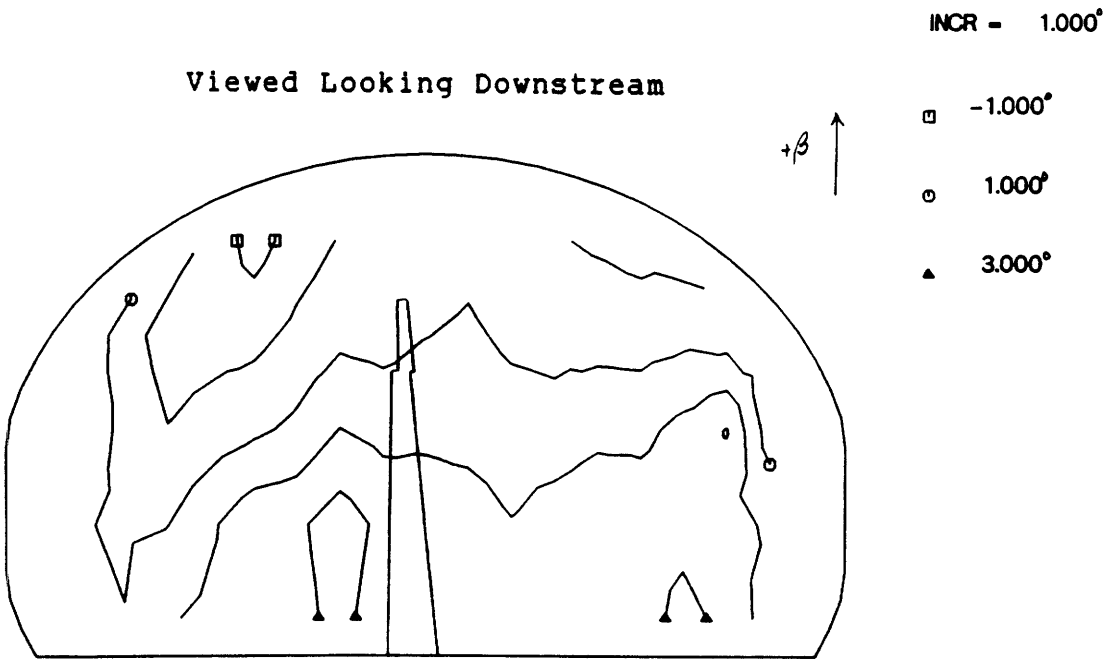

Figure B-189: Yaw angle contours at test section entrance; α_{geom}=6°, δ_{le}=δ_{te}=10°.

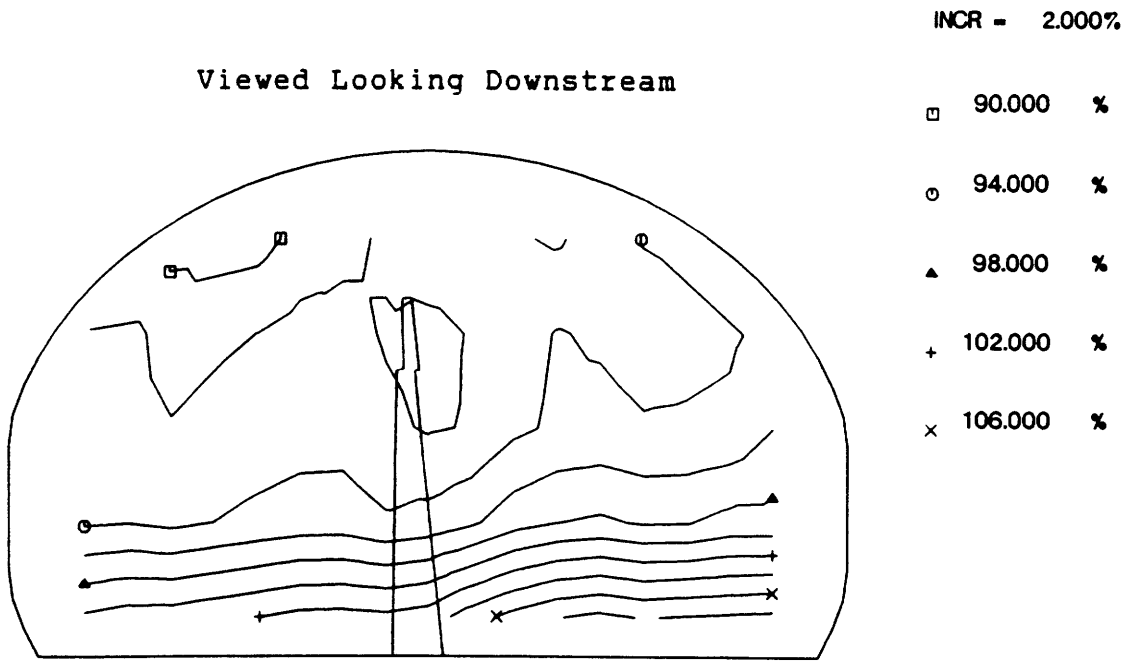

Figure B-190: Dynamic pressure contours at test section entrance; α_{geom}=6°, δ_{le}=δ_{te}=10°.

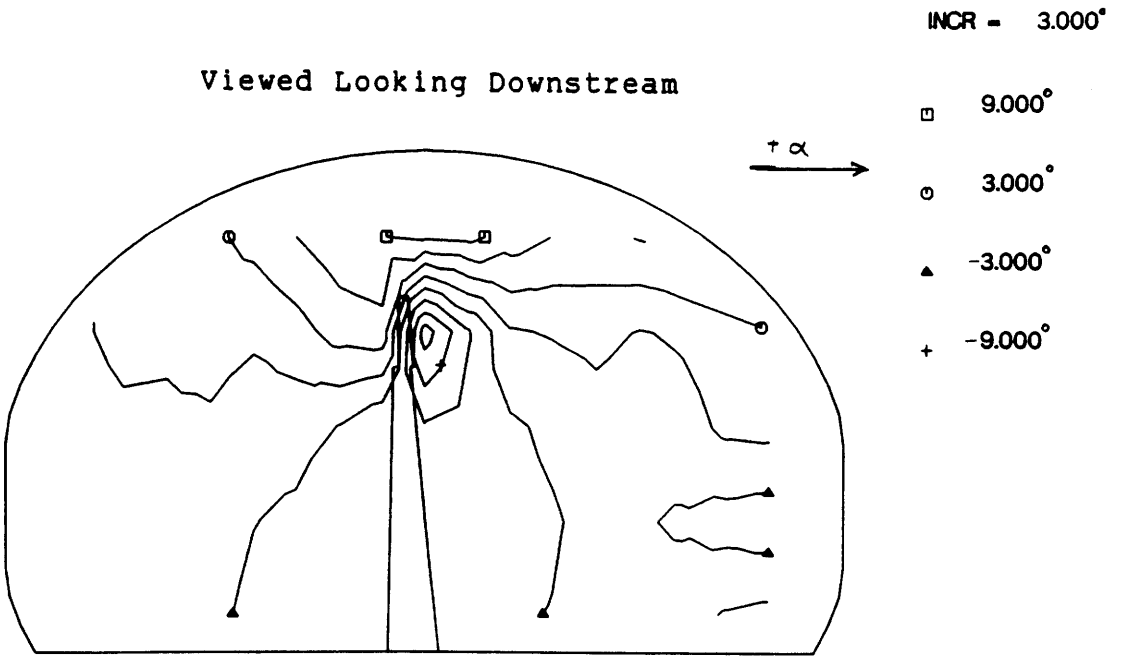

Figure B-191: Pitch angle contours at test section exit; α_{geom}=6°, δ_{le}=δ_{te}=10°.

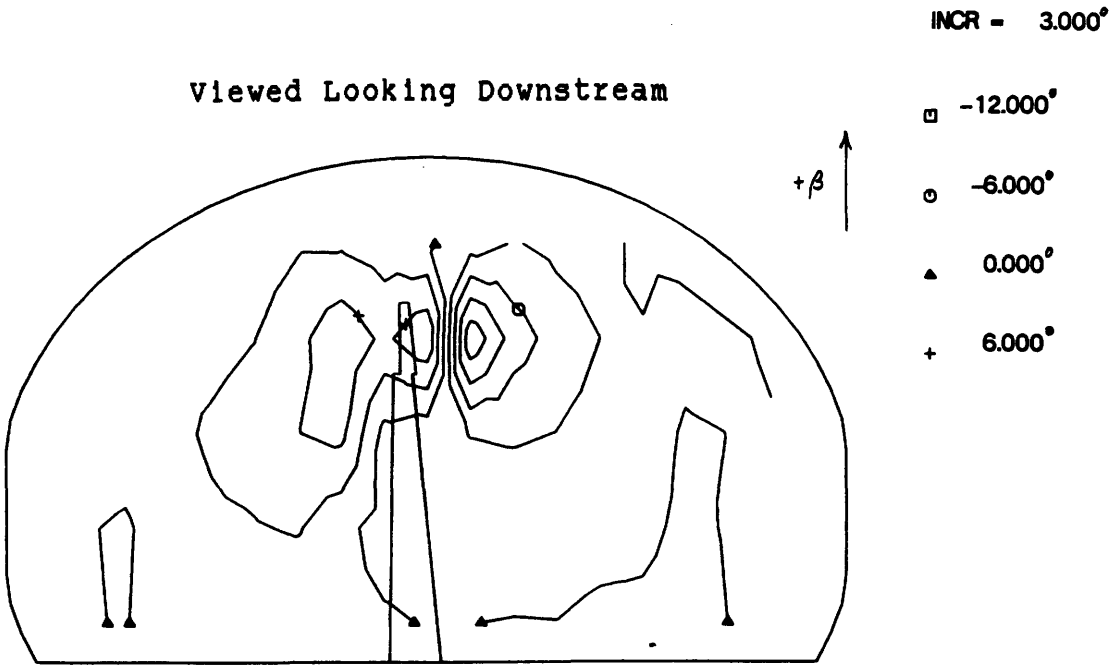

Figure B-192: Yaw angle contours at test section exit; α_{geom}=6°, δ_{le}=δ_{te}=10°.

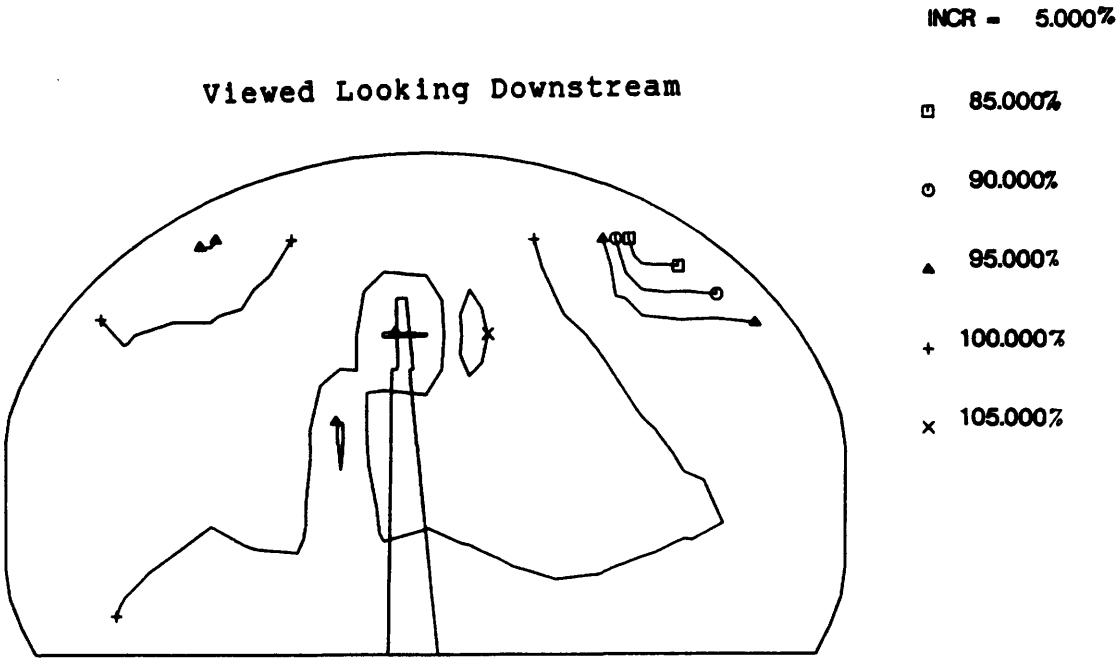

Figure B-193: dynamic pressure contours at test section exit; α_{geom}=6°, δ_{le}=δ_{te}=10°.